CHARACTERIZATION OF ELECTROCHEMICAL AND ELECTRONIC MATERIALS BY *IN SITU* AND ABERRATION CORRECTED SCANNING TRANSMISSION ELECTRON MICROSCOPY

A Dissertation

Presented to the Faculty of the Graduate School

Of Cornell University

In Partial Fulfillment of the Requirements for the Degree of

Doctor of Philosophy

by

Megan Elizabeth Holtz

December 2017

CHARACTERIZATION OF ELECTROCHEMICAL AND ELECTRONIC MATERIALS BY *IN SITU* AND ABERRATION-CORRECTED TRANSMISSION ELECTRON MICROSCOPY

Megan Elizabeth Holtz, Ph. D.

Cornell University 2017

Scanning transmission electron microscopy (STEM) is a key tool in the advancement of materials science. As nanoscale materials and atomically sharp interfaces become increasingly technologically relevant, STEM provides feedback on the individual atoms, defects and interfaces that matter in the material. Two areas where STEM characterization is critical for materials advancement are electrochemical energy materials, such as battery electrodes and fuel cell electrocatalysts, and complex oxide materials, which exhibit a diverse array of properties.

Electrochemical energy systems, including battery electrodes and electrocatalysts for fuel cells, are critical for the future of clean transportation. For these materials, investigation of the nanoscale processes which occur in liquid electrolytes is critical for understanding their performance in real devices. Encapsulating a thin layer of liquid in the TEM for *in situ* characterization is an exciting approach for gaining a detailed understanding of the underlying mechanisms of energy conversion and storage. The first half of this dissertation discusses the development and use of liquid-cell and electrochemical-cell TEM. First, I discuss the limitations and opportunities of EELS in thick liquids. I further discuss an electrochemical cell for the TEM, and its application to fuel cell electrocatalysts and battery materials. I was able to observe Pt-Ni octahedral catalyst particles degrade and lose their shape, and detect lithium ions move in a charging and discharging battery cathode ($LiFePO_4$) with nanoscale detail by mapping the electronic structure.

The second part of the dissertation focuses on complex oxides, which host a wide range of electronic and magnetic properties. Oxide interfaces, such as thin-film heterostructures and domain walls, are often atomically abrupt and produce novel functionalities. In particular, ferroelectric domain walls are rich sources of emergent phenomena – such as two-dimensional conductive sheets that form in an otherwise insulating solid – due to their unusual electronic properties or symmetry breaking. We probed how ferroelectric distortions change at domain walls with STEM for $ErMnO_3$. From the STEM images, we calculated the order parameter at many domain walls in $ErMnO_3$ to create a statistical picture of the ferroelectricity at these topological defects, and also observed how the order parameter changes near vortex structures. We further apply these methods to lutetium ferrite superlattices, where we use feedback from STEM to design a near-room-temperature multiferroic material in which ferroelectricity enhances the magnetism. We find that there are confined charged domain walls in the superlattice that additionally boost magnetism.

BIOGRAPHICAL SKETCH

Megan Holtz was born in Stuttgart, Germany to Dr. Susan Holtz and Dr. Mark Holtz, and spent most of her childhood in Lubbock, Texas. She has one younger brother, Eric, who she lived with until her graduation from Monterey High School in 2006. Then, she started studying physics at Trinity University in San Antonio, Texas. She spent three happy summers as an REU student at Texas Tech University, where she became enthused about scientific research. Then, at Trinity, she helped install a squeaky wind turbine on the roof of the physics building, hooked up some solar panels, and fabricated organic photovoltaic cells in a home-made dry box. In 2010, Megan made the journey north to Cornell in her black 1998 Volvo S70, where she started as a PhD student in David Muller's group in the School of Applied Physics. She spent the first half of her PhD developing methods for *in situ* liquid and electrochemical cell transmission electron microscopy. During the second half of her PhD, she characterized ferroelectric polarizations and domain walls in hexagonal manganites and ferrites by mapping the picometer atomic displacements that generate polarization. Megan's favorite times in Ithaca involve enjoying the natural wonders of the gorges with Elliot Padgett, who she married on August 19, 2017. Megan plans to continue her research of oxide materials along with electron microscopy in Darrell Schlom's group at Cornell, and then wherever life may take her.

To my parents, Mark and Susan.

ACKNOWLEDGEMENTS

First and foremost, I would like to express my sincere gratitude to my advisor, Prof. David Muller. His support made my time at Cornell possible. He afforded me flexibility and expert guidance that allowed me to work on many diverse and interesting projects. I am thankful for all he has done to share his expertise in electron microscopy, physics, materials science, giving talks, and writing papers - as well as his patience and good humor while teaching me. I have enjoyed being a part of his group these seven years.

I sincerely thank Prof. Abruña for sitting on my committee and being a second advisor for the energy materials and *in situ* part of my time at Cornell. His encouragement and enthusiasm are very much appreciated. I would also like to thank Prof. Schlom for serving on my committee and providing interesting samples to investigate. I have enjoyed the collaboration with him and his group so much that I am looking forward to starting as his postdoc next year.

I would also like to thank Dennis Meier and Andres Cano, and his postdoc Konstantin Shapovalov, who provided samples, theory, and enthusiasm for the $ErMnO_3$ project.

None of the work in this thesis would have been possible without the help of the TEM facility managers, especially John Grazul and Mick Thomas. Besides keeping the microscopes running, they make the labs a cheerful and encouraging place. I would also like to thank Dr. Kirkland, for his help on the NION and sharing scripts and advice. Finally, I would like to thank Mariena, who keeps the floors of PSB lively.

I owe a great debt of gratitude to the students in the Muller group who trained me. Especially Julia Mundy, who took me under her wing in the lab and got me going with interesting oxide projects. She has been one of my allies and friends. Without the help of Pinshane Huang, I may have been lost and confused in the sea of graduate school. Her compassionate advising helped me through many struggles. Also, special thanks to Lena Kourkoutis, who I look up to, and

Robert Hovden, whose curiosity on many fronts is inspiring. They have all inspired me and pushed me to be a better scientist and microscopist.

My contemporary Muller group students: Qingyun Mao, Barnaby Levin, and Kayla Nguyen, and Paul Cueva, we have gone through the bulk of graduate school together, and I thank them for the good times and interesting work that we have shared. I would also like to thank the younger Muller group students: Elliot Padgett, Yimo Han, Celesta Chang, Michael Cao, and Ela Correa, for their questions that pushed me to learn more, and for keeping the office a fun place to be. Extra thanks to Elliot Padgett for proof-reading sections of this dissertation. Also, I would like to thank the post-docs, Ye Zhu and Zhen Chen, although my cross section with them was limited I have learned in those interactions. Finally, thanks to the undergraduates in the lab, Nina Andrejevic and Pratiti Deb, both of whose enthusiasm for science was motivational and I enjoyed sharing an office with them. Finally, thanks to Vera Beermann, our visiting scholar, whose kind ways and interesting nanoparticles precipitated us doing an experiment which (against the odds) worked, resulting in Chapter 4.

Thank you to all of Prof. Abruña's students who I have had fruitful and exciting collaboration with, especially in the first half of my PhD. Particularly, Yingchao (Alex) Yu, who was my close collaborator on all things liquid and electrochemical cell. Alex taught me a lot, in and out of the lab. Also, the others who helped: Deli Wang, Li Xiao, Nikki Ritzert, Eric Rus, Joaquin Rodriguez Lopez, Yao Yang, and last but certainly not least, Burak Ulgut, who – with his floating potentiostat – made reasonable electrochemistry happen in a TEM after a lot of failed effort.

Thanks to the other EMC^2 collaborators, Jimmy O'Dea, Deniz Gunceler, Shankar Sundararaman, and Katie Schwarz. I very much enjoyed working together.

I have also enjoyed close collaboration with the Schlom Group students. In particular, Julia Mundy and Charles Brooks who grew interesting samples brightened the 2nd floor Duffield

office. I also enjoyed imaging the high-quality samples from Hanjong Paik, Arsen Soukiassian, Carolina Adamo, Hari Nair, Rachel Steinhardt, and Rainer Held.

I owe thanks to the centers at Cornell and the funding agencies that have made this work possible. Particularly the Cornell Center for Materials Research Shared Facilities, where I made extensive use of the Electron Microscopy Facilities, which are supported through the NSF MRSEC program (DMR-1719875). The research on electrochemical energy systems was funded as an Energy Materials Center at Cornell (emc^2), an Energy Frontier Research Center funded by the U. S. Department of Energy, Office of Basic Energy Sciences under Award Number DESC0001086. The research on complex oxides was funded by the U.S. Department of Energy, Office of Basic Energy Sciences, Division of Materials Sciences and Engineering under Award DESC0002334.

My friends that ate lunch and/or played board games together over the years: Andrea Katz, Austin Griffith, Asha Jain, Brian Abbett, Erin Lamb, Alan Lamb, Yi Jiang, Michael Cao. They have supported and encouraged me, and kept things fun.

Special thanks go to my parents, whose stories of graduate school made me keen to go, and whose unwavering support has kept me going. Thanks to Eric, I couldn't have asked for a better brother and friend. And finally, thanks to Elliot, whose curiosity for science and drive to help the world made me love him. I look forward to wherever life takes us.

TABLE OF CONTENTS

LIST OF FIGURES

LIST OF TABLES

CHAPTER 1

INTRODUCTION

In the past two decades, the field of (scanning) transmission electron microscopy, or (S)TEM, has undergone a revolution that has dramatically expanded the toolbox of available techniques for materials characterization. Aberration correctors sharpened the STEM probe to smaller than one angstrom, rendering atomic resolution imaging almost routine [1,2]. Aberration correction has also increased the electron beam current tenfold [1], making electron energy loss spectroscopy (EELS) capable of atom-by-atom determination of composition [3,4] and bonding from spectroscopic fingerprints and their fine structure [5]. Several frontiers are under development – notably high energy resolution spectroscopy [6], *in situ* techniques [7], and scanning diffraction measurements [8,9] – each of which opens pathways to new and exciting scientific opportunities. As researchers seek to develop new functional materials by design, TEM provides a path for investigating and understanding the roles of individual atoms, defects and interfaces that govern the properties of materials.

I have devoted my dissertation research to two areas of materials research where STEM characterization has been essential in the development of new science and technology. The first area is materials for electrochemical energy systems, including battery electrodes and electrocatalysts for fuel cells, which are critical for the future of renewable energy. In these heterogeneous materials, it is critical to understand the materials performance and degradation on the nanometer scale. Because these electrochemical processes typically occur in electrolyte, encapsulating a thin layer of liquid in the TEM for *in situ* characterization is an exciting approach for gaining a detailed understanding of the underlying mechanisms of energy conversion and storage.

The second area is the field of complex oxides, which host a wide range of electronic and magnetic properties. Oxide interfaces, such as thin-film heterostructures and domain walls, are often atomically abrupt and produce novel functionalities. For example, in ferroelectric materials, domain walls and vortices are rich sources of emergent phenomena – such as two-dimensional conductive sheets that form in an otherwise insulating solid – due to their unusual electronic properties or symmetry breaking. By experimentally probing these atomically abrupt features with statistical measurements from atomic resolution STEM data, one can address their fundamental physics and work towards realizing oxide electronic devices.

This dissertation contains two parts: one on *in situ* TEM of electrochemical energy materials, and one on aberration corrected STEM on complex oxide materials. This chapter will outline both parts of the thesis and provide introductory background information for each.

For the *in situ* introduction, I will first provide an overview of *in situ* liquid-cell STEM (Section 1.1), and then cover two of the main challenges: electron beam effects (Section 1.2) and beam spreading in thick liquid layers (Section 1.3). Then I will briefly introduce fuel cells and batteries, two potentially fruitful applications for liquid-cell microscopy (Section 1.4). This will launch into a discussion of the limitations of EELS in liquids in Chapter 2, *in situ* electrochemistry and fuel cell studies in Chapter 3, the application of these tools to the study of the degradation of octahedral PtNi fuel cell electrocatalysts in Chapter 4, and the spectroscopic study of Li-ion motion in a charging and discharging battery in Chapter 5.

For the section on STEM of complex oxides, I will first introduce the motivation and the system in Section 1.5, and the measurement of the polarization and order parameter in Section 1.6. I will then study the inner structure of domain walls and vortices in hexagonal $ErMnO_3$ in Chapter 6. In Chapter 7 I will investigate the ferroelectricity at all relevant length scales in room-temperature

multiferroic lutetium ferrite superlattices. This will be followed by a discussion of interface modes in phonon scattering by fast electrons in Chapter 8.

1.1 Liquid Cell STEM

Scanning transmission electron microscopy is a powerful tool that can reveal structure, composition, and electronic structure information down to the atomic scale, but its conventional use is restricted to thin, solid specimens. The capability of imaging in liquids would open doors to a broad range of studies in materials science, biology, geology, fluid physics and beyond [10,11]. However, there is an inherent difficulty in imaging high-vapor pressure liquids, like water in the high vacuum of an electron microscope. One method to image in liquids is to encapsulate liquid in a sealed or flow cell with electron transparent membranes, developed early in the TEM community [12,13], which has become a popular method used today. In addition to maintaining a liquid in the electron microscope, good imaging conditions must be maintained. For TEM, this requires that the liquid be a thin layer to avoid the deleterious effects of multiple scattering of the electron beam. Recent developments in microfabrication have enabled the fabrication of the thin "liquid cell", an encapsulated pouch of liquid that is kept thin by two electron transparent silicon nitride windows on a silicon-processed chip, and is clamped in a TEM holder with the use of O-rings to prevent liquid exposure to the high vacuum of the microscope (for example, see Figure 1.1) [10,14]. The two chips can be patterned with electrodes for electrochemical experiments. For materials scientists, this enables real-time viewing of nanoparticle growth, material corrosion, battery operation and degradation, and fuel cell catalyst nanoparticle coalescence at nanometer length scales. For a comprehensive overview of all things liquid cell, please refer to Francis Ross's 2017 book [7].

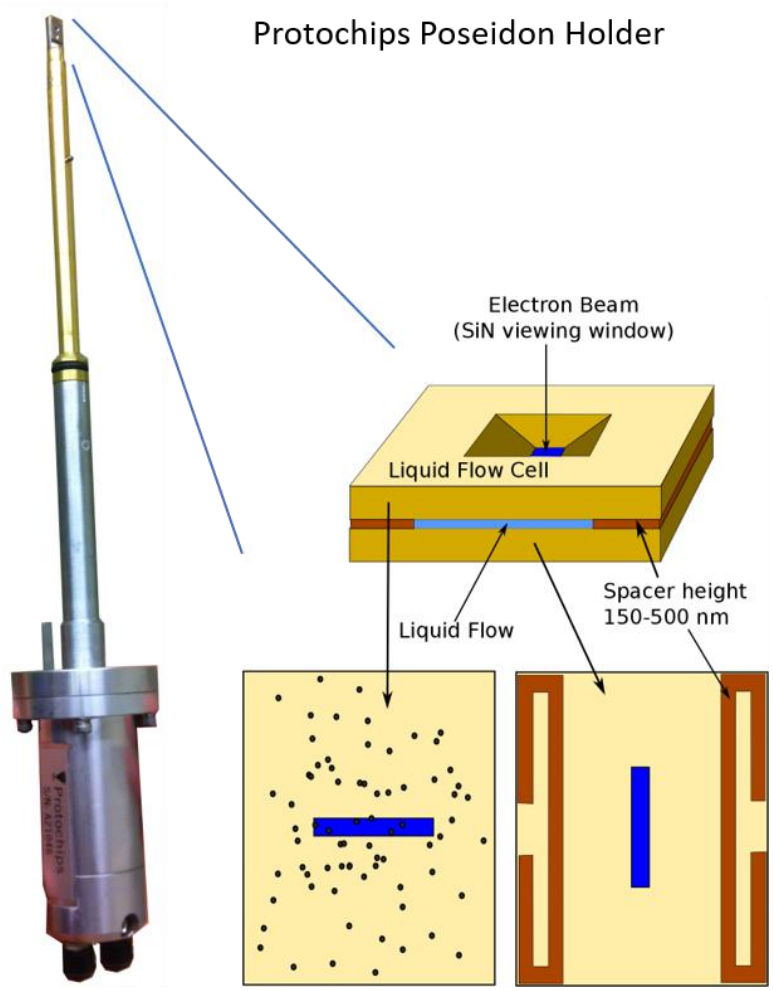

Figure 1.1. Liquid cell schematic. Left hand side: photo of the liquid cell holder. At the tip of the holder, there is a small microfluidic cell comprised of 2 silicon based chips (shown at right) that form a sandwich with a spacer that can be between 0 and 2 microns thick, but is typically 150-500 nm. Microfluidic tubing inside the holder allows liquid flow from a syringe pump through the holder to a waste beaker.

There are two key challenges in liquid cell microscopy: one challenge relates to how the electron beam interacts with the specimen and liquid in the cell, which provides an intrinsic limitation on the dose that can be supplied (and thus the obtainable resolution) to avoid the electron beam from being the dominant effect in the cell. The other challenge is maintaining good imaging resolution through thick liquid layers. How the resolution degrades with liquid thickness can be

understood by considering multiple scattering of the electron beam. This largely an engineering challenge to design the thinnest liquid cell, but can also be improved by selecting an imaging mode with the highest signal to background imaging conditions – typically high angle annular dark field (HAADF) STEM, although in extremely thick specimens incoherent bright field (IBF) may be preferable. These two challenges will be briefly discussed.

1.2 Electron Beam Considerations for Liquids

Above all other experimental challenges, electron beam induced damage is a major limitation on the *in situ* liquid cell TEM technique. In the case of aqueous solution in the liquid cell, the electron beam drives radiolysis which generates reactive species such as solvated electrons, protons and radicals. In the region that the electron scatters in the liquid, the ionized species that are generated often recombine, but those that do not then diffuse away from the initial "spur." Under a steady-state dose, these ionized species soon reach an equilibrium concentration in the solution [15]. These reactive species can chemically react with the materials of interest in the liquid cell to drive reactions that may not be the intended subject of study in the liquid cell. Generation of hydrogen can form bubbles [16] (in the form H_2) or the protons can alter the pH [15]. The hydrated electrons can be strong reducing agents, generating metals from metal cations in solution [17–23]. For example, in Figure 1.2, in an aqueous solution of a silver nitrate precursor with sodium citrate surfactant, a dendritic silver nano-composite growth begins to form within a few seconds of imaging with the electron beam. After 5 minutes, the metal deposit is more than a micron across! The only reducing agent applied was the electron beam.

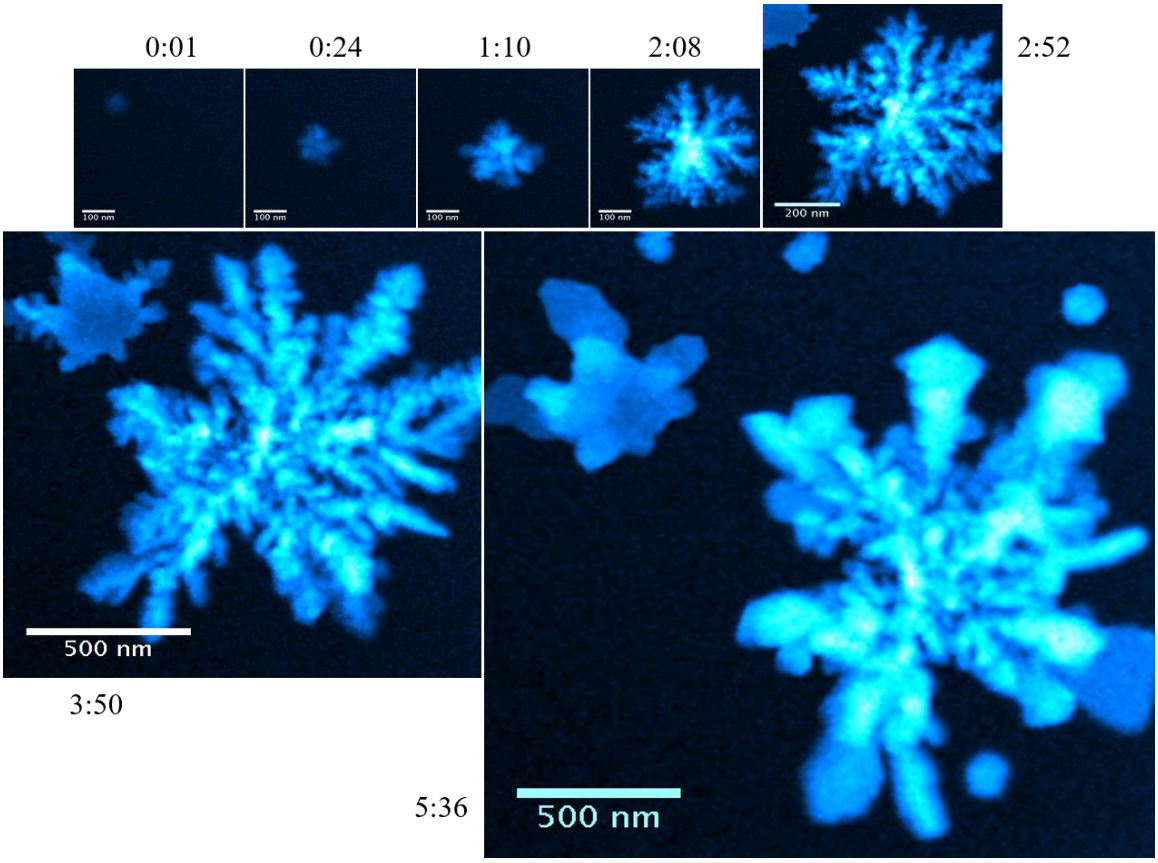

Figure 1.2. *In situ* STEM images of the growth of a star-shaped silver nano-composite observed in a ~500 nm thick aqueous solution, in real time. Understanding the nucleation and growth of silver nanoparticles is important to the synthesis of functional nanomaterials with preferred morphology, such as electrocatalysts for energy conversion, biosensors, and antimicrobial agents. This also demonstrates the reducing power of the electron beam. Work done in collaboration with Yingchao Yu.

Electron beam induced damage is so universal to liquid cell techniques that a significant fraction of the literature leverages the electron beam as the main stimulus in the *in situ* study, reporting metal nucleation and growth and bubble formation [7,16,17]. Because the aim of most studies is not to explore electron radiation effects, efforts must be made to understand beam dose limitations. One promising direction is to use chemical scavengers to mitigate the effects of ionized species or radicals on the material at interest [24]. Another approach is to lower the beam dose, and

image at a low enough dose rate and under a total maximum dose that electron beam induced effects are not manifested. This dose can be determined from tabulated values or from performing control experiments to asses if the electron beam impacts the material of interest without any stimulus applied. While this dose threshold may not display any outward effects, it may still have unwanted effects during the *in situ* experiments, so additional controls are required, such as observing areas which did not experience the stimulus (such as off of the electrode in an electrochemical cell) and comparing to *ex situ* experiments or to experiments run while the beam is not continually imaging.

When the dose is minimized to avoid electron beam damage in solution, an inherent trade-off is made in terms of contrast and resolution. Because the signal to noise ratio in the images is limited by Poisson statistics, large numbers of counts are required to achieve high resolution. In particular the dose required to form an image with a certain signal to noise ratio (SNR) with contrast *C* and resolution *r* obeys [25]:

$$dose \propto \frac{(SNR)^2}{C^2 r^2}$$

This means that while it may be reasonable to expect atomic resolution movies of beam-induced phenomena, such as the beautiful work done by Yuk [18] and Zheng [17], in other studies where the electron beam effects are deleterious, microscopists may be required to use resolutions of 1-10 nm, which would allow operation with 10^2 – 10^4 times less dose than Ångstrom-resolution imaging requires. In addition, because *in situ* studies typically require many images, not just one, each image must account for only a fraction of the total dose limit. Thus, in cases where the electron beam induced phenomena are not the main interest, the resolution may be limited by radiation damage considerations, instead of by the thickness of the liquid cell.

1.3 Beam Spreading in Liquids

As the electron beam passes through materials, it may elastically scatter to a finite angle to the incident probe. In a specimen that is many mean free paths thick, what was once an atomically sharp STEM probe will become quite diffuse, spreading out several microns and ultimately limiting resolution [26–28]. Because the probe increases in size as it propagates through the material, spatial resolution will be improved if the specimen is located on the top surface of the liquid cell in STEM mode, because the interaction with the object of interest will still be with a sharp probe. For TEM mode, the resolution will be improved if the electron beam interacts with the sample of interest last, so the specimen should be near the exit surface of the liquid cell. This is the well-known top-bottom effect [28].

Monte Carlo simulations are straightforward to implement to describe beam broadening for customized specimen geometries [29]. Electron trajectories are simulated given cross sections for elastic scattering in the material, as shown in Figure 1.3a for a 200 kV beam scattering in liquid. By running large numbers of electron trajectories, histograms of the electron beam profile can be made, as in Figure 1.3b. In this figure, the scattering geometry is a 500 nm thick liquid with a gold nanoparticle in the middle of the liquid layer, and the probe profiles only consider electrons that would make it to the bright field (BF), incoherent bright field (IBF) and high angle annular dark field (HAADF) STEM detectors. The Monte Carlo method thus allows exploration of the behavior of the electron beam with various specimen and detector geometries, and has been useful in understanding contrast and resolution in liquid cell studies [30,31].

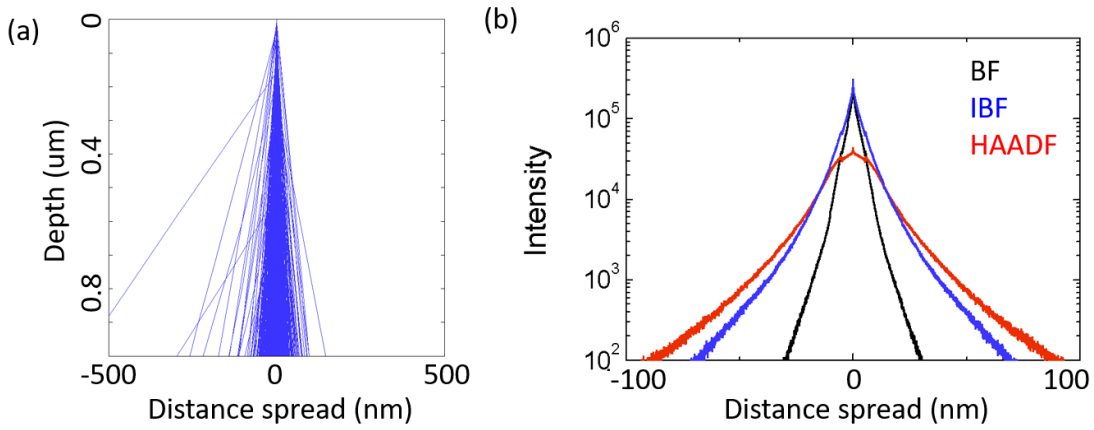

Figure 1.3. Monte Carlo simulations illustrating beam spreading in liquid. (a) electron trajectories through 1 micron of water. (b) the probe profile of electrons that make it to 3 different STEM detectors for a 10 nm gold nanoparticle in the middle of 500 nm of water.

The ideal thickness for STEM specimens would be well under one mean free path (corresponding to 110 nm of water for 200 kV electrons). In slightly thicker liquid cells (100 – 500 nm), the resolution will not be as strongly affected as the contrast will be. This is because in thickness regimes where there is still some unscattered beam left, corresponding to the peak in intensity in Figure 1.3b at the center of the beam, the resolution will be determined by the initial probe, but the multiply scattered, broadened skirt of the beam will contribute to the background contrast [32]. At thicknesses so large that there is no unscattered beam, the resolution will degrade rapidly.

It is a well-known challenge that for electron energy-loss spectroscopy, the specimens must be extremely thin. In Chapter 2, we will discuss how the liquid thickness impacts EELS studies in the microscope.

1.4 Applications of the Electrochemical Cell

Electrochemistry is the study of chemical reactions that occur with charge transport, usually including interfaces between a solid "electrode" and a liquid "electrolyte." These reactions are typically driven by an externally applied potential or current. Electrochemical reactions are the bread-and-butter of many fields within energy generation and storage, in systems such as pseudo-capacitors, photo- and electro- catalysis, fuel cells, and batteries. By the incorporation of electrodes into the liquid cell, electrochemical reactions can be studied *in situ* [14]. The design of an electrochemical cell chip and some fuel cell studies are discussed in Chapter 3. A larger study of octahedrally-shaped Pt-Ni nanoparticles is discussed in Chapter 4. An *in situ* TEM battery study of $LiFePO_4$ is presented in Chapter 5.

Fuel cells are a particularly intriguing technology because they directly convert the chemical energy in a fuel, such as that stored in the bonds of H_2, into electricity. Because there is no combustion step in a fuel cell, the efficiency of energy conversion is not limited by the Carnot cycle efficiency. Fuel cells are a clean alternative to the internal combustion engine, and may play a part in energy storage by re-conversion of hydrogen fuel to electricity. There are many ways to engineer a fuel cell, but one of the most popular designs is the proton exchange membrane fuel cell (PEMFC) presented in Figure 1.4a. As its name suggests, the center of a PEMFC is a membrane in acidic media which allows proton transport, but is electrically insulating. It uses hydrogen as the fuel, which is split at the anode into its constituent protons and electrons. The protons pass through the membrane and the electrons pass through an external circuit to the cathode, where the oxygen reduction reaction (ORR) occurs, converting the oxygen, protons and electrons into water. One of the key challenges in these types of fuel cells is that the ORR reaction is hard to catalyze, and requires a large amount of expensive platinum to provide significant power performance in the cell. Making the best use of that platinum by going towards well dispersed, high surface-area-to-volume

nanoparticles, or by using better electrocatalysts such as higher activity platinum alloys, are directions which have been under intense exploration in the field. Here, we will study degradation of Pt and Pt alloy nanocatalysts on carbon supports in the electrochemical cell and see how Pt surface area is lost due to Pt coalescence, surface area loss, and migration due to carbon corrosion.

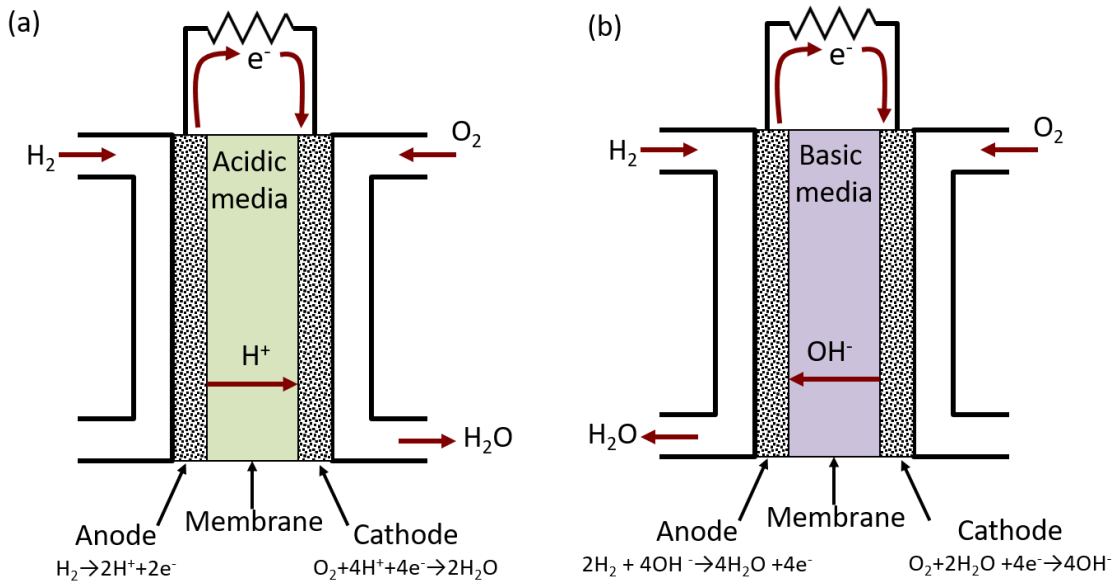

Figure 1.4. Fuel cell schematics of PEMFCs (a) and alkaline anion exchange membrane fuel cells (b).

A second type of fuel cell which is gaining attention for its improved ORR kinetics is the alkaline anion exchange membrane fuel cell (AAEMFC) (Figure 1.4.b), which has the potential to use less expensive cathode electrocatalysts but has not been significantly studied due to the difficulty in finding a membrane that is stable in basic media while allowing efficient transport of OH^- ions. Recent work at Cornell by the Coates group [33] has demonstrated alkaline membranes with high stability. Here we image them in the electrochemical cell and observe one of the main mechanisms of clogging of the cathode: the formation of carbonate agglomerates which occur due to CO_2 contamination in the basic media.

Rechargeable batteries represent another technology with great potential for impacting in the future of renewable energy. Because most types of renewable energy are intermittent in nature (for example, solar and wind), energy storage systems must be designed for energy demand to be met. Additionally, we are already seeing a turn towards electric cars which are largely powered by batteries. One of the most popular technologies is the lithium ion battery, due to its high energy density. Lithium ion batteries work by shuttling lithium ions out of the cathode, where they are more energetically stable, across an electrolyte and into the anode (Figure 1.5). When the battery is left to discharge, the lithium ions move out of the anode and across the electrolyte, back into the cathode.

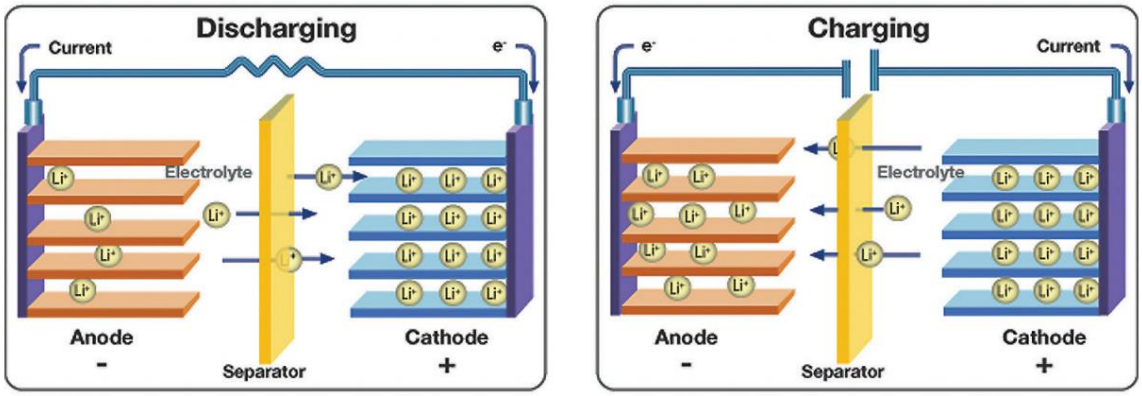

Figure 1.5. Schematic of a Li-ion battery. During discharge, left, the lithium ions move from the anode to the cathode, which is more energetically favorable. Electrons pass through the external circuit, powering a device. During charge, a voltage is applied to move the lithium ions from the cathode to the anode. In commercial Li-ion batteries, the cathode is often a transition metal oxide or phosphate and the anode is often graphite. Taken from Thermo Fischer Scientific [34].

How well the lithium ions move into and out of the electrode – or how they lithiate and delithiate – is a key aspect in the battery's success. This is affected by internal defects, which clog the lithium transport channels, grain-level properties such as how the grains are oriented, and

structure-level properties such as how much the material expands or shrinks upon the insertion or removal of lithium (too much and the material may crack or be irreversibly altered). As new battery materials are developed, how they lithiate on the atomic and grain length scales as well as any surface reconstructions that may take place will be important to understand for their overall performance.

1.5 Hexagonal Ferroelectrics

Complex oxides host an amazing variety of electronic properties, including superconductivity, magnetism, ferroelectricity and ionic conduction, largely due to strong electron correlations [35,36]. Because of their adaptability, oxide materials are now being used for applications as diverse as batteries, liquid crystal displays (LCDs), and information storage. Controlling oxide interfaces – as we do for conventional silicon-based electronics – can further open doors to realizing new oxide devices.

One primary class of oxide materials where there has been a great deal of effort is the perovskites, which have the ABO_3 structure. Many different chemistries can be incorporated into the perovskite structure, which can be combined into heterointerfaces which can strain the material or yield emergent phenomena [37,38]. This large flexibility has allowed tuning of the diverse array of properties mentioned above. A second class of oxide materials that is gaining attention is the hexagonal manganites and ferrites, RBO_3 where R = Y, In, Ho … Lu, Sc, and B = Mn, Fe. The baseline $P6_3/mmc$ structure is paraelectric, but in most of these materials, a zone-tripling structural distortion (the trimer distortion) tilts the BO_5 bipyramids and buckles the R-planes and drives geometric, improper ferroelectricity [39–41]. This results in a polar structure with either two R atoms up, one atom down (↑↑↓) in the polarization up structure, or two atoms down, one atom up (↓↓↑) in the polarization down structure – forming six $P6_3cm$ structural domains. This class of

materials has attracted much attention for exhibiting multiferroic behavior and for having domain walls that both display emergent phenomena and interesting symmetry breaking [42–46].

One exciting avenue for development in oxide electronics is in the pursuit of multiferroic materials [46–49], or materials that couple both electric and magnetic ordering. These materials would allow the switching of a magnetic memory moment by applying an electric field, which promises to be more energy efficient than the typical method of passing a current to switch a spin. Researchers have made great strides towards these materials, but they have yet to demonstrate easy switching of strong ordering at room temperature. Multiferroic materials are rare, however, due to the competing nature of ferroelectricity (requiring an insulating material, usually with a transition metal in a $3d^0$ state) and magnetism (requiring an uncoupled spin, usually occupying a transition metal 3d state) [50]. The hexagonal improper ferroelectrics get around this requirement by having structural distortions which can couple to both the electric and magnetic ordering of the system [49], and so are a promising route to multiferroic materials.

Additionally, the intersections of two ferroelectric domains form domain walls, which are a different variety of oxide interfaces than the better known thin-film heterostructures, and can also produce novel functionalities. Ferroelectric domain walls are promising candidates for next-generation circuit elements due to their unusual electronic properties – for example, forming a two-dimensional conductive sheet in an otherwise insulating solid – and because of their highly controllable nature that allows them to be formed, moved and erased on demand. Because of their flexibility and interesting electronic properties, one dream would be to make nanoscale circuitry out of domain walls that could be reconfigured and adapted on the fly. Recently, it was shown that it was possible to toggle between conductive and resistive states at “charged” ferroelectric domain walls by applying an electric field [51]. At “charged” domain walls, a polarity mismatch drives local charge compensation at the domain wall, driving the electronic reconstruction. This allows reversible electric-field controlled switching between resistive and conductive domain wall states,

corresponding to binary switch (shown in Figure 1.6) and paves the way toward digital devices made from domain wall circuitry.

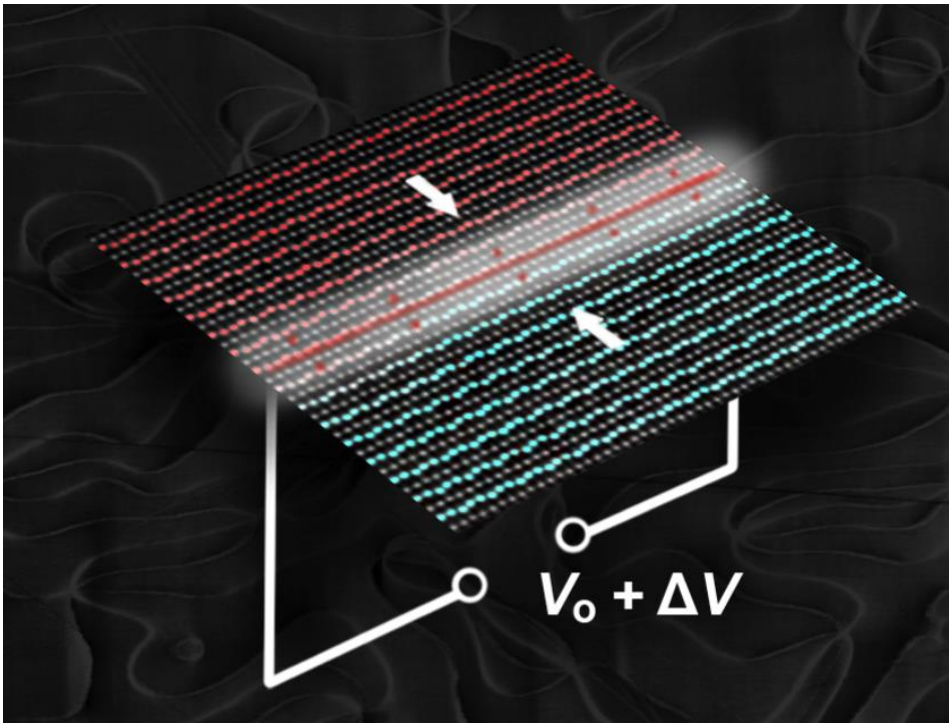

Figure 1.6. Conceptualization of a ferroelectric domain wall acting as a switch, (Mundy et al [51]). The forefront is an atomic resolution STEM images with the polarization down domain in red and the polarization up domain in turquoise. The head-to-head domain wall has a build-up of positive charge, which drives electrons from the bulk to shield the charge build-up. The electronic transport of these electrons can be controlled by a voltage: the electrons are not conducting unless a potential is applied to the domain wall, when they go from a highly-localized polaronic state to a conductive, itinerant Bloch state. Thus, the domain wall acts as a switch which is open when no voltage is applied and closed when there is a voltage applied.

By using STEM to experimentally probe these atomic-sized features, we can reveal their fundamental physics and work towards realizing oxide electronics, such as atomically thin transistors or all-domain-wall electronics. In the following chapters, I will study the evolution of the order parameter at domain walls and vortices in bulk $ErMnO_3$, to determine the fundamental length scales of these topological defects and what their local charge build-up might be. I also map the ferroelectricity at all relevant length scales in the multiferroic superlattices of $(LuFeO_3)_m/(LuFe_2O_4)$.

1.6 Measuring polarization and order parameter with atom tracking

In proper perovskite ferroelectric materials, a structural instability towards the polar state is the main driver of the ferroelectric transition. This is the case for many ABO_3 perovskite systems such as BaTiO3, where bonding of the B-site cation with an oxygen anion displaces the B-site from the center of the A-site cage [52]. In improper ferroelectrics, ferroelectricity is generated as a part of a more complicated structural distortion or as a by-product of the system. For instance, ferroelectricity could be generated by octahedral rotations [53] in cubic systems or as tilting of bipyramids [40] in hexagonal systems. Because these structural displacements are on the picometer scale, and vary atom-by-atom at domain walls, surfaces, and vortices, atomic-resolution STEM is poised to observe the ferroelectricity with atom tracking. By finding the location of every atomic column, we can learn about the improper ferroelectricity from the picometer scale displacements to the domain architecture on the 10's of nanometers length scale.

For the hexagonal manganites and ferrites, the ferroelectricity is particularly easy to measure by HAADF-STEM, because the heavy Lu or Er ions show a clear trimerization pattern that reflects the polar nature of the structure. The polarization monotonically tracks the magnitude of this trimer distortion [49], rendering HAADF-STEM a local probe of ferroelectricity – see Figure 1.7.

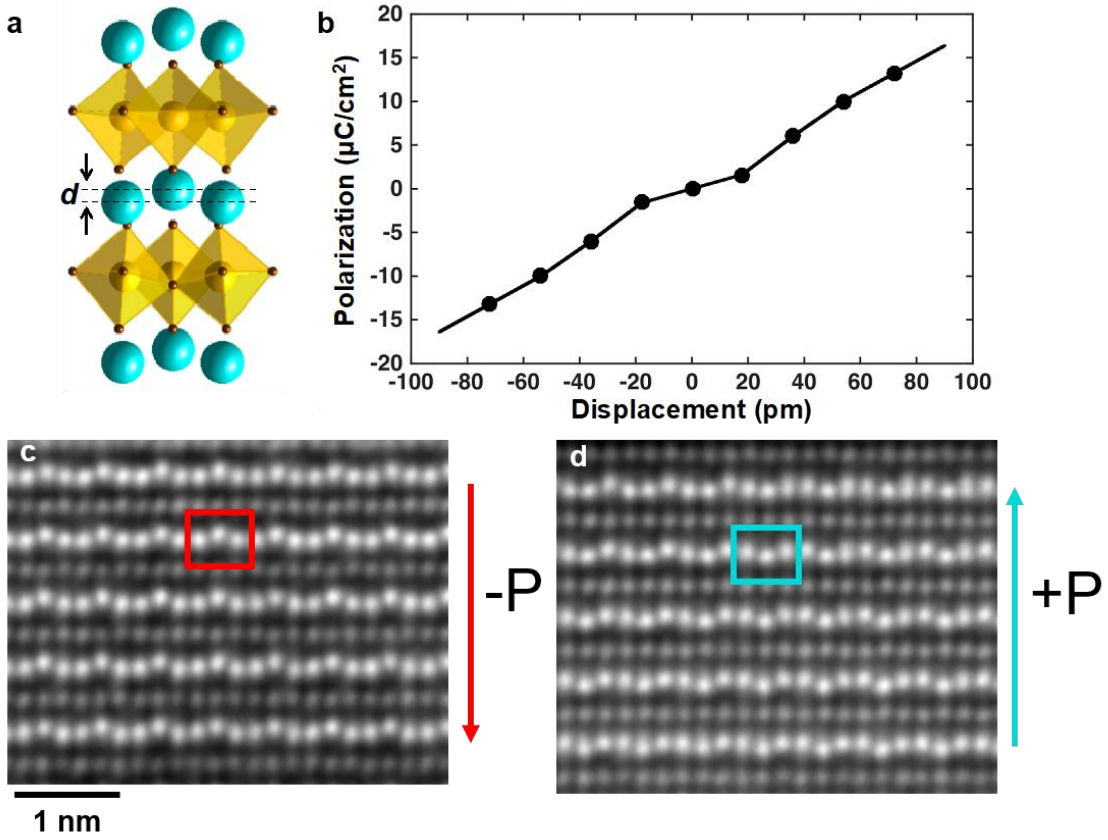

Figure 1.7. Ferroelectric displacement in hexagonal ferrites and manganites. (a) The magnitude of the lutetium displacement in $LuFeO_3$, shown as "*d*" in the cartoon, can be measured by HAADF-STEM. Lutetium is shown in turquoise, iron in yellow and oxygen in brown. (b) Using first-principles calculations, this displacement can be directly correlated to the polarization of the structure. [49,54] DFT performed by Hena Das in Craig Fennie's group. (c) STEM image showing a region of "down" polarization and (d) "up" polarization.

The order parameter of the ferroelectricity can be directly measured by fitting the atomic column positions measured by STEM to a sinusoidal curve [55]. Figure 1.8 illustrates how the atomic displacements follow a sinusoidal curve: $u_i = Q\cos(\Phi - kx_i)$ that depends on the order parameter, $\vec{Q} \equiv (Q\cos\Phi, Q\sin\Phi)$, with Q representing the trimerization amplitude and Φ the

domain. Here, x_i describes the displacement of the i^{th} atomic column and k the reciprocal vector, $2\pi/x_{110}$ where x_{110} is the in-plane spacing between atoms in the projection image.

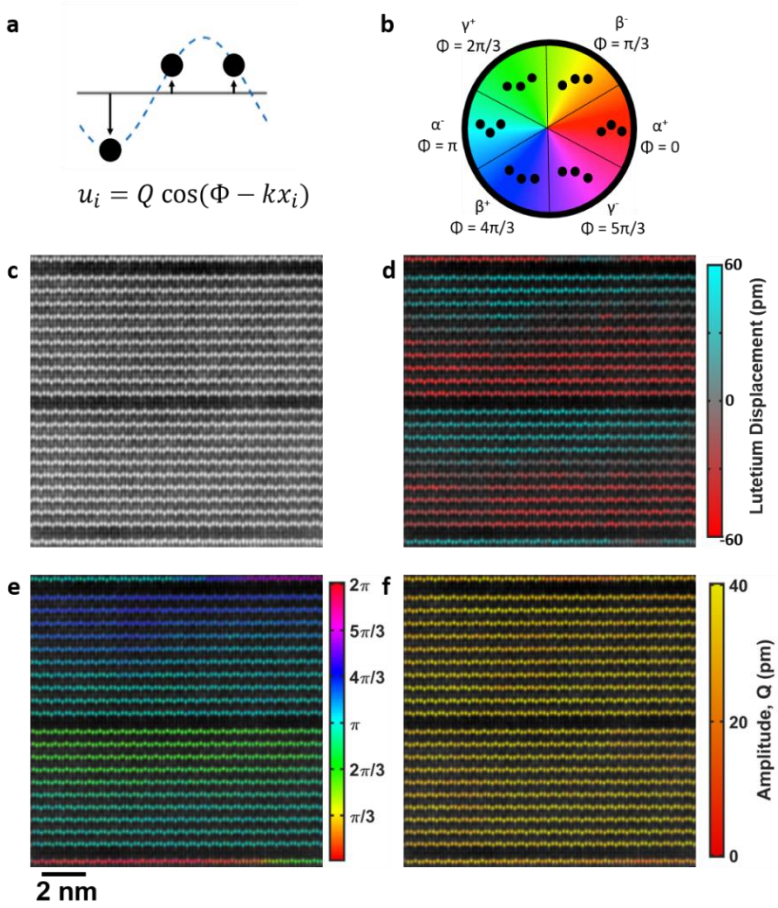

Figure 1.8. Mapping displacements in STEM measures the local polarization and order parameter in a $(LuFeO_3)_9/(LuFe_2O_4)$ superlattice. (a) Cartoon of Lu displacements, relating the displacement (u) to Φ and Q, with position x across the film, where $k = 2\pi/3x_o$, where x_o is the in-plane atomic spacing. (b) Wheel corresponding to the six trimerization domains, where the dots represent configurations of Lu as observed in the [110] projection direction. (c) STEM image of the $(LuFeO_3)_9/(LuFe_2O_4)$ superlattice, processed. (d) color overlay of the image representing the polarization. (e) Φ overlay showing the trimerization domains and (f) Q overlay, showing that the amplitude.

There are six ferroelectric trimerization domains which can be mapped to phase space, Φ, where the domains have a value of $n\pi/3$ where n = 1,2,3,4,5,6. At intermediate values of Φ between ferroelectric domains, the polarization is damped, forming 6 paraelectric domains at the halfway points between ferroelectric domains at $\Phi = n\pi/3 - \pi/6$. From the Landau free energy [39], and which has been observed experimentally in hexagonal manganites [55], when the ferroelectric domain changes from one domain to another, it goes in the $\pm \pi/3$ direction, passing through the paraelectric state.

1.7 Vibrational Spectroscopy by EELS

The development of a new generation of monochromators on aberration corrected STEM machines has enabled EELS at 10 meV energy resolution with 1 Ångstrom spatial resolution [6,56,57]. Because the full width at half maximum (FWHM) of the zero-loss peak has typically been 0.3 eV or greater (even up to 1 eV) in EELS machines without monochromation, and around 0.1 eV in machines with monochromation, the width of this curve has precluded energy loss measurements from very low energy features. In fact, because the zero-loss tail can be quite wide, typical limitations on what is observable in the low loss range has excluded measurements of features 3-5 times the FWHM of the zero-loss beam. Cutting down on the FWHM and tails of the zero-loss peak is therefore essential to observing low-energy features, and monochromators have been often employed to observe the band gap, various interband transitions, and plasmon losses. Typical vibrational features in spectra range from 40 meV to a couple hundred meV, so improving the energy resolution of STEM EELS from 100 meV to 10 meV opens new doors to studying spatially resolved (and momentum resolved) phonon spectra.

Phonons, like plasmons, are collective modes that can be excited by fast electron beams and can be described by dielectric formulations in the semiclassical or relativistic regimes [58,59].

While the community has done much work on plasmons in terms of their delocalization [60] and surface and interface modes [61–65], the extension into the very low phonon excitations has not yet been discussed. The last chapter of the thesis, Chapter 8, will discuss phonon and interface modes in thin film geometries.

1.8 Conclusion

STEM is an ever-expanding set of tools to perform experiments for materials science. Liquid electrochemical cell microscopy is a promising way to view the nanoscale dynamics of materials processes such as those in batteries and fuel cells. Because of that promise, there has been a rapid increase in the publications in the field since 2011. While many exciting studies have been done, one overarching challenge has been radiation damage in the liquid cell – and many papers have been written, and entire conference sessions have been held to better understand its effects. It is required of the liquid cell microscopist to run control experiments, and always interrogate the data for evidence of radiation damage. Only through the most careful studies and most open discussions about what is really going on in the liquid cell will reliable results for materials science be obtained.

Atomic resolution STEM opens the door to studying picometer scale displacements which may be driven by defects, impurities, and ferroelectricity. In particular, the atomic scale structure of hexagonal ferroelectric materials opens doors to exciting new materials science in terms of multiferroic materials and all-domain-wall devices, and into the physics of symmetry breaking at the smallest (electronic) length scales.

And finally, the advent of highly monochromatic beams now allows the observation of phonons, and their interface modes and delocalization is now an intense area of study.

References

[1] P. E. Batson, N. Dellby, and O. L. Krivanek, Nature **418**, 617 (2002).

[2] H. Müller, S. Uhlemann, P. Hartel, and M. Haider, 442 (2006).

[3] M. Bosman, V. J. Keast, J. L. García-Muñoz, A. J. D'Alfonso, S. D. Findlay, and L. J. Allen, Phys. Rev. Lett. **99**, 86102 (2007).

[4] K. Kimoto, T. Asaka, T. Nagai, M. Saito, Y. Matsui, and K. Ishizuka, Nature **450**, 702 (2007).

[5] D. A. Muller, L. F. Kourkoutis, M. Murfitt, J. H. Song, H. Y. Hwang, J. Silcox, N. Dellby, and O. L. Krivanek, Science **319**, 1073 (2008).

[6] O. L. Krivanek, T. C. Lovejoy, N. Dellby, T. Aoki, R. W. Carpenter, P. Rez, E. Soignard, J. Zhu, P. E. Batson, M. J. Lagos, R. F. Egerton, and P. a Crozier, Nature **514**, 209 (2014).

[7] F. M. Ross, editor , *Liquid Cell Electron Microscopy* (Cambridge University Press, Cambridge, 2017).

[8] V. B. Ozdol, C. Gammer, X. G. Jin, P. Ercius, C. Ophus, J. Ciston, and A. M. Minor, Appl. Phys. Lett. **106**, (2015).

[9] M. W. Tate, P. Purohit, D. Chamberlain, K. X. Nguyen, R. Hovden, C. S. Chang, P. Deb, E. Turgut, J. T. Heron, D. G. Schlom, D. C. Ralph, G. D. Fuchs, K. S. Shanks, H. T. Philipp, D. A. Muller, and S. M. Gruner, Microsc. Microanal. **22**, 237 (2016).

[10] N. de Jonge and F. M. Ross, Nat. Nanotechnol. **6**, 695 (2011).

[11] F. M. Ross, Science **350**, aaa9886 (2015).

[12] I. M. Abrams and J. W. McBain, Science **100**, 273 (1944).

[13] D. D. Double and A. Hellawell, Nature **261**, 486 (1976).

[14] M. J. Williamson, R. M. Tromp, P. M. Vereecken, R. Hull, and F. M. Ross, Nat. Mater. **2**, 532 (2003).

[15] N. M. Schneider, M. M. Norton, B. J. Mendel, J. M. Grogan, F. M. Ross, and H. H. Bau, J. Phys. Chem. C **118**, 22373 (2014).

[16] J. M. Grogan, N. M. Schneider, F. M. Ross, and H. H. Bau, Nano Lett. **14**, 359 (2014).

[17] H. Zheng, R. K. Smith, Y. Jun, C. Kisielowski, U. Dahmen, and A. P. Alivisatos, Science **324**, 1309 (2009).

[18] J. M. Yuk, J. Park, P. Ercius, K. Kim, D. J. Hellebusch, M. F. Crommie, J. Y. Lee, A. Zettl, and A. P. Alivisatos, Science **336**, 61 (2012).

[19] T. J. Woehl, J. E. Evans, I. Arslan, W. D. Ristenpart, and N. D. Browning, ACS Nano **6**, 8599 (2012).

[20] H.-G. Liao, L. Cui, S. Whitelam, and H. Zheng, Science **336**, 1011 (2012).

[21] K. L. Jungjohann, S. Bliznakov, P. W. Sutter, E. A. Stach, and E. A. Sutter, Nano Lett. **13**, 2964 (2013).

[22] A. De Clercq, W. Dachraoui, O. Margeat, K. Pelzer, C. R. Henry, and S. Giorgio, J. Phys. Chem. Lett. **5**, 2126 (2014).

[23] L. R. Parent, D. B. Robinson, T. J. Woehl, W. D. Ristenpart, J. E. Evans, N. D. Browning, and I. Arslan, ACS Nano **6**, 3589 (2012).

[24] E. Sutter, K. Jungjohann, S. Bliznakov, A. Courty, E. Maisonhaute, S. Tenney, and P. Sutter, Nat. Commun. **5**, 4946 (2014).

[25] R. F. Egerton, in *Eur. Microsc. Conf.* (2012), pp. 1–2.

[26] N. de Jonge, N. Poirier-Demers, H. Demers, D. B. Peckys, and D. Drouin, Ultramicroscopy **110**, 1114 (2010).

[27] N. de Jonge, D. B. Peckys, G. J. Kremers, and D. W. Piston, Proc. Natl. Acad. Sci. U. S. A. **106**, 2159 (2009).

[28] L. Reimer and H. Kohl, *Transmission Electron Microscopy Physics of Image Formation* (Springer, New York, NY, 2008).

[29] D. C. Joy, *Monte Carlo Modeling for Electron Micrsocopy and Microanalysis* (Oxford University Press, New York, NY, 1995).

[30] H. Demers, N. Poirier-Demers, D. Drouin, and N. de Jonge, Microsc. Microanal. **16**, 795 (2010).

[31] H. Demers, R. Ramachandra, D. Drouin, and N. de Jonge, Microsc. Microanal. **18**, 582 (2012).

[32] K. X. Nguyen, M. E. Holtz, J. Richmond-Decker, and D. A. Muller, Microsc. Microanal. **22**, 754 (2016).

[33] K. J. T. Noonan, K. M. Hugar, H. a Kostalik, E. B. Lobkovsky, H. D. Abruña, and G. W. Coates, J. Am. Chem. Soc. **134**, 18161 (2012).

[34] P. Voelker, R&D Mag. 1 (2014).

[35] C. H. Ahn, J.-M. Triscone, and J. Mannhart, Nature **424**, 1015 (2003).

[36] E. Dagotto, Science **309**, 257 (2005).

[37] J. Mannhart, D. H. A. Blank, H. Y. Hwang, A. J. Millis, and J.-M. Triscone, MRS Bull. **33**, 1027 (2008).

[38] A. Ohtomo and H. Y. Hwang, Nature **427**, 423 (2004).

[39] S. Artyukhin, K. T. Delaney, N. a Spaldin, and M. Mostovoy, Nat. Mater. **13**, 42 (2014).

[40] B. B. Van Aken, T. T. M. Palstra, A. Filippetti, and N. a Spaldin, Nat. Mater. **3**, 164 (2004).

[41] C. J. Fennie and K. M. Rabe, Phys. Rev. B - Condens. Matter Mater. Phys. **72**, 1 (2005).

[42] T. Choi, Y. Horibe, H. T. Yi, Y. J. Choi, W. Wu, and S.-W. Cheong, Nat. Mater. **9**, 253 (2010).

[43] J. Seidel, R. K. Vasudevan, and N. Valanoor, Adv. Electron. Mater. **2**, 1 (2016).

[44] J. Seidel, L. W. Martin, Q. He, Q. Zhan, Y. H. Chu, A. Rother, M. E. Hawkridge, P. Maksymovych, P. Yu, M. Gajek, N. Balke, S. V Kalinin, S. Gemming, F. Wang, G. Catalan, J. F. Scott, N. A. Spaldin, J. Orenstein, and R. Ramesh, Nat. Mater. **8**, 229 (2009).

[45] S.-Z. Lin, X. Wang, Y. Kamiya, G.-W. Chern, F. Fan, D. Fan, B. Casas, Y. Liu, V. Kiryukhin, W. H. Zurek, C. D. Batista, and S.-W. Cheong, Nat. Phys. **10**, 970 (2014).

[46] S.-W. Cheong and M. Mostovoy, Nat. Mater. **6**, 13 (2007).

[47] M. Fiebig, T. Lottermoser, D. Fröhlich, A. V. Goltsev, and R. V. Pisarev, Nature **419**, 818 (2002).

[48] Q. Zhang, G. Tan, L. Gu, Y. Yao, C. Jin, Y. Wang, X. Duan, and R. Yu, Sci. Rep. **3**, 2741 (2013).

[49] H. Das, A. L. Wysocki, Y. Geng, W. Wu, and C. J. Fennie, Nat. Commun. **5**, 2998 (2014).

[50] N. A. Hill and A. Filippetti, J. Magn. Magn. Mater. **242**–**245**, 976 (2002).

[51] J. A. Mundy, J. Schaab, Y. Kumagai, A. Cano, M. Stengel, I. P. Krug, D. M. Gottlob, H. Doğanay, M. E. Holtz, R. Held, Z. Yan, E. Bourret, C. M. Schneider, D. G. Schlom, D. A. Muller, R. Ramesh, N. A. Spaldin, and D. Meier, Nat. Mater. **16**, 622 (2017).

[52] H. D. Megaw, Acta Crystallogr. **5**, 739 (1952).

[53] N. A. Benedek and C. J. Fennie, Phys. Rev. Lett. **106**, 3 (2011).

[54] J. A. Mundy, C. M. Brooks, M. E. Holtz, J. A. Moyer, H. Das, A. F. Rébola, J. T. Heron, J. D. Clarkson, S. M. Disseler, Z. Liu, A. Farhan, R. Held, R. Hovden, E. Padgett, Q. Mao, H. Paik, R. Misra, L. F. Kourkoutis, E. Arenholz, A. Scholl, J. A. Borchers, W. D. Ratcliff, R. Ramesh, C. J. Fennie, P. Schiffer, D. A. Muller, and D. G. Schlom, Nature **537**, 523 (2016).

[55] M. E. Holtz, K. Shapovalov, J. Mundy, C. S. Chang, Z. Yan, E. Bourret, D. A. Muller, D. Meier, and A. Cano, Nano Lett. acs. nanolett.7b01288 (2017).

[56] C. Dwyer, T. Aoki, P. Rez, S. L. Y. Chang, T. C. Lovejoy, and O. L. Krivanek, Phys. Rev. Lett. **256101**, 1 (2016).

[57] M. J. Lagos, A. Trügler, U. Hohenester, and P. E. Batson, Nature **543**, 529 (2017).

[58] R. H. Ritchie, Phys. Rev. **106**, 874 (1957).

[59] R. F. Egerton, *Electron Energy-Loss Spectroscopy in the Electron Microscope*, 3rd ed. (Plenum Press, New York, 2011).

[60] D. A. Muller and J. Silcox, Ultramicroscopy **59**, 195 (1995).

[61] P. E. Batson, Ultramicroscopy **11**, 299 (1983).

[62] M. Couillard, A. Yurtsever, and D. A. Muller, Phys. Rev. B - Condens. Matter Mater. Phys. **77**, 1 (2008).

[63] J. P. R. Bolton and M. Chen, J. Phys. Condens. Matter **7**, 3389 (1995).

[64] J. P. R. Bolton and M. Chen, J. Phys. Condens. Matter **7**, 3373 (1995).

[65] C. H. Chen and J. Silcox, Phys. Rev. B **20**, 3605 (1979).

CHAPTER 2

ELECTRON ENERGY-LOSS SPECTROSCOPY IN LIQUIDS

2.1 Introduction

The driving goal for liquid state *in situ* microscopy is to fully understand the fundamental mechanisms underlying processes in biological and material science, and a critical component of this is identifying the chemical state and/or elemental composition of the material being studied. Much of the recent progress in liquid cell *in situ* electron microscopy has been in observing morphological and structural changes that occur on the sub-nanometer to micrometer scale, but progress has been slower for techniques aimed at finding elemental and electronic structure information. The analytical electron microscope, or AEM, specializes in answering questions regarding composition (elemental and chemical) as well as electronic structures of materials, and can do so at the atomic scale for conventional crystalline samples in scanning transmission mode (STEM), with comparable work at lower resolution in conventional transmission electron microscopy (TEM) mode. The AEM is often capable of two types of spectroscopic analysis methods: electron energy-loss spectroscopy (EELS) and x-ray energy-dispersive spectroscopy (XEDS) [1]. These tools have recently been explored for liquid cell studies, providing elemental information on the micro-to-nanoscale and electronic structure information of liquids and dynamic processes from valence EELS. In this chapter, we will compare EELS and XEDS for liquid cell microscopy, discuss the thickness limitations of EELS in liquid, discuss low loss EELS for liquids, and finally examine a study of valence EELS on copper deposition.[1]

[1] This chapter is based on a book chapter discussing of EELS and XEDS in liquids by M.E. Holtz, D.A. Muller, and N.J. Zaluzec [2], and a journal article that first discussed EELS in liquids by M.E. Holtz, Y. Yu, J. Gao, H.D. Abruña, and D.A. Muller [3].

2.2 AEM for Liquids

A simple picture of the relevant physics for electron energy-loss spectroscopy begins with the incident electron beam striking a region of interest in the liquid cell and exciting bound electrons from occupied state to unoccupied states in the observed material.[1] After scattering from a bound electron state, the probing electron loses the amount of energy corresponding to the transition energy between the ground and excited states, and this energy loss is measured by EELS. The electron in the excited state then subsequently relaxes into a lower energy state, releasing the energy by either emitting a photon (such an x-ray), by ejecting another electron (auger transitions), or by heating the material (exciting lattice vibrations). EELS provides elemental identification from the energy signatures of the primary core-level transitions (core-loss EELS). Additionally, EELS reveals the localized electronic state information from either the fine-structure features of the core edges or from lower energy valence-level transitions near the Fermi energy (valence EELS). The incident electron beam can also excite collective oscillations of valence electrons in the material, known as plasmons. Plasmons generally have energies between 10-30 eV and are a prominent feature of the valence EELS signal. EELS can measure the energy lost by these mechanisms with typical energy resolutions of 0.5 – 1 eV and as low as 0.1 eV when the instrument employs a monochromated electron source.

XEDS provides elemental identification from the measurement of characteristic energies of the x-rays emitted from the region of interest, which result from the decay transitions by electrons from their excited states. XEDS also detects bremsstrahlung radiation, which is radiation with a broad energy spread that is produced as the electron loses angular momentum and energy in the specimen. The characteristic energies from single-electron core transitions provide signal for elemental analysis and mapping, while bremsstrahlung radiation is present as a continuum or background signal. Ultra high-energy resolution XEDS systems exist which can also provide chemical/valence

state information, however, none of these have be employed in liquid cell studies, principally due to their extremely low collection solid angles and thus low detection efficiency.

Both EELS and XEDS involve interfacing ancillary spectrometers to the electron optical column of the instrument used for imaging. In the case of EELS it is generally a magnetic sector spectrometer located after the objective lens, while in the case of XEDS it is a solid state semiconductor detector located in the objective lens area (of the TEM/STEM or SEM) and thus the immediate vicinity of the liquid cell.

Spectroscopic imaging modes are possible using both EELS and XEDS. One method for creating spectroscopic images is to collect an energy loss or x-ray spectrum over an array of points as the incident beam is scanned across a selected region of the specimen in STEM mode. The resulting hyperspectral data cube can then be post-facto analyzed and the integrated elemental signals can be used to create spectroscopic maps of the region of interest. A limitation of the point-by-point method for acquiring spectra the amount of time needed to acquire statistically relevant signal at each location.

An alternate mode for spectroscopic imaging exists for EELS known as energy-filtered TEM (EFTEM). In this mode, an analyst operates the instrument using a relatively large illuminated region in TEM mode. After interacting with the specimen, the forward scattered electrons (which includes both elastic and inelastic signal) are directed into an imaging spectrometer, where a small range of electron energies are selected and are subsequently used to create an image of the specimen at energy losses chosen by the energy-selecting slit. These filtered images provide a means for spectroscopic imaging of large areas of the specimen, but only within fixed energy intervals. Mapping of elemental signals in EFTEM is achieved by recording images for "energy slices" before and after characteristic loss events and then computationally processing to extract any intervening characteristic data [4].

In the limit of infinite amounts of time and data space, both of the aforementioned spectroscopic methodologies can in principle achieve identical results, however practical details dictate which mode is used for a particular experiment. EFTEM for broad sweeping overviews, while hyperspectral imaging for detailed assessments using small focused probes.

A comparison of XEDS and EELS in liquids in the AEM environment is given in Table 2.1.

Table 2.1: Comparison of XEDS and EELS for liquid cell studies.

	XEDS	EELS
Relevant physics	Incident electron excites core level electron. Higher energy electron relaxes into core hole, releasing a characteristic x-ray	Incident electron excites valence or core level electron or collective mode (ie plasmon), and incident electron loses a corresponding amount of energy
What is measured	X-rays emitted from the region of interest in the liquid cell (specimen + media +windows) dispersed by energy.	Energy distribution of electrons passing through the region of interest in the liquid cell (specimen + media +windows)
Location of the detector	Proximate to the liquid cell in the objective lens area of the AEM, where a solid state detector collects from 0.1 to ~ 1 sR of the x-ray emission.	Remote to the liquid cell, after the projector lenses where an electron spectrometer collects 10-30 mrad of the central beam of the scattered electrons.
Kinds of information	Elemental identification, thickness of the region of interest	Elemental identification, bonding environment, local electronic structure information, thickness of the region of interest
Spatial resolution	Defined by interaction volume of the broadened electron beam in the liquid cell, the probe size and the location of the region of interest in the liquid cell.	Defined by broadened electron probe in the sample, defined by the probe size and the location of the region of interest in the liquid cell.
Thickness dependence	Increased thickness can degrade spatial resolution, but generally not XEDS signal. Highest spatial resolution when the region of interest is proximate to the electron entrance window.	Spectra degraded primarily by multiple inelastic scattering of the electron beam, resulting in multiple energy losses obscuring the signal after 3 to 6 mean free paths (~300-

		600 nm at 200 keV) for core and valence EELS respectively.
Beam Dose and Data Acquisition Times	Beam dose intensive, requires long acquisition times.	Low loss: low beam doses, fast data acquisition for dynamic spectral imaging; High loss: large beam doses, longer data acquisition
Higher sensitivity to	Z > 6 and particularly medium to heavy elements, with limitations due to the elemental composition of the window and media	Lighter elements Z<30, with limitations due to the elemental composition of the window and media
Spectroscopic imaging	In STEM mode, collect spectra as you scan the beam from pixel to pixel, and then form spectroscopic images by integrating the peaks corresponding to elements. In TEM mode spectra from large regions of interest are readily achievable, giving spatially averaged information.	In STEM mode, collect spectra as you scan the beam from pixel to pixel, and then form spectroscopic images by integrating the peaks corresponding to elements with appropriate background subtraction. In EFTEM mode, image electrons that have lost particular energies.
Strengths	Works in thick liquids, easy to map Z > 6 and heavier elements, modified liquid holders and optimized detector geometry required.	Beam sensitive materials (valence EELS), rapid spectroscopic imaging (EFTEM), unmodified holders can be used.

While EELS and XEDS have been widely used in conventional (thin, solid) TEM specimens in vacuum for decades, they have only recently been applied to studies in liquids in the AEM [5–9]. *In situ* spectroscopy in the analytical electron microscope is challenging due to the degradation of the EELS signal in thick liquids, as well as the geometrical challenges of detecting XEDS signals from specimens in liquid cell holders.

The principle challenge for the application of EELS in liquid cell studies is the rapid deterioration of signal arising from multiple inelastic scattering events in the environment (specimen + liquid + media). Multiple scattering leads to compounded energy loss events which become increasingly difficult to interpret [4]. For regions of interest thicker than one mean free path of the electron in the material (~ 100-150 nm at 200 keV) [4], the singly scattered EELS signal becomes weaker. The thickness degradation of the EELS signal is exacerbated for higher energy (core loss) transitions because multiple scattering events of lower-energy valence signals

create a large background, resulting in a strong decrease in signal to background ratio for the core losses. In contrast, because there are fewer lower-energy transitions below the valence EELS regime, valence EELS is resolvable in thicker samples than core-loss EELS [6]. Despite these limitations, EELS analysis can be successfully performed to obtain a wide variety of information about the sample and the liquid for experiments involving thin media. The types of information obtainable and the thickness limitations of both core and valence EELS that have been explored will be discussed later in this chapter.

While EELS in liquid media is fundamentally limited by the physics of multiple scattering, XEDS suffers a different technical problem: namely, signal detection. The initial construction geometry of liquid cell holders in TEM/STEM or SEMs was focused on imaging methodologies and protection of the instrument from liquid leakage into the vacuum system. Absent from these holder designs was an optimized line-of-sight path from the point of generation of the x-ray to an appropriate detector, making XEDS studies impossible in first-generation *in situ* holders [6,8]. Recent modifications of the *in situ* TEM holders have enabled XEDS analysis by providing this line of sight path from the specimen in liquid to the XEDS detector. Because x-rays interact very weakly with both the liquid media and the encapsulating SiN_x windows, the XEDS signal is significantly less sensitive to the thickness of the liquid media than EELS [8]. This makes XEDS an effective technique for elemental analysis in thicker liquids typical in many *in situ* studies [8,9].

During any microanalysis of specimens in liquids, it is incumbent upon the analyst to realize that the electron beam will not only interact with specimen, but also alter the chemical/elemental environment of the liquid surrounding the specimen area in the cell. This interaction can range from minor to serious effects that can obfuscate observations. Analytical spectroscopies such as EELS and XEDS inherently require larger electron beam doses than imaging due to the smaller inelastic cross section compared to the elastic cross section for most materials. The larger dose required by spectroscopy means that the beam interaction and subsequent irradiation effects can be correspondingly more severe. Both core-loss EELS and XEDS elemental mapping are dose

intensive methodologies requiring long acquisition times to accumulate sufficient statistics compared to any other existing electron imaging methodology. Even for beam sensitive samples, valence EELS is nearly always possible, due to its larger scattering cross sections and thus higher intensity in the low loss scattering spectral regime, enabling spectroscopic imaging with relatively short acquisition times. For comparison, low loss valence EELS studies can be done in seconds, but statistically significant elemental maps involving core loss EELS and/or XEDS can take minutes (or longer). To avoid beam damage, lower resolution studies are likely to be effective. Thus, as with any liquid state TEM experiment, *in situ* analysis must be done with radiological/beam effects in mind.

2.3 Thickness Determination by EELS

The composite thickness of the liquid cell (windows + media + specimen) can be determined using Beer's Law (or the n=0 Poisson distribution), which predicts an exponentially decaying unscattered intensity as observed in the zero-loss peak [4,10]:

$$I = I_0 e^{-t/\lambda} \qquad \text{Eq. 2.1}$$

By integrating the zero loss peak intensity (I) and comparing it to the integrated intensity over the entire spectrum (I_o), the thickness in terms of the inelastic mean free path (t/λ) can be measured. For thick specimens, it is important to record the EELS spectra out to high energies to capture most of the scattering. A large dispersion (0.3 eV) and large collection angle (>20 mrad) are used to detect most of the scattered electrons. However, if all the scattered electrons over the energy range acquired are not collected, a power law fit to the tail of the spectrum can be used to extrapolate the curve for a more accurate estimate of I_o. For EELS acquired out to 510 eV, the power law extrapolation introduces a 1% correction above $t/\lambda = 7$ in the liquid and grows to 4% for $t/\lambda = 9$.

All thickness values reported here were determined using Beer's Law after extending the spectrum until it approached zero using a power law fit to the tail.

The conversion from thickness in terms of the inelastic mean free path (λ) to the thickness (t) in nm is done by estimating λ from the plasmon scattering. Here we estimate λ assuming that plasmon losses are the dominant loss mechanism in the sample, which, from simple inspection of a single scattering measurement, is a good approximation. The simple single-pole plasmon model, which is equivalent to assuming that the electrons in the fluid behave as free electrons, turns out to be reasonably valid as discussed later, and gives the simple result [4]:

$$\lambda = \frac{a_0}{\gamma\theta_{E_p}\ln(\theta_c/\theta_{E_p})} \qquad \text{Eq. 2.2}$$

where a_0 is the Bohr radius, γ is the Lorentz factor, θ_c is the collection angle (~20 mrad). In addition, we define

$$\theta_{E_p} = \frac{E_p}{\gamma m_e v^2} = \frac{E_p}{E_i(1+\gamma^{-1})} \qquad \text{Eq. 2.3}$$

where m_e and v are the rest mass and velocity of the electron, respectively. E_i is the incident energy (200 keV) and E_p is the plasmon energy. The derivation of this formula assumes the Born approximation – the incident field is the primary field causing electron oscillation – and is thus only valid over the range where $E_i >> E_p$. In general, this is true for a 200 keV incident beam and if, on average, the inelastic scattering events lose the plasmon energy. This method gives a weighted average of λ for the liquid and the nitride membranes. However, the nitride membranes are thin compared to the liquid layer. While Eq. 2.2 can provide reasonable values of λ for free-electron materials, it tends to overestimate λ by a few percent [4], but it is preferred since it avoids requiring *a priori* knowledge of material parameters such as effective atomic number and relies only upon the plasmon energy, incident beam energy, and collection angle, which are all experimentally

measurable and not free fitting parameters. For collection angles greater than 20 mrad, the dependency of λ on the collection angle flattens off [4,10–12], so a large collection angle prevents small experimental differences from drastically changing results, and allows the collection of most of the scattered electrons. More elaborate empirical fits have been attempted [12,13], but for the thicknesses typical in our liquid cell and collection angles larger than 20 mrad, the differences are less than 10%. As the characteristic elastic scattering angles are much larger than the characteristic inelastic scattering angles, the convolution of multiple elastic and inelastic scattering in the liquid will result in a measurement that again satisfies Beer's law for a fully-angle-integrated inelastic distribution (see the discussion leading to Eq. (3.112) in Egerton [4]). Thus, from the EELS analysis, the total thickness of the liquid cell can be estimated from Eq. 2.1.

From STEM-EELS measurements, the calculated thicknesses for various locations across the viewing membrane are plotted as points in Figure 2.1(a-b) with the contours representing a parabolic fit. In Figure 2.1(a), 25 micron wide viewing windows with a water liquid layer are shown with a spacer ~250 nm thick, and in Figure 2.1(b), 50 micron wide viewing windows with ethylene glycol are shown with a spacer ~500 nm thick. As expected, the increase in thickness seen in the center of the viewing membrane is caused by the SiN_x membranes bowing out due to the pressure differential between the cell and TEM vacuum. A schematic of the bowing of the nitride membranes is shown in Figure 2.1(c), representing two independent orthogonal parabolas. The total thickness is found from the distance between the top and bottom membranes, as shown in Figure 2.1(d). The thickness profile in Figure 2.1(d) corresponds to the fitted contour lines shown in Figure 2.1(b). We find that the thickness is smallest at the corners, where the limiting factor is the spacer. However, in the center of the window, both the spacer and the bulging of the membranes contribute to an increased thickness, with thicker layers (~1 μm) obtained with the wider 40 μm windows and with thinner layers (~650 nm) for the narrower 25 μm windows. Thus, the thickness values appear reasonable from the geometry and are consistent with previously reported thicknesses [5,14]. From

this, it is clear that to achieve the highest resolution, one needs not only a thin spacing between the two chips, but also a narrow viewing window to limit bulging.

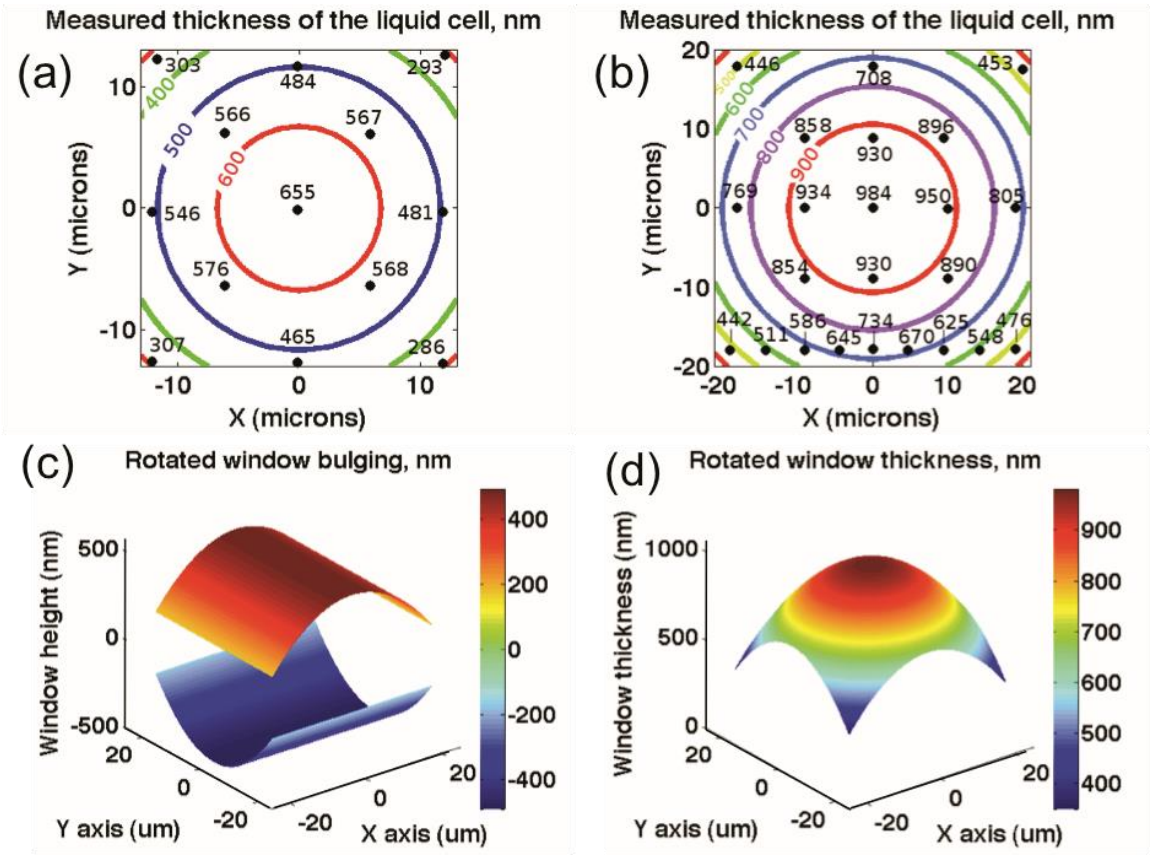

Figure 2.1. Measurement of the variations in liquid thickness due to the bulging of the SiN_x windows. STEM-EELS measurements points with a parabolic fit contours are shown for (a) water between 25-mm wide windows with a 150 nm Au spacer and (b) ethylene glycol between 40 mm wide windows with a 500 nm SU-8 spacer. c: A three-dimensional representation of the bulging of the two rotated SiNx membranes, assuming each window bows out as an independent orthogonal parabola and (d) the total thickness between the windows from (c). The profile shown in (d) corresponds to the contour lines in (b).

One of the primary uses of EELS in liquids is the investigation of the liquids themselves. In many situations, it is essential to determine the presence of liquid. For water, EELS spectra will display a characteristic interband transition [5], shown in Figure 2.2. Additionally, the plasmon peak and presence of multiply-scattered or bulk plasmon peaks are often a indicator of liquid presence, since the mean free path in liquid is roughly 3 orders of magnitude smaller than the mean free path in gas. In many cases, a SiN_x membrane cell that is filled with gas (i.e. no liquid present) is approximately one inelastic mean free path thick, because it is composed of two silicon nitride viewing membranes that are each ~ 50 nm thick. The gas in the cell contributes a relatively small amount to the total scattering in this mode. The addition of liquid increases the effective thickness of the media in the cell. With the cell + media thicker than one mean free path, the probability for single scattering decreases as the first order (n=1) Poisson distribution, so the first plasmon peak diminishes (Figures 2.2, also see Figure 2.4). Similarly, the probability for multiple scattering increases in thicker media and the second and bulk plasmon peak intensities grow correspondingly.

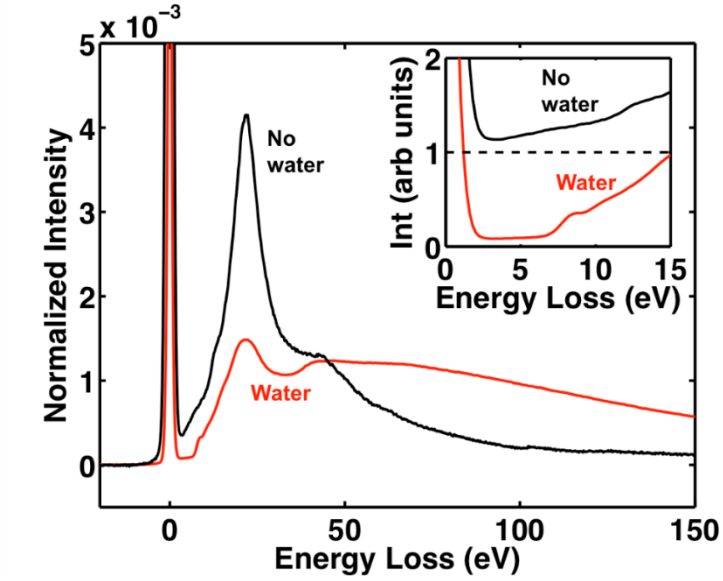

Figure 2.2. EELS spectra of a liquid cell before flowing water and one with water. The EELS of the empty cell represents the signal from passing through two 50 nm thick silicon nitride windows and a pocket of gas in between them, which is in total 0.9 t/λ thick. The first plasmon is the dominant inelastic

signal from the empty cell spectrum. The water-filled cell is 2.6 t/λ thick so the scattering is dominated by the thick liquid layer, with absorption starting at the exciton peak at 6.9 eV (see inset). The plasmon peak is observed at 21.4 eV. The intensity of the first plasmon peak is lower with liquid than without due to multiple scattering, creating a bulk plasmon at higher energies. For the main figure, spectra were normalized by the total electron beam dose for the spectrum acquisition (i.e. the integrated intensity of the spectrum).

XEDS can also provide a measure of thickness of the region of interest (including the specimen + cell + media) by comparing the characteristic and bremsstrahlung signal, which are both linear in thickness and beam current to first order approximation [8].

2.4 Thickness Limitations on EELS through Liquids

EELS can potentially provide information about the composition, electronic and dielectric properties of a material, if the specimen is sufficiently thin. Core-level EELS facilitates elemental identification as well as insight into the oxidation state and bonding environment from the fine-structure of the near edge profile [1]. In thin specimens with thicknesses less than one mean free path, sub-nanometer to atomic resolution is possible for core-loss EELS [15–18]. Energy losses to the valence electrons can reveal the electronic structure of materials, such at the optical gap and electron density of the specimen. Recently, EELS has been used in *in situ* experiments to determine liquid presence and thickness [6,19]. In thin liquids, studies have identified elements [6] and bonding states [20], and in moderately thick liquids studies have explored electronic structure information [6,7]. Energy-filtered TEM (EFTEM) can track chemical changes in dynamic processes on the nanometer scale [7]. EFTEM can also improve imaging conditions in liquid by selecting only the elastically scattered electrons to reduce chromatic blur, in which the electrons of

different energies come to different focal points. Thus, the wealth of information provided by EELS makes it an attractive technique for exploring processes in thin ($t/\lambda < 2$) liquid layers.

The primary challenge for EELS in liquids is that the signal is degraded in thick specimens ($t/\lambda > 1$), since the incident electron can lose energy from multiple inelastic scattering events which occur along the entire scattering path length (specimen + surrounding media + cell windows) as the probe propagates through the liquid cell. The effects of multiple scattering dominate the EELS spectra, which is observable in the multiply scattered plasmon peak that becomes larger with increasing water thickness, as can be seen in Figure 2.3(a). Fortunately, for a specimen whose composition is different from both the surrounding media and the cell windows, these EELS edges can remain distinct and are still detectable in thin liquid, as shown for core-loss EELS in Figure 2.3(b) of iron phosphate nanoparticles in a 180 nm thick liquid layer.

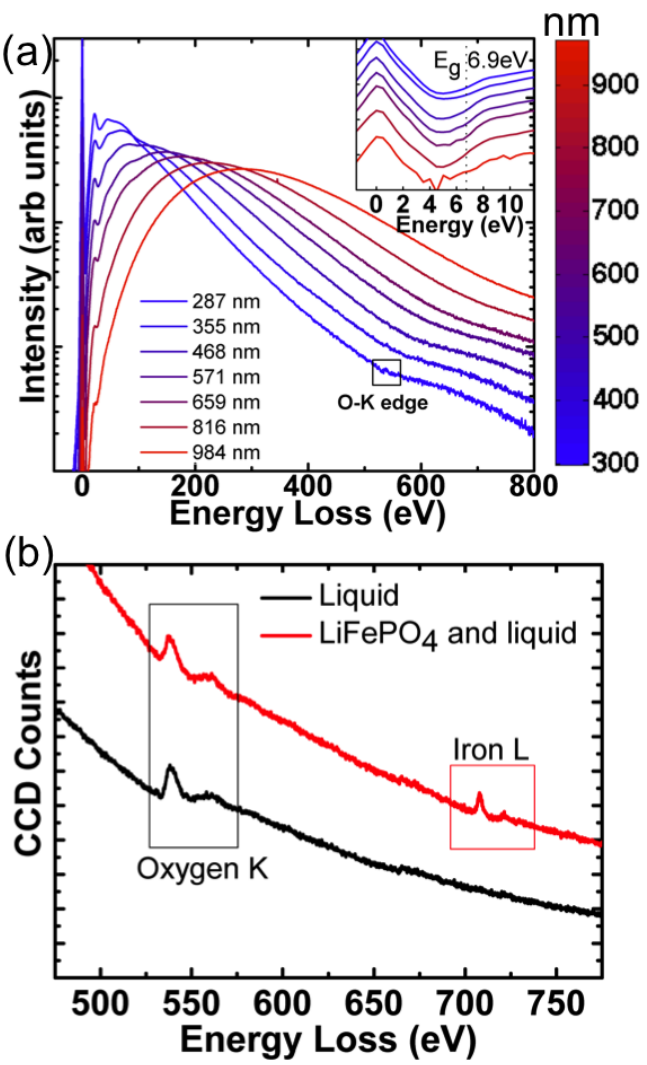

Figure 2.3. STEM-EELS measurements through water and nanoparticles in water. (a) EELS of water as a function of thickness. The core-loss O-K edge is resolvable for the thinnest layer only, while the optical gap at 6.9 eV is resolvable out to 6.5 inelastic mean free paths, or ~650 nm (inset). (b) Core-loss EELS of $LiFePO_4$ nanoparticles in 180 nm of aqueous solution. The Fe-L edge is visible on the particle, while the O-K edge is visible in both the particle and the liquid. Adapted from Holtz *et al*. Microscopy and Microanalysis 2013[5]

2.4.1 Core Loss EELS

For any EELS edge, the effects of multiple scattering are manifest in two ways. First, the transition height of the edge will decrease with thickness since some signal from that edge may additionally lose energy by another scattering event. Second, the background from lower-energy scattering events will increase, further lowering the signal to background ratio. Thus, EELS features with higher energy (core-loss edges) degrade more rapidly with thickness since there are larger amounts of lower-energy scattering events which convolve with the signal. Because the dominant energy-loss feature in thick regions is the plasmon peak, core-loss edges above the plasmon energy are generally not observable in liquid media thicker than two or three inelastic mean free paths ($t/\lambda > 2\text{-}3$). This makes core-loss EELS for elemental identification only practical in liquids thinner than a few inelastic mean free paths. Figure 2.3(a) shows the bulk plasmon peak in water, which overwhelms the oxygen-K edge in all but the thinnest ($t/\lambda < 3$) liquid layers. While core-loss EELS can identify elements present in the liquid up to three inelastic mean free paths, as demonstrated in Figure 2.3(b), quantification of the amount of the element present and its oxidation state will be challenging in all but the thinnest specimens ($t/\lambda < 1$). Because the SiN_x windows themselves are 50 nm thick ($t/\lambda \sim 0.5$ for 200 keV) each, elemental and chemical quantification from core-loss EELS in liquid media is likely to be difficult without using thinner viewing membranes, such as graphene [21].

Fourier-Log deconvolution, a commonly used method to remove the multiple scattering signal from EELS [4,22,23], helps define core-loss peaks from the background in moderately thin samples ($t/\lambda < 3$). For reliable deconvolution of the spectra, the collection angles are bigger than the convergence angle and the largest plasmon single scattering angle, which renders the effect of subsequent elastic scattering on the inelastic ratios negligible. However, once the peak is obscured by lower-energy multiple scattering events, deconvolution cannot extract the signal and, in

addition, noise amplified across large energy ranges (ringing artifacts) makes the spectrum uninterpretable.

2.4.2 Valence EELS

Valence EELS, which provides information about the local electronic structure of the material through collective excitations and interband transitions. They are also well separated from the lower-lying phonon modes, and thus are far less affected by plural scattering from lower energy transitions than core-loss excitations. Experimentally, we observe that the valence EELS signal, such as the optical gap, is resolvable up to t/λ ~ 6-7 in the liquid as seen in the insets of Figure 2.3(a).

The valence EELS features at and below the plasmon energy will become obscured when the fraction of the beam that has only scattered once is no longer detectable, and this will be governed by Poisson statistics. Since there are only modest amounts of signal in the very low-loss regime, the background from this low intensity multiply scattered signal is low and thus the signal to background ratios are relatively high. The Poisson distribution dictates how much signal is present, by giving the likelihood P of n scattering events to occur in a specimen of thickness t/λ, where λ is the (inelastic) mean free path:

$$P(n) = \frac{(t/\lambda)^n}{n!} e^{-(t/\lambda)} \qquad \text{Eq. 2.4}$$

The probability for no scattering (n=0), single scattering (n=1), and multiple scattering (sum over n>1) are shown in Figure 2.4. From Poisson's first order distribution, we expect that the fraction of the signal that scatters one time to fall to 1% of the total signal at roughly 6.5 inelastic mean free paths. Once the singly scattered signal is below the 1% level, we expect it would be difficult to resolve in the experimental EELS data. Indeed, the experimental valence spectra (shown

in the inset of Figure 2.2a) have features that are resolvable for thickness up to roughly 6 inelastic mean free paths [6]. Thus, the thickness limitation for valence EELS is nearly twice as thick as the limitation for core-loss EELS, because there is little lower-energy signal to obscure the valence EELS peaks. The lower thickness dependence and the large cross sections of valence EELS makes it an attractive technique for effective signal collection in thicker liquid volumes.

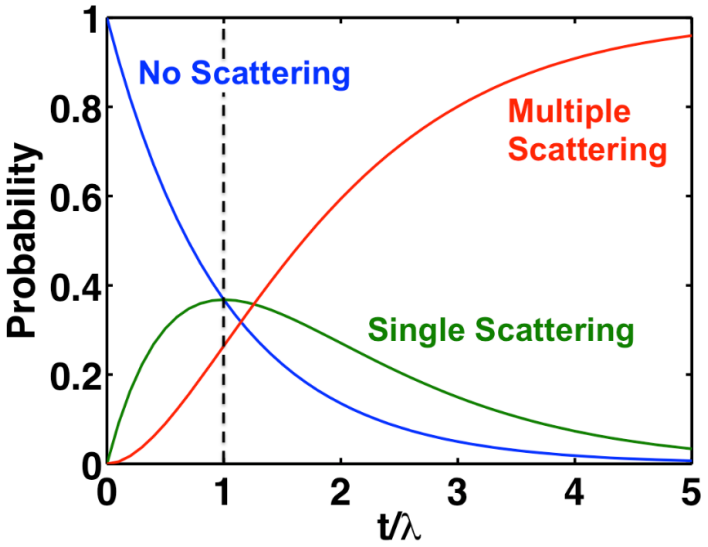

Figure 2.4. The Poisson distribution, which gives the probability for scattering *n* times for a given thickness in terms of the mean free path (λ). The probability for no scattering falls exponentially, and the probability for single scattering peaks at one mean free path. The sum of Poisson distributions for $n>1$ shows the probability for multiple scattering, which grows as thickness increases. A liquid cell with no liquid in it is roughly $t/\lambda = 1$ due to the thickness of the nitride viewing membranes.

There are two energy regimes where it is possible to maximize the signal to background ratio for an EELS measurement of a nanoparticle in a liquid. One regime is well past the bulk plasmon, where the core-loss signal, as discussed earlier, is only resolvable in liquid layers less than 3 t/λ thick. The other regime is below the first plasmon of the liquid and, particularly, in the optical gap of the liquid. In the optical gap, there is no energy loss mechanism and hence little scattering from

the liquid at those energy losses, thus offering an energy window with little background inelastic scattering.

2.5 Low Loss EELS Measurements of Liquids

We have performed valence EELS measurements on a variety of liquids likely to be used in *in situ* experiments, as shown in Figure 2.5(a). The determination of the optical gap, plasmon energy and local electron density of the liquid by valence EELS is demonstrated for propylene carbonate (a commonly used solvent in lithium ion battery applications), ethylene glycol (a polymer precursor), water, and copper sulfate $CuSO_4/H_2O$ (studied for applications in nanoparticle growth and electroplating). As a control experiment, EELS from a 50 nm thick SiN_x membrane is also shown in Figure 2.5(a). Plotted on the same scale, the liquid in the SiN_x/liquid/SiN_x structure dominates the EELS signal. A summary of the properties of the liquids is shown in Table 2.2.

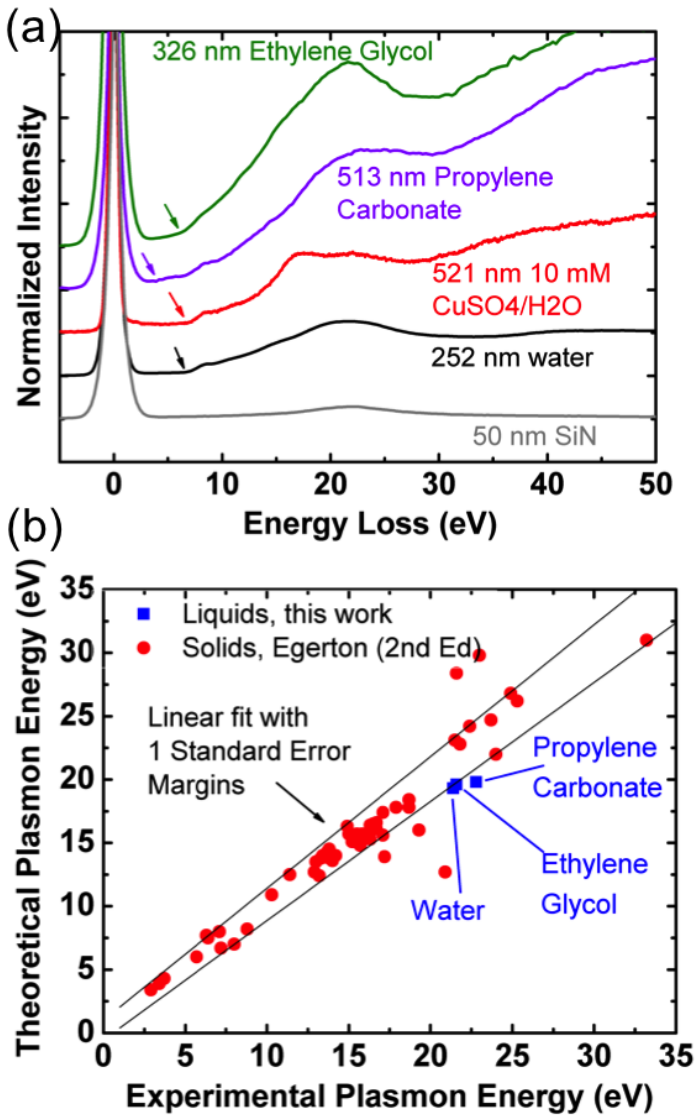

Figure 2.5. Valence EELS and plasmon energy of liquids. a) Valence electron energy-loss spectroscopy of ethylene glycol, propylene carbonate, 10 mM of $CuSO_4/H_2O$, and water. Arrows point to the optical gap. The background spectrum from the SiN_x membranes alone shows no dominant features on the same scale without the presence of liquid. b) Theoretical free- electron estimates of the plasmon energy compared to experimental plasmon energy for solids (Egerton, 1986) and measurements of the pure liquids. The solid lines are the one-sigma standard error margins of a linear fit. Adapted from Holtz et al. Microscopy and Microanalysis 2013[5]

Table 2.2: Electronic Structure Properties Found from Valence EELS of Four Liquids*

Liquid	Theoretical Plasmon Energy (eV)	Plasmon Energy by EELS (eV)	Measured Local Electron Density (cm^{-3})	Inelastic Mean Free Path (nm) – Eq. 2	Optical Gap by EELS (eV)	Optical Gap by UV-VIS (eV)
Water	19.3	21.4	3.30×10^{23}	106	6.9	6.5[†]
10 mM $CuSO_4/H_2O$	—	22.1	3.52×10^{23}	103	5.8	4.1
Propylene carbonate	19.8	22.8	3.75×10^{23}	100	4.2	5.2
Ethylene glycol	19.6	21.6	3.36×10^{23}	105	6.3	6.3

* The optical gap and the plasmon energy are found from the data in Figure 2.5. The local electron density and the inelastic mean free path are calculated from the plasmon energy and Eq. 2.5 and Eq. 2.2, respectively. The optical gap determined by UV-VIS or noted from the CRC Handbook

[†]From Ref. [24]

2.5.1 Plasmon Energy of Liquids

The incident electron beam excites collective oscillations of valence electrons in the material, known as plasmons. Plasmons generally have energies between 10-30 eV and are a prominent feature of the valence EELS signal. The local electron density n_o (valence electrons/m^3) is found using the free-electron model for the plasmon energy,

$$E_p = \hbar\sqrt{\frac{n_0 e^2}{\varepsilon_0 m_e}} \qquad \text{Eq. 2.5}$$

where $\hbar$ is Planck's constant divided by 2π, e is the elementary charge, ε_0 is the permittivity of free space, and m_e is the mass of the electron. Alternatively, the theoretical plasmon energy can be

calculated from bulk materials properties by estimating the local electron density as $n_0 = n_e N_A \rho / A$ where n_e is the number of valence electrons per molecule, N_A is Avogadro's number, ρ is the density of the material, and A is the atomic weight. The theoretical versus experimental plasmon energies are shown in Figure 2.5(b), compared to solids listed in Egerton [25]. For the solids, a linear fit with a slope of 1 is found, and the lines corresponding to one standard error margins are shown. The theoretical plasmon energy of the liquids matches reasonably well with the plasmon energy measured by EELS, confirming that the liquid behaves similarly to solids under the free electron model. Optical measurements have corroborated that the 21 eV peak in water is a collective electron oscillation [26].

While it might seem surprising that a liquid responds to an external charge disturbance in a manner closer to that of a free-electron metal than an isolated molecule, it should not be unexpected considering that most insulators behave similarly as well [4]. The key ingredients for collective oscillations are effective screening and a uniform background over the appropriate length scales. For instance, in water the Thomas-Fermi screening length [27] for the valence electrons is ~0.4A, smaller than the size of the molecule, which has 10 electrons/molecule. Because there can be screening of electrons even on an individual water molecule, the first condition for collective oscillations is met. However, an isolated water molecule will not appear as a uniform density of charge at long wavelengths, while a liquid will – this second condition is also important and is discussed in the next paragraph. A plasmon is a charge density fluctuation made of up virtual excitations of electron hole pairs in a collective manner leading to a net displacement at a given wavelength of the entire Fermi Sphere (the full momentum-dependent electronic structure of occupied states), so the energy for the electron-hole pair excitations must be less than the plasmon energy, E_p, i.e. in an insulator with an optical gap E_g, $E_g << E_p$. This is a necessary condition for electrons in insulators (and liquids) to behave like free electrons: single particle interactions with energies around the optical gap will then not significantly displace the measured plasmon energy

from the free plasmon energy (Egerton, 2011). As the energy of the virtual excitations increases, their lifetime must decrease, which from the energy-time uncertainty principle leads to a broadening of the resulting plasmon peak. Additional damping can occur depending on the exact details of the single particle electronic structure at those energies. Metals and small-gap semiconductors would then be expected to have sharper plasmon peaks than large gap insulators. The plasmon line width in water (10 eV) is not that different from silica, silicon nitride or most other insulators.

The second condition for collective oscillations is that the density sampled is uniform. This turns out to be met for liquids, and can be understood by considering the lifetime of the plasmons, which have energy spreads of around 10 eV. From the energy-time uncertainty principle, the spread in energy corresponds to a lifetime of 7×10^{-17} s. As an order of magnitude estimate, the charge oscillation spreads out at the speed of sound in the electron gas, which has an upper bound given by the Fermi velocity. Estimating this from the measured valence band width of ~ 5 eV, the plasmon travels ~ 0.9 Å, which is less than the scale of a water molecule, and provides evidence that the sampled electron density is uniform. The plasmon travel distance and lifetime correspond well to results calculated from time-dependent density functional theory, which shows ~1 Å distances and ~7-10 × 10^{-17} s lifetimes [28]. Although the oscillation does not propagate beyond a single molecule, collective motion is still possible because the Thomas-Fermi screening length of the electrons in the molecule (~0.4 Å) is smaller than the size of the molecule, allowing for electron interaction and screening on the same molecule (as there is more than one valence electron per molecule). Furthermore, the oscillating water molecule is surrounded by other water molecules of equal density and polarizability, so a relatively uniform electron density is sampled even at longer length scales, which satisfies the compressibility sum rule [29], forcing the frequency of the collective displacement of the Fermi sphere to the free-electron limit at small momentum transfer. The details of the single particle excitations then determine the lifetimes of the quasiparticle

excitations, which are very short lived in molecules compared to simple metals with more traditional single-particle band structures. The free electron formula underlying Eq. 2.2 and Eq. 2.5 will hold so long as the collective excitation cross sections exceed the single particle transitions and the valence orbitals are relatively uniform over the volume sampled by the excited state. The approximation should work well for *s* and *p* orbitals, but less well for the localized, narrow *d* and *f* states.

2.5.2 Measurement of the Optical Gap

The optical gap of a fluid is the minimum amount of energy required to excite an electron from the highest occupied molecular orbital to the lowest unoccupied state in the liquid, usually an excitonic state. Many liquids have relatively large optical gaps, while chemically active nanoparticles tend to exhibit strong excitations at lower energies. Thus the energy loss region below the optical gap can act as a transparent window through the liquid, where nanoparticle excitations can be observed with a relatively low background from the thick liquid layer, which will be discussed later for $LiFePO_4$. Furthermore, when the optical gap of the liquid is of interest, valence EELS enables a reliable determination of the optical gap of extremely small and/or localized amounts of liquid (~zeptoliters, zL; 10^{-21} L). The optical analog of EELS, ultra-violet and visible absorption spectroscopy (UV-VIS), can distinguish the optical gaps of liquids but only in bulk quantities (~mL). This demonstrates the strength of using valence EELS to qualitatively analyze the various types of liquids even for extremely small, localized volumes (~zL), although either probe broadening (Demers, et al., 2012) or delocalization (Muller & Silcox, 1995) will limit spatial resolution to the nm regime. This may provide details on how the electronic structure of a system changes during a chemical reaction if the species are changing across the viewing window, as we will demonstrate later with electron beam-induced reduction of copper sulfate to copper.

Local measurements of the optical gap of the liquid are possible using EELS, if the optical gap is larger than 3-5 times the width of the ZLP to avoid overlap and errors in background extrapolation. To find the location of the optical gap, we linearly fit the flat region after the ZLP and the sloped region after the optical gap and find the point of intersection between the two regions. For systems where the ZLP is not cleanly resolved from the optical excitations, more elaborate fitting functions are needed. In the copper sulfate solution, Cherenkov radiation is present, resulting in an increase in the intensity below the optical gap due to the electrons travelling faster than the speed of light in the medium (as discussed later). Because the raised background level would give an overestimate of the optical gap, we instead fit to the pre-zero-loss dark level and the sloped region after the optical gap and find that intersection. The precision of the optical gap measurement is limited by the energy resolution determined by the full width at half maximum of the ZLP as the spectrum is convolved with the ZLP; this shifts the onset by a value on the order of half the ZLP width. The optical gap measurements agree with UV-VIS measurements of pure liquids, but for the 10 mM copper sulfate solution the optical gap measured by EELS is between copper sulfate and water, likely because the scattering probability from the low concentration of $CuSO_4$ is much lower in the thin liquid layer.

2.5.3 Copper Deposition

The potential for EELS in understanding *in situ* chemical reactions is demonstrated by the electron beam-induced deposition of metallic clusters of copper on the top SiN_x membrane window during imaging. A 10 mM $CuSO_4/H_2O$ solution was irradiated at a beam dose rate of 30 e-/nm^2s. As the electrons impinge on the sample, the copper cations are reduced and clusters form and grow, as shown in Figure 2.6(a). Valence EELS, in Figure 2.6(b), confirms the growth of metallic copper: in the regions of zero to low deposition, the plasmon feature looks much like that of water. On the other hand, in regions of heavy copper deposition, peaks corresponding to metallic copper appear

around 17 eV. For this study, the EELS delocalization through the thick liquid is less than the resolution due to beam spreading.

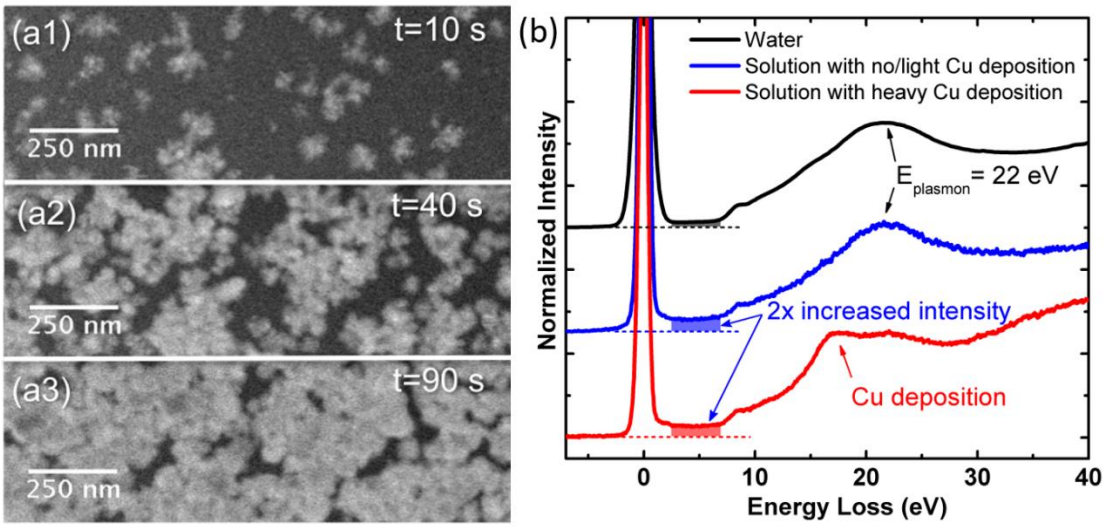

Figure 2.6. *In situ* STEM imaging of beam-induced Cu deposition in 10 mM CuSO4/H2O after (a1) 10, (a2) 40, and (a3) 90 s, at a 30 e-/nm^2 s dose rate. b: STEM-EELS after light Cu deposition (~2 s) and heavy Cu deposition (~90 s) are compared to water. The 10 mM $CuSO_4$ solution shows increased Cherenkov radiation compared with that of H_2O. After prolonged deposition, the EELS spectrum develops a peak at 17 eV, which is characteristic of bulk Cu.

Additionally, the $CuSO_4$ solution can be distinguished from water by the two-fold increase in intensity seen below the optical gap. From the optical absorption data, there is a 1.5 eV peak in the $CuSO_4$ solution, corresponding to a Cu^{2+} e_g to t_{2g} transition, which gives it a blue color [30]. With an energy resolution of 0.6 eV, the tail of the ZLP overwhelms this peak and it does not appear in the spectra. The detection of this peak may be possible with a monochromated beam, which would illustrate the advantages of high-energy resolution for the identification of a wider range of optical fingerprints. Although metallic copper is expected to produce a signal in the optical gap of the liquid, the signal in this region is identical in both the solution with and without metallic copper,

so it appears to be uncorrelated with the presence of metallic copper. This is understandable considering that the amount of metallic copper is small – by comparing the area under the plasmon peaks of the low copper deposition to heavy copper deposition, the contribution from metallic copper is roughly 20% of the total signal.

Due to the flat nature of the below-gap intensity, and because it is uncorrelated with metallic copper, we believe it corresponds to Cherenkov radiation. Cherenkov radiation occurs when the charged electrons pass through a medium faster than the speed of light in the medium, $v > c/n$, where v is the relativistic speed of the particle, c is the speed of light in vacuum and $n = \sqrt{\varepsilon}$ where n is the index of refraction and ε is the frequency dependent dielectric constant in the medium. Thus, for 200 keV electrons, we expect Cherenkov radiation in materials with index of refraction n greater than 1.44 (or for 300 keV electrons, $n > 1.29$). The appearance of Cherenkov radiation in the $CuSO_4$ solution indicates the increased index of refraction of $CuSO_4$ above 1.44 compared to pure water with index of refraction at 1.33. The small amount of Cherenkov radiation seen in water may be due to impurities. This finding follows the Frank-Tamm result, which states the energy lost per unit path of the particles is proportional to $[1 - (c^2/\varepsilon v^2)]$ [31]. This background is likely to be more pronounced at 300 keV, where even pure water will display a Cherenkov background.

2.6 EFTEM

The preceding discussion concentrated mainly on spectroscopic aspects of EELS, we briefly turn next to its complementary imaging mode, EFTEM. For the case of *in situ* liquid studies, EFTEM mode is particularly useful when applied to dynamic or time resolved measurements, as we will take advantage of in Chapter 5. EFTEM mode enables the formation of images resulting from electrons that have lost a fixed amount of energy defined by means of an operator-defined energy window within the optics of a suitably equipped imaging spectrometer [4]. In this operating

mode, a large area integrating digital camera at the output of the imaging spectrometer is used to rapidly record and process electron scattering from discrete transitions selected by the analyst. Selection of high signal to background ratio energy windows can result in imaging times of seconds or less. This mode can be used to enable dynamical imaging of chemical processes for spectroscopic signals with large cross sections, such as the valence transitions.

Valence transitions are especially sensitive as a monitor of electronic structure changes during *in situ* electrochemical or chemical reactions. For example, this procedure has been used to study charging and discharging of a battery cathode material $LiFePO_4$, where the electronic structure reveals if the material is in a charged or discharged state as discussed in Chapter 5 [7]. Dynamic imaging of the specimen and solution are achievable, as long as the cross-sections are large to provide rapid imaging.

In addition to mapping high signal/background transitions as illustrate above, EFTEM can also be used to improve image resolution in thick materials. By selecting the zero-loss (or elastic) signal, image blurring due to chromatic defocusing can be can be minimized, which is particularly acute in thick ($t/\lambda > 2$) regimes. For very thick specimens where the zero-loss image has very little remaining signal, selecting the bulk plasmon peak is the best choice. The correction of chromatic defocus can also be achieved in instruments equipped with combined spherical and chromatic aberration correctors. This correction will significantly enhance the intensity of signal in all EFTEM imaging experiments [32], thus improving the overall performance of EFTEM. However, the application of chromatic aberration correctors to date in liquid cell studies has been limited, principally due to the modest number of instruments having such chromatic aberration corrector technology installed.

2.7 Conclusion

Electron Energy Loss Spectroscopy and X-ray Energy Dispersive Spectroscopy are challenging but also powerful techniques for elemental and chemical identification of materials suspended in liquids. EELS is degraded quickly by multiple scattering in liquid media. Nevertheless, core-loss EELS can determine composition and bonding in media which is thinner than 2-3 mean free paths, while valence EELS can offer electronic structure information out to ~ 6 mean free paths. Valence EELS gives insight into electronic structure properties such as the local electronic density and optical gap, and we find that plasmon scattering in the liquid follows the free electron model. Looking for low-energy signals below the plasmon energy and especially in the optical gap of the liquid provides a high signal to background ratio. Additionally, the larger cross-sections for valence EELS provide a higher dose efficiency, making it more useful for rapid imaging. For electron beam-induced deposition of copper, plasmon peaks indicate the presence of metallic copper in heavy growth regions and Cherenkov radiation below the optical gap identifies the higher dielectric constant of the copper sulfate solution compared to water. In comparison, XEDS is significantly less affected by thick liquid media in the cells and offers routine elemental identification in liquids for media thickness which significantly exceeds that of EELS. EELS and XEDS are complementary and can be combined to elucidate sub-micron to nanoscale features.

Both EELS and XEDS require careful control of experimental conditions and specimens and media that are stable over the time scale of any spectroscopic measurements. Careful attention must be paid to stability of the media and specimens under the electron beam to radiation damage. Because the dose required for inelastic imaging is typically greater than the dose required for elastic imaging, the dose-limited resolution is worse for hyperspectral imaging compared to standard elastic imaging modes. Due to dose constraints, dynamical imaging with EELS and XEDS may be limited in specimens and media that are sensitive to beam irradiation. To avoid putting a large dose

on the sample, it may be necessary to perform dynamic imaging with the elastic scattering signal and to intermittently interrogate the composition of the sample with core-loss EELS and XEDS. Achieving dynamic imaging or spectroscopy will rely on large cross sections to enable rapid acquisition times. Valence EELS often provides large cross-sections that can be imaged quickly (~1-2 sec/spectral image) in EFTEM mode, however, interpretation of the spectra can be ambiguous if there is little presumed knowledge about the system. For XEDS, the acquisition rates will continue to improve as x-ray detector solid angles become greater, but for statistically comparable signals, acquisition times of tens of seconds to minutes per hyperspectral image may be required for the foreseeable future.

For the successful application of core-loss EELS and/or XEDS in liquids, forming the thinnest liquid cell is paramount. One promising approach to making the cells thinner is to use graphene instead of SiN_x as windows to encapsulate the liquid, or alternatively to develop ultra-thin SiN_x windows with intervening support bars having slightly thicker dimension. Of the two, graphene liquid cells will produce the thinnest liquid layers as well as reducing the scattering with the encapsulating material. However, because graphene is more flexible than SiN_x windows, liquid cells formed using graphene to replace SiN_x on standard silicon chips are likely to bulge substantially more, possibly resulting even thicker liquid layers. One alternative to reduce the effective thickness is to use at higher operating voltages, avoiding 100 keV instruments in favor of 200 keV and 300 keV tools, which increase the mean free path of the electron in liquid and thus reduce the total amount of scattering.

2.8 Materials and Methods

A liquid-flow TEM holder incorporating a microfluidic cell was developed by Protochips, Inc. and is described by Klein *et al* [14]. The holder houses a microfluidic cell consisting of two silicon-

processed chips with thin (~50 nm) silicon nitride membranes that form a viewing window when the chips are overlapped. To ensure that the two 20-40 micron by 200 micron wide silicon nitride membranes overlap to form a viewing window with thin regions in every loading of the holder, the windows are oriented orthogonal to each other. The microfluidic cell is encapsulated in the titanium tip of the holder with o-rings to prevent any liquid from leaking into the vacuum. The liquid is able to flow in to and out of the holder and is fed by an external syringe pump. The liquid flow enables multi-stage reactions in the tip of the holder. A holder schematic is given in the introduction (Figure 1.1).

Imaging and EELS were performed using a monochromated FEI Tecnai F-20 STEM/TEM operated at 200 kV and equipped with a Gatan 865 HR-GIF spectrometer for EELS analysis. While the monochromator was not employed here, the study did benefit from the system's improved energy stability. EELS was performed, both in the STEM geometry, compatible with high-angle annular dark field (HAADF) imaging, and in EFTEM mode. The convergence and collection angles for STEM EELS were 9-10 mrad and 20-30 mrad, respectively. HAADF-STEM was used for its high signal-to-background ratio for particles with high-Z offered by the dark field detector, and its insensitivity to chromatic blur from energy losses in the sample. EFTEM with a 5 eV slit was explored as an option for short-time acquisitions of large images in relatively thin liquid layers. Since the energy slit was narrow, chromatic blur did not limit our spatial resolution, and we did not find it necessary to use an objective aperture in EFTEM mode.

References

[1] J. Goldstein, D. Joy, D. Maher, J. Silcox, and N. J. Zaluzec, *Introduction to Analytical Electron Microscopy*, 1st ed. (Plenum Press, New York, NY, 1979).

[2] M. E. Holtz, D. A. Muller, and N. J. Zaluzec, in *Liq. Cell Electron Microsc.*, edited by F. M. Ross (Cambridge University Press, Cambridge, 2016), pp. 408–433.

[3] M. E. Holtz, Y. Yu, J. Gao, H. D. Abruña, and D. A. Muller, Microsc. Microanal. **19**, 1027 (2013).

[4] R. F. Egerton, *Electron Energy-Loss Spectroscopy in the Electron Microscope*, 3rd ed. (Plenum Press, New York, 2011).

[5] K. L. Jungjohann, J. E. Evans, J. A. Aguiar, I. Arslan, and N. D. Browning, Microsc. Microanal. **18**, 621 (2012).

[6] M. E. Holtz, Y. Yu, J. Gao, H. D. Abruña, and D. A. Muller, Microsc. Microanal. **19**, 1027 (2013).

[7] M. E. Holtz, Y. Yu, D. Gunceler, J. Gao, R. Sundararaman, K. A. Schwarz, T. A. Arias, H. D. Abruña, and D. A. Muller, Nano Lett. **14**, 1453 (2014).

[8] N. J. Zaluzec, M. G. Burke, S. J. Haigh, and M. a Kulzick, Microsc. Microanal. **20**, 323 (2014).

[9] E. a Lewis, S. J. Haigh, T. J. a Slater, Z. He, M. a Kulzick, M. G. Burke, and N. J. Zaluzec, Chem. Commun. (Camb). **50**, 10019 (2014).

[10] T. Malis, S. C. Cheng, and R. F. Egerton, J. Electron Microsc. Tech. **8**, 193 (1988).

[11] G. A. Botton, G. Lesperance, C. E. Gallerneault, and M. D. Ball, J. Microsc. **180**, 217 (1995).

[12] H. R. Zhang, R. F. Egerton, and M. Malac, Micron **43**, 8 (2012).

[13] K. Iakoubovskii, K. Mitsuishi, Y. Nakayama, and K. Furuya, Microsc. Res. Tech. **71**, 626 (2008).

[14] K. L. Klein, I. M. Anderson, and N. De Jonge, J. Microsc. **242**, 117 (2011).

[15] M. Scheinfein, J. Vac. Sci. Technol. B Microelectron. Nanom. Struct. **4**, 326 (1986).

[16] P. E. Batson, Nature **366**, 727 (1993).

[17] D. A. Muller, Y. Tzou, R. Raj, and J. Silcox, Nature **366**, 725 (1993).

[18] D. A. Muller, L. F. Kourkoutis, M. Murfitt, J. H. Song, H. Y. Hwang, J. Silcox, N. Dellby, and O. L. Krivanek, Science **319**, 1073 (2008).

[19] K. L. Klein, N. de Jonge, and I. M. Anderson, Microsc. Microanal. **17**, 780 (2011).

[20] T. L. Daulton, B. J. Little, K. Lowe, and J. Jones-Meehan, Microsc Microanal **7**, 470 (2001).

[21] J. M. Yuk, J. Park, P. Ercius, K. Kim, D. J. Hellebusch, M. F. Crommie, J. Y. Lee, A. Zettl, and A. P. Alivisatos, Science **336**, 61 (2012).

[22] D. W. Johnson and J. C. H. Spence, J. Phys. D-Applied Phys. **7**, 771 (1974).

[23] J. C. H. Spence, Ultramicroscopy **4**, 9 (1979).

[24] W. M. Haynes and D. R. Lide, *CRC Handbook of Chemistry and Physics: A Ready-Reference Book of Chemical and Physical Data*, 92nd ed. (Taylor & Francis Group, 2011).

[25] R. F. Egerton, *Electron Energy-Loss Spectroscopy in the Electron Microscope*, 2nd ed. (Plenum Press, New York, 1986).

[26] J. M. Heller, R. N. Hamm, R. D. Birkhoff, and L. R. Painter, J. Chem. Phys. **60**, 3483 (1974).

[27] N. W. Ashcroft and N. D. Mermin, *Solid State Physics* (Brooks Cole, 1976).

[28] I. Tavernelli, Phys. Rev. B **73**, 94204 (2006).

[29] D. Pines and P. Nozières, *The Theory of Quantum Liquids* (Addison-Wesley Publishing Company, Advanced Book Program, Reading, MA, 1989).

[30] G. Jancso, Radiat. Phys. Chem. **74**, 168 (2005).

[31] J. D. Jackson, *Classical Electrodynamics* (Wiley, 1999).

[32] N. J. Zaluzec, Ultramicroscopy **151**, 240 (2015).

CHAPTER 3

ELECTROCHEMISTRY AND FUEL CELL STUDIES IN THE TEM

3.1 Introduction

Electrochemistry in the TEM opens doors to studying processes and materials relevant to electrochemical energy storage and generation – such as batteries, capacitors, and fuel cells – as well as corrosion and electrochemical deposition processes at the nanometer scale. Energy storage materials, such as battery electrodes, often display inhomogeneous behavior at the nanoscale [1], requiring high spatial resolution techniques that can provide information on individual grains and particles during operation. Fuel cell catalysts, such as platinum supported on carbon black (Pt/C), are generally comprised of nanoparticles, and so nanometer resolution is necessary to observe their spatially dependent degradation during operation. Electrochemical cell TEM thus fills a unique characterization need – providing not only measurement of electrochemical signals but also providing spatial resolution at the nanoscale with temporal resolution on the order of seconds.[2]

Some of the earliest liquid cell studies with modern, silicon nitride windows were designed for electrochemical experiments [2,3]. By integrating electrodes onto the microfluidic cell chips, and coupling those electrodes to external potentiostats, the groundwork was laid for advances in electrochemical *in situ* TEM design. Significant advancements in silicon microfabrication methods for chip design and designing holders capable of flowing liquids through the holder while remaining vacuum compatible made the tool more available. While the system was being developed commercially by Protochips, our team at Cornell began designing a broadly applicable *in situ* TEM liquid cell chip to enable studies that correlate quantitative electrochemistry with the

[2] Work in this chapter is done in collaboration with the Abruña group, in particular, Yingchao Yu and Johary Rivera.

microstructure of the active material in the TEM. Protochips fabricated the chip we designed, which has demonstrated reliable electrochemical performance even for surface-sensitive measurements such as cyclic voltammetry of fuel cell catalysts, and has become the leading electrochemical cell chip used for quantitative *in situ* TEM studies today [4–12]. In this chapter, we will first discuss critical factors behind chip performance and demonstrate cyclic voltammetry of platinum nanoparticles, a rigorous test-case for electrochemistry.

With the electrochemical cell holder, we were interested in studying fuel cell catalysts during cycling and under extreme potential conditions. One of the main degradation mechanisms of catalyst nanoparticles is coarsening, where the particles lose their high surface area to volume ratio [13,14]. Here we explore examples of degradation applicable to fuel cells, for the most part imaging Pt and Pt-Co nanoparticles on HSC or Vulcan carbon supports. We observe non-uniform carbon support corrosion, which leads to nanoparticle coalescence in Section 3.4. During cycling, we see the carbon support flexing, showing more dynamic behavior than expected from *ex situ* studies and reflecting the capacitive nature of the carbon surface. Switching gears to alkaline fuel cells, we observe the carbonate formation that leads to clogging of gas and liquid pathways when the alkaline media is exposed to CO_2 (Section 3.5).

3.2 Chip Design[3]

Our liquid cell design is described in Figure 3.1. The holder is a Protochips Poseidon liquid cell, using chips that we designed and Protochips fabricated to mimic a typical electrochemical cell (Figure 3.1a-b). The tip of the holder is a microfluidic flow cell with silicon nitride viewing

[3] The chip design was proposed by Prof. Abruña, Prof. Muller, Dr. Yu and the author, and executed at Protochips led by John Damiano.

membranes that confine a liquid, shown in cross section in Figure 3.1a. Figure 3.1b illustrates the top chip, with three patterned electrodes optimized for electrochemical cycling and imaging.

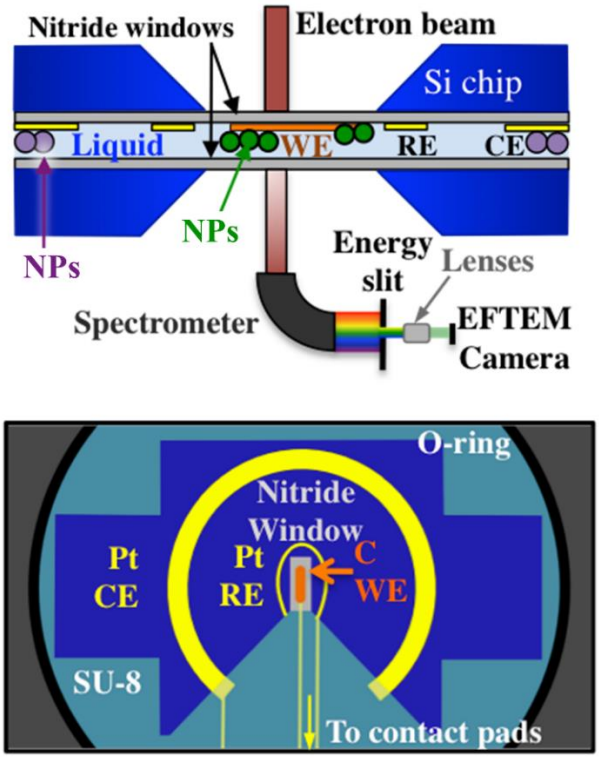

Figure 3.1. Schematic of the *in situ* electrochemistry TEM holder. (top) Cross-sectional view of the holder, with silicon nitride membranes encapsulating a fluid layer. The working electrode (WE), made of carbon, lies in the viewing window, with nanoparticles (NPs) deposited on top. The platinum counter electrode (CE) may be coated with the same or different nanoparticles. Here we include an illustration of EFTEM mode, in which energies are selected by a slit to be imaged. (bottom) Schematic of the top chip, with three patterned electrodes: a carbon WE on the viewing membrane, Pt reference electrode (RE), which is not used in the battery experiment, and Pt CE. The connection leads are covered by SU8, and the contact pads to the holder do not contact the liquid, to minimize electrochemical activity outside the viewing window.

For quantitative electrochemistry, the chip must not introduce extraneous electrochemical signals so the process of interest may be studied. We use an inert, electron-transparent glassy carbon working electrode which offers significantly lower scattering than previous metal electrodes. Because the glassy carbon is weakly scattering, there is little loss in spatial resolution and contrast, which is instead dominated by scattering in the liquid instead. Spatial resolution is more often limited by the low doses needed to control radiation damage than by beam spreading in the cell, as discussed in Chapter 1. Electrochemically, the glassy carbon is clean, with a featureless background signal from the capacitive response of the liquid. The working electrode is entirely in the viewing window, and electrical leads are covered in the photoresist SU8 to prevent additional electrochemical response.

Traditional silicon-processing methods use a chromium adhesion layer and gold electrodes. However, chromium diffuses rapidly through gold (especially at grain boundaries) and can affect and even dominate the electrochemical signal. We used titanium adhesion layers under the platinum reference and counter electrodes, which has been shown to be reliable. The reference electrode is near the working electrode to minimize uncompensated resistance, and the counter electrode is large and far away to provide ample current and prevent species migration. The electrodes have a rounded shape to promote uniform fields within the cell.

3.3 Cyclic Voltammogram of Platinum[4]

One of our first goals upon receiving the chips was to perform a cyclic voltammogram of platinum. This was partly because we were interested in observing nanometer sized Pt fuel cell catalysts coalesce during cycling, but moreover it was a test case for quantitative electrochemistry.

[4] This work was done in collaboration with Dr. Yingchao Yu, Dr. Burak Ulgut, and Johary Rivera under Prof. Abruña

The features in the cyclic voltammogram of platinum are surface effects, including hydrogen adsorption and desorption (at negative potentials) and oxide formation and reduction (at positive potentials), which are very sensitive to contaminants at the sub-monolayer level.

We performed cyclic voltammetry of a film of platinum, shown in Figure 3.2a-b, in the TEM in 0.1 M H_2SO_4. The *in situ* electrochemistry reproduced the characteristic voltametric profile of a polycrystalline platinum electrode at an appropriate current scale, regardless of the electron beam. In thin liquid layers, the ohmic drop in the solution becomes significant, as evidenced by the slanted curve in Figure 3.2db. This implies an inherent compromise between the highest spatial resolution imaging and quantitative electrochemistry. We find that this setup replicates the results of a conventional electrochemical cell while permitting nanometer resolution while imaging.

The platinum reference electrode (Pt/PtO) behaves as a pseudo-reference, which may change depending on the chemical conditions in the electrochemical cell. The reaction governing the platinum reference electrode is $Pt + O \leftrightarrow PtO$, which lies at about 0.8 V higher than the reversible hydrogen electrode (RHE) in acidic media. However, the reference potential can shift dramatically by introducing small amounts of hydrogen. For example, if one sweeps to too negative or positive potentials, hydrogen will be generated on the working or counter electrode, respectively. Since the microfluidic cell is small, the hydrogen diffuses throughout and comes near the reference electrode, causing the reference to be the couple (H_2/H^+), shifting the potential closer to standard hydrogen electrode (SHE). To ensure that the correct reference is being accessed, it is key to control the amounts of gas in the cell, requiring well controlled potentials. In conventional electrochemical cell experiments, it is additionally prudent to degas the electrolyte to remove oxygen. We suspect that degassing the electrolyte prior to the experiment will not prevent instability in the reference electrode, because gas can easily diffuse through our microfluidic tubes and because even the smallest amounts of gas generated on the electrode surface may affect the potential.

For the rest of this chapter, since we have a Pt/PtO reference electrode, we will cite potentials with respect to Pt. However, if we suspect hydrogen gas is present in the cell – resulting in a large positive shift of features in the cyclic voltammogram – we will instead reference SHE, which better reflects the H_2/H^+ reaction.

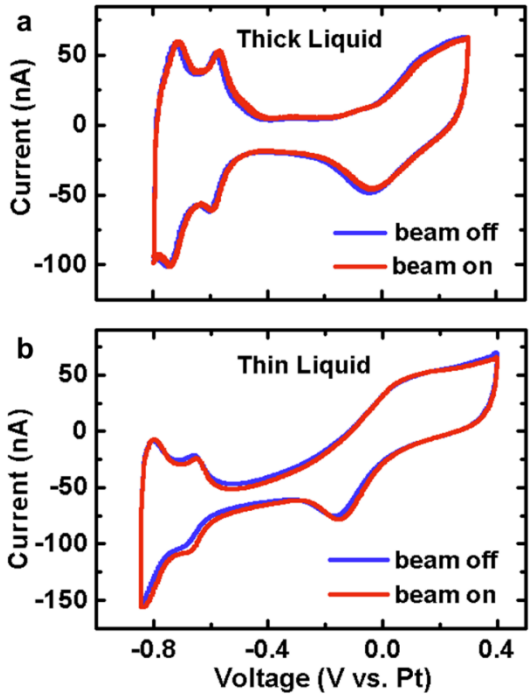

Figure 3.2. Cyclic voltammetry of a polycrystalline Pt film *in situ*. The chips exhibited electrochemical activity qualitatively similar to that of an *ex situ* microelectrode, as shown for the Pt cyclic voltammetry (CV) in 0.1 M H_2SO_4/H_2O for thick (a) and thin (b) layers. In extremely thin liquid layers (~150 nm) the voltammetric profile exhibits a significant ohmic drop as seen in (b).

These platinum cyclic voltammograms represent the polycrystalline platinum film which was deposited as a contact electrode under the glassy carbon working electrode. The glassy carbon working electrode did not provide a continuous surface coverage to prevent the signal from the platinum underlayer from dominating the signal. Fabrication of chips which had the platinum and

glassy carbon contact fully under the protective SU8 layer did not display this signal. After this modification, the glassy carbon working electrode with no nanoparticles deposited on it displayed a featureless background signal originating from the capacitive response of the liquid (Figure 3.3, black line). After depositing platinum nanoparticles onto the chip, we see a cyclic voltammogram of platinum nanoparticles on Vulcan in 0.1M NaOH measured in the TEM (Figure 3.3, red line).

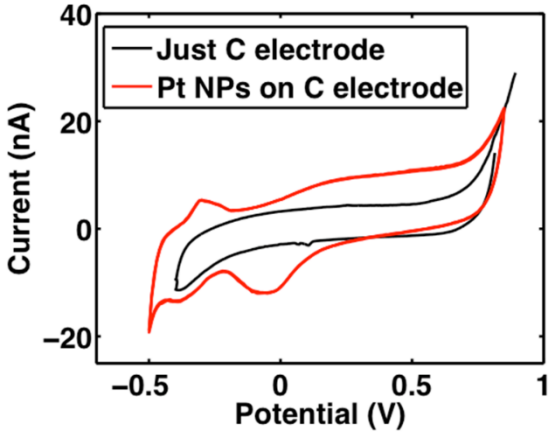

Figure 3.3. Cyclic voltammetry of the chip with and without Pt nanoparticles deposited on the working electrode. Cyclic voltammetry (CV) of the chip alone (no Pt deposited) shows a minimal electrochemical response, while the nanoparticles show the expected response. Potential is with respect to Pt. CVs performed this time in alkaline media: 0.1M NaOH.

If operated under different circumstances, Pt/HSC, a common fuel cell catalyst, can also perform electrolysis. Adjusting the potential to below that of hydrogen evolution, as observed by the dip in the current at low potentials in the cyclic voltammograms (Figure 3.2), the hydrogen evolution reaction proceeds ($H^+ + e^- \rightarrow \frac{1}{2} H_2$) at potentials below 0 V vs RHE (-0.8 V vs Pt). If enough H_2 is formed, it can no longer remain dissolved in solution and forms a bubble. Similarly, at potentials above 1.2 V vs RHE (0.4 V vs Pt), the oxygen evolution reaction proceeds ($2H_2O \rightarrow 4e^- + 4H^+ + O_2$) and a bubble of oxygen may form.

Here we observe electrochemical bubble formation by HAADF-STEM imaging and EELS (Figure 3.4). In the STEM images (Figure 3.4a), the Pt/HSC aggregates initially have low contrast, indicating thick liquid is present over the entire field of view. After a low potential (-0.25 V vs SHE) is applied for 90 seconds, a hydrogen bubble is formed near the particles (region with dark background and high contrast from particles). The potential is returned to open circuit potential after 90s, and the bubble begins to dissipate, completely disappearing 22s after the potential is returned to open circuit. At high potentials, a similar phenomenon is observed when an oxygen bubble is formed, although much higher overpotentials (2 V vs SHE) are applied to obtain a bubble since oxygen may remain in solution at higher concentrations.

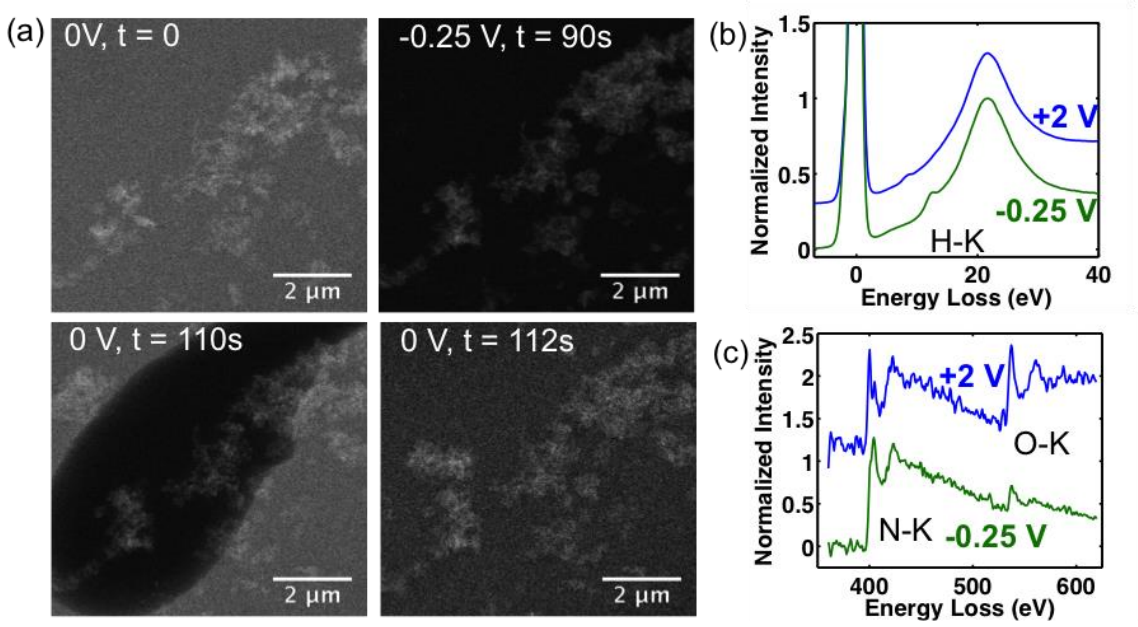

Figure 3.4. Electrochemical generation of gas in the electrochemical cell in 0.1 M H_2SO_4. (a) HAADF STEM images show hydrogen bubble formation near Pt at large negative potentials, that disappears upon returning to open circuit potential. The negative potential turned on at t=0 and held for 90 s. (b) EELS finds hydrogen bubbles at low potentials (peak near 13 eV) and (c) oxygen bubbles at high potentials.

When EELS is performed in the bubble at low potential, a peak near 14 eV corresponding to hydrogen appears (Figure 3.4b), which is not present in the bubble at high potential. At high potential (Figure 3.4c), we instead see a larger peak corresponding to oxygen at 532 eV, indicating the additional presence of oxygen. At low potential, there is a small oxygen peak, corresponding to water vapor in the bubble, residual liquid water, or oxygen in the SiN_x membrane [15]. There is a strong nitrogen edge for both high and low potential due to the SiN_x membrane. Thus, EELS confirms the composition of the bubble expected from electrochemistry, providing evidence these bubbles are generated by electrochemistry instead of by the electron beam, as observed in other works [16–18].

3.4 Carbon Support Corrosion[5]

The morphology of the support structure for catalysts in fuel cells is important in determining their degradation and transport behavior. Of particular interest is to understand the degradation mechanism of the electrocatalysts, which generally undergo coarsening and lowers their active surface area. Here we image Pt_3Co/HSC as it undergoes coarsening (Figure 3.5). The cyclic voltammogram is on the first generation of chips which is dominated by the Pt film instead of the Pt_3Co nanoparticles (Figure 3.5a). To accelerate degradation so it is observable in the time frame of our beam dose limitations, we test the stability by holding the potential. At low potential, the particles remain stable. However, when we apply a higher voltage of +1.0V, we see the onset of carbon support corrosion (Figure 3.5b). Carbon support corrosion begins at the ‘neck’ of two carbon ensembles where the current density is highest, as observed in the image at 38 s. As the carbon crumples, nanoparticles start to migrate on the surface, followed by sintering events (86 s – 260 s).

[5] This work was done in collaboration with Dr. Yingchao Yu and Dr. Johary Rivera.

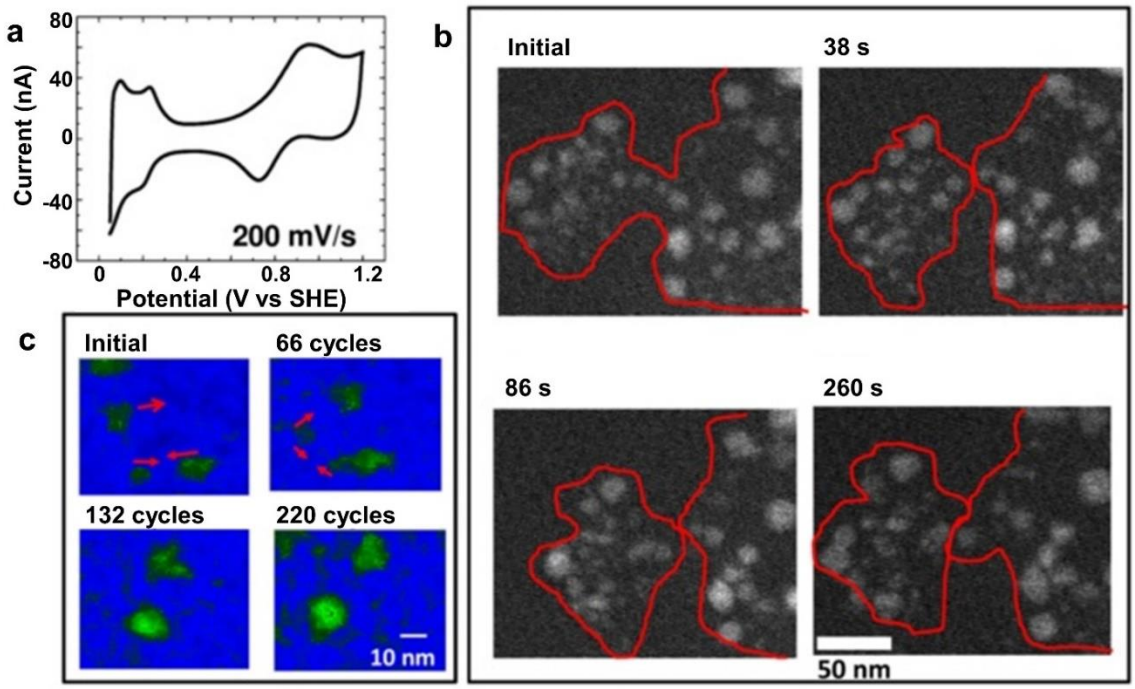

Figure 3.5. *In situ* TEM study of Pt_3Co/HSC showing carbon support corrosion and nanoparticle coalescence. (a) Cyclic voltammetry (CV) of Pt nanoparticles on a carbon working electrode in 0.1M H_2SO_4 at a scan rate of 200 mV/s. The CV curve is performed inside electron microscope during imaging. (b) Time-resolved HAADF images of Pt_3Co at a constant voltage of +1.0 V (vs. Pt), with a red curve highlighting the boundary of the carbon support. We observe nanoparticle migration and coalescence assisted by carbon support corrosion during the electrochemical aging. (c) Coalescence behavior of Pt_3Co, as a function of cycles. False-color is used to enhance contrast.

We can further cycle the voltage to observe the coarsening process, shown in the false-colored HAADF-STEM image in Figure 3.5c. These images are small fractions of the entire field of view – which are much larger to prevent beam damage. We observe multiple Pt_3Co particles in green move toward each other (66 cycles) and merge (132 cycles). During these studies, we ensure that the electron beam does not affect the nanoparticles without cycling on the time scale of the electrochemical experiments. These results suggest that stabilization of catalyst support,

minimization of nanoparticle movement or reduced loading are potentially valuable for slowing down the degradation of PEMFCs system.

One surprising thing observed during *in situ* cycling of Pt/HSC and Pt/Vulcan was that the carbon bended or flexed during cycling. During cyclic voltammetry, the carbon aggregates swell at low potential and relax at high potential (Figure 3.6a-c). The carbon branch that is highlighted reversibly oscillates tens of nanometers with the voltage (Figure 3.6d). At low potential, the branch moves away from its neighbor, and then relaxes at high potential. We suspect that the dynamics of the HSC are of capacitive origin, attracting and possibly intercalating protons at negative potentials. The lower mobility and larger size of the sulfate anions inhibits similar behavior at high potentials. If the carbon oscillation occurs in a fuel cell, it may degrade gas diffusion pathways or lead to Pt coalescence. As discussed in Figure 3.5, and as we will discuss in Chapter 4, carbon support degradation at high potentials may lead to platinum coalescence. This suggests carbon support movement may adversely affect cell lifetimes.

In situ cyclic voltammetry of Pt nanoparticles on HSC is shown in Figure 3.6e. The working electrode, which contains the electrochemically active sample, is confined to the viewing membrane. Even with our small electrode and current scale (5 nA), the measurement has minimal noise. As the sweep rate is increased, the current increases roughly as the square root of the sweep rate. From hydrogen adsorption/desorption (HAD) measurements, we find roughly 2x10-5 cm^2 of platinum surface area on the electrode. From tomography done by Padgett, et al [19], that surface area corresponds to ~10^5 primary carbon particles and 25 picograms of platinum.

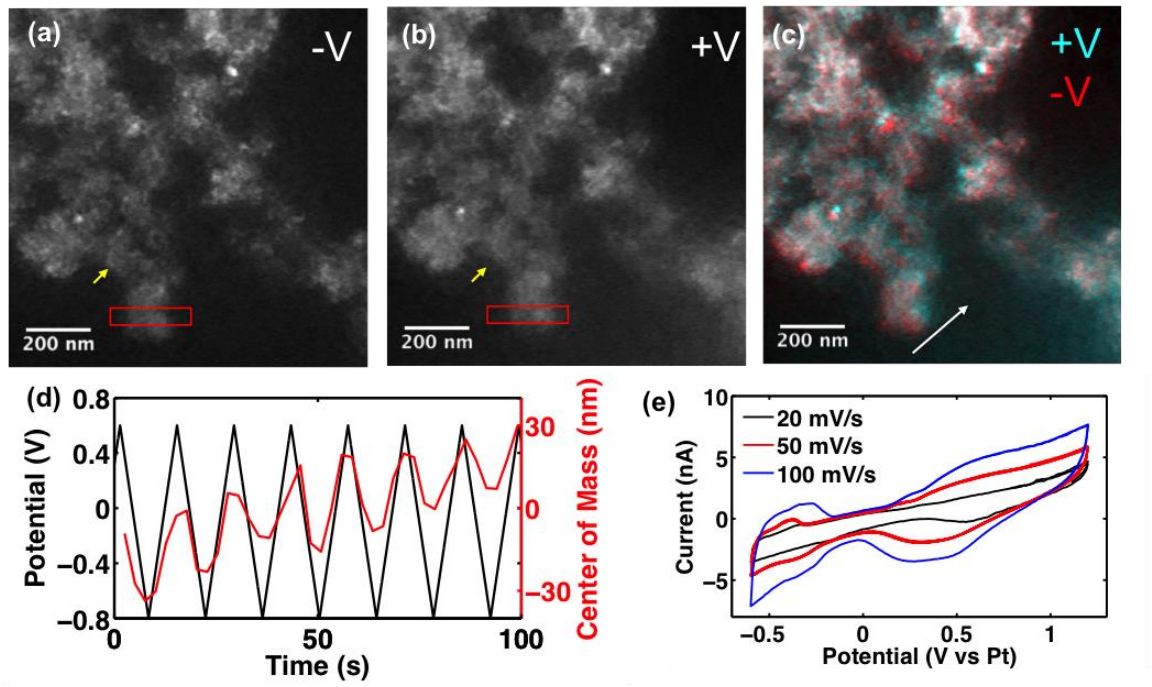

Figure 3.6. *In situ* cycling of Pt/HSC in 0.1 M H_2SO_4 showing carbon bending. HAADF-STEM images at (a) negative potentials and (b) positive potentials, with a color overlay in (c). At low potential, the carbon aggregates swell, suggesting proton intercalation, which relaxes at positive potentials. (d) Position of the particle marked by the red box, plotted with voltage. Particle moves more to the right at high potential. (e) Cyclic voltammetry of Pt with sweep rate, at low current density. HAD estimates ~2×10^{-5} cm^2 Pt surface area.

3.5 Alkaline Fuel Cells and Carbonate Formation[6]

Alkaline fuel cells can yield high oxygen reduction kinetics compared to their acidic counterparts. This allows the use of significantly less platinum, or even non-noble and lower-cost catalysts, in the alkaline fuel cell, reducing the cost. One of the major limitations of alkaline fuel cells is that they require pure oxygen instead of air on the intake. This is because small amounts of carbon dioxide that get into the cell can cause carbonate formation upon contact with the electrolyte

[6] This work was done in collaboration with Dr. Johary Rivera under Prof. Abruña.

(eg. $CO_2 + 2NaOH \rightarrow Na_2CO_3 + H_2O$). The carbonate particles can clog the electrode, preventing further gas flow and causing fuel starvation.

In PEMFCs, NAFION is widely used as a proton conductor in the membrane. For alkaline fuel cells, an alkaline anion exchange membrane (AAEM) must have high OH^- conductivity, be stable under basic media, and have minimal swelling when hydrated. Recently, new phosphonium-based AAEMs have been developed at Cornell in the Coates group, enabling high OH^- mobility across the membrane and good stability [20]. Here we investigate this material in conjunction with our typical Pt/HSC catalyst to attempt *in situ* electrochemical cell experiments under more realistic conditions (i.e. with a membrane), and investigate membrane swelling and carbonate formation.

Figure 3.7a shows *in situ* STEM of platinum nanoparticles separated from the counter electrode by a phosphonium alkaline anion exchange membrane. The membrane is diluted with solvent to provide a drop-cast membrane that is electron transparent, which is dispersed across all three electrodes. The membrane is quite beam sensitive, and only tolerates minimal beam dose. The cyclic voltammogram of the nanoparticles in 0.1M NaOH is shown in Figure 3.7b. Imaging during this cyclic voltammogram produced no significant changes observed in the STEM image. After flowing in methanol, the cyclic voltammogram displays a methanol oxidation process (Figure 3.7b). During methanol oxidation, we see formation of particles that are likely carbonates (initial: Figure 3.7c, final: Figure 3.7d), which block pores and poison the fuel cell. The particles are generated by the electrochemistry but assisted in agglomeration by the electron beam - small particles appear over the entire electrode, and only while performing methanol oxidation. Post-mortem XEDS analysis suggests that the particles contain sodium, carbon and oxygen, indicative of sodium carbonate.

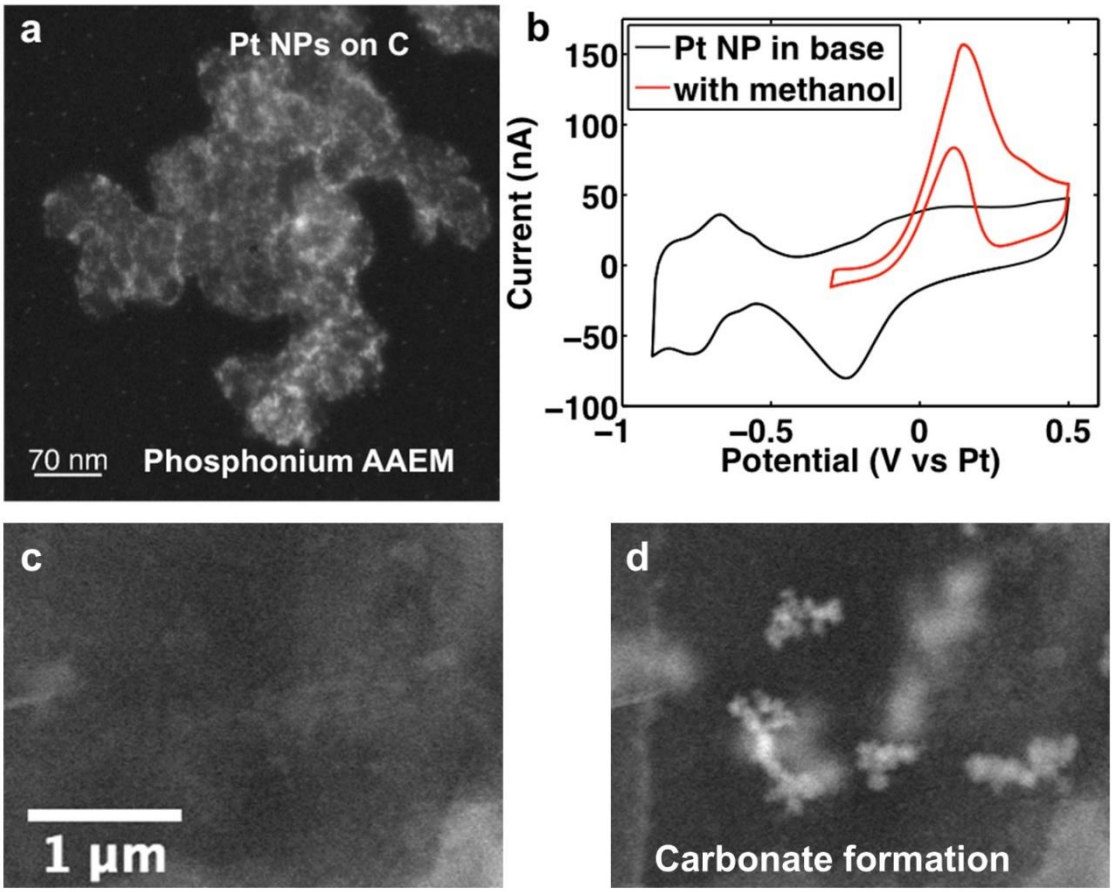

Figure 3.7. *In situ* data of AAEM operation in an alkaline solution, showing carbonate formation. (a) HAADF-STEM image in a gas-filled electrochemical cell of Pt/HSC with a phosphonium AAEM. (b) Cyclic voltammogram in 0.1M NaOH, showing typical Pt features, and in 0.1M NaOH and 0.1M methanol with a hydrated phosphonium alkaline anion exchange membrane and Pt catalyst. STEM images of (c) before and (d) after methanol oxidation on the membrane. What appear to be carbonate particles appear after cycling. The particles are easily moved and agglomerated under the electron beam.

3.6 Conclusions

The *in situ* TEM electrochemical cell is a promising field, especially for energy materials found in fuel cell and battery systems. Because fuel cell and battery materials are inhomogeneous on the nanometer scale, the nanometer scale observation of these materials can offer new insight into the

degradation and operation of this technologically important class of materials. Particular care is needed in the setup of the electrochemical cell chip to mimic operation of standard microelectrochemical cells. While the setup presented here will work in many cases, the confined nature of the two-chip sandwich geometry in the TEM holder does not prevent species diffusion from the counter electrode to the working electrode. Additionally, the use of platinum as the reference electrode leaves something to be desired because the potential is affected by pH (becoming completely unreliable near neutral pHs) and the presence of gas in the cell can swing the potential hundreds of millivolts. Careful considerations of these limitations and future designs of the electrochemical will (and already have in the case of the reference electrode) improve the situation significantly.

References

[1] R. Malik, A. Abdellahi, and G. Ceder, J. Electrochem. Soc. **160**, A3179 (2013).

[2] F. M. Ross, IBM J. Res. Dev. **44**, 489 (2000).

[3] M. J. Williamson, R. M. Tromp, P. M. Vereecken, R. Hull, and F. M. Ross, Nat. Mater. **2**, 532 (2003).

[4] M. E. Holtz, Y. Yu, D. Gunceler, J. Gao, R. Sundararaman, K. A. Schwarz, T. A. Arias, H. D. Abruña, and D. A. Muller, Nano Lett. **14**, 1453 (2014).

[5] G.-Z. Zhu, S. Prabhudev, J. Yang, C. M. Gabardo, G. a. Botton, and L. Soleymani, J. Phys. Chem. C **118**, 22111 (2014).

[6] R. R. Unocic, R. L. Sacci, G. M. Brown, G. M. Veith, N. J. Dudney, K. L. More, F. S. Walden II, D. S. Gardiner, J. Damiano, and D. P. Nackashi, Microsc. Microanal. **20**, 452 (2014).

[7] B. L. Mehdi, J. Qian, E. Nasybulin, C. Park, D. A. Welch, R. Faller, H. Mehta, W. A. Henderson, W. Xu, C. M. Wang, J. E. Evans, J. Liu, J. G. Zhang, K. T. Mueller, and N. D. Browning, Nano Lett. **15**, 2168 (2015).

[8] S. Nagashima, K. Yoshida, T. Hiroyama, K. Liu, Y. Kang, T. Ikai, H. Kato, T. Nagami, and K. Kishita, Microsc. Microanal. **21**, 1295 (2015).

[9] J. Liu, B. Wei, J. D. Sloppy, L. Ouyang, C. Ni, and D. C. Martin, ACS Macro Lett. **4**, 897

(2015).

[10] R. L. Sacci, J. M. Black, N. Balke, N. J. Dudney, K. L. More, and R. R. Unocic, Nano Lett. **15**, 2011 (2015).

[11] B. L. Mehdi, A. Stevens, J. Qian, C. Park, W. Xu, W. A. Henderson, J.-G. Zhang, K. T. Mueller, and N. D. Browning, Sci. Rep. **6**, 34267 (2016).

[12] L. Wang, J. Wen, H. Sheng, and D. J. Miller, Nanoscale **8**, 17250 (2016).

[13] M. S. Wilson, F. H. Garzon, K. E. Sickafus, and S. Gottesfeld, J. Electrochem. Soc. **140**, 2872 (1993).

[14] J. C. Meier, I. Katsounaros, C. Galeano, H. J. Bongard, A. a. Topalov, A. Kostka, A. Karschin, F. Schüth, and K. J. J. Mayrhofer, Energy Environ. Sci. **5**, 9319 (2012).

[15] N. J. Zaluzec, Microsc. Microanal. **21**, 959 (2015).

[16] J. M. Grogan, N. M. Schneider, F. M. Ross, and H. H. Bau, Nano Lett. **14**, 359 (2014).

[17] L. Liu, Y. Liu, W. Wu, C. M. Miller, and E. C. Dickey, Analyst **140**, 6330 (2015).

[18] C. Wang, T. Shokuhfar, and R. F. Klie, Adv. Mater. **28**, 7716 (2016).

[19] E. Padgett, N. Andrejevic, Z. Liu, K. Moriyama, R. Kukreja, S. Kumaraguru, W. Gu, Y. Jiang, V. Elser, and D. A. Muller, Microsc. Microanal. **22**, 1284 (2016).

[20] K. J. T. Noonan, K. M. Hugar, H. a Kostalik, E. B. Lobkovsky, H. D. Abruña, and G. W. Coates, J. Am. Chem. Soc. **134**, 18161 (2012).

CHAPTER 4

REAL-TIME IMAGING OF ACTIVATION AND DEGRADATION OF OCTAHEDRAL PT-NI FUEL CELL CATALYSTS AT THE NANOSCALE[7]

Octahedrally shaped Pt-Ni alloy nanoparticles have demonstrated unprecedented electrocatalytic activity for the oxygen reduction reaction (ORR), sparking interest as future catalysts for low-temperature fuel cell cathodes. While shape is of utmost importance for their activity and stability, the structural dynamics and surface chemical processes associated with activation and degradation have remained largely unknown. In fact, stability and shape issues currently prohibit the use of shaped catalysts in fuel cell devices. Here, we present real-time scanning transmission electron microscope imaging of the activation and degradation of carbon supported Pt-Ni alloy nanoparticles using an *in situ* electrochemical liquid cell. We track structural and morphological changes of particles and facets, monitor carbon corrosion, translational particle motion and coalescence, and investigate electrochemical dissolution/redeposition processes of the nanocatalyst under working conditions. We find morphological stability of the alloy octahedra in potential windows of regular fuel cell operation during the *in situ* experiment. Shape transformations of individual particles, selective Ni dissolution, and particle coalescence were observed during cycling reaching from fuel cell operation modes to detrimental fuel cell start/stop regimes. Carbon support motion, particle motion, and particle coalescence were observed as the main micro-structural dynamic responses at high potential, which we attribute to carbon corrosion as expected at these potentials. The present study provides new vivid visual understanding of the fundamental structural dynamics of shaped nanocatalysts during fuel cell operation and will thereby aid in the development of more stable, practical catalysts.

[7] This work will be submitted as: V Beermann*, M.E. Holtz*, E. Padgett, D.A. Muller, P. Strasser (2017).

4.1 Introduction

Heightened interest in alternative renewable power sources has increased technological and scientific focus on fuel cell technologies. A large part of such research and development is focused on novel cathode catalyst materials for the oxygen reduction reaction (ORR) where efficiency losses have remained high. New catalyst systems based on alloying Pt with transition metals like Fe, Co, Ni, and Cu in unshaped alloy nanoparticles have led to improved ORR activities [1–4]. At least an order of magnitude improvement in catalytic ORR activity over these conventional alloy nanoparticles has been reported for shape-controlled octahedral Pt-Ni alloy particles, because they exclusively expose highly active (111) Pt-Ni facets [5–13]. While unshaped Pt-M alloy fuel cell catalysts are beginning to be deployed in commercial applications [14,15], shape-controlled particles still face challenges in terms of stability, especially in the final MEA device [14,16]. Shaped Pt-Ni nanoparticles have been observed to quickly lose their octahedral shape after cycling, in part due to nickel dissolution [4,17–21]. The detailed degradation processes of octahedral Pt-Ni particles have remained elusive. Hence, better understanding of their structural behavior and degradation is critically required before these high-activity catalysts can be deployed in commercial applications.

Many physical characterization methods have been used to gain a better understanding of the morphology and composition of fuel cell catalyst materials before and after degradation. Most of the work to date has relied on *ex situ* characterization techniques, often involving scattering from x-ray, light or electrons to describe the initial or post mortem material. For fuel cell catalyst nanoparticles, transmission electron microscopy (TEM) is a popular method to determine the particle shape and distribution on the support material, as well as elemental distribution and stability. Identical location TEM (IL TEM) has been used extensively for some Pt-based nanoparticle material to track and study changes of identical particles or catalyst parts before and

after electrochemical treatment [22–28]. In addition to *ex situ* techniques, there has been a recent surge of interest and capability in *in situ* and *operando* methods that enable probing the material under working conditions, garnering valuable understanding of material operation and degradation [1,29–44]. Lately, several groups reported *in situ* electrochemical TEM investigations on fuel cell materials [45,46] and lithium ion battery materials [32,47–51]. These experiments typically use liquid-cell systems in conventional TEMs with SiN windows on chips encapsulating a thin liquid layer. Using this powerful tool, it is possible to perform conventional electrochemistry and electrocatalysis while imaging the reactive particles of interest in real time on the nanometer scale, obtaining invaluable *operando* information about the nanocatalyst at work.

In this study, we investigate the degradation of carbon-supported octahedral shaped Pt-Ni nanoparticle catalysts for advanced fuel cell cathodes. We use an *in situ* electrochemical liquid-cell and scanning transmission electron microscopy (STEM) to track individual particles under electrochemical conditions that arise or are applied at the cathode. We monitor the translational, structure-morphological, and – thanks to atomic number contrast in high angle annular dark field (HAADF) STEM – compositional dynamics and evolution of individual nanoparticles as well as ensembles of nanoparticles in real time and with nanometer-scale resolution. This study gives new insight of how initially shape-controlled nano-octahedra transform into unshaped and partially agglomerated particle clusters, and provides visualization of how the degradation of the carbon support affects the catalyst material.

4.2 PtNi Catalyst

We investigated ~8 nm octahedral Pt-Ni nanoparticles that exhibited an average composition of $Pt_{34}Ni_{66}$ and were supported on Vulcan carbon supports (Figure 4.1a). These supported Pt-Ni/C nanooctahedra showed electrochemical ORR activity that was about 25x greater than commercial

Pt/C, and, from a more practical perspective, were large enough to be imaged in an *in situ* TEM liquid environment at low beam doses. In addition to octahedral Pt-Ni nanoparticles, the catalyst also contained a minor alloy phase consisting of 20-30 nm Ni-rich particles, which enabled study of rapid electrochemical dissolution processes of undesired alloy phases during catalyst [52]. Figure 4.1 a shows the catalyst particles *ex situ* as synthesized: the initial octahedral shape is evident from the faceting of the particles, which are homogeneously distributed on the carbon support. After *ex situ* voltammetric stability tests in perchloric acid, the octahedral particles lost their sharp faceting and showed agglomeration (shown in Figure 4.1b). To better understand this degradation, we perform an *in situ* study of the real time nanometer-scale evolution of the octahedral fuel cell catalysts.

The *in situ* TEM experiments were carried out in a Protochips Poseidon holder and a flow cell chip equipped with a silicon nitride window. The cross section and top view of the chip are illustrated in Figure 4.1c showing the carbon working electrode and the Pt reference and counter electrode [32,44]. The platinum reference electrode was calibrated in 0.1 M perchloric acid using the well-known characteristics of the hydrogen underpotential deposition region of platinum-based materials, as shown in Figure 4.1d. With that, 0.0 V_{RHE} was correlated to -0.8 V_{Pt}. All further potentials are reported against the reversible hydrogen electrode (RHE) based on this calibration to allow better comparability to literature. The cell had a liquid thickness of 300 nm, estimated by electron energy loss spectroscopy [53].

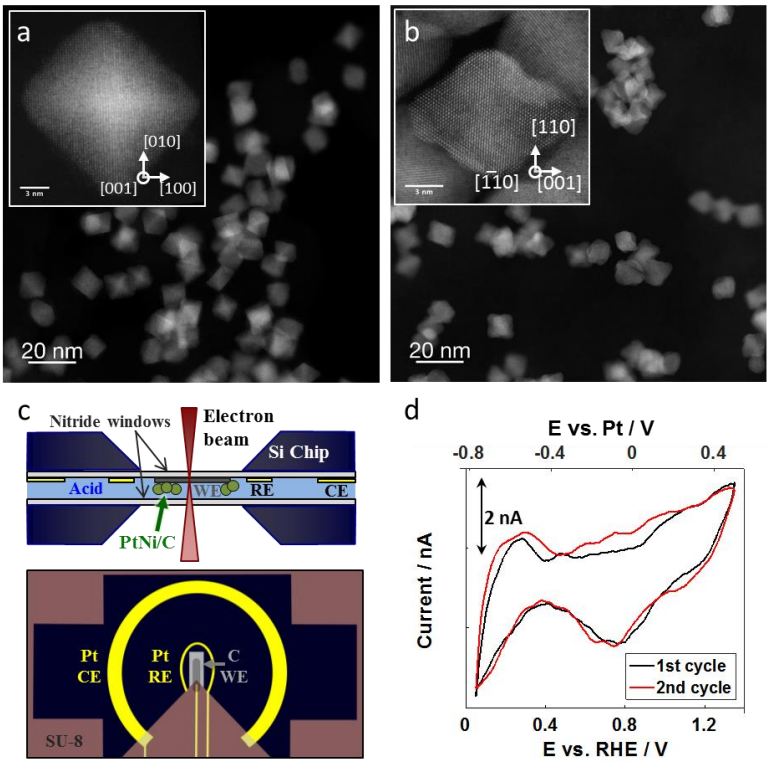

Figure 4.1: Pt-Ni octahedral nanoparticles in the electrochemical cell. (a) Particles *ex situ* before cycling, showing octahedral shape with faceting in the {111} planes and (b) *ex situ* after electrochemical treatment similar to the *in situ* experiment, where facets are curved and particles are agglomerated. (c) Overview of electrochemical cell setup. (d) Cyclic voltammogram of Pt-Ni nanoparticles on the carbon working electrode inside the electrochemical cell in 0.1 M $HClO_4$ with a sweep rate of 100 mV s^{-1}.

Prior to the *in situ* TEM electrochemical investigations, we identified a suitable beam dose that did not visibly affect the octahedral particles in the electrolyte for the duration of the applied electrode potential. Even though the beam alone may not influence the particles, the combination of beam and electrochemical cycling may have an effect. To account for this, we compared the final state (after electrode potential cycling) of particles that were imaged during the *in situ* experiment to other particles that were not continuously imaged in the electrochemical cell, to crosscheck for similar transformations. We further compared particles that were on the electrode

to those that were not on the electrode to ensure that the effects were electrochemical rather than chemical inside the liquid cell (Figure 4.2). As a final check, we qualitatively compared the data from *in situ* experiments to that of *ex situ* experiments. Overall, we found that the electrochemical effects observed were neither artefacts from the electron beam, nor from the chemical environment in the cell. However, the *in situ* experiments appeared to be harsher on the particles due to the additional effects of the electron beam.

We initially flowed a solution of 0.1 M $HClO_4$ / H_2O into the cell at 300 μL/hr to wet the cell and then flowed solution at 50 μL/hr during the experiment using a syringe pump. A "floating-type" Gamry potentiostat was used for the *in situ* TEM measurements. *In situ* microscopy was performed using a monochromated FEI Tecnai F-20 STEM/TEM operated at 200 kV and equipped with a Gatan 865 HR-GIF spectrometer for EELS analysis. Electron beam conditions were selected to optimize imaging conditions while minimizing beam damage, ranging from 30 – 60 e^- / nm^2s for HAADF-STEM imaging with a 9.6 mrad convergence angle. During control experiments with no electrochemical biasing, we observed that an electron beam dose rate of 110 e^- / nm^2s induced damage while 60 e^- / nm^2s did not show significant change after 10 minutes of imaging. For the *in situ* movies, denoising through imageJ was run to enhance signal to noise [54–56]. *Ex situ* imaging was performed using a monochromated FEI Titan Themis CryoS/TEM operated at 300 kV, with a 21.4 mrad convergence angle.

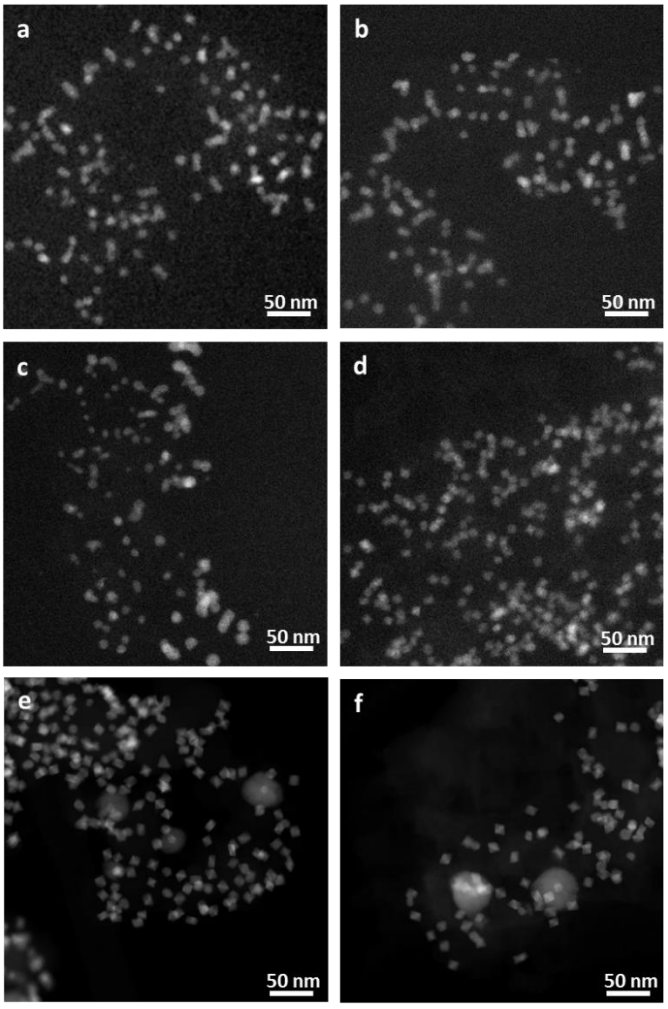

Figure 4.2 Comparisons of octahedral shape change with and without the electron beam. HAADF STEM images of particles before (a) and after (b) *in situ* cycling from 0 to +1.2 V_{RHE} with continual imaging. The carbon support corrodes and there is some coalescence and shape degradation. Images of the particles which are on (c) and off (d) the electrode in the *in situ* cell after cycling where neither region was exposed to the electron beam. Particles on the electrode show rounded surfaces and those off the electrode maintain their octahedral shape and size. HAADF STEM images of the *ex situ* particles in an aberration corrected STEM before (e) and after (f) the same electrochemical procedure, showing less shape change than the *in situ* experiment, although some shape change is observed.

4.3 *In Situ* PtNi Catalyst Activation

We performed *in situ* electrochemical STEM investigations using different electrochemical electrode potential cycling protocols, resembling those routinely applied to single fuel cells to electrochemically activate and stress-test their catalysts [4,21,57,58], cycle in standard operating ranges, and cycle under extreme potentials to simulate start/stop conditions.

First, the octahedral nanoparticles were cycled 20 times inside a potential range between 0.0 and +1.0 V_{RHE} with 100 mV s^{-1} to mimic an activation procedure. Figure 4.3a the applied potential profile with selected marked time points corresponding to the STEM images shown in Figure 4.3b-g. The selected field of view displays a collection of octahedral nanoparticles surrounding a larger Ni rich particle. During the electrochemical treatment, there was no discernible change in the octahedral particle structure. However, the large Ni-rich particle marked by the arrow in Figure 4.3b-g gradually dissolved during the applied potential cycling. After 10 cycles (Figure 4.3c) the particle started to lose mass (observed by a change in diameter and in the overall HAADF intensity) and after 15 cycles (Figure 4.3f) only a small fraction remained. The dissolution process takes place over several potential cycles, first becoming less dense, then appearing sponge-like and porous, and finally disappearing completely. The dissolved Ni-rich particle leaves behind an octahedral particle, which may have been contained inside the Ni-rich phase, evidenced by the bright contrast in the center (see Figure 4.3b). The dissolution of another Ni-rich particle was observed between Figure 4.3b (where it is a fractional particle already) and Figure 4.3c in the central lower part of the frame. After the first 20 cycles, there were still Ni-rich particles remaining in areas outside of the region imaged in Figure 4.3, and after an additional 20 cycles (total of 40 cycles), the remaining Ni-rich particles elsewhere on the electrode also disappeared.

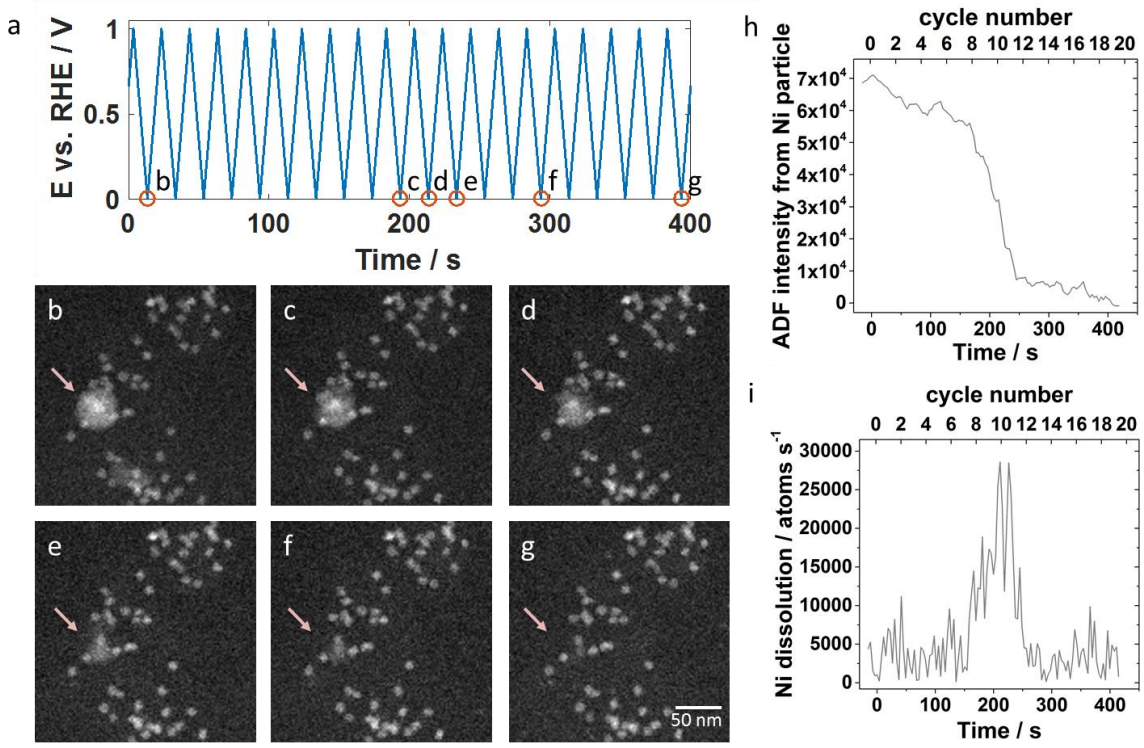

Figure 4.3: *In situ* imaging of the catalyst structure during electrochemical potential cycling between 0.0 and +1.0 V_{RHE} in 0.1 M $HClO_4$ for 20 CV with 100 mV s^{-1} sweep rate. (a) Potential profile over time with marked points corresponding to the images in (b-g). A Ni-rich particle marked by the arrow disappears during cycling, first becoming less dense, then spongy, finally dissolving completely. (h) ADF intensities of the Ni-rich particles over time during potential cycling and (i) the resulting Ni dissolution rate.

The opportunity to image the Ni dissolution process in real time allows us to estimate an average dissolution rate. Annular dark field (ADF) intensities of the Ni particle were obtained by integrating over a region containing the Ni particle, subtracting off the background intensity from a neighboring region to account for liquid thickness variation, and subtracting off the average intensity of the last 5 frames, when the Ni particle had fully disappeared. In Figure 4.3h, we first see a gradual decrease in ADF intensity, which corresponds in the image to the particle becoming less dense, then spongy. Then, the particle dissolves rapidly, decreasing in size drastically between

cycle 9 and 13. The dissolution rate, plotted in Figure 4.3i, reaches values of around 10,000 to 30,000 atoms per second during cycles 9 through 13. Thereafter, the remaining amount of Ni-rich particle that remains slowly dissolves away – perhaps due to low surface area or Pt enrichment as Ni is selectively removed. This is the first quantitative observation of the nanometer-scale reaction dynamics of a selective Ni dissolution process during the disappearance of Ni-rich alloy particle.

To compare the activation processes during the *in situ* experiments and corresponding *ex situ* treatments, *ex situ* experiments in a conventional three-electrode cell set up were carried out using identical protocols. The observed cyclic voltammetry current in the *in situ* cell may differ from an *ex situ* experiment for several reasons, including the small area of the working electrode, the electrolyte that has not been degassed, and the different diffusion geometry in the thin encapsulated cell. Nevertheless, some trends in the *in situ* cyclic voltammograms are noteworthy as they are showing the same processes as observed in the STEM images. With increasing cycle number, the current at higher potentials due to Ni dissolution trails off, and the redox waves inside the H_{upd} region become sharper, which is consistent with generating a cleaner, Pt-richer, and more facetted surface due to Ni dissolution and Pt diffusion. Unlike *in situ*, we noticed several residual large Ni-rich nanoparticles after 40 *ex situ* cycles. Thus, we conclude that the *in situ* conditions were more corrosive than the *ex situ* conditions, possibly due to the confined liquid cell environment and electron beam effects, as well as the lower geometric Pt loading.

Our observations show that the typical electrochemical activation comprised of cyclic voltammetry in liquid does not harm the shape or distribution of the Pt-Ni octahedra, validating the suitability of these commonly used activation procedures. Furthermore, the undesired Ni-rich clusters dissolve within minutes of the activation protocol [18,19]. In all, this is the first time that the activation dynamics of a shaped Pt alloy fuel cell catalyst by electrochemical dealloying and selective corrosion has been imaged in real time.

4.4 PtNi Catalyst Degradation in Extreme Conditions

Next, we studied the impact of sequential sets of potential cycles separated by periods with constant applied electrode potential, a frequently used test cycle motif for automotive or stationary PEM fuel cells. The potential versus time profile is given in Figure 4.4a, again with marked time points for the snapshots shown in Figure 4.4b-h. An initial potential hold at +0.8 V_{RHE} is followed by cyclic voltammetry with an upper potential of +1.2 V_{RHE} with 100 mV s^{-1} sweep rate. Then, there is a subsequent fixed potential hold at +1.2 V_{RHE}, followed by cyclic voltammetry to an upper potential of +1.4 V_{RHE} at 100 mV s^{-1}. This is finished with another fixed potential hold at +1.4 V_{RHE}. For this experiment, we imaged a region of the octahedral Pt-Ni nanoparticles that was previously not immersed in electrolyte, and did not show evidence of previous cycling.

During the hold at +0.8 V_{RHE} carbon remained stable and we saw no changes in catalyst structure (Figure 4.4c). When cycling to +1.2 V_{RHE}, a slight movement of the carbon support was observed. We also observed the nucleation and growth of stringy, new Pt deposits, which is likely due to chemical Pt redeposition as we will discuss in the following paragraph (Figure 3d). During the hold at +1.2 V_{RHE} (Figure 4.4e) the redeposited Pt abruptly moves, as if it was not firmly attached and became dislodged when held at elevated potential. When the Pt redeposits appear to collide with other parts of the sample or working electrode, their motion slows or stops. At the same time, the Pt-Ni nanoparticles started to grow slowly in size (Figure 4.4f), as expected from both electrochemical and beam-induced redeposition. Upon cycling to +1.4 V_{RHE}, the redeposited Pt again becomes mobile and swings about, while carbon-supported Pt-Ni particles also move notably. Additional stringy Pt deposits form. Finally, holding the potential at +1.4 V_{RHE} again causes abrupt motion of the redeposited Pt (Figure 4.4h), while carbon corrosion appears to occur rapidly enough to cause sustained motions of the carbon-supported Pt-Ni particles (Figure 4.4i) and PtNi particle growth continues.

Several phenomena were observed in this experiment – including growth and motion of stringy Pt deposits, PtNi nanoparticle growth, and Pt catalyst structure changes which are likely due to carbon corrosion – which we will discuss in the following paragraphs.

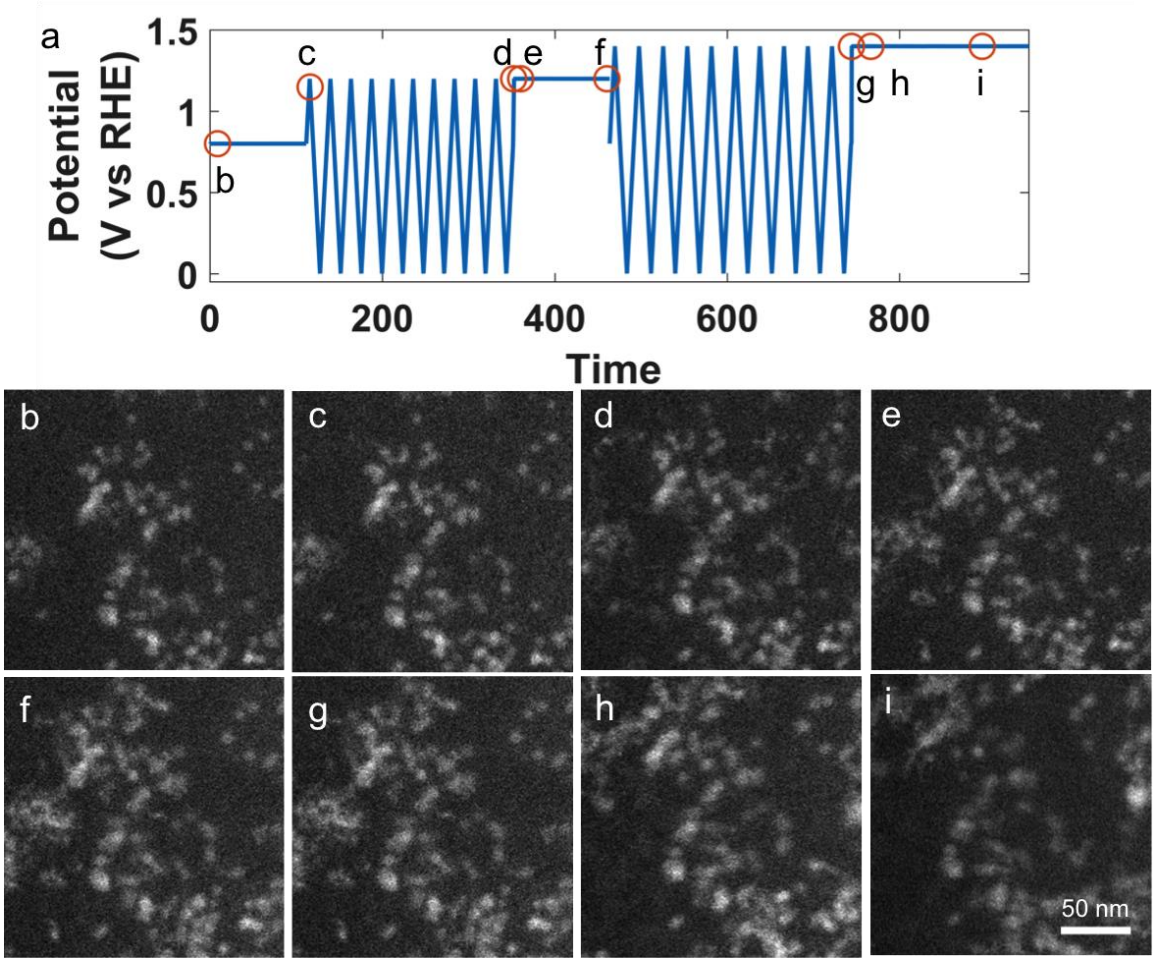

Figure 4.4 *In situ* imaging of the impact on the catalyst structure of an electrochemical sequence consisting of electrochemical potential cycling between 0.0 to +1.2 V_{RHE} and 0.0 to +1.4 V_{RHE} for 10 CV with 100 mV s^{-1} and holding on different upper potentials in 0.1 M $HClO_4$. (*a*) Potential profile over time with marked points for shown images. (*b-i*) Images taken at the marked potential and cycle number.

There are two potential causes of the observed stringy Pt redeposition: chemical redeposition, which is driven by a reducing chemical environment in the cell such as one generated by the

electron beam [59], or electrochemical reduction, which occurs at low, reducing potentials only at locations which have electrical contact with the working electrode. We observe that these Pt deposits form faster during cyclic voltammetry than during potential holds. There may be two reasonable explanations for this: 1) electrochemically assisted deposition might occur during the sweep to low potentials, or 2) the Pt is chemically deposited, and happens faster during the cyclic voltammetry because of increased Pt dissolution during the cyclic voltammetry, so there is more Pt in solution to be chemically deposited. Because the deposition appears to be faster at the cyclic voltammetry with upper potentials of 1.4 V_{RHE} compared to 1.2 V_{RHE}, it is more likely that redeposition is chemically driven. This is because the time spent at lower potential is the same, meaning the electrochemical deposition would be expected to be similar, but there is more time spent at higher potentials, and accordingly more Pt will be dissolved. We thus conclude that we observe chemical Pt redeposition that is driven by the reducing effects of the electron beam, which is similar to the formation of so-called pure Pt deposits (referred to as "Pt bands") reduced by dissolved hydrogen inside fuel cell membranes [60]. Unlike in a fuel cell, however, the chemically redeposited Pt in this experiment is not embedded in a polymer matrix and has a different reduction process, and is therefore highly mobile and morphologically different from fuel cell Pt bands.

We observed the most severe and sudden changes to the catalyst structure precisely at the transitions from the voltammetric cycling to the potentiostatic holds with chronoamperometric monitoring of the current density. The redeposited, lightly attached, stringy Pt becomes loose, very mobile and detached from the catalyst support when carbon corrosion at high potentials starts to occur. They appear to move until they collide with another feature in the catalyst structure. Furthermore, the particle motion and coalescence was correlated with the applied electrode potential during both cyclings and holds, corroborating the detrimental effect of the anodic upper potentials. Thus, our *in situ* STEM studies evidenced how strongly platinum oxidation and

dissolution accelerated at the atomic scale with increasing upper turning potentials as predicted by the mean-field Butler-Volmer relation [61–63].

In addition to the stringy Pt formation, we also observe the initial Pt-Ni octahedral particles grow over the course of the treatment. During the potential holds at high electrode potentials, catalyst particles continued to grow and lose their shape. This may be due to the formation of Pt deposition by the electron beam.

Carbon corrosion is expected to become significant at potentials of +1.1 V_{RHE} and higher [64–67]. At these high potentials (around 1.2 V_{RHE}), we observe two types of PtNi nanoparticle motion. One is that we see carbon support motion and crumpling, which may be an effect of carbon corrosion, where the catalyst nanoparticles in one region of the carbon support appear to move together as the carbon bends. The second effect is that the corrosion appears to weaken the attachment of particles on the carbon support, causing additional particle migration, coalescence and agglomeration. Both of these effects were more severe at higher potentials. We found that holding at higher potentials as opposed to potential cycling intensified and accelerated particle catalyst degradation.

Upon comparison of *ex situ* and *in situ* conditions, the *ex situ* conditions again were less harmful to the catalyst structure than the *in situ* ones. After *ex situ* cycling up to +1.2 V_{RHE} the octahedral particle shape was still clearly discernible, while edges and the corners were degraded after cycling to +1.4 V_{RHE}. While the general trends were consistent, the impact of the applied electrode potential on the shape, particle distribution and carbon corrosion was evidently less pronounced under the *ex situ* conditions, which is reasonable due to the absence of electron beam driven processes.

Finally, we imaged the structural evolution of octahedral Pt-Ni fuel cell catalysts under conditions simulating startup/shutdown and air or fuel starvation, which often cause uncontrolled potential steps in cathodic or anodic directions [68–70]. To achieve that, we first applied 10 potential cycles to an elevated upper potential of +1.2 V_{RHE} after which the electrode potential experienced a potential step to above +1.4 V_{RHE}. The Pt-Ni nanoparticles in this experiment had only undergone the activation profile corresponding to Figure 4.3.

During the 10 potential cycles to +1.2 V_{RHE} the octahedral shape of most particles appears largely unaffected, but a few experienced coalescence with close neighboring particles (Figure 4.5b-d, pink arrow) or small motions on the support (Figure 4.5b-d, yellow arrow). Considering that the upper potential lies outside the window where carbon is kinetically stable, we speculate that the motion and coalescence may be due to carbon support corrosion.

The final anodic potential step dramatically affected the global catalyst structure (Figure 4.5e-g) and would have catastrophic consequences for the fuel cell performance. The particles became highly mobile on the carbon support, as shown in the images in Figure 4.5, with the majority of particles colliding on the timescale of seconds into an agglomerate with a long, branching geometry. They appear to align their crystal facets before fusing together. We observe similar agglomeration in neighboring regions on the electrode outside the field of view, showing this occurred independent of beam effects. After a catastrophic, abrupt agglomeration, the catalyst particles continued to move on the carbon surface as carbon corrosion continues.

The corresponding *ex situ* images acquired after the same electrochemical treatment confirm the observed trends. Although individual particles still appeared to be octahedrally shaped they agglomerated at their crystal facets. From the *in situ* magnification in Figure 4.5, it is difficult to unambiguously identify the remaining particles as octahedral or unshaped, due to the low beam dose which is required to avoid radiation damage.

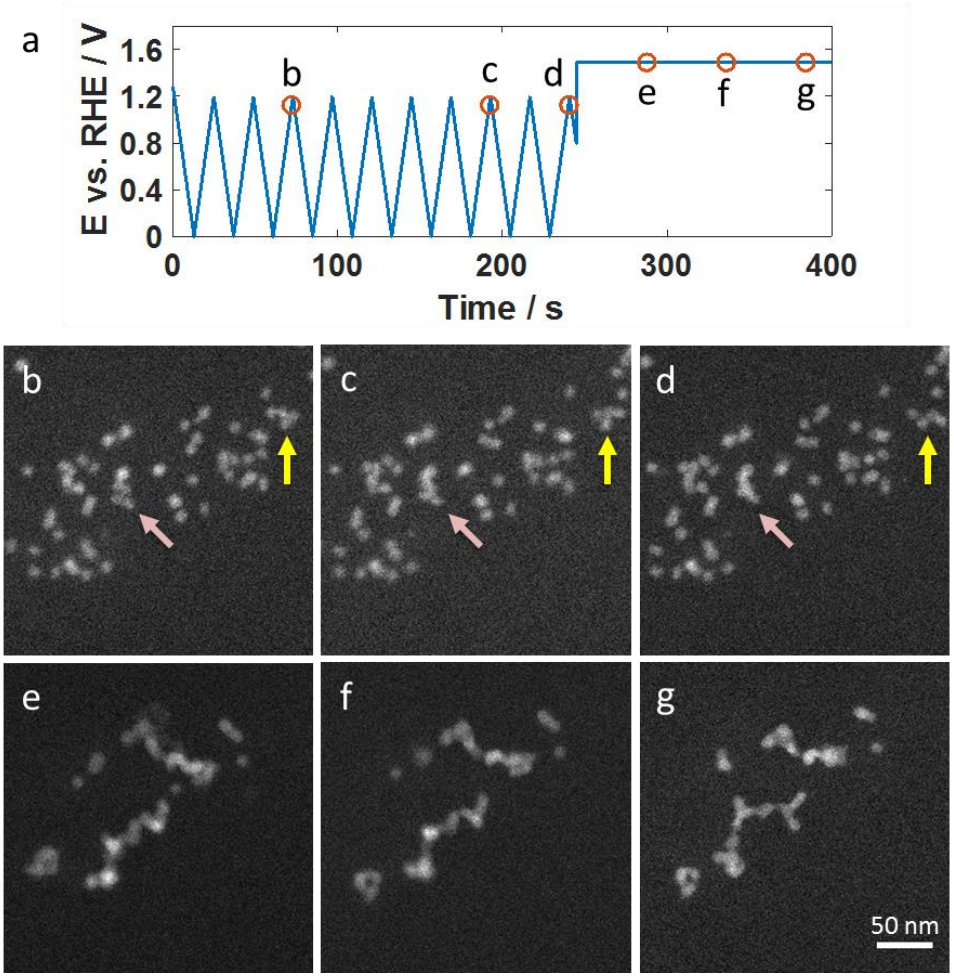

Figure 4.5: Catastrophic effects of going to uncontrolled high potentials on octahedral shape of Pt-Ni nanoparticles. HAADF-STEM *in situ* imaging of the catalyst structure during electrochemical potential cycling between 0.0 and +1.2 V_{RHE} for 20 CV with 100 mV s^{-1} sweep rate, followed by a step into a high potential. (a) Potential profile over time with marked points corresponding to the images in (b-g). Some changes to catalyst particles are noted during cycling in (b-d) – for example, coalescence as indicated by the pink arrow and particle motion as indicated by the yellow arrow (e-g). After cycling, going to a high potential, we see dramatic coalescence, where the Pt-Ni nanoparticles agglomerate into wires.

We should additionally note that the octahedral Pt-Ni particles were dispersed onto the carbon support as entire particle ensembles, that is, after their synthesis, rather than grown directly onto it,

which likely resulted in weaker interactions between particles and support compared Pt/carbon catalysts synthesized with impregnation methods, where a Pt molecular precursor is reduced on the carbon in a dispersed state. Further studies will investigate the particle mobility as a function of different particle attachment methods. Previous *in situ* TEM investigations of Pt-Co nanoparticles grown onto the support by impregnation methods found less particle migration despite extreme carbon corrosion at high potentials [71]. Additionally, this experiment was done in liquid (without the presence of ionomer or membrane) and the presence of ionomer may alter the effects of carbon corrosion.

Our findings provide a first-of-its-kind real-time visual demonstration of the catastrophic effects of uncontrolled fuel cell cathode potential excursions to values of startup/shutdown. Our results further underline the critical importance of a strict continuous upper electrode potential control. Two distinct mechanisms could contribute to the rapid coalescence at high potential: first, the instantaneous formation of Pt and Ni surface oxides induced by the abrupt anodic potential step may have lowered the particle attachment and caused enhanced mobility; more likely, however, is the mechanism involving sudden corrosion and removal of the carbon support leaving Pt-Ni particles unanchored and causing strongly enhanced particle movement by surface and bulk diffusion until the detached particles have found neighboring particles to agglomerate with.

4.5 Conclusions

We have presented STEM imaging of fuel cell catalyst activation and degradation processes in an *in situ* electrochemical cell. We investigated high activity octahedral Pt-Ni nanoparticle fuel cell catalysts [52]. Our *in situ* studies have revealed new insight into fuel cell catalyst degradation mechanisms, such as carbon support corrosion, selective dissolution of non-noble metals, catalyst particle shape degradation, and particle coarsening by coalescence and Pt redeposition. To the best

of our knowledge this is the first such *in situ* electrochemical liquid cell TEM experiment for shaped fuel cell cathode materials.

During catalyst activation, we observed the nanometer-scale reaction dynamics of a selective Ni dissolution process, observing the Ni-rich particles become spongy before fully dissolving. We observe that octahedral Pt-Ni alloy catalyst remained morphologically stable during moderate potential cycling up to +1.0 V_{RHE}, while cycling to and holding at 1.2 V_{RHE} and 1.4 V_{RHE} caused increasingly severe coarsening. During cyclic voltammetry to high potentials, we observed the electron beam reduction of stringy deposits similar to Pt bands caused by hydrogen cross-over in membrane electrode assemblies. At high potential holds, Pt redeposition quickly obscures the octahedral shape. Additionally, carbon corrosion was observed to increase particle migration and coalescence, with Pt-Ni nanoparticles appearing to typically coalesce on their {111} facets.

This study dramatically visualizes the dynamics of fuel cell catalyst activation and degradation at the nanometer scale. From these results we develop a better understanding of detrimental nanoscale effects which occur under different fuel cell conditions.

4.6 Experimental

Platinum(II)acetylacetonate ($Pt(acac)_2$, Pt 48% min.), nickel(II)acetylacetonate ($Ni(acac)_2$, 95.0 %), tungsten hexacarbonyl ($W(CO)_6$, 97.0 %) and oleic acid (OAc, 90 %) were obtained from Alfa Aesar. Oleylamine (OAm, 98.0 %) was obtained from Sigma Aldrich. All chemicals were used as received.

We investigated ~8 nm octahedral Pt-Ni nanoparticles that exhibited an average composition of $Pt_{34}Ni_{66}$ and were supported on Vulcan XC 72R carbon supports. The synthesis of Pt-Ni/C octahedral nanoparticles was described earlier [52]. Shortly, $Pt(acac)_2$, $Ni(acac)_2$, OAm and OAc

were stirred under nitrogen atmosphere at 60 °C for 10 min, followed by raising the temperature to 130 °C. $W(CO)_6$ was added rapidly, nitrogen purging was stopped and the reaction mixture was heated to 230 °C and then stirred for 50 minutes. After cooling down to RT toluene and ethanol (EtOH) were added to the reaction mixture. The supernatant was removed by centrifugation and re-dispersed in toluene. The dispersion was added to a dispersion of Vulcan XC 72R in toluene. The mixture was sonicated with an ultrasonic horn for 30 min. Afterwards EtOH was added and the catalyst was centrifuged, washed with EtOH and freeze dried. In the subsequent annealing step the supported particles were heated with 10 K min^{-1} to 180 °C in a tube furnace in synthetic air atmosphere for 30 min. After purging nitrogen for 30 min the atmosphere was changed to hydrogen and the temperature was raised with 10 K min^{-1} to 300 °C for 1 h.

For TEM investigations a Protochips Poseidon electrochemical cell holder was used. The liquid flow cell portion [72,73] and the electrochemical cell design [32] has been discussed previously. The Pt-Ni catalyst nanoparticles were dispersed into isopropanol solution and drop cast onto the chips with electrodes after cleaning. The Pt-Ni catalyst was then dispensed on the carbon working electrode, as well as the platinum reference and counter electrodes. Because the reference and counter electrodes are made of platinum and are large compared to the dispersed nanoparticles, they should not affect electrode behavior. We initially flowed a solution of 0.1 M $HClO_4$ / H_2O (diluted from 70 % conc. $HClO_4$, 99.999 % trace metal bases, Sigma Aldrich with milli-Q water) into the cell at 300 μL/hr to wet the cell and then flowed solution at 50 μL/hr during the experiment using a syringe pump (Infuse/Withdraw Pump 11 Pico Plus Elite, Harvard Apparatus). The electrolyte layer thickness was 300 nm, estimated by electron energy loss spectroscopy [72]. A "floating-type" Gamry potentiostat was used for the *in situ* TEM measurements. The platinum reference electrode was calibrated in 0.1 M perchloric acid using the well-known characteristics of the hydrogen underpotential deposition region of platinum-based materials, as shown in Figure

4.1d. With that, 0.0 V_{RHE} was correlated to -0.8 V_{Pt}. All potentials are reported against the reversible hydrogen electrode (RHE) based on this calibration to allow better comparability to literature.

In situ microscopy was performed using a monochromated FEI Tecnai F-20 STEM/TEM operated at 200 kV and equipped with a Gatan 865 HR-GIF spectrometer for EELS analysis. Electron beam conditions were selected to optimize imaging conditions while minimizing beam damage, ranging from 30 – 60 e^- / nm^2s for HAADF-STEM imaging with a 9.6 mrad convergence angle. During control experiments with no electrochemical biasing, we observed that a beam dose of 110 e^- / nm^2s induced damage while a dose around 60 e^- / nm^2s did not show significant change after 10 minutes of imaging. For the movies in the supplemental, denoising through imageJ was run to enhance signal to noise [54–56]. *Ex situ* imaging was performed using a monochromated FEI Titan Themis CryoS/TEM operated at 300 kV, with a 21.4 mrad convergence angle.

For *ex situ* electrochemical characterization a conventional three electrode cell with a Pt gauze as counter electrode (Pt furled Pt 5x5 cm^2 mesh), a reference electrode (MMS Hg/Hg_2SO_4 with the potential E= -0.723 V_{RHE}) and a glassy carbon working electrode (5 mm diameter) was used. The working electrode always was lowered into the electrolyte under potential control at +0.05 V_{RHE}. A 0.1 M $HClO_4$ was used for electrochemical measurements (diluted from 70 % conc. $HClO_4$, 99.999 % trace metal bases, Sigma Aldrich with milli-Q water). All measurements were performed with a BioLogics Science Instruments potentiostat SP-200. To prepare an ink 2.5 mg of catalyst were added into 2.5 mL water, 7 µL Nafion (5 wt%) and 0.5 mL isopropanol (≥ 99.5 %) and ultrasonicated for 15 minutes. 10 µL of the ink were placed on a glassy carbon rotating disk electrode, which results in a Pt loading of 6-7 µg cm^{-2}. The film was dried at 60 °C for 7 minutes.

References

[1] M. Oezaslan, F. Hasché, and P. Strasser, Chem. Mater. **23**, 2159 (2011).

[2] U. a Paulus, a Wokaun, G. G. Scherer, P. S. Institut, and C.-V. Psi, J. Phys. Chem. B **106**, 4181 (2002).

[3] C. Wang, M. Chi, G. Wang, D. Van Der Vliet, D. Li, K. More, H. H. Wang, J. A. Schlueter, N. M. Markovic, and V. R. Stamenkovic, Adv. Funct. Mater. **21**, 147 (2011).

[4] S. Rudi, X. Tuaev, and P. Strasser, Electrocatalysis **3**, 265 (2012).

[5] V. R. Stamenkovic, B. Fowler, B. S. Mun, G. Wang, P. N. Ross, C. A. Lucas, and N. M. Markovic, Science **315**, 493 (2007).

[6] J. Zhang, H. Yang, J. Fang, and S. Zou, Nano Lett. **10**, 638 (2010).

[7] S.-I. Choi, S. Xie, M. Shao, J. H. Odell, N. Lu, H.-C. Peng, L. Protsailo, S. Guerrero, J. Park, X. Xia, J. Wang, M. J. Kim, and Y. Xia, Nano Lett. **13**, 3420 (2013).

[8] S. Il Choi, S. Xie, M. Shao, N. Lu, S. Guerrero, J. H. Odell, J. Park, J. Wang, M. J. Kim, and Y. Xia, ChemSusChem **7**, 1476 (2014).

[9] X. Huang, Z. Zhao, L. Cao, Y. Chen, E. Zhu, Z. Lin, M. Li, A. Yan, A. Zettl, Y. M. Wang, X. Duan, T. Mueller, and Y. Huang, Science **348**, 1230 (2015).

[10] P. Strasser, Science **349**, 379 (2015).

[11] L. Gan, C. Cui, M. Heggen, F. Dionigi, S. Rudi, and P. Strasser, Science **346**, 1502 (2014).

[12] N. Erini, V. Beermann, M. Gocyla, M. Gliech, M. Heggen, R. E. Dunin-Borkowski, and P. Strasser, Angew. Chemie - Int. Ed. **56**, 6533 (2017).

[13] R. M. Arán-Ais, J. Solla-Gullón, M. Gocyla, M. Heggen, R. E. Dunin-Borkowski, P. Strasser, E. Herrero, and J. M. Feliu, Nano Energy **27**, 390 (2016).

[14] D. W. H. Banham and S. Ye, ACS Energy Lett. acsenergylett.6b00644 (2017).

[15] N. Konno, S. Mizuno, H. Nakaji, and Y. Ishikawa, SAE Int. J. Altern. Powertrains **4**, 123 (2015).

[16] A. Kongkanand and M. F. Mathias, J. Phys. Chem. Lett. **7**, 1127 (2016).

[17] C. Cui, L. Gan, M. Heggen, S. Rudi, and P. Strasser, Nat. Mater. **12**, 765 (2013).

[18] L. Gan, C. Cui, S. Rudi, and P. Strasser, Top. Catal. **57**, 236 (2014).

[19] L. Gan, M. Heggen, S. Rudi, and P. Strasser, Nano Lett. **12**, 5423 (2012).

[20] V. Beermann, M. Gocyla, E. Willinger, S. Rudi, M. Heggen, R. E. Dunin-Borkowski, M.-G. Willinger, and P. Strasser, Nano Lett. **16**, 1719 (2016).

[21] S. Rudi, L. Gan, C. Cui, M. Gliech, and P. Strasser, J. Electrochem. Soc. **162**, 403 (2015).

[22] R. M. Arán-Ais, Y. Yu, R. Hovden, J. Solla-Gullón, E. Herrero, J. M. Feliu, and H. D. Abruña, J. Am. Chem. Soc. **137**, 14992 (2015).

[23] K. J. J. Mayrhofer, J. C. Meier, S. J. Ashton, G. K. H. Wiberg, F. Kraus, M. Hanzlik, and M. Arenz, Electrochem. Commun. **10**, 1144 (2008).

[24] K. J. J. Mayrhofer, S. J. Ashton, J. C. Meier, G. K. H. Wiberg, M. Hanzlik, and M. Arenz, J. Power Sources **185**, 734 (2008).

[25] A. Zana, J. Speder, M. Roefzaad, L. Altmann, M. Baumer, and M. Arenz, J. Electrochem. Soc. **160**, F608 (2013).

[26] J. C. Meier, I. Katsounaros, C. Galeano, H. J. Bongard, A. a. Topalov, A. Kostka, A. Karschin, F. Schüth, and K. J. J. Mayrhofer, Energy Environ. Sci. **5**, 9319 (2012).

[27] F. R. Nikkuni, B. Vion-Dury, L. Dubau, F. Maillard, E. A. Ticianelli, and M. Chatenet, Appl. Catal. B Environ. **156**–**157**, 301 (2014).

[28] A. Zadick, L. Dubau, A. Zalineeva, C. Coutanceau, and M. Chatenet, Electrochem. Commun. **48**, 1 (2014).

[29] N. Erini, R. Loukrakpam, V. Petkov, E. A. Baranova, R. Yang, D. Teschner, Y. Huang, S. R. Brankovic, and P. Strasser, ACS Catal. **4**, 1859 (2014).

[30] T. Reier, Z. Pawolek, S. Cherevko, M. Bruns, T. Jones, D. Teschner, S. Selve, A. Bergmann, H. N. Nong, R. Schl??gl, K. J. J. Mayrhofer, and P. Strasser, J. Am. Chem. Soc. **137**, 13031 (2015).

[31] A. Bergmann, E. Martinez-Moreno, D. Teschner, P. Chernev, M. Gliech, J. F. de Araújo, T. Reier, H. Dau, and P. Strasser, Nat. Commun. **6**, 8625 (2015).

[32] M. E. Holtz, Y. Yu, D. Gunceler, J. Gao, R. Sundararaman, K. A. Schwarz, T. A. Arias, H. D. Abruña, and D. A. Muller, Nano Lett. **14**, 1453 (2014).

[33] F. Maillard, E. R. Savinova, P. A. Simonov, V. I. Zaikovskii, and U. Stimming, J. Phys. Chem. B **108**, 17893 (2004).

[34] S. Park, Tong, A. Wieckowski, and M. J. Weaver, Langmuir **18**, 3233 (2002).

[35] R. Rizo, M. Lázaro, E. Pastor, and G. García, Molecules **21**, 1225 (2016).

[36] Q. Wang, G. Q. Sun, L. H. Jiang, Q. Xin, S. G. Sun, Y. X. Jiang, S. P. Chen, Z. Jusys, and R. J. Behm, Phys. Chem. Chem. Phys. **9**, 2686 (2007).

[37] X. Tuaev, S. Rudi, V. Petkov, A. Hoell, and P. Strasser, ACS Nano **7**, 5666 (2013).

[38] B. Abécassis, F. Testard, O. Spalla, and P. Barboux, Nano Lett. **7**, 1723 (2007).

[39] F. Zheng, S. Alayoglu, J. Guo, V. Pushkarev, Y. Li, P. Glans, J. Chen, and G. Somorjai, Nano Lett. **11**, 847 (2011).

[40] N. de Jonge and F. M. Ross, Nat. Nanotechnol. **6**, 695 (2011).

[41] M. J. Williamson, R. M. Tromp, P. M. Vereecken, R. Hull, and F. M. Ross, Nat. Mater. **2**, 532 (2003).

[42] F. M. Ross, editor , *Liquid Cell Electron Microscopy* (Cambridge University Press, Cambridge, 2017).

[43] H. Zheng, R. K. Smith, Y. Jun, C. Kisielowski, U. Dahmen, and A. P. Alivisatos, Science **324**, 1309 (2009).

[44] R. R. Unocic, R. L. Sacci, G. M. Brown, G. M. Veith, N. J. Dudney, K. L. More, F. S. Walden II, D. S. Gardiner, J. Damiano, and D. P. Nackashi, Microsc. Microanal. **20**, 452 (2014).

[45] G.-Z. Zhu, S. Prabhudev, J. Yang, C. M. Gabardo, G. a. Botton, and L. Soleymani, J. Phys. Chem. C **118**, 22111 (2014).

[46] N. Hodnik, G. Dehm, and K. J. J. Mayrhofer, Acc. Chem. Res. **49**, 2015 (2016).

[47] S. Nagashima, K. Yoshida, T. Hiroyama, K. Liu, Y. Kang, T. Ikai, H. Kato, T. Nagami, and K. Kishita, Microsc. Microanal. **21**, 1295 (2015).

[48] H. Kato, SAE Int. J. Altern. Powertrains **5**, 2016 (2016).

[49] Z. Zeng, W.-I. Liang, H.-G. Liao, H. L. Xin, Y.-H. Chu, and H. Zheng, Nano Lett. **14**, 1745 (2014).

[50] Z. Zeng, X. Zhang, K. Bustillo, K. Niu, C. Gammer, J. Xu, and H. Zheng, Nano Lett. **15**, 5214 (2015).

[51] Z. Zeng, W.-I. Liang, Y.-H. Chu, and H. Zheng, Faraday Discuss. **176**, 95 (2014).

[52] V. Beermann, M. Gocyla, S. Kühl, E. Padgett, H. Schmies, M. Goerlin, N. Erini, M. Shviro, M. Heggen, R. E. Dunin-Borkowski, D. A. Muller, and P. Strasser, J. Am. Chem. Soc. **139**, 16536 (2017).

[53] M. E. Holtz, Y. Yu, J. Gao, H. D. Abruña, and D. A. Muller, Microsc. Microanal. **19**, (2013).

[54] F. Luisier, C. Vonesch, T. Blu, and M. Unser, Signal Processing **90**, 415 (2010).

[55] F. Luisier, The SURE-LET Approach to Image Denoising, Swiss Federal Institute of Technology Lausanne, 2010.

[56] F. Luisier, C. Vonesch, T. Blu, and M. Unser, in *Proc. Sixth IEEE Int. Symp. Biomed. Imaging From Nano to Micro* (Boston, MA, 2009), pp. 310–313.

[57] L. Zheng, J. Sun, L. Xiong, R. Jin, J. Li, X. Li, D. Zheng, Q. Liu, L. Niu, S. Yang, and J. Xia, Fuel Cells **10**, 384 (2010).

[58] R. M. Arán-Ais, F. J. Vidal-Iglesias, J. Solla-Gullón, E. Herrero, and J. M. Feliu, Electroanalysis **27**, 945 (2015).

[59] N. M. Schneider, M. M. Norton, B. J. Mendel, J. M. Grogan, F. M. Ross, and H. H. Bau, J. Phys. Chem. C **118**, 22373 (2014).

[60] E. F. Holby, W. Sheng, Y. Shao-Horn, and D. Morgan, Energy Environ. Sci. **2**, 865 (2009).

[61] S. Cherevko, A. R. Zeradjanin, G. P. Keeley, and K. J. J. Mayrhofer, J. Electrochem. Soc. **161**, H822 (2014).

[62] S. Cherevko, G. P. Keeley, S. Geiger, A. R. Zeradjanin, N. Hodnik, N. Kulyk, and K. J. J. Mayrhofer, ChemElectroChem **2**, 1471 (2015).

[63] A. A. Topalov, I. Katsounaros, M. Auinger, S. Cherevko, J. C. Meier, S. O. Klemm, and K. J. J. Mayrhofer, Angew. Chemie - Int. Ed. **51**, 12613 (2012).

[64] D. a. Stevens, M. T. Hicks, G. M. Haugen, and J. R. Dahn, J. Electrochem. Soc. **152**, A2309 (2005).

[65] R. Makharia, S. Kocha, P. Yu, M. A. Sweikart, W. Gu, F. Wagner, and H. A. Gasteiger, ECS Trans. **1**, 3 (2006).

[66] J. Willsau and J. Heitbaum, J. Electroanal. Chem. Interfacial Electrochem. **161**, 93 (1984).

[67] E. Guilminot, a. Corcella, F. Charlot, F. Maillard, and M. Chatenet, J. Electrochem. Soc. **154**, B96 (2007).

[68] C. Qin, J. Wang, D. Yang, B. Li, and C. Zhang, Catalysts **6**, 197 (2016).

[69] N. Zamel, R. Hanke-Rauschenbach, S. Kirsch, A. Bhattarai, and D. Gerteisen, Int. J. Hydrogen Energy **38**, 15318 (2013).

[70] A. Rabis, P. Rodriguez, and T. J. Schmidt, ACS Catal. **2**, 864 (2012).

[71] Y. Yu, M. E. Holtz, H. L. Xin, D. Wang, H. D. Abruña, and D. A. Muller, Microsc. Microanal. **19**, 1666 (2013).

[72] M. E. Holtz, Y. Yu, J. Gao, H. D. Abruña, and D. A. Muller, Microsc. Microanal. **19**, 1027 (2013).

[73] K. L. Klein, I. M. Anderson, and N. De Jonge, J. Microsc. **242**, 117 (2011).

CHAPTER 5

NANOSCALE IMAGING OF LITHIUM ION DISTRIBUTION DURING *IN SITU* OPERATION OF BATTERY ELECTRODE AND ELECTROLYTE

A major challenge in the development of new battery materials is understanding their fundamental mechanisms of operation and degradation. Their microscopically inhomogeneous nature calls for characterization tools that provide *operando* and localized information from individual grains and particles. Here we describe an approach that enables imaging the nanoscale distribution of ions during electrochemical charging of a battery in a transmission electron microscope liquid flow cell. We use valence energy-loss spectroscopy to track both solvated and intercalated ions, with electronic structure fingerprints of the solvated ions identified using an *ab initio* non-linear response theory. Equipped with the new electrochemical cell holder, nanoscale spectroscopy and theory, we have determined the lithiation state of a $LiFePO_4$ electrode and surrounding aqueous electrolyte in real time with nanoscale resolution during electrochemical charge and discharge. We follow lithium transfer between electrode and electrolyte and image charging dynamics in the cathode. We observe competing delithiation mechanisms such as core-shell and anisotropic growth occurring in parallel for different particles under the same conditions. This technique represents a general approach for the *operando* nanoscale imaging of electrochemically active ions in the electrode and electrolyte in a wide range of electrical energy storage systems.[8]

[8] This work was published as: M.E. Holtz*, Y. Yu*, D. Gunceler, J. Gao, R. Sundararaman, K.A. Schwarz, T.A. Arias, H.D. Abruña, and D.A. Muller, Nano Lett. **14**, 1453 (2014).

5.1 Introduction

The integration of renewable, and often intermittent, energy sources such as solar and wind into the energy landscape, as well as the electrification of transportation, requires dramatic advances in electrical energy conversion and storage technologies including fuel cells, batteries and supercapacitors [1–6]. Advancing our understanding necessitates the development of experimental tools capable of *operando* characterization that can discern mechanisms of operation and degradation in the native operating environment. Energy storage materials, such as battery electrodes, often display inhomogeneous behavior on the nanoscale [7]. Thus, the most illuminating and useful characterization methods are those capable of providing detailed mechanistic information of charge/discharge dynamics of *individual* grains and particles. TEM investigations specialize in revealing structural and compositional information with nanoscale spatial resolution and sub-second temporal resolution. Unfortunately, conventional TEM is not compatible with studies of many electrochemical energy storage processes because they occur in liquid environments. Recently, the development of TEM holders that encapsulate thin liquid layers promise *in situ* imaging and spectroscopy on the nanoscale [8–12]. Incorporating electrodes [13,14] enables *in situ* imaging of electrochemical processes [15–17], including electrodeposition [13] and dendrite growth [18]. However, quantitative electrochemistry in the electron microscope remains a major challenge.

Here we develop broadly-applicable, *quantitative* electrochemistry in a liquid cell TEM holder that can be correlated with microstructure and local electronic structure changes during operation, even for surface-sensitive catalysts such as those used in fuel cells. To follow the underlying ion redistributions, we demonstrate a method for spectroscopic imaging of nanoscale processes during electrochemical operation and follow the charging and discharging dynamics of a battery electrode. TEM detection of lithium through a liquid is difficult, because lithium is a weak elastic scatterer

and multiple scattering from the liquid overwhelms the inelastic core-loss signal in electron energy-loss spectroscopy (EELS). In this work, we successfully observed the lithiation state by valence energy-filtered TEM (EFTEM), which probes the low-energy regime (~1-10 eV), and allows us to work in thicker liquid layers than is typically feasible with core-level spectroscopy [10]. Valence EELS can provide electronic structure information, allowing us to track battery charging and discharging as ions are being transferred between electrode and electrolyte. This method is analogous to observing color changes in optical spectroscopy during battery cycling on the micron scale [19,20], except that valence EFTEM achieves nanometer resolution. While electronic structure features in the lithiated and delithiated electrode have been documented [21], identifying electronic structure fingerprints in the solution is less well explored because there are many solvated species in solution that are difficult to distinguish. Here we employed *ab initio* theory to calculate optical gaps of the relevant solvated species [22]. We took solution effects into account with a hybrid functional [23] including a nonlinear description of the polarization response of the surrounding liquid [24], which gives a more physical model of bound solvent charges near the solute than linear models do. For the first time, we applied this technique to calculate excited electronic states and found quantitative matches to experimental excitation energies. By combining electrochemistry in the TEM with valence spectroscopic imaging and theory, we were able to identify the lithiation state of both the electrode and electrolyte during *in situ* operation.

A key mechanistic aspect in the performance of lithium-ion battery electrodes is how the lithium ions intercalate and deintercalate from the electrode during cycling. Here, as a demonstration of tracking lithiation and degradation in an *in situ* battery in the TEM, we studied the cathode material $LiFePO_4$, which has surged in interest due to its attractive capacity, ability to sustain high charging and discharging rates, abundance, low toxicity, relative operational safety, and low cost [5,25]. There is much discussion in the literature on the mechanism of lithiation and delithiation [5,7,26–33], with evidence of a two-phase reaction or a metastable solid

solution [5,31]. Within the two-phase reaction pathway, there are different theories for the propagation of lithiation, one of which suggests concurrent transformation [29,34] and the other particle-by-particle intercalation [27,30,33,35]. Some disagreement may be attributed to many-particle effects, where bulk measurements (both *in situ* and *ex situ*) convolve signals from the entire area of the electrode probed [7]. *Ex situ* studies are inherently compromised by removal of the particles from their native – and often reactive – environment, which leads to questions of relaxation or reactions caused by the foreign surroundings. *In situ* studies of $LiFePO_4$ in an open-cell configuration have nicely demonstrated anisotropic growth of the phase, although the open-cell configuration does not allow the use of standard liquid electrolytes [36]. In this study, we probe, in real time, the evolution of individual grains and nanoparticles of $LiFePO_4$ in the native environment of a battery in a liquid cell TEM. Particles are seen to delithiate, one at a time, in a mosaic fashion, with most particles either lithium-rich or lithium-poor. We are also able to directly image the phase transformations and see different delithiation mechanisms in neighboring particles, and have observed core-shell structures and anisotropic growth in different particles within the same agglomerate on the electrode.

Having established the electrochemical performance of the TEM holder, we studied $LiFePO_4$, a widely used Li-ion cathode material, in 0.5 M Li_2SO_4 aqueous electrolyte. Because aqueous electrolytes have safety benefits over organic-based electrolytes, such as the commonly used carbonates, and due to its high abundance, low weight and non-toxicity, researchers have considered aqueous electrolytes in addition to the more traditional carbonates [37]. We find the use of an aqueous electrolyte to be practical for technique development as carbonates are more viscous than aqueous electrolytes, leading to higher flow pressures and potentially more window breakages. In the event of electrolyte leakage, aqueous liquids will dissipate quickly while carbonate electrolytes lead to contamination of the microscope column.

5.2 Spectroscopic Fingerprints for *In Situ* Identification

To elucidate the lithiation mechanism we must examine how the lithium ions intercalate into/out of the electrode. In the TEM, lithiation can be tracked by morphological changes or structural changes using electron diffraction [27,38], although morphology does not give chemical maps and diffraction spots are quickly obscured in thicker liquid films. As a light element, lithium scatters electrons weakly, making elastic imaging challenging, and the energy-dispersive X-ray signal for lithium has too low an energy to enable detection. Instead, we tracked the lithiation state of the battery using EELS, which offers chemical fingerprints (core-loss EELS) and electronic structure information (valence EELS). Yet, using EELS to identify lithium in liquids presents two obstacles. First, EELS is degraded by multiple scattering events in thick liquids [10]. Second, the lithium-K edge resides at 54 eV and is lost in the superimposed bulk plasmon of the thick films of liquid. As a consequence, previous liquid cell studies have performed their lithium edge spectroscopy separately and *ex situ* [39]. Additionally, the lithium-K edge overlaps with many transition metal M edges such as iron [40]. This makes core-loss EELS of the lithium practically impossible to detect in the liquid cell TEM.

Valence EELS, which interrogates electronic structure, can detect the state of lithiation of battery electrodes in liquid electrolytes. During discharge and charge, lithium ions move in and out of the electrode, filling and emptying valence bands, thereby changing the electronic structure. These electronic structure shifts are accessible by optical spectroscopy, where lithiation has been observed on the micron scale in electrodes as they change color as a function of their state of lithiation [19,20]. Valence EELS surveys the same electronic levels as ultraviolet-visible (UV-VIS) spectroscopy. Optical absorption spectra track the imaginary part of the energy-dependent dielectric constant, $\mathrm{Im}(\varepsilon)$, and the electron energy-loss function in EELS is proportional to $\mathrm{Im}(\varepsilon)/[\mathrm{Re}(\varepsilon)^2 + \mathrm{Im}(\varepsilon)^2]$. An advantage of valence EELS is its high spatial resolution, which is

ultimately limited to the nanoscale by the delocalization of the low-energy excitations [41]. While delocalization prevents atomic-resolution valence EFTEM studies, resolution in the liquid environment is often more strongly limited by multiple scattering or by the low-dose imaging conditions required. Valence EELS provides strong signals due to large scattering cross sections and low background from the liquid. The electronic structure shift usually occurs where the electrolyte is stable, at energies below its optical gap (~6-7 eV) where the electrolyte is transparent. Taking advantage of the electronic structure shifts in battery electrodes during cycling is a practical method to track the lithiation state.

The spectroscopic characteristics of the battery cathode $LiFePO_4$ and electrolyte 0.5 M Li_2SO_4/H_2O are shown in Figure 5.1. The monochromated valence EELS of dry $LiFePO_4$ is shown in Figure 5.1a. There is a fingerprint of the delithiated $FePO_4$ at 5 eV, which is not present in the lithiated $LiFePO_4$. This corresponds to the electronic structure shift in $FePO_4$ as it lithiates to $LiFePO_4$. As lithium ions interact with the Fe-3d bands, the corresponding peak at 5 eV disappears [21,42]. Thus, this peak enables quick spectroscopic mapping of the state of lithiation [43].

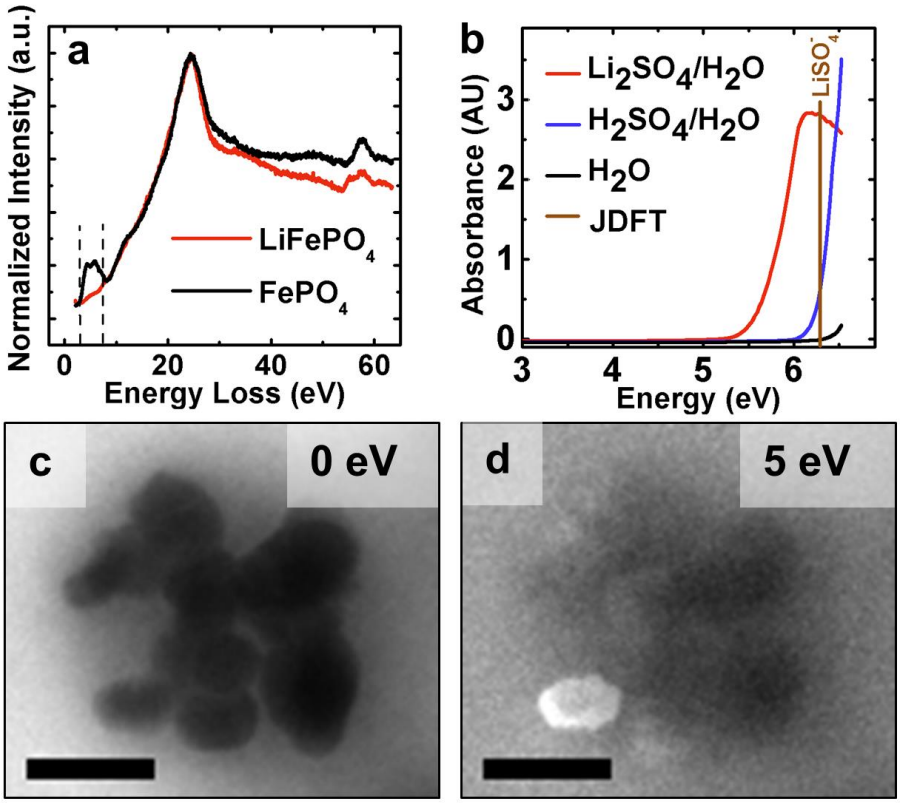

Figure 5.1. Spectroscopy of $LiFePO_4$ and the delithiated counterpart $FePO_4$ and the Li_2SO_4 aqueous electrolyte. (a) Monochromated EELS, with an energy resolution of 0.2 eV, of a dry sample shows a peak at 5 eV for $FePO_4$ but not for $LiFePO_4$. (b) UV-VIS spectra of the electrolyte 0.5 M Li_2SO_4/H_2O, 0.5 M H_2SO_4/H_2O, and pure water. There is an absorption peak at 6 eV for the Li_2SO_4 solution. The JDFT calculated gaps of the solvated species in solution indicate that the 6 eV peak is caused by $LiSO_4^-$. EFTEM of $LiFePO_4$ in 0.5 M Li_2SO_4/H_2O with a 5 eV energy slit around (c) 0 eV where the liquid dominates the signal and the particles look fairly homogeneous, showing no diffraction contrast, and at (d) 5 eV, which highlights the $FePO_4$. Scale bar is 200 nm. Using the 5 eV EFTEM image we can locate delithiated regions.

Figure 5.1b presents the UV-VIS spectra of 0.5 M Li_2SO_4 electrolyte, and for comparison 0.5 M H_2SO_4 and water. There is a peak in the 0.5 M Li_2SO_4 solution at 6.2 eV, not present in sulfuric acid or water. Because of the alkaline pH of the Li_2SO_4 electrolyte (pH ca. 8), there is a low

concentration of protonated species. Using equilibrium constants we can identify the predominant solvated species in solution as: 0.63 M Li^+, 0.37 M $LiSO_4^-$, 0.13 M SO_4^{2-}, with less than 10^{-6} M of LiOH, HSO_4^- and $LiHSO_4$. We uniquely identified that the absorption peak at 6.2 eV in the electrolyte is due to solvated $LiSO_4^-$ using *ab initio* theory. Because electronic screening from the surrounding electrolyte shifts the optical gaps of the relevant species on the same order as their separations (~1 eV), we developed a novel *ab initio* approach to calculate excited states while accounting for the surrounding liquid. We employed joint density-functional theory (JDFT) to compute the electronic structure information of solvated species in thermodynamic equilibrium with a liquid environment [22]. Using a hybrid functional for the solute [23] and a nonlinear description of the polarization response of the surrounding liquid [24], this approach yielded an *ab initio* optical gap of solvated $LiSO_4^-$ of 6.3 eV, in excellent agreement with experimental absorption peak at 6.2 eV. Thus, the presence of this peak indicates a lithiated solution. Other solvated species in the solution have peaks at higher energies. This theory shows remarkable agreement with experiment, and has been repeated for other solvated ions measured by UV-VIS. In the 5 eV EFTEM images we have two fingerprints: one of the delithiated cathode material $FePO_4$ at 5 eV, and one for the lithiated liquid electrolyte at 6.2 eV.

5.3 *In Situ* Charging and Discharging of $LiFePO_4$

We used EFTEM to obtain spectroscopic mapping of the 5 eV signal with a 5 eV wide slit (energy range from 2.5 to 7.5 eV), which captured the state of lithiation of both the particle and the solution. The 0 eV and 5 eV spectroscopic images of $LiFePO_4$ particles in a 200 nm thick 0.5 M Li_2SO_4 electrolyte are shown in Figure 5.1c-d, respectively. In the elastic 0 eV EFTEM image, the particles appear fairly homogeneous with no evident diffraction contrast. In the 5 eV EFTEM image, the delithiated regions of the particles are brighter, enabling us to differentiate delithiated and lithiated particles rapidly on the nanoscale. The solution has a high intensity, indicating a

lithiated solution, as would be expected. Our convergence and collection angles are relatively large, which minimizes diffraction contrast. We can estimate the extent of the diffraction contrast, which is an elastic effect, by examining the elastic only (0 eV) EFTEM images that are recorded interlaced with the 5 eV images. We see little diffraction contrast in the cathode material, but a high level of contrast in the 5 eV image. Hence, we conclude that the contrast changes are chemical in origin and not due to diffraction contrast. We used electron beam conditions that minimized beam interactions in a control experiment, where irradiation without cycling had no apparent affect on morphology or composition. Another control experiment with the same electron beam conditions showed similar effects over the entire electrode, not just in the region imaged. This method of EFTEM enables rapid (second-long) mapping of the nanoscale lithium distribution in both the electrode and the electrolyte.

Having an electrochemical cell for the TEM and a technique to observe the lithiation state, we assembled an *in situ* battery using an activated carbon anode, 0.5 M Li_2SO_4 aqueous electrolyte, and a $LiFePO_4$ cathode. We imaged at 5 eV with a 5 eV wide energy window to track the state of lithiation (Figure 5.2a) and recorded electrochemical data (Figure 5.2b-c) simultaneously. Figure 5.2b shows the current profile (applied current was ±10 nA) applied between the anode and cathode. From an estimate of the amount of active material present on the electrode and the specific capacity from *ex situ* aqueous studies (31 mAh/g), this corresponds approximately to a charge/discharge rate of about 10 C (time to charge or discharge to theoretical capacity is $1/10^{th}$ of an hour, or 6 minutes). Figure 5.2c shows the resulting voltage profile measured between the cathode ($LiFePO_4$) and the anode (activated carbon). Because the potential difference for the deintercalation (intercalation) of lithium ions between $LiFePO_4$ and $FePO_4$ is 1 V [44], charging (discharging) occurs within the potential range of our experiment. Since we are charging above 1.2 V, it is possible that there could be gaseous evolution (specifically, oxygen formation at the cathode). However, given that at the electrodes employed the overpotentials for hydrogen and oxygen evolution are large, we do not

feel that under these experimental conditions that this is a concern. If we do generate oxygen, it is relatively soluble in the liquid and is able to dissipate before bubble formation. We would also expect to see bubbles in the elastic 0 eV EFTEM images, which we do not. The rapid cycling rate (10C) enabled multiple charge-discharge cycles to be acquired in the course of the experiment and decreased the electron beam exposure time.

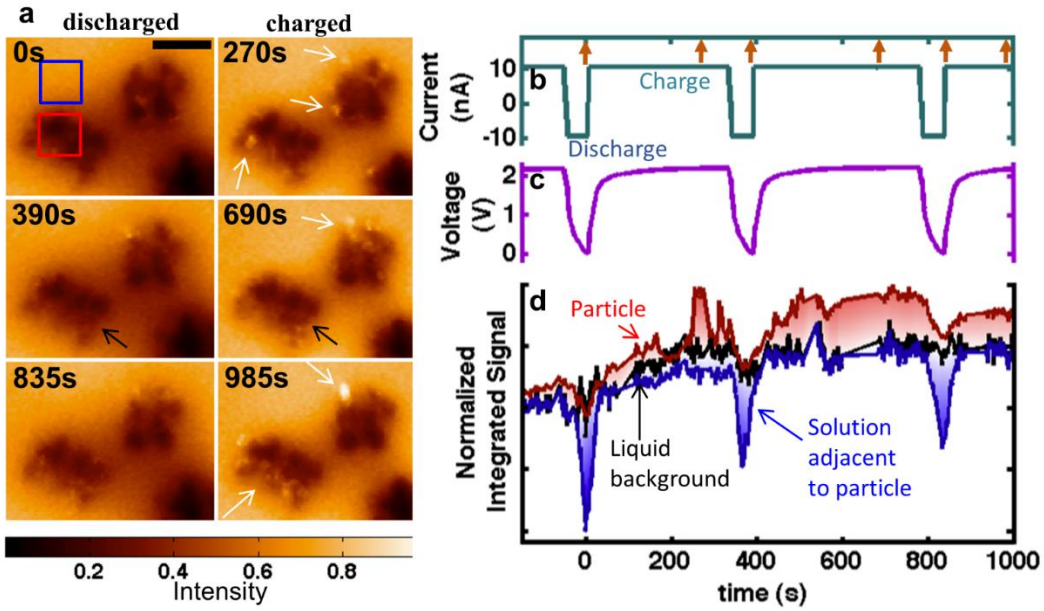

Figure 5.2. *In situ* charging and discharging of the cathode material $LiFePO_4$ in 0.5 M Li_2SO_4 aqueous electrolyte. (a) 5eV spectroscopic EFTEM images of charging and discharging at indicated times. Scale bar is 400 nm. Bright regions are delithiated $FePO_4$ and dark regions are $LiFePO_4$. There are more bright regions of $FePO_4$ at the end of charge cycles and less during the discharges. White arrows point towards "bright" charged particles while black arrows point towards "dark" discharged particles. (b) Current profile corresponding to 10C. Time = 0 s corresponds to the start of our study, which began on the third charge cycle (not on the first) after assembly. Arrows on the top axis indicate the times of the images shown in (a). The corresponding voltage profile is in (c), referencing the activated carbon counter electrode. (d) Integrated intensity over various regions, tracking with the voltage profile, from the regions shown by the boxes in (a). The solution becomes very dark during discharges and returns to the

background level during charge. Regions of the particle are seen to light up and disappear, potentially due to delithiating and fracturing off of the particle cluster. During times when no imaging occurred, the data are linearly extrapolated, and for comparison the intensity is brought to the same level by subtraction.

There are clear differences in the 5 eV spectroscopic images between the charged (Figure 5.2a, right) and the discharged state (Figure 5.2a, left) in both the particles and the solution. In the charged state, compared to the discharged state, particles show more bright regions - indicated by white arrows - corresponding to delithiated $FePO_4$. Additionally, the cluster of particles is overall brighter in the charged image, especially around the edges of the cluster, than in the discharged image, as marked by black arrows. The brightest particles may correspond to completely delithiated $FePO_4$, whereas the overall slight increase in intensity in the particles may indicate partially delithiated particles. On discharge, these bright regions of $FePO_4$ disappear, transitioning back to $LiFePO_4$. If we spatially integrate the 5 eV EFTEM intensity over a cluster of particles, inside the region of the red box in Figure 5.2d, we see an average increase in intensity on charge and a decrease on discharge. The intensity of the particles in Figure 5.2d was raised to the background level of the solution. Radiation damage is expected to be irreversible and uncorrelated with voltage cycle, and the appearance of the bright regions of $FePO_4$ and lithiated solution is repeatable/reproducible and correlated with charge state, indicating that the electron beam did not cause the observed responses. This demonstrates tracking of the lithiation state of battery electrodes at the nanoscale.

We next examined the 5 eV EFTEM intensity in the solution adjacent to the particles. There is a local decrease in intensity in the solution surrounding the particles during discharge, which can be seen in Figure 5.2a. The spatially integrated signal from the solution adjacent to the particle (blue) drops dramatically during discharge, plotted in Figure 5.2d. Far away from the particles, the

intensity in the solution remains relatively constant (black trace). From UV-VIS measurements and JDFT calculations, the bright intensity in the solution is caused by $LiSO_4^-$. As the particles lithiate during discharge, the adjacent solution becomes depleted of Li^+ and $LiSO_4^-$, causing the drop in the 5 eV signal. The profile of the intensity drop matches that of a diffusional concentration profile, supporting that it is due to depletion of species near the electrode. Additionally, the intensity change appears in the inelastic but not in the elastic images, indicating a chemical change. We thus observe the expected delithiation of the solution in the 5 eV EFTEM images as the particles are being lithiated. Thus, valence EFTEM can track the lithium ions in the particles and solution during battery cycling.

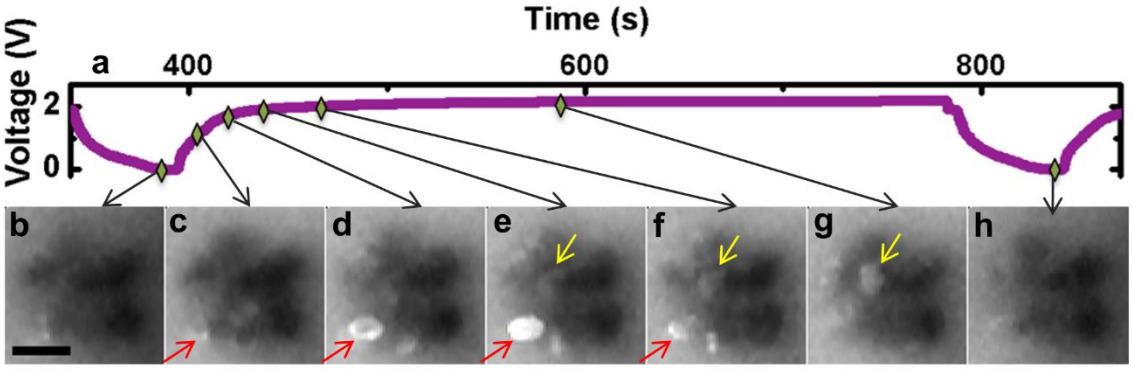

Figure 5.3. Temporal evolution of a $LiFePO_4/FePO_4$ cluster during one charge/discharge cycle. The voltage profile is shown in (a), corresponding to the second imaged cycle (fourth cycle after assembly). The 5 eV EFTEM image in (b) is for the completely discharged state, with a scale bar of 200 nm. At the bottom of (c) and (d) we see the emergence of core-shell structures. In (d) a bright particle appears with a core-shell structure that fills in brighter in (e), and partially disappears in (f). More regions of bright $FePO_4$ develop in (g), and the particle returns to the discharged state in (h) where it is darker. In general, images taken for the charged state (d-g) have more bright regions than the images taken in the discharged state, (a) and (h), which have significantly more dark sections. Red arrows indicate particles delithiating by a core-shell pathway and yellow arrows indicate delithiation propagating from left to right through the particle.

With the capability to locate ions at the nanoscale, we explored the mechanism of lithiation and delithiation of individual cathode nanoparticles. There are several proposed mechanisms of lithiation for $LiFePO_4$, [27,29–31,45] which have been reported to depend on particle size, coating, synthesis methods, charging rate and other experimental conditions [46]. These methods typically rely on bulk particle analysis which convolutes the effects of many particles [7]. We observed the evolution of many individual particles under high rate conditions in aqueous solution. The evolution of one cluster of particles is shown in Figure 5.3, corresponding to the voltage profile in Figure 5.3a. In Figure 5.3b the cell is discharged, and the particles and solution are dark, corresponding to a lithiated particle and a delithiated solution. During charge, the red arrows track the evolution of an individual particle. In Figure 5.3c, the start of nucleation is seen. In Figure 5.3d, we see a core-shell type structure, which completely transforms into $FePO_4$ in Figure 5.3e. In Figure 5.3f, the particle appears to have mostly fractured off. We track the evolution of a representative particle denoted by the yellow arrows, where the edge of the particle transitions to $FePO_4$, and the delithiation front propagates anisotropically across the particle until it is completely delithiated in Figure 5.3g. We return to the discharged state in Figure 5.3h, and the bright regions disappear, converting to $LiFePO_4$.

The delithiation of individual particles as seen in Figure 5.2a and in Figure 5.3 demonstrates slow nucleation during the transformation, indicating particle-by-particle delithation. Growth of the phase is also slow enough for us to image (Figure 5.3) and we see particles that are not fully transformed – in contrast with the "domino cascade" model that predicts the full transformation of individual particles once nucleated. We observed core-shell structures, but more commonly delithiation started at an edge and then moved through the rest of the particle supporting anisotropic growth. The anisotropic growth we report here is also observed with open-cell *in situ* high-resolution TEM images [36]. Also, stronger regions of delithiation are seen on the edges of agglomerates, where the particle may be in better electrical contact with the current collector.

However, the same particles are not always the active ones. The kinetics are consistent with a diffusional response, which is not surprising, considering the high cycling rate and thin liquid layer. Strikingly, the particles exhibit an inhomogeneous response at the nanoscale and many of the particles are inactive at any moment in time. This inhomogeneous response is likely a characteristic of the kinetics and the mechanism of Li-ion insertion and de-insertion associated with multi-particle polycrystalline $LiFePO_4$, and similar inhomogeneity has been noted *ex situ* by scanning transmission x-ray spectroscopy at much lower (40 nm) spatial resolution [35]. This highlights the advantages of nanoscale imaging during cycling, as bulk analysis can rarely deconvolve these effects.

We observe degradation mechanisms in the $LiFePO_4$ particles during the course the rapid charge/discharge cycles. We see gradual mass loss of the $LiFePO_4$ throughout the experiment from our observations from elastic 0 eV EFTEM images (20% diminution in particle area in 5 cycles). The fracturing and mass loss were observed in a control experiment to occur over the entire electrode, even where it was not exposed to the electron beam during cycling. This is consistent with our observations in the 5 eV EFTEM images during cycling. As particles delithiated, they often disappeared from the field of view, followed by the formation of another delithiated region – seen in Figure 5.3e and 5.3f. A plausible explanation is that as the particles delithiate, and given the rapid cycling (10 C) conditions, lattice strain causes regions to physically detach from the particle and float away in the solution. In fact, fracturing has been observed in *ex situ* studies [26,47]. After fracturing, a fresh surface of $LiFePO_4$ is exposed, enabling further delithiation, as found in Sn(II) oxide by *in situ* x-ray tomography [48].

5.4 Conclusions

This work demonstrates the unique ability of liquid cell *in situ* TEM coupled with spectroscopy and theory to observe the lithium insertion and de-insertion dynamics and degradation of $LiFePO_4$ in real time. These techniques may provide valuable insights into operation and other degradation pathways in a wide range of electrical energy conversion and storage devices such as batteries, fuel cells and supercapacitors.

References

[1] J. M. Tarascon and M. Armand, Nature **414**, 359 (2001).

[2] M. S. Whittingham, Proc. Ieee **100**, 1518 (2012).

[3] J. R. Dahn, T. Zheng, Y. H. Liu, and J. S. Xue, Science **270**, 590 (1995).

[4] M. S. Whittingham, Science **192**, 1126 (1976).

[5] A. K. Padhi, K. S. Nanjundaswamy, and J. B. Goodenough, J. Electrochem. Soc. **144**, 1188 (1997).

[6] P. S. Herle, B. Ellis, N. Coombs, and L. F. Nazar, Nat. Mater. **3**, 147 (2004).

[7] R. Malik, A. Abdellahi, and G. Ceder, J. Electrochem. Soc. **160**, A3179 (2013).

[8] N. de Jonge and F. M. Ross, Nat. Nanotechnol. **6**, 695 (2011).

[9] J. M. Yuk, J. Park, P. Ercius, K. Kim, D. J. Hellebusch, M. F. Crommie, J. Y. Lee, A. Zettl, and A. P. Alivisatos, Science **336**, 61 (2012).

[10] M. E. Holtz, Y. Yu, J. Gao, H. D. Abruña, and D. A. Muller, Microsc. Microanal. **19**, 1027 (2013).

[11] K. L. Jungjohann, J. E. Evans, J. A. Aguiar, I. Arslan, and N. D. Browning, Microsc. Microanal. **18**, 621 (2012).

[12] H. Zheng, R. K. Smith, Y. Jun, C. Kisielowski, U. Dahmen, and A. P. Alivisatos, Science **324**, 1309 (2009).

[13] M. J. Williamson, R. M. Tromp, P. M. Vereecken, R. Hull, and F. M. Ross, Nat. Mater. **2**, 532 (2003).

[14] J. M. Grogan and H. H. Bau, J. Microelectromechanical Syst. **19**, 885 (2010).

[15] R. R. Unocic, L. A. Adamczyk, N. J. Dudney, D. H. Alsem, N. J. Salmon, and K. L. More, Microsc. Microanal. **17**, 1564 (2011).

[16] J. Y. Huang, L. Zhong, C. M. Wang, J. P. Sullivan, W. Xu, L. Q. Zhang, S. X. Mao, N. S. Hudak, X. H. Liu, A. Subramanian, H. Fan, L. Qi, A. Kushima, and J. Li, Science **330**, 1515 (2010).

[17] X. H. Liu, L. Q. Zhang, L. Zhong, Y. Liu, H. Zheng, J. W. Wang, J.-H. Cho, S. A. Dayeh, S. T. Picraux, J. P. Sullivan, S. X. Mao, Z. Z. Ye, and J. Y. Huang, Nano Lett. **11**, 2251 (2011).

[18] E. R. White, S. B. Singer, V. Augustyn, W. A. Hubbard, M. Mecklenburg, B. Dunn, and B. C. Regan, ACS Nano **6**, 6308 (2012).

[19] S. J. Harris, A. Timmons, D. R. Baker, and C. Monroe, Chem. Phys. Lett. **485**, 265 (2010).

[20] M. U. M. Patel, R. Demir-Cakan, M. Morcrette, J. M. Tarascon, M. Gaberscek, and R. Dominko, ChemSusChem **6**, 1177 (2013).

[21] M. K. Kinyanjui, P. Axmann, M. Wohlfahrt-Mehrens, P. Moreau, F. Boucher, and U. Kaiser, J. Physics-Condensed Matter **22**, 275501 (2010).

[22] R. Sundararaman, K. Letchworth-Weaver, and T. A. Arias, (2012).

[23] M. Ernzerhof and G. E. Scuseria, J. Chem. Phys. **110**, 5029 (1999).

[24] D. Gunceler, K. Letchworth-Weaver, R. Sundararaman, K. A. Schwarz, and T. A. Arias, Model. Simul. Mater. Sci. Eng. **21**, 74005 (2013).

[25] J. J. Chen and M. S. Whittingham, Electrochem. Commun. **8**, 855 (2006).

[26] G. Y. Chen, X. Y. Song, and T. J. Richardson, Electrochem. Solid State Lett. **9**, A295 (2006).

[27] G. Brunetti, D. Robert, P. Bayle-Guillemaud, J. L. Rouviere, E. F. Rauch, J. F. Martin, J. F. Colin, F. Bertin, and C. Cayron, Chem. Mater. **23**, 4515 (2011).

[28] J. L. Jones, J. T. Hung, and Y. S. Meng, J. Power Sources **189**, 702 (2009).

[29] L. Laffont, C. Delacourt, P. Gibot, M. Y. Wu, P. Kooyman, C. Masquelier, and J. M. Tarascon, Chem. Mater. **18**, 5520 (2006).

[30] C. Delmas, M. Maccario, L. Croguennec, F. Le Cras, and F. Weill, Nat. Mater. **7**, 665 (2008).

[31] N. Sharma, X. W. Guo, G. D. Du, Z. P. Guo, J. Z. Wang, Z. X. Wang, and V. K. Peterson, J. Am. Chem. Soc. **134**, 7867 (2012).

[32] R. Malik, F. Zhou, and G. Ceder, Nat. Mater. **10**, 587 (2011).

[33] W. Dreyer, J. Jamnik, C. Guhlke, R. Huth, J. Moskon, and M. Gaberscek, Nat. Mater. **9**, 448 (2010).

[34] S.-P. Badi, M. Wagemaker, B. L. Ellis, D. P. Singh, W. J. H. Borghols, W. H. Kan, D. H. Ryan, F. M. Mulder, and L. F. Nazar, J. Mater. Chem. **21**, 10085 (2011).

[35] W. C. Chueh, F. El Gabaly, J. D. Sugar, N. C. Bartelt, A. H. McDaniel, K. R. Fenton, K. R. Zavadil, T. Tyliszczak, W. Lai, and K. F. McCarty, Nano Lett. **13**, 866 (2013).

[36] Y. Zhu, J. W. Wang, Y. Liu, X. Liu, A. Kushima, Y. Liu, Y. Xu, S. X. Mao, J. Li, C. Wang, and J. Y. Huang, Adv. Mater. **25**, 5461 (2013).

[37] Y. G. Wang, J. Yi, and Y. Y. Xia, Adv. Energy Mater. **2**, 830 (2012).

[38] C.-M. Wang, W. Xu, J. Liu, J.-G. Zhang, L. V Saraf, B. W. Arey, D. Choi, Z.-G. Yang, J. Xiao, S. Thevuthasan, and D. R. Baer, Nano Lett. **11**, 1874 (2011).

[39] M. Gu, L. R. Parent, B. L. Mehdi, R. R. Unocic, M. T. McDowell, R. L. Sacci, W. Xu, J. G. Connell, P. Xu, P. Abellan, X. Chen, Y. Zhang, D. E. Perea, J. E. Evans, L. J. Lauhon, J.-G. Zhang, J. Liu, N. D. Browning, Y. Cui, I. Arslan, and C.-M. Wang, Nano Lett. (2013).

[40] P. Moreau and F. Boucher, Micron **43**, 16 (2012).

[41] D. A. Muller and J. Silcox, Ultramicroscopy **59**, 195 (1995).

[42] W. Sigle, R. Amin, K. Weichert, P. A. van Aken, and J. Maier, Electrochem. Solid State Lett. **12**, A151 (2009).

[43] P. Moreau, V. Mauchamp, F. Pailloux, and F. Boucher, Appl. Phys. Lett. **94**, 123111 (2009).

[44] J. Y. Luo, W. J. Cui, P. He, and Y. Y. Xia, Nat. Chem. **2**, 760 (2010).

[45] C. V Ramana, A. Mauger, F. Gendron, C. M. Julien, and K. Zaghib, J. Power Sources **187**, 555 (2009).

[46] W. J. Zhang, J. Power Sources **196**, 2962 (2011).

[47] D. Y. Wang, X. D. Wu, Z. X. Wang, and L. Q. Chen, J. Power Sources **140**, 125 (2005).

[48] M. Ebner, F. Marone, M. Stampanoni, and V. Wood, Science **342**, 716 (2013).

CHAPTER 6

TOPOLOGICAL DEFECTS IN HEXAGONAL MANGANIES – INNER STRUCTURE AND EMERGENT ELECTROSTATICS

Diverse topological defects arise in hexagonal manganites, such as ferroelectric vortices, as well as neutral and charged domain walls. The topological defects are intriguing because their low symmetry enables unusual couplings between structural, charge and spin degrees of freedom, holding great potential for novel types of functional 2D and 1D systems. Despite the considerable advances in analyzing the different topological defects in hexagonal manganites, the understanding of their key intrinsic properties is still rather limited and disconnected. In particular, a rapidly increasing number of structural variants is reported without clarifying their relation, leading to a zoo of seemingly unrelated topological textures. Here, we combine picometer-precise scanning-transmission-electron microscopy with Landau-theory modeling to clarify the inner structure of topological defects in $Er_{1-x}Zr_xMnO_3$. By performing a comprehensive parametrization of the inner atomic structure, we demonstrate that one primary length scale drives the morphology of both vortices and domain walls. Our findings lead to a unifying general picture of this type of structural topological defects. We further derive novel fundamental and universal properties, such as unusual bound-charge distributions and electrostatics at the ferroelectric vortex cores with emergent U(1) symmetry.[9]

6.1 **Introduction**

[9] This work comes from Ref [38], in close collaboration with Konstantin Shapovalov, Andrés Cano (Université de Bordeaux) and Dennis Meier (ETH Zürich).

Condensed-matter systems host a wide variety of topological defects that promote novel states of matter and unconventional phase transformations, such as the Kosterliz-Thouless transition [1,2]. Particularly interesting are the defects that arise in ferroic materials, with intriguing examples such as (multi-)ferroic domain walls [3], discrete vortices [4,5], and skyrmions [6]. These topologically protected nano-textures hold great potential for future device applications, e.g., serving as information carriers in next-generation memory [7,8]. Furthermore, they enable the study of universal, topology-driven phenomena related to otherwise inaccessible defects in the same universality class. This is exemplified in the current research trend to employ hexagonal manganites (RMnO$_3$, R = Sc, Y, In, Dy - Lu) as test systems for cosmology related questions [9–11].

Recent high-resolution scanning probe measurements revealed an additional degree of complexity emerging from the structural topological defects in RMnO$_3$ [4,12–17]. The ferroelectric domain walls and vortices were found to exhibit very diverse – and seemingly unrelated – inner structures and properties [18]. Pioneering domain wall studies on TmMnO$_3$ and YMnO$_3$ [14,15], for instance, suggested the existence of atomically sharp and well-defined zigzag walls, whereas rather meandering and broadened walls were reported in ErMnO$_3$ and In(Mn,Ga)O$_3$, respectively [19,20]. Thus, in spite of the significant technical progress that has been made in imaging these atomic-scale objects, many findings remain intriguing but disconnected bits of information. Similarly, localized and spatially extended vortex structures were observed, with the identification of U(1) symmetry emerging at the core of these vortices in (Y,In)MnO$_3$ being a major new discovery [16,17]. The zoo of experimental observations is mirrored by individual theoretical breakthroughs applying notions as distant as homotopy groups and density functional theory [17,18,21,22].

In this work, we develop a unifying understanding of the inner structure of both structural domain walls and vortices in RMnO$_3$. Combining high-angle annular dark field scanning

transmission electron microscopy (HAADF-STEM) and Landau theory, we quantify the domain walls and vortices in the prototype improper ferroelectric $ErMnO_3$. This quantification can be readily matched with previous descriptions based on density functional theory, and thus linked to the microscopic physics of these unconventional ferroelectrics [21–24]. Our findings reveal that, fundamentally, the inner structure of both these defects is controlled by the same length scale (ξ_6) [25]. In particular, we demonstrate the direct link between this length-scale and the emergence of U(1) symmetry at the structural vortices. In addition, we find that this emergent U(1) symmetry leads to unusual multipolar electrostatics, regardless of the properties of the surrounding domains.

6.2 Order parameter and domain states

The hexagonal manganite $ErMnO_3$ displays improper ferroelectricity ($T_c \approx 1470$ K [26]) with a spontaneous polarization ($P \parallel c$) of ≈ 6 μC cm^{-2} at room temperature [25]. This polarization emerges as a by-product of the *P6₃/mmc* symmetry breaking and the corresponding structural distortion [23]. The distortion follows the zone-boundary K_3 mode with wavevector $\boldsymbol{q} = (1/3, 1/3, 0)$ (in units of the lattice constant in the reciprocal space) and results in periodic tilts of the MnO_5 bipyramids and displacements of the Er ions along the c axis that triple the crystallographic unit cell. The overall distortion is such that the Er displacements display either an ↑↑↓ pattern, with positive polarization, or ↓↓↑ pattern with negative polarization [27]. Both positive and negative polarizations have three possible permutations, leading to a total of six structural domains [4,14–17,19,28,29].

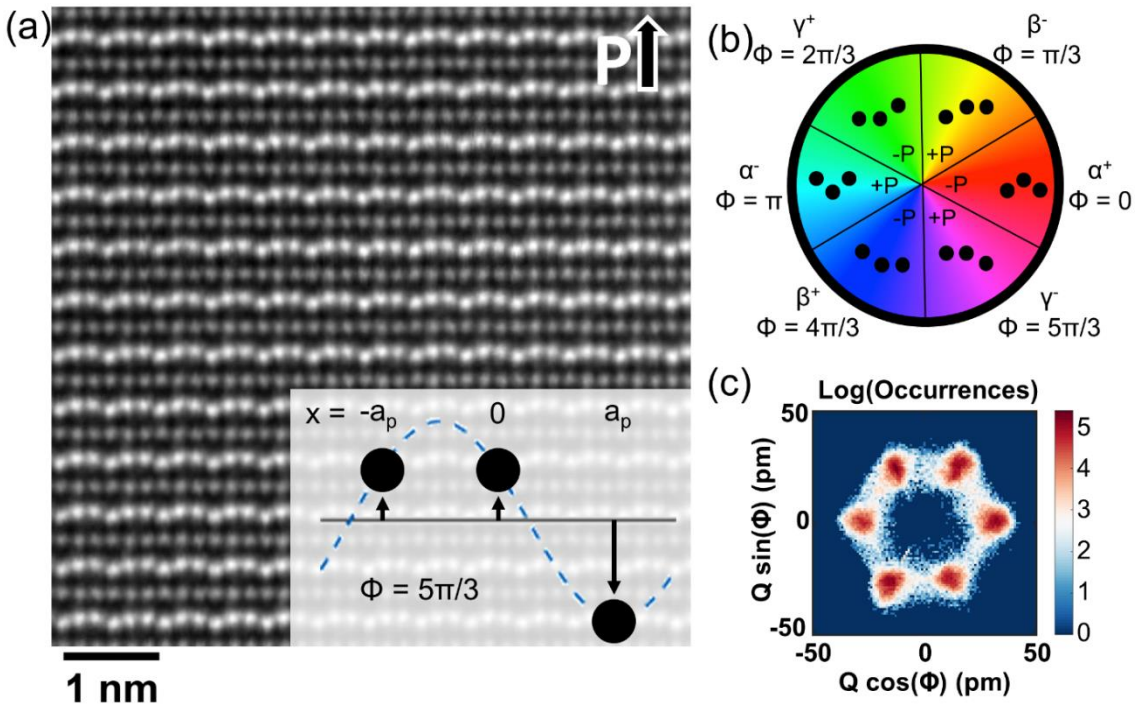

Figure 6.1: Ferroelectric displacement pattern and domain population. (a) High-angle annular dark field scanning transmission electron microscopy (HAADF-STEM) image of $ErMnO_3$, viewed along the *P6₃cm* $[1\bar{1}0]$ zone axis. The brighter Er atomic positions show the ferroelectric trimer distortion according to eq 1. (b) Sketch of the six possible structural domains with color overlay according to the phase Φ. (c) Histogram of the measured values of *Q* and Φ across 80 images near domain walls and 3 images with vortices, with intensity on a logarithmic scale.

Figure 6.1a shows a representative HAADF-STEM scan viewed down the $[1\bar{1}0]$ direction in $ErMnO_3$. This image represents a single ↑↑↓ pattern of Er atoms as illustrated in the inset to Figure 6.1a. The Er displacements from the *P6₃/mmc* paraelectric phase can be described by

$$u(\boldsymbol{r_n}) = u_0 + Q_1 \cos \boldsymbol{q} \cdot \boldsymbol{r_n} + Q_2 \sin \boldsymbol{q} \cdot \boldsymbol{r_n}. \quad (1)$$

Here $u_0 \propto P$ represents a uniform distortion that can be related to the polar Γ_2^- mode, while $\boldsymbol{Q} = (Q_1, Q_2) \equiv (Q \cos \Phi, Q \sin \Phi)$ is the primary order parameter of the structural trimerization associated with the K_3 mode (the aforementioned tilt of the MnO_5 bipyramids can be parameterized

by $\boldsymbol{Q}$ in the same way, modulo a prefactor). The value Q represents the amplitude of the sinusoidal wave that describes the trimer distortion, and relates the maximum displacement between erbium atoms to it as $1.5 \times Q$. Thus, eq 1 establishes the link between the observable atomic displacements and the key variable $\boldsymbol{Q}$ of the trimerization transition (see also ref [16]).

The transition into the trimerized state and the corresponding emergence of topological defects can be rationalized in terms of Landau theory [21,23,29], considering the free-energy expansion in powers of Q, Φ and their gradients:

$$F(\boldsymbol{Q}; T) = \frac{a(T)}{2} Q^2 + \frac{b}{4} Q^4 + \frac{1}{6}(c + c' \cos^2 3\Phi) Q^6 + \frac{g}{2}[(\nabla Q)^2 + Q^2 (\nabla \Phi)^2]. \quad (2)$$

This expansion represents the canonical Landau free energy in its simplest form, in which secondary variables are implicitly integrated out (so that P is automatically linked to $\boldsymbol{Q}$ via the relation $P \sim Q^3 \cos 3\Phi$). As customary, the key dependence on the temperature is assumed to be $a(T) = a' \cdot (T - T_c)$. The parameters a', b, c and g represent positive constants. The coefficient c', in contrast, determines whether the system develops a ferroelectric ($c' < 0$) or non-ferroelectric ($c' > 0$) state according to the minimization of eq 2 and the P-Q relation [29]. Since $ErMnO_3$ is ferroelectric, we assume $c' < 0$ in the following.

The free energy (eq 2) contains two characteristic length scales. On one hand, we have the standard correlation length $\xi = \sqrt{g/|a(T)|}$ associated to the amplitude of the trimerization. On the other hand, we have the characteristic length $\xi_6 = \sqrt{g/(3|c'|Q_0^4)} \simeq \xi \sqrt{b^2/(3|a(T)||c'|)}$ emerging below T_c in relation to the phase of the trimerization ($Q_0 \simeq \sqrt{|a(T)|/b}$ is the bulk value of the trimerization amplitude). These two length scales are a generic feature of the hexagonal manganites and their universality class [25,29]. We note that ξ_6 can be tuned by means of both temperature and chemical doping. Dopings of Er→In and Mn→Ga, for instance, are expected to

increase ξ_6 as they effectively reduce the Z_6 anisotropy ($In(Ga,Mn)O_3$ is nonferroelectric with $c' > 0$ [20] and, hence, $|c'| \to 0$ is expected during such dopings).

The Z_6 anisotropy term in eq 2 leads to the six symmetry-allowed trimerization domains illustrated in Figure 6.1b, which correspond to $\Phi_n = \frac{n\pi}{3}$ $(n = 0, 1, \dots, 5)$ for $c' < 0$. Figure 6.1c shows the statistical analysis of $\boldsymbol{Q}$ according to eq 1 obtained from multiple HAADF-STEM images covering 1.2 x 10^4 nm^2. Six maxima are visible in the measured distribution of occurrences of Q and Φ, revealing that all six domain states are populated in our images of the $ErMnO_3$ sample.

Interestingly, Figure 6.1c also shows a finite population of trimerization states with $\Phi \neq \frac{n\pi}{3}$ other than the six discrete values found in bulk domains. This points towards additional trimerization features and a complex order-parameter distribution, which will be discussed in the following.

6.3 Charged and neutral domain walls

We begin our analysis with isolated topological defects that arise in the form of ferroelectric domain walls. Figure 6.2a,b shows $ErMnO_3$ HAADF-STEM images, where the displacement pattern of Er atoms changes gradually from positive to negative polarization: ↑↑↓ $(+P)$ to ↓↓↑ $(-P)$ up to a permutation. This inversion of the polarization (black arrows) implies the presence of ferroelectric 180° domain walls. Similar changes have been reported in other hexagonal manganites, demonstrating the general character of our observations (see e.g. ref [14,16,17,20]).

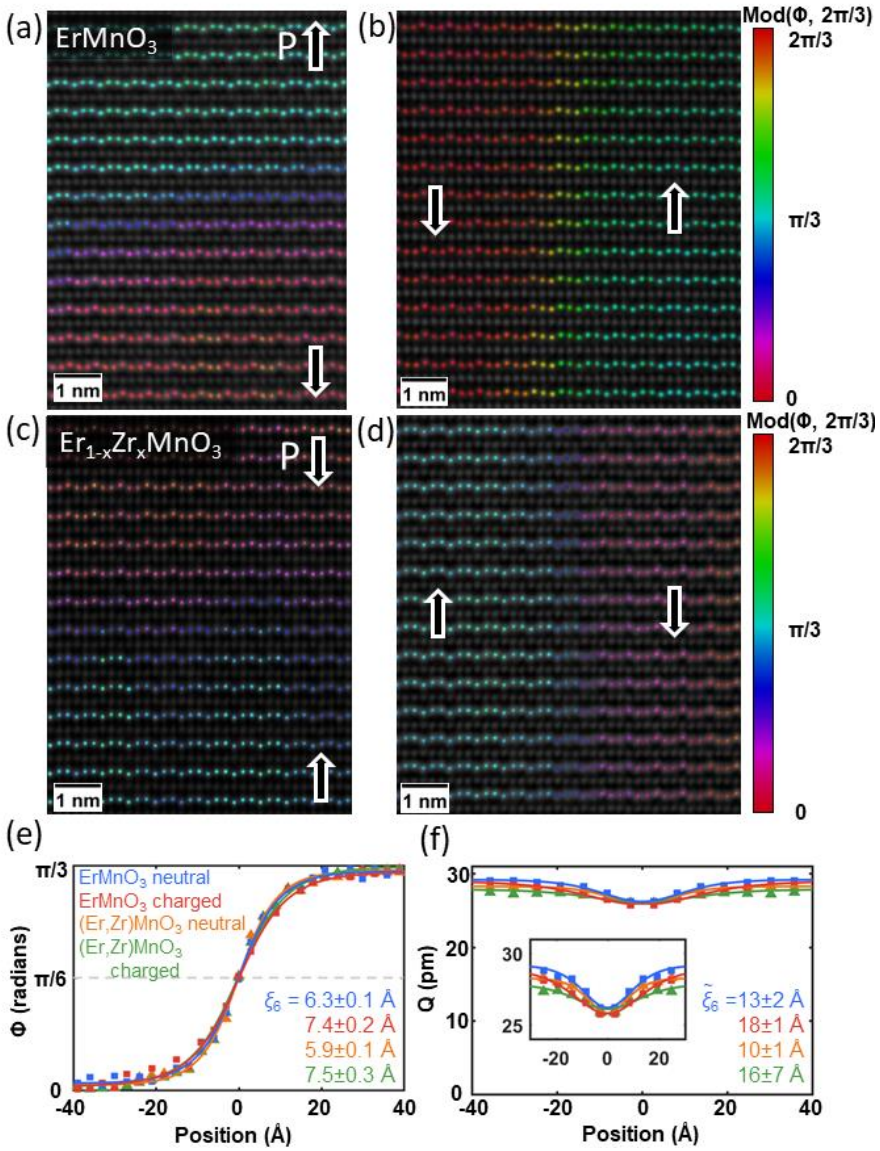

Figure 6.2: Inner structure of charged and neutral domain walls. (a–d) HAADF-STEM images of domain walls in $ErMnO_3$ (a,b) and $Er_{1-x}Zr_xMnO_3$, x = 0.01 (c,d) with color overlay of the phase according to eq 1. The following types of domain walls are identified: negatively charged tail-to-tail (a), positively charged head-to-head (c), and neutral (b,d) domain walls. (e,f) Quantification of the phase and the amplitude as a function of position relative to the domain wall center. Data is averaged across many neutral and charged domain walls in $ErMnO_3$ and $Er_{1-x}Zr_xMnO_3$, with ξ_6 and $\tilde{\xi}_6$ measured by fitting to eqs 4 and 5.

Figure 6.2b shows a neutral domain wall, corresponding to the standard situation in proper ferroelectrics. Here the *P* component that changes across the wall is parallel to the wall, so that $\nabla \cdot \boldsymbol{P} = 0$. Thus, this wall avoids the emergence of bound charges. In Figure 6.2a we observe a different situation in which the change in *P* is transverse to the wall ($\nabla \cdot \boldsymbol{P} \neq 0$). The latter represents a stable charged domain wall, which is a distinct fingerprint of the *improper* nature of the ferroelectricity in hexagonal manganites [12].

In order to test the influence of perturbations in the electronic structure, we perform analogous measurements on $Er_{1-x}Zr_xMnO_3$ (x = 0.01, Figure 6.2c and d). The substitution of Er^{3+} by Zr^{4+} reduces the number of hole carriers [30] and alters the electronic domain wall transport and electrostatics [31]. A quantitative analysis of the domain wall structure in both undoped and Zr-doped samples is presented in Figure 6.2e,f for trimerization angle Φ and amplitude Q. We find that the distributions of the trimerization angle Φ (averaged along the direction of the wall) in Figure 6.2e reflects that both neutral and charged domain walls have a non-zero width, with neutral walls being slightly narrower than charged walls. All neutral walls observed in our sample are structurally equivalent, corresponding to so-called type A walls as defined in ref [19] and also described in ref [14,15,19,20].

The distribution of atomic displacements across the domain wall in $ErMnO_3$ and $Er_{1-x}Zr_xMnO_3$ can be rationalized according to the Landau energy (eq 2) in terms of the corresponding material parameters. The solid lines in Figure 6.2e,f are obtained from the analytical solution of the minimization problem for the Landau energy, which reproduces the experimental data remarkably well. Specifically, the trimerization phase Φ is obtained from the Euler-Lagrange equation $\partial F/\partial\Phi = \vec{\nabla} \cdot \partial F/\partial(\nabla\Phi)$ under the approximation of low anisotropy of the Landau energy, i.e. assuming that the amplitude keeps its bulk value Q_0 across the wall [32,33]. Thus, the equation reduces to

$$\sin 6\Phi - \xi_6^2 \frac{d^2(6\Phi)}{dx^2} = 0, \qquad (3)$$

where x is the coordinate perpendicular to the wall. The nonlinear Equation 3 is mathematically equivalent to the equation of motion of a pendulum, from which we obtain the evolution of Φ across a wall separating domains with $\Phi_n = n\pi/3$ and Φ_{n+1} as

$$\Phi(x) = \Phi_n + \frac{2}{3}\arctan(e^{x/\xi_6}). \qquad (4)$$

The correction $\delta Q(x)$ to the constant-amplitude approximation $[Q(x) = Q_0 + \delta Q(x)]$ is due to the coupling with Φ and is obtained by substituting eq 4 into the second Euler-Lagrange equation $\partial F/\partial Q = \vec{\nabla} \cdot \partial F/\partial(\nabla Q)$ and linearizing it with respect to $\delta Q(x)$. This yields

$$\delta Q(x) \approx -\frac{\xi^2}{\kappa\, \xi_6\, \widetilde{\xi_6}} \frac{Q_0}{\cosh^2(x/\widetilde{\xi_6})}, \qquad (5)$$

where $\widetilde{\xi_6} = \xi_6\sqrt{1 + \xi^2/\xi_6^2}$ and κ is a constant resulting from the interplay between ξ and ξ_6 ($\kappa \approx 9/\sqrt{2\pi}$ for $\xi \sim \xi_6$ and $\kappa \approx 9/2$ for $\xi_6 \gg \xi$). In Figure 6.2d, κ is a fitting parameter that effectively incorporates higher order corrections. The validity of this approximate solution (see Figures 2e and 2f) reveals that the Z_6 anisotropy is moderate in our system.

This analysis also reveals that the fundamental domain wall width, as obtained from the trimerization phase Φ in Figure 6.2e, is defined by ξ_6 (rather than ξ). From the fitting to eq 4 we find $\xi_6^{\text{charged}} = 7.4 \pm 0.2$ Å (7.5 ± 0.3 Å) and $\xi_6^{\text{neutral}} = 6.3 \pm 0.1$ Å (5.9 ± 0.1 Å) for $ErMnO_3$ ($Er_{1-x}Zr_xMnO_3$). From fitting the trimerization amplitude Q in Figure 6.2f to eq 5, we find values of $\tilde{\xi}_6^{\text{charged}} = 18 \pm 1$ Å (16 ± 7 Å) and $\tilde{\xi}_6^{\text{neutral}} = 13 \pm 2$ Å (10 ± 1 Å) for $ErMnO_3$ ($Er_{1-x}Zr_xMnO_3$). Error bars represent the statistical uncertainty in the mean. An additional source of error originates from domains that overlap in the projection direction, leading to apparently wider domain walls as discussed in ref [17]. In order to minimize such broadening effects, we use a thinner specimen

(~20-50 nm) with a lower domain wall density and, hence, less overlap of domains. In fact, the contrast of the atomic columns does not show evidence for domain overlap in our images (see Figure 6.3). An overlap of two domains in projection is clearly visible as a reduction in contrast on a specific atomic position as well as smearing of the atomic column [17]. The overlapping domain wall effect is not observed in our thinner samples and which is fundamentally different from the atomic displacements from intermediate Φ values. While we do observe domain wall overlap in thicker regions of the specimen, as seen in Figure 6.3d, this is not generally observed in our thinner regions (20-50 nm). From our statistics, we exclude images which are taken in thicker regions of the specimen that may show an overlap of two domains in projection.

We also note that some misalignment of the domain walls with respect to the crystal lattice generally appears at large scales, as can be seen in Figure 6.2. In our statistical analysis of the walls, we averaged over more than 35 domain walls for each type of wall shown in Figure 6.2. In order to minimize additional sources of uncertainty (e.g. due to the meandering nature of the walls), we only considered areas in which the walls do not deviate more than 5 degrees from the vertical (or the horizontal) for the analysis in Figure 6.2e,f .

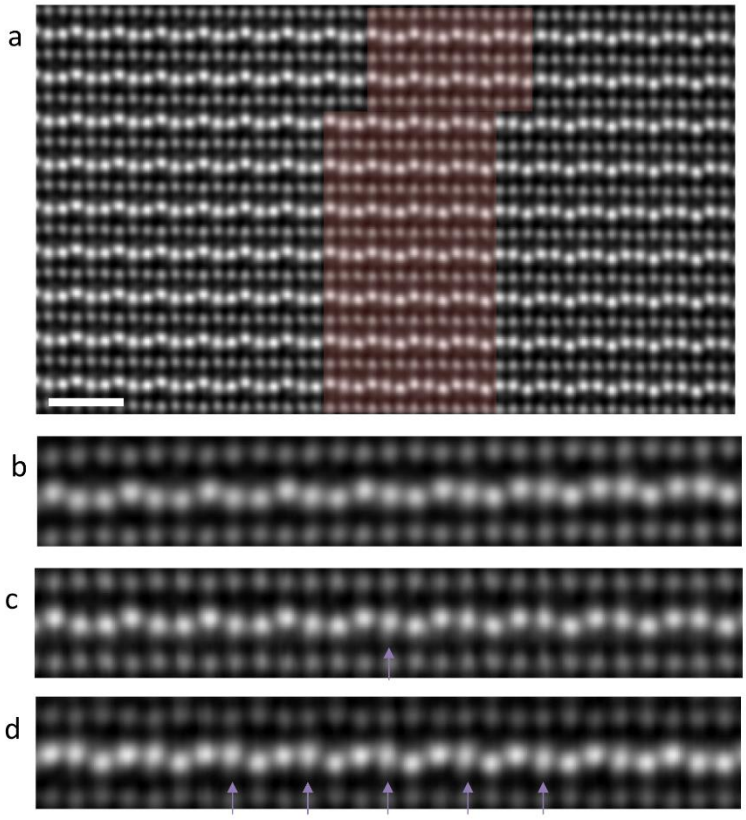

Figure 6.3: Projection effects of thick regions on domain wall width. (a) HAADF-STEM image of a neutral domain wall, with a 1 nm scale bar. The unit cells around the domain wall are highlighted. (b) Zoomed-in region showing the progression of the atomic columns across a domain wall in a thin region. In comparison to reference 17, there is not a decrease in atomic contrast or a smearing of atomic positions, indicating there are not regions of the image that have two overlapping domains in projection. (c) Slightly thicker region where we see minimal smearing if any. (d) The thickest region, where we see two domains overlapping in projection, where the atomic column intensity is lower due to electron beam channeling on the two atomic columns (pointed out by the arrows).

The obtained difference between ξ_6^{charged} and ξ_6^{neutral} can be understood as the result of the anisotropy in the gradient term ($\frac{g}{2}|\partial_i \mathbf{Q}|^2 \rightarrow \frac{g_i}{2}|\partial_i \mathbf{Q}|^2$ in eq 2, with $g_x = g_y \neq g_z$), as it is in tune with the difference that is obtained from DFT calculations of the corresponding parameters [21].

Additional modifications may occur due to the chemical environment as indicated by the width of the neutral domain walls, which are about 6% thinner in $Er_{1-x}Zr_xMnO_3$ than in $ErMnO_3$. It remains to be demonstrated, however, whether the observed change is due to the doping of Zr or other growth-related parameters.

Furthermore, our analysis supports our experimental observation that the system displays low-symmetry regions with $\Phi \neq \frac{n\pi}{3}$ due to the gradual evolution of the trimerization across the domain walls. These regions explain the emergence of the continuous distribution of tilt angles Φ in Figure 6.1c that blurs the six discrete states expected according to the Z_6-symmetry of the bulk. The low-symmetry regions are expected to gain an increasingly dominant weight as the ferroelectric transition temperature is approached or if the six-fold anisotropy is reduced, since they grow as $\xi_6 \sim |c'|^{-1/2}\,|T - T_c|^{-1}$. Interestingly, we note that the phase change across the trimerization domain walls is systematically slightly below its nominal value $\pm\pi/3$, which can be related to the residual symmetry breaking discussed in ref [29]. To reproduce this feature in Figure 6.2e, we renormalize the solution (eq 4) to the corresponding experimental values in the bulk. The result is virtually indistinguishable from what can be obtained self-consistently using the Landau energy in ref [29].

Equation 4 is in fact the $k = 1$ case in the family of solutions to eq 3 that can be parametrized as $\Phi\,(x,k) = \frac{1}{6}\left[\pi + 2\,\mathrm{am}\left(\frac{x}{k\,\xi_6}\middle|k^2\right)\right]$, where $\mathrm{am}(u|m)$ is the Jacobi amplitude function. In this family, the solutions with $k < 1$ describe the topological stripe domain states that occur when the system is grown below the trimerization transition temperature [34]. Accordingly, when $k \to 1^-$, these solutions lead to stripe domains of size $2k\,\xi_6\,K(k)$ separated by domain walls of width ξ_6 (here, $K(k)$ is the complete elliptic integral of the first kind). Interestingly, if extended to the cylindrical geometry, this set of solutions can also provide the description of the phase in trimerization vortices discussed below.

6.4 Vortex structures

After clarifying the inner structure of the domain walls, we now turn to the topological defects that are observed in the form of a vortex-like distribution of the trimerization order parameter. This distribution is found wherever domain walls intersect, which systematically happens in groups of six [4]. Figure 6.4 shows HAADF-STEM data of such a trimerization vortex in $Er_{1-x}Zr_xMnO_3$. Figure 6.4a shows the data for the trimerization phase, Φ, where in the HAADF-STEM image we can see six domains with different Φ_n's merge at the central point of the vortex. The domain merging is analyzed in the Figure 6.4b, where we plot the trimerization phase Φ as a function of the angle θ around the central point of the vortex for different distances from this point (STEM data are marked by dots). Here, Φ exhibits step-like variations for distances $\gtrsim 3$ nm where it corresponds to a discrete set of trimerization domains separated by domain walls, in what we call the outer vortex region. In contrast, below ~ 3 nm, Φ becomes a continuous function and eventually displays a linear increase, $\Phi = \theta$, in the innermost part of the vortex (here and hereafter we use cylindrical (r, θ, z) coordinates). This analysis thus reveals that the center of the vortex is in fact a singular point in which $|\nabla\Phi(\theta)| \approx 1/r$ diverges.

The data for the trimerization amplitude is shown in Figure 6.4c, for the same HAADF-STEM image. Figure 6.4d shows the trimerization amplitude Q drops to zero at the vortex central point, recovering its bulk value within a distance of ≈22 Å for $Er_{1-x}Zr_xMnO_3$ (≈18 Å in $ErMnO_3$). The bulk value of Q is near 28 pm (i.e. 42 pm of maximal relative displacement between Er atoms) – agreeing with previously reported values of Er displacements in the literature [19].

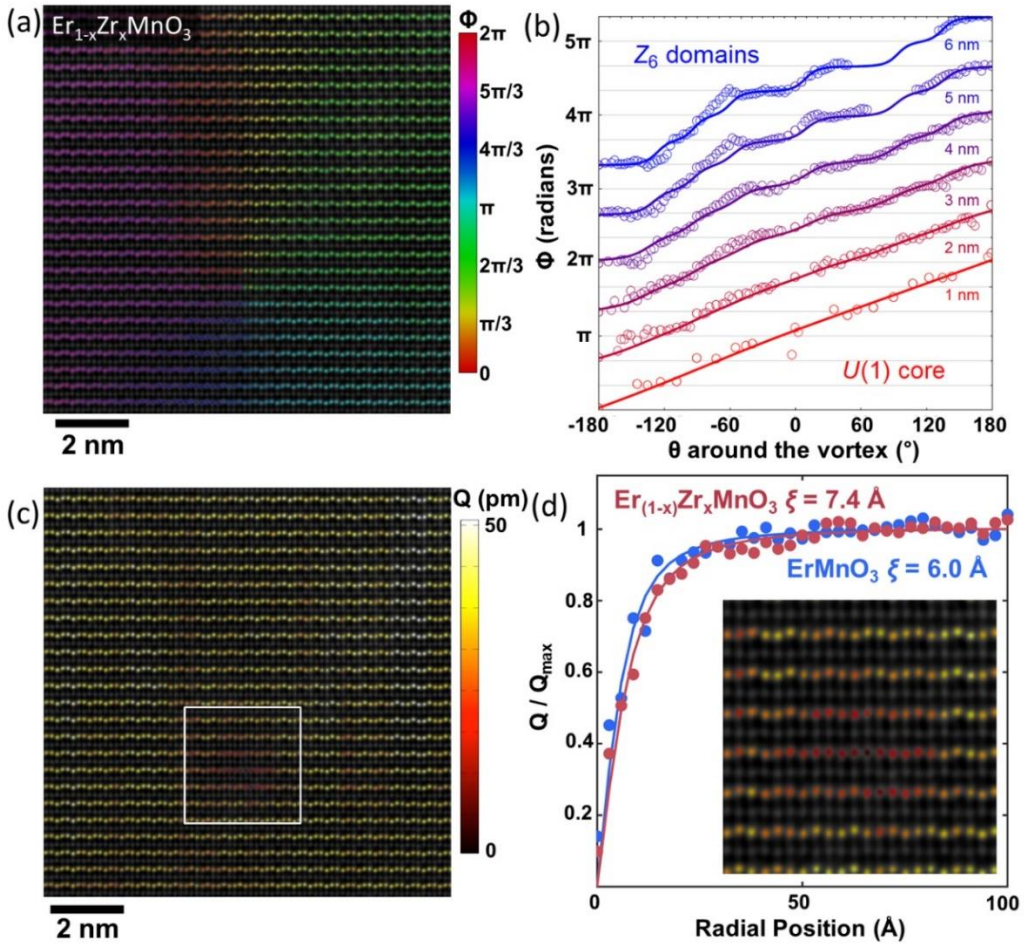

Figure 6.4: Atomic vortex structure. (a) HAADF-STEM overlay of the phase of the vortex in $Er_{1-x}Zr_xMnO_3$, showing a clockwise progression of phase from 0 to 2π. (b) The evolution of the phase wrapping around the vortex core at different radii in $Er_{1-x}Zr_xMnO_3$. Within 3 nm of the vortex, the phase progresses continuously, while farther from the vortex the phase levels off at one of the 6 distinct domains. Dots represent experimental measurement and solid lines show phase-field simulated results. (c) Same HAADF-STEM image as (a) with amplitude overlay, showing a decrease of Q at the vortex core. (d) Plot of the amplitude Q as a function of radial distance from the vortex core for both the doped and undoped specimen, showing the amplitude drop to nearly zero at the core and approach bulk values far from the core. Dots represent experimental measurement and solid lines show analytical expression $Q(r) = \frac{r/\xi}{\sqrt{2+(r/\xi)^2}} Q_0$ with fitted $\xi = 7.4$ Å for the Zr-doped specimen and $\xi = 6.0$ Å for the undoped specimen.

The features observed near the vortex can be accurately reproduced by finite element modeling based on the minimization of the free energy in eq 2 as summarized in Figure 6.5. The coefficients of the Landau description are chosen to reproduce the correlation lengths ξ (see below) and ξ_6 obtained experimentally. Figure 6.5a,b presents the distribution of trimerization phase and amplitude in the vortex with a similar structure as the one in Figure 6.4a, and Figure 6.5c,d shows a symmetric vortex in which the six domains are equally represented. The calculated distribution of the phase from Figure 6.5a is also plotted in Figure 6.4b (solid lines), showing good agreement between theory and experiment.

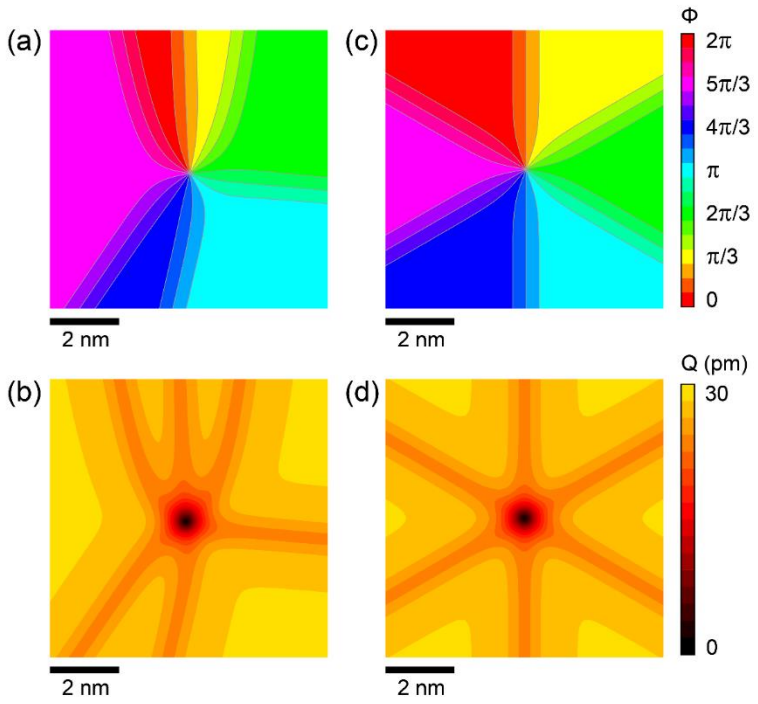

Figure 6.5: Contour plot for the local evolution of the trimerization order parameter at vortices. (a), (b) Numerical simulations of the phase (a) and the amplitude (b) of a non-symmetrical vortex, with the asymmetries present in Figure 6.4. (c), (d) Same as (a), (b), for a symmetric vortex. Theory work was done by Konstantin Shapovalov and Andres Cano.

The key features of the vortices can also be captured by a more phenomenological description based on the same analytical approach that reproduces the domain walls and topological stripes. One of the main conclusions of the analysis is that, in terms of the trimerization phase, the size of the vortex inner region is controlled by the characteristic length ξ_6, i.e. the same length that controls the size of the domain walls in the outer vortex region. In fact, the transition from the outer to the inner region can be seen as the result of domain walls overlapping as they approach the center of the vortex. Furthermore, the continuous winding of Φ in the inner vortex region (seen as the gradual increase of Φ in Figure 6.4b) is a striking manifestation of the fact the trimerization cannot adapt to spatial variations below ξ_6. Accordingly, we find that the curvature of the walls is also limited by this characteristic length ξ_6.

Remarkably, the symmetry of the host lattice is irrelevant for the inner vortex region where the vortices become continuous with emergent *U(1)* symmetry. As a result of this $Z_6 \rightarrow U(1)$ transformation, the central part of the trimerization vortex becomes completely analogous to a superfluid vortex. In fact, the interplay between Φ and Q is such that the minimization of the Landau energy (eq 2) in this inner *U(1)* region gives that the trimerization amplitude is $Q(r) \approx \frac{r/\xi}{\sqrt{2+(r/\xi)^2}} Q_0$. As a consequence, the vortex develops a "hard" core of the size $\sim \xi$ where the trimerization amplitude drops linearly to zero. This behavior is reproduced in Figure 6.4d, where we show this distribution of the trimerization amplitude (solid line) along with $Q(r)$ extracted from TEM (dots).

As we see, the stiffnesses associated to ξ_6 and ξ ultimately generate a transition between several distinct regions of the trimerization vortices: from the outermost Z_6 part that displays well-defined domains ($\Phi_n = \frac{n\pi}{3}, Q = \text{const.}$), to the inner vortex regions where the discrete nature of Φ is lost [U(1) symmetry, $\Phi \approx \theta$, size $\sim \xi_6$] and Q drops to zero [$Q(r) \approx \frac{r/\xi}{\sqrt{2+(r/\xi)^2}} Q_0$, size $\sim \xi$].

We note that ξ_6 and ξ are two independent scales of the system that can easily be of different orders of magnitude, especially near the trimerization transition where $\xi_6/\xi = \sqrt{b^2/(3|a(T)||c'|)} \to \infty$ as $T \to T_c$ or by means of the appropriate doping (such that $|c'| \to 0$). In that case, the vortex inner regions will dominate the response of the system and enforce an emergent $U(1)$ behavior of the order parameter with Q close to its bulk value. Thus, we are identifying ξ_6 as the principal characteristic length defining the morphology of topological defects in h-*R*MnO_3.

6.5 Emergent electrostatics at domain walls and vortices

Our data gained on $ErMnO_3$ and $Er_{1-x}Zr_xMnO_3$ demonstrates that the global structure of the topological defects observed in these systems is primarily determined by the trimerization order parameter, with their electric-charge properties playing only a minor role. The local electrostatics is a source of diverse functional behavior, potentially co-determining the interaction between topological defects and the interplay with other charged defects, such as oxygen vacancies, interstitials, and dopants. Furthermore, we expect the local charges that emerge at the topological defects to extend to distances $\sim \xi_6$, i.e., a distance which is largely independent of the surrounding electrostatics. Hence, the local charges are expected to be distributed over divergingly large areas near the transition point and/or in systems with reduced anisotropy. In this case the topological defects will all display the same emergent symmetries associated to their inner structure, leading to a generalized electrostatics that will draw apart from the surrounding bulk.

Figure 6.6a,b shows calculations comparing the charge distribution and the polarization across the domain walls directed perpendicularly to the *c*-direction in two types of material – in a ferroelectric ($c' < 0$) and in a paraelectric ($c' > 0$) *R*MnO_3. Figure 6.6a corresponds to a positively charged ferroelectric head-to-head wall similar to that seen in Figure 6.2c. The calculations show that the charge of the domain wall is distributed over the distance $\sim \xi_6$, corresponding to the

variation in the polarization and, hence, the variation of the trimerization phase. A qualitatively different type of wall is shown in Figure 6.6b. The latter exemplifies a domain wall separating non-ferroelectric domains as can be realized under certain conditions in hexagonal $InMnO_3$ [35,36]. In this case, there is a non-zero electric polarization induced at the domain wall due to the continuous change of the trimerization phase across the wall. Despite $\nabla \cdot P \neq 0$ at the wall, the charge integrated over it is zero, and so the wall is neutral in the sense that no long-range electric fields are generated by the bound charges. However, the distribution of charge provides a dipolar character due to the localization of the polarization – in fact, the wall represents a ferroelectric 2D system with tunable size ξ_6.

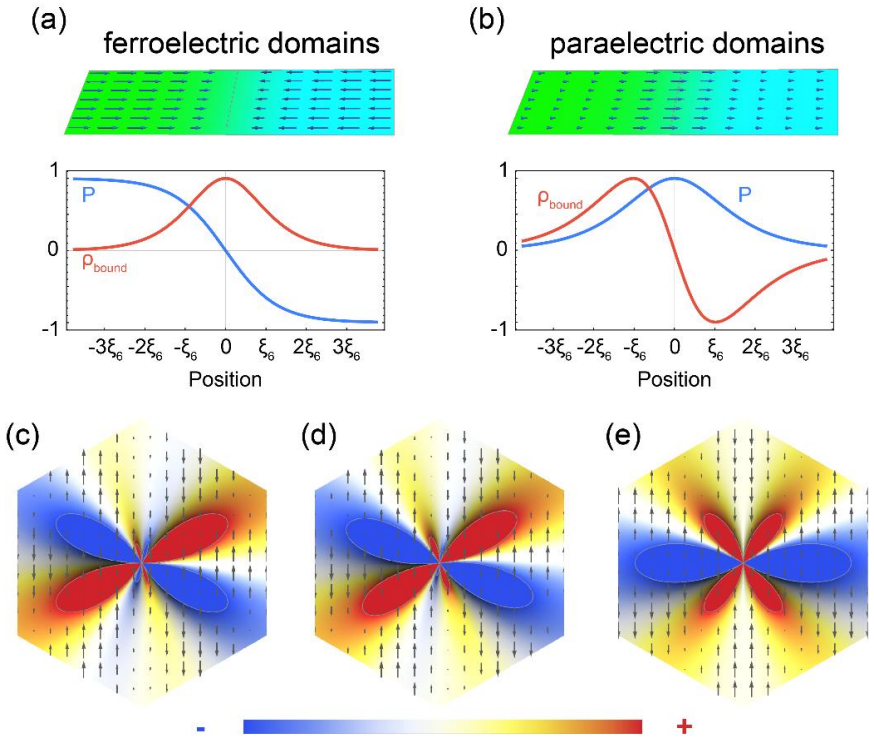

Figure 6.6: Emergent electrostatics at trimerization domain walls and vortices. (a,b) Trimerization domain wall separating ferroelectric (a) and non-ferroelectric (b) domains. The arrows in the top panels represent the electric polarization resulting from the trimerization. In both cases, we observe the emergence of a non-zero distribution of bound charges localized at the wall

due to the longitudinal variation of the polarization across the wall (bottom panels). (c-e) Density plot of the bound-charge distribution emerging at the core of the trimerization vortices (i.e. within a distance $\lesssim \xi_6$) for various orientations of the trimerization pattern with respect to the crystallographic axes Φ_0 (see eq 7), with superimposed arrows representing the electric polarization. The values of Φ_0 are: 0 (c), $\pi/18$ (d), and $\pi/6$ (e). In general, we observe eight bound-charge lobes of different size due to the gradual modulation of polarization within the core (c,d). The relative orientation of the trimerization pattern determines the size of the lobes, some of which can become vanishingly small as in (e). Theory work was done by Konstantin Shapovalov and Andres Cano.

Despite the strikingly different nature of the domain walls in Figure 6.6a,b, we note that their meeting points (i.e., the vortices) exhibit the same features due to the emerging U(1) symmetry. Most remarkably, the inner vortex region displays rather unexpected electrostatics irrespective of the ferroelectric or non-ferroelectric character of the corresponding domains (Figure 6.6c-e). Specifically, the trimerization at the center of the vortices becomes sinusoidally modulated and generates a gradual distribution of polarization

$$P \propto \frac{(r/\xi)^3}{[2+(r/\xi)^2\,]^{3/2}} \cos(3(\Phi - \Phi_0)) Q_0^3\ \hat{\mathbf{z}}. \qquad (6)$$

Equation 6 applies for vortices lying in the *xz*- or *yz*-plane, where Φ_0 denotes the trimerization origin with respect to the *z* axis. As such, it is a universal distribution that leads to an intriguing pattern of bound charges in which both radial and angular variations of the polarization play a role. The charge distribution is

$$\rho_{\text{bound}} = \nabla \cdot \boldsymbol{P} = \frac{-3(r/\xi)^2}{2[2+(r/\xi)^2]^{5/2}} [(r/\xi)^2 \sin(4\Phi - 3\Phi_0) + [4 + \left(\frac{r}{\xi}\right)^2] \sin(2\Phi - 3\Phi_0)] \rho_0 \quad . \qquad (7)$$

Equations 6 and 7 can be traced back to the emergent U(1) symmetry and reveal that, as the central point of the vortex is approached, bound charges delocalize from the nominal positions of the walls to form a more complex pattern. Outside the hard-core of the vortex ($\xi < r < \xi_6$) an octupolar-like charge pattern occurs as illustrated in Figure 6.6c-e. In contrast, the distribution transforms into a quadrupolar-like one in the hard-core region ($r < \xi$), in which, however, the charge is strongly suppressed due to the vanishing of the trimerization amplitude near the $\nabla\Phi$ singularity.

Similar to the trimerization domain walls, the vortex bound charges require screening by mobile charge carriers and are thus anticipated to lead to anomalous electronic transport behavior. Since the size of the vortex inner region can be rather small far from T_c, the related transport phenomena can be hidden from established probe techniques such as conductive atomic force microscopy (cAFM). Our theory shows, however, that the vortex inner regions grow with ξ_6. In consequence we anticipate that, irrespective of whether or not bulk ferroelectricity appears below the transition, the anomalous vortex transport can be detectable if the structural transition is driven to an experimentally accessible interval (e.g. by means finite-size effects in thin films or epitaxial strain [37]). Alternatively, vortex transport may be obtained by doping to engineer the effective anisotropy of the system.

6.6 Conclusions

Hexagonal manganites develop a rich variety of topological defects, including neutral, positively and negatively charged domain walls, as well as special vortices. Our work explains the atomic structure of these topological objects by combining state-of-the-art scanning transmission electron microscopy and the universal framework of the Landau theory of phase transitions. Independent of their specific 2D or 1D nature, they exhibit an inner structure that is fundamentally

determined by a single critical length scale (ξ_6). This length scale relates to the structural stiffness of the system rather than to its charge properties. As a consequence, domain walls with diverging electrostatic potentials and neutral domain walls have a similar structural width, representing a striking example for the unique consequences of improper ferroelectricity at the atomic scale. Furthermore, completely new and so far unexplored electrostatics arise at the vortices where improper ferroelectric domain walls intersect. Here, the hexagonal bulk structure becomes irrelevant, leading to octupolar- and quadrupole-like electrostatic field configurations. Similar to the charged domain walls, vortices thus represent a promising source for unusual electronic transport properties at the nanoscale.

References

[1] Nobel Media AB (2014).

[2] N. D. Mermin, Rev. Mod. Phys. **51**, 591 (1979).

[3] D. Meier, J. Phys. Condens. Matter **27**, 463003 (2015).

[4] T. Choi, Y. Horibe, H. T. Yi, Y. J. Choi, W. Wu, and S.-W. Cheong, Nat. Mater. **9**, 253 (2010).

[5] J. Seidel, R. K. Vasudevan, and N. Valanoor, Adv. Electron. Mater. **2**, 1 (2016).

[6] R. Wiesendanger, Nat. Rev. Mater. **1**, 16044 (2016).

[7] A. Bauer and C. Pfleiderer, *Topological Structures in Ferroic Materials* (Springer International Publishing, Cham, 2016).

[8] A. Fert, V. Cros, and J. Sampaio, Nat. Nanotechnol. **8**, 152 (2013).

[9] S. M. Griffin, M. Lilienblum, K. T. Delaney, Y. Kumagai, M. Fiebig, and N. A. Spaldin, Phys. Rev. X **2**, 1 (2012).

[10] S.-Z. Lin, X. Wang, Y. Kamiya, G.-W. Chern, F. Fan, D. Fan, B. Casas, Y. Liu, V. Kiryukhin, W. H. Zurek, C. D. Batista, and S.-W. Cheong, Nat. Phys. **10**, 970 (2014).

[11] Q. N. Meier, M. Lilienblum, S. M. Griffin, K. Conder, E. Pomjakushina, Z. Yan, E. Bourret, D. Meier, F. Lichtenberg, E. K. H. Salje, N. A. Spaldin, M. Fiebig, and A. Cano, (2017).

[12] D. Meier, J. Seidel, a. Cano, K. Delaney, Y. Kumagai, M. Mostovoy, N. a. Spaldin, R. Ramesh, and M. Fiebig, Nat. Mater. **11**, 284 (2012).

[13] Y. Geng, H. Das, A. L. Wysocki, X. Wang, S.-W. Cheong, M. Mostovoy, C. J. Fennie, and W. Wu, Nat. Mater. **13**, 163 (2014).

[14] Q. H. Zhang, L. J. Wang, X. K. Wei, R. C. Yu, L. Gu, A. Hirata, M. W. Chen, C. Q. Jin, Y. Yao, Y. G. Wang, and X. F. Duan, Phys. Rev. B - Condens. Matter Mater. Phys. **85**, 2 (2012).

[15] T. Matsumoto, R. Ishikawa, T. Tohei, H. Kimura, Q. Yao, H. Zhao, X. Wang, D. Chen, Z. Cheng, N. Shibata, and Y. Ikuhara, Nano Lett. **13**, 4594 (2013).

[16] Q. Zhang, G. Tan, L. Gu, Y. Yao, C. Jin, Y. Wang, X. Duan, and R. Yu, Sci. Rep. **3**, 2741 (2013).

[17] J. Li, F. Chiang, Z. Chen, C. Ma, M. Chu, C. Chen, H. Tian, H. Yang, and J. Li, Sci. Rep. **6**, 28047 (2016).

[18] F.-T. Huang and S.-W. Cheong, Nat. Rev. Mater. **2**, 17004 (2017).

[19] M. G. Han, Y. Zhu, L. Wu, T. Aoki, V. Volkov, X. Wang, S. C. Chae, Y. S. Oh, and S. W. Cheong, Adv. Mater. **25**, 2415 (2013).

[20] F.-T. Huang, X. Wang, S. M. Griffin, Y. Kumagai, O. Gindele, M.-W. Chu, Y. Horibe, N. A. Spaldin, and S.-W. Cheong, Phys. Rev. Lett. **113**, 267602 (2014).

[21] S. Artyukhin, K. T. Delaney, N. a Spaldin, and M. Mostovoy, Nat. Mater. **13**, 42 (2014).

[22] Y. Kumagai and N. a Spaldin, Nat. Commun. **4**, 1540 (2013).

[23] C. J. Fennie and K. M. Rabe, Phys. Rev. B - Condens. Matter Mater. Phys. **72**, 1 (2005).

[24] B. B. Van Aken, T. T. M. Palstra, A. Filippetti, and N. a Spaldin, Nat. Mater. **3**, 164 (2004).

[25] M. Lilienblum, T. Lottermoser, S. Manz, S. M. Selbach, A. Cano, and M. Fiebig, Nat. Phys. **advance on**, (2015).

[26] S. C. Chae, N. Lee, Y. Horibe, M. Tanimura, S. Mori, B. Gao, S. Carr, and S. W. Cheong, Phys. Rev. Lett. **108**, 1 (2012).

[27] H. Das, A. L. Wysocki, Y. Geng, W. Wu, and C. J. Fennie, Nat. Commun. **5**, 2998 (2014).

[28] J. A. Mundy, C. M. Brooks, M. E. Holtz, J. A. Moyer, H. Das, A. F. Rébola, J. T. Heron, J. D. Clarkson, S. M. Disseler, Z. Liu, A. Farhan, R. Held, R. Hovden, E. Padgett, Q. Mao, H. Paik, R. Misra, L. F. Kourkoutis, E. Arenholz, A. Scholl, J. A. Borchers, W. D. Ratcliff, R. Ramesh, C. J. Fennie, P. Schiffer, D. A. Muller, and D. G. Schlom, Nature **537**, 523 (2016).

[29] A. Cano, Phys. Rev. B **89**, 214107 (2014).

[30] B. B. Van Aken, J.-W. G. Bos, R. A. de Groot, and T. T. M. Palstra, Phys. Rev. B **63**, 125127 (2001).

[31] J. Schaab, A. Cano, M. Lilienblum, Z. Yan, E. Bourret, R. Ramesh, M. Fiebig, and D. Meier, Adv. Electron. Mater. **2**, (2016).

[32] A. K. Tagantsev, L. E. Cross, and J. Fousek, *Domains in Ferroic Crystals and Thin Films* (Springer New York, New York, NY, 2010).

[33] B. A. Strukov and A. P. Levanyuk, *Ferroelectric Phenomena in Crystals* (Springer Berlin Heidelberg, Berlin, Heidelberg, 1998).

[34] S. C. Chae, Y. Horibe, D. Y. Jeong, S. Rodan, N. Lee, and S.-W. Cheong, Proc. Natl. Acad. Sci. **107**, 21366 (2010).

[35] Y. Kumagai, A. A. Belik, M. Lilienblum, N. Leo, M. Fiebig, and N. A. Spaldin, Phys. Rev. B - Condens. Matter Mater. Phys. **85**, 1 (2012).

[36] F. T. Huang, X. Wang, Y. S. Oh, K. Kurushima, S. Mori, Y. Horibe, and S. W. Cheong, Phys. Rev. B - Condens. Matter Mater. Phys. **87**, 2 (2013).

[37] H. Pang, F. Zhang, M. Zeng, X. Gao, M. Qin, X. Lu, J. Gao, J. Dai, and Q. Li, Npj Quantum Mater. **1**, 16015 (2016).

[38] M. E. Holtz, K. Shapovalov, J. Mundy, C. S. Chang, Z. Yan, E. Bourret, D. A. Muller, D. Meier, and A. Cano, Nano Lett. acs. nanolett.7b01288 (2017).

CHAPTER 7

DOMAIN WALLS IN MULTIFERROIC LUTETIUM FERRITE SUPERLATTICES

The defining feature of ferroics is the ability of an external stimulus—electric field, magnetic field, or stress—to move domain walls [1]. These topological defects and their motion enable many useful attributes, e.g., memories that can be reversibly written between stable states [2–4] as well as enhanced conductivity [5], permittivity [6], permeability, and piezoelectricity [7]. Although methods are known to drastically increase their density [8,9], the placement of domain walls with atomic precision has until now evaded control. Here we engineer the location of domain walls with monolayer precision and create a novel multiferroic in which ferroelectricity enhances magnetism at all relevant length scales. Starting with hexagonal $LuFeO_3$, a geometric ferroelectric with the greatest known planar rumpling [10], we introduce individual extra monolayers of FeO during growth to construct formula-unit-thick syntactic layers of ferrimagnetic $LuFe_2O_4$ [11,12] within the $LuFeO_3$ matrix, i.e. $(LuFeO_3)_m/(LuFe_2O_4)_1$ superlattices. The severe rumpling imposed by the neighbouring $LuFeO_3$ drives the ferrimagnetic $LuFe_2O_4$ into a simultaneously ferroelectric state, while also reducing the $LuFe_2O_4$ spin frustration. This increases the magnetic transition temperature significantly—to 281 K for $(LuFeO_3)_9/(LuFe_2O_4)_1$. Moreover, $LuFeO_3$ can form charged ferroelectric domain walls [13], which we align to the $LuFe_2O_4$ bilayers with monolayer precision. Charge transfers to these domain walls to alleviate the otherwise electrostatically unstable polarization arrangement [14], further boosting the magnetic moment. Moreover, the ferroelectric order couples to the ferrimagnetism, enabling direct electric-field control of magnetism at 200

kelvin. We further explore the domain wall architecture by measuring order parameter statistics, and observe how this changes after biasing by piezoresponse force microcopy.[10]

7.1 Introduction

Topological defects have shown many novel phenomena, such as enhanced conductivity [5], permittivity [6], permeability, and piezoelectricity [7]. In electrically and magnetically ordered materials, these topological defects form as ferroic domain walls, vortices and skyrmions. One of the defining features of these materials is that under external stimulus, such as electric or magnetic field, these domain walls move [1]. Recently, some domain walls have displayed electric field control of their conductivity [15]. This opens doors to key functionalities, such as reversible memory which can be written between two stable states [2,3,16].

Particularly interesting is the simultaneous ordering of electronic and magnetic ground states into so-called multiferroics. The coupling between the electrical and magnetic ground states into a magnetoelectric multiferroic is rare [1], but enormously promising for next-generation memory materials [17]. Known magnetoelectric multiferroics are very far from being implemented in memory applications because they have antiferromagnetic or weak ferromagnetic alignments [13,18–20], or have simultaneous ordering far below room temperature [21]. $LuFe_2O_4$ was purported to be simultaneously ferrimagnetic and ferroelectric at 250 K, the highest temperature of any known material [11]. Although its ferrimagnetic ordering is widely affirmed [12], recent studies find that $LuFe_2O_4$ is not ferroelectric [22,23]. Interestingly, a robust high-temperature ferroelectric with a closely related structure exists: hexagonal $LuFeO_3$. Although metastable, hexagonal $LuFeO_3$ has been grown in thin film form by epitaxial stabilization [24]. Isostructural to $YMnO_3$, it is an improper ferroelectric [10,25], where the rumpling of the Lu-O

[10] This work comes from Ref [35] and a work in progress, in close collaboration with Julia Mundy.

planes and corresponding tilt of the Fe-O trigonal bipyramids lead to geometric ferroelectricity that persists well above room temperature [26,27]. At low temperature hexagonal $LuFeO_3$ orders antiferromagnetically (T_N); slight canting of the spins gives rise to weak ferromagnetism [10,26,27].

Here we engineer a new multiferroic through the atomic-layer integration of $LuFe_2O_4$ and $LuFeO_3$ by reactive molecular-beam epitaxy. The resulting superlattice $(LuFeO_3)_9/(LuFe_2O_4)_1$ is strongly magnetic up to 281 K and exhibits short-range ferromagnetic fluctuations that persist, together with ferroelectricity, above room temperature. We corroborate this result using methods that are insensitive to magnetic impurity phases (e.g., neutron diffraction) or electrical leakage (e.g., high-resolution electron microscopy) and show how our results are consistent with first-principles calculations.

Figure 7.1a shows high-angle annular dark field scanning transmission electron microscopy (HAADF-STEM) images of the $LuFeO_3$ and $LuFe_2O_4$ end-members and Figure 7.1b the $(LuFeO_3)_m/(LuFe_2O_4)_1$ superlattices for $m = 1$ to $m = 10$. X-ray diffraction (XRD) patterns support the high structural quality observed. The characteristic "up-up-down" pattern of the lutetium atoms in $LuFeO_3$ [26,28], which is also present in the hexagonal manganites [29], is evident and reflects the polar nature of these superlattices. The polarization monotonically tracks the magnitude of this lutetium trimer distortion [10], rendering HAADF-STEM a local probe of ferroelectricity. Inspecting the images in Figure 7.1, we note that distortions are present in the $(LuFeO_3)_m/(LuFe_2O_4)_1$ series for $m \geq 2$. The ferroelectric rumpling was not observed in $LuFe_2O_4$, consistent with prior work [30], or the $(LuFeO_3)_1/(LuFe_2O_4)_n$ series at room-temperature.

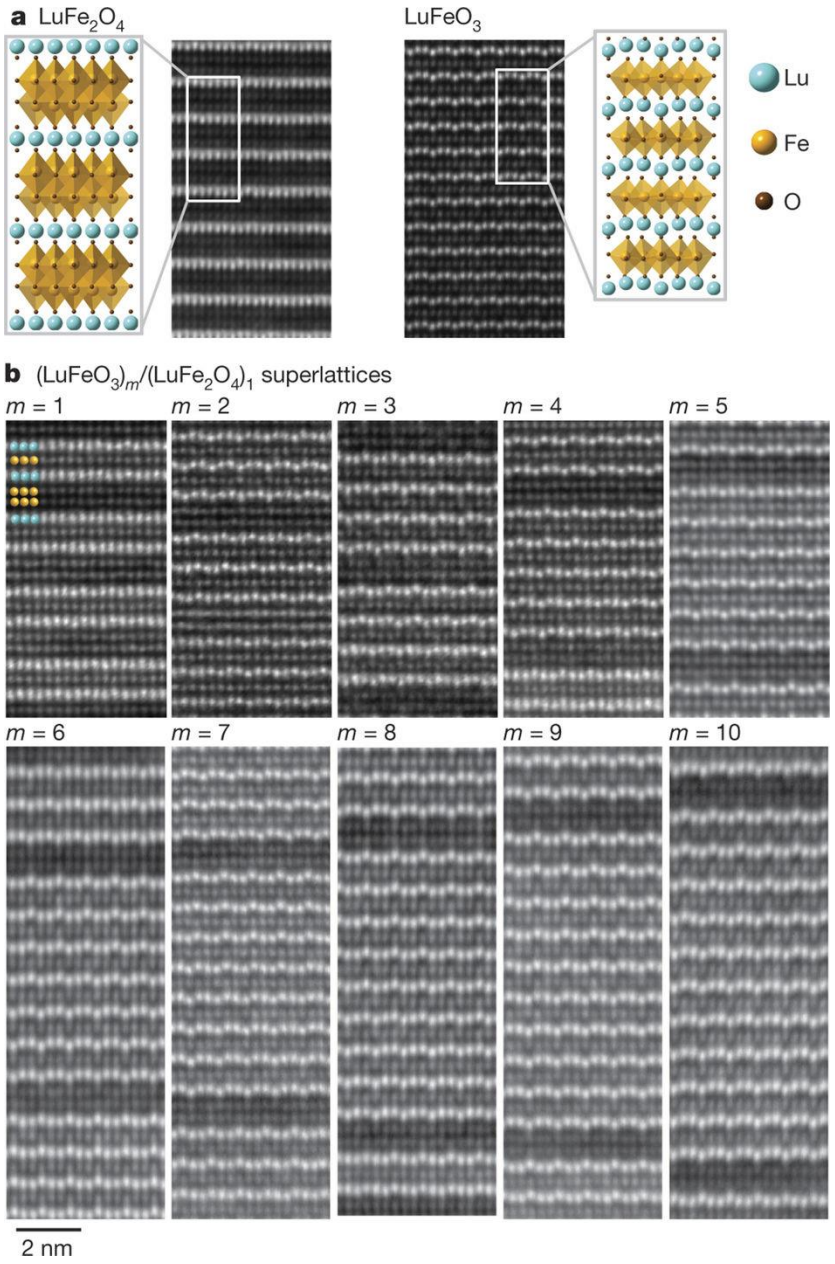

Figure 7.1. HAADF-STEM images of $(LuFeO_3)_m/(LuFe_2O_4)$ superlattices. **a**, End-members $LuFe_2O_4$ (left) and $LuFeO_3$ (right) with schematics of the crystal structures with lutetium (Lu), iron (Fe) and oxygen (O) in turquoise, yellow and brown, respectively. **b**, $(LuFeO_3)_m/(LuFe_2O_4)_1$ superlattice series for $1 \leq m \leq 10$. Samples are imaged along the $LuFeO_3$ $P6_3cm$ [100] zone axis. $LuFe_2O_4$ is imaged down the equivalent zone axis, which, owing to the primitive unit cell of $LuFe_2O_4$, is the [120] zone axis.

In these hexagonal $(LuFeO_3)_m/(LuFe_2O_4)$ superlattices, we additionally find a new way to control domain wall properties. By confining domains in the c-axis direction, we effectively control placement of "charged" domain walls, so-called because $\nabla \cdot \vec{P} \neq 0$. These walls either have the polarization pointing outwards (← →) in the "tail to tail" configuration, or inwards (→ ←) in a "head to head" configuration. By confining the domains in the c-axis direction, this allows unprecedented control over where these domain walls are located in the sample, which would be a beneficial step towards control in all-domain-wall devices. Additionally, the confinement of the domain walls in the narrow, 2D planes of the $LuFeO_3$ is an intriguing opportunity to study their properties.

Here, we extract this order parameter to see how the order parameter behaves in sheets of hexagonal ferrite which are forced to contain domain walls. We observe how the order parameter changes from domain to domain in the confined environment, and measure the fundamental length scale of the domain wall change grow as the confinement thickness does. We also observe the change of domain wall before and after biasing, through an *ex situ* TEM biasing experiment, in which the specimen is biased in a piezoresponse force microcope (PFM), before TEM sample preparation by FIB and imaging. This study enables indirect study of how the domain wall motion propagates through the film during electrical biasing.

7.2 Ferroelectricity-Enhanced Magnetism and Magnetoelectric Coupling

The magnetic properties of the $(LuFeO_3)_m/(LuFe_2O_4)_n$ superlattices were characterized with a superconducting quantum interference device (SQUID) magnetometer[11]. Field cooled magnetization vs. temperature (*M-T)* curves are displayed in Figure 7.2. The shapes of the *M-T* curves for the superlattices are the same as that of $LuFe_2O_4$, implying that the magnetization

[11] Experiments performed by Jarrett Moyer, Peter Schiffer, UIUC

observed in the superlattices most likely is ferrimagnetic of the same kind as $LuFe_2O_4$ [22]. The saturation magnetization of $(LuFeO_3)_9/(LuFe_2O_4)_1$ is shown in Figure 7.2b—the saturation magnetization remains to ~350 K, suggesting that short-range ferromagnetic fluctuations persist well above room temperature. In Figure 7.2c, T_C is plotted as a function of the fraction of the iron ions that sit in $LuFeO_3$ layers, $^{m}/_{m+2n}$. Strikingly, the superlattice transitions are higher than thin films of both of the constituent layers, $LuFeO_3$ (T_N = 147 K) and $LuFe_2O_4$ (T_C = 219 K; slightly different from single crystals due to substrate choice [31] and our conservative definition of T_C). This enhancement was previously observed in single crystalline $Lu_2Fe_3O_7$ [32]. For the $(LuFeO_3)_m/(LuFe_2O_4)_1$ series, the ferromagnetic Curie temperature increases to T_C = 281 K for m = 9. We corroborate this enhancement in T_C with neutron diffraction characterization of a $(LuFeO_3)_6/(LuFe_2O_4)_2$ superlattice; neutron scattering is insensitive to small impurity phases which could impact bulk characterization. Not only is the onset of magnetic order revealed by neutron scattering consistent with that measured by SQUID, but the magnetic ordering corresponds to a reflection in the superlattice structure not present in bulk $LuFe_2O_4$. Further, it is coherent through six superlattice repeats along the *c*-direction.

In addition to T_C, the magnetic moment and ferroelectric polarization can also be tracked across the superlattice series. The saturated magnetic moment per $LuFe_2O_4$ iron cation at 50 K is plotted in Figure 7.2d. There is a sharp deviation in the $(LuFeO_3)_m/(LuFe_2O_4)_1$ superlattices for $m \geq 2$: here the $LuFe_2O_4$ moment increases with m reaching ~2 μ_B/Fe for the m = 15 superlattice. Finally, we quantify the ferroelectric lutetium distortions from HAADF-STEM images such as those in Figure 7.1. The polarization resulting from this displacement is plotted in Figure 7.2e. Notably, the polarization sharply increases in the $(LuFeO_3)_m/(LuFe_2O_4)_1$ superlattices at $m \geq 2$, reaching ~6 $\mu C/cm^2$ for the high m superlattices.

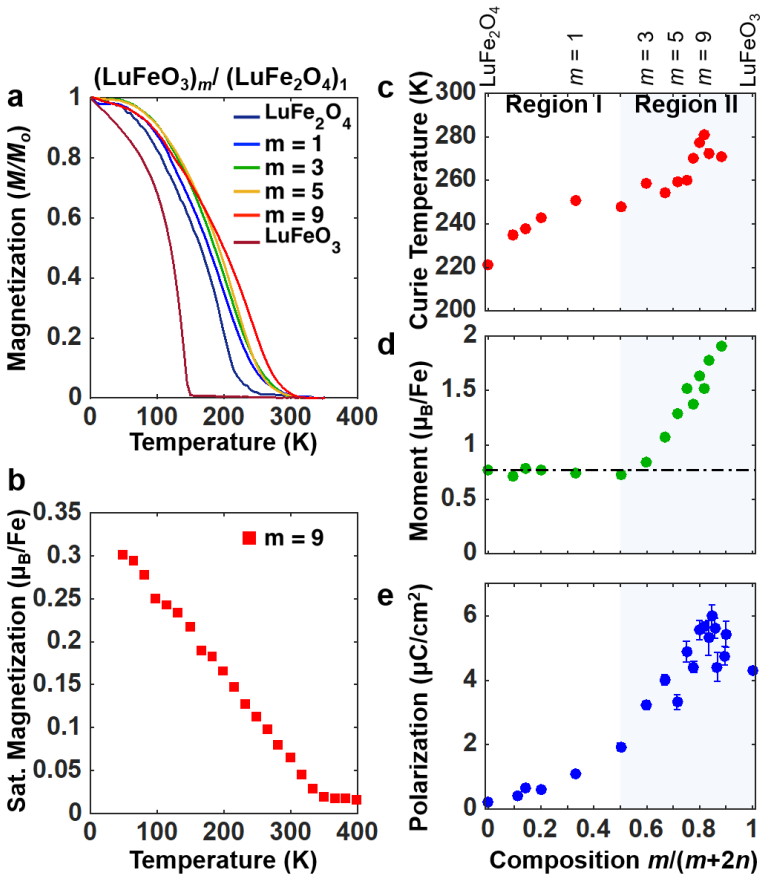

Figure 7.2. Magnetic characterization of the $(LuFeO_3)_m/(LuFe_2O_4)_n$ superlattices. **a**, *M*-*T* curves for a series of $(LuFeO_3)_m/(LuFe_2O_4)_1$ superlattices cooled in a 1 kOe field. **b**, Saturation magnetization of the $(LuFeO_3)_9/(LuFe_2O_4)_1$ superlattice. **c**, The ferromagnetic Curie temperature extracted from the curves including those in **a**. The ferromagnetic Curie temperature reaches a maximum of 281 K for the $(LuFeO_3)_9/(LuFe_2O_4)_1$ compound. **d**, The total moment per $LuFe_2O_4$ iron atom at 50 K assuming the moment of $LuFeO_3$ remains constant. **e**, Average polarization from HAADF-STEM for superlattice layering plotted as a function of the composition for the $(LuFeO_3)_m/(LuFe_2O_4)_1$ and $(LuFeO_3)_1/(LuFe_2O_4)_n$ series. Ferroelectric distortions are observed for the $(LuFeO_3)_m/(LuFe_2O_4)_1$ superlattices with $m \geq 2$; the polarization reaches ~ 6 μC/cm^2. The magnetic data was done by Jarrett Moyer and Peter Schiffer.

The observed enhancement of the magnetic transition temperature and moment shown in Figure 7.2c,d could arise from the $LuFe_2O_4$ matrix incurring structural, stoichiometric or spin-lattice changes when epitaxially integrated with the $LuFeO_3$ layers. Figure 7.2 suggests two distinct regions with a separate interplay of these effects: Region I for $0 < {}^{m}/_{m+2n} < 0.5$ where the T_C saturates at ~250 K and Region II for $0.5 \leq {}^{m}/_{m+2n} < 1$ where a further increase of T_C to 281 K is coupled with an enhanced magnetic moment and ferroelectric distortions.

The behaviour of the Region II superlattices is elucidated by first-principles density functional theory (DFT) calculations[12]. We determine that $LuFe_2O_4$ has an antiferroelectric charge-ordered ground state, "COI," as shown in Figure 7.3a. The ferroelectric charge-ordered state "COII" shown in Figure 7.3b has a higher energy. The magnetization as a function of temperature for the COI ground state and low-energy COII state calculated from the Ising spin model are shown in Figure 7.3a,b, respectively. The COII state is found to be susceptible to the tri-fold lutetium distortions characteristic of $LuFeO_3$ (but not observed in the $LuFe_2O_4$ state in bulk)—these distortions are clamped by symmetry in COI. Artificially increasing the distortion vector, *Q*, in the COII state tunes the relative strength of the in-plane interactions and reduces the magnetic frustration; this in turn increases the magnetic transition T_C as shown in Figure 7.3b. While this already suggests that the enhancement of T_C in the $(LuFeO_3)_m/(LuFe_2O_4)_1$ superlattices is attributable to the lutetium distortions imposed by the $LuFeO_3$ layers, we also calculated the structure of the m = 1, 3 and 5 superlattices directly. While all superlattice structures calculated display the lutetium distortions observed in the COII structure, DFT calculations of the m = 3 superlattice find the most stable configuration corresponds to a "Fe^{3+}-doped" structure at the double iron layers rather than the COII state with iron charge ordering. The Fe^{3+}-doped structure consists of bilayers with a 2:1 ratio

[12] Done by Hena Das, Alejandro F. Rébola, and Craig J. Fennie

between Fe^{3+} and Fe^{2+}. Here, the net magnetization is due to ferromagnetically aligned Fe^{2+} ions located at the centre of Fe^{3+} hexagons and is higher than in $LuFe_2O_4$.

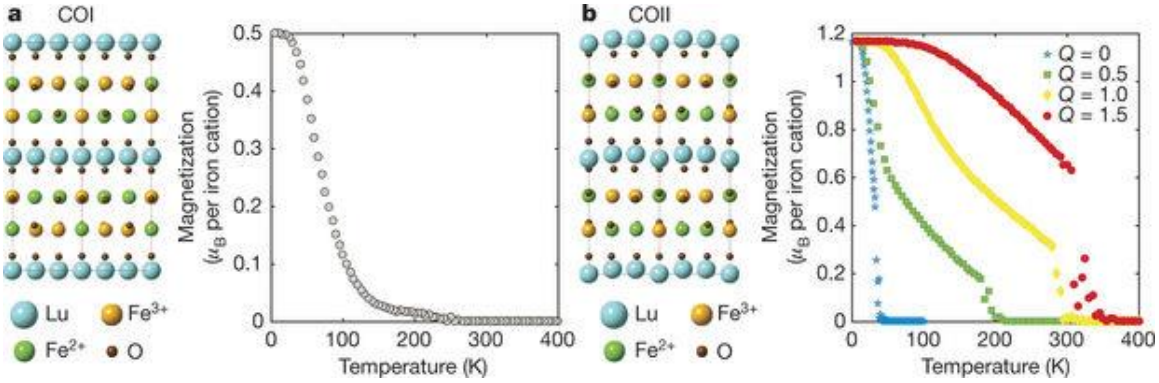

Figure 7.3. First-principles calculations of the spin configuration of $LuFe_2O_4$. **a**, **b**, Monoclinic structures of the $LuFe_2O_4$ system for the Fe^{2+}/Fe^{3+} antiferroelectric charge-ordered (COI) state (**a**; space group C2/m) and the ferroelectric charge-ordered (COII) state (**b**; space group Cm). The saturation magnetization per iron cation was calculated as a function of temperature (right panels). For the COII configuration (**b**), the temperature-dependent saturation magnetization per iron cation is calculated as a function of Q, the amplitude of the atomic distortions from the high-symmetry structure. In the COII state, the magnetic transition temperature increases with the magnitude of the structural distortion associated with the ferroelectric state. The DFT work was done by Hena Das, Alejandro Rebola, and Craig Fennie.

PFM was used[13] to investigate the local ferroelectric switching in the $(LuFeO_3)_9/(LuFe_2O_4)_1$ film. The poled domain structure persists for at least 100 hours after writing, demonstrating the ability to reversibly and robustly switch the spontaneous polarization. We demonstrate that the near room-temperature ferrimagnetism observed in the $(LuFeO_3)_9/(LuFe_2O_4)_1$ directly couples to the

[13] PFM done by James Clarkson and Julia Mundy

ferroelectric order. A $(LuFeO_3)_9/(LuFe_2O_4)_1$ film was electrically poled at 300 K to construct distinct "up" and "down" *c*-oriented polar domains as shown in Figure 7.4a. The resulting magnetic order was then imaged at 200 K and 320 K using x-ray magnetic circular dichroic photoemission electron microscopy (XMCD PEEM) on the Fe-L_3 edge.[14] As shown in the ratio images in Figure 7.4b,c the magnetic ordering directly correlates to the electrical poled domain structure, demonstrating magnetoelectric coupling between ferroelectricity and magnetism. Between the 200 K and 320 K, the dichroic contrast on the iron sites drops by ~70% consistent with the reduction in the magnetization observed at these temperatures in the same film by SQUID. Figure 7.4d shows a line profile of the dichroic signal as a function of temperature.

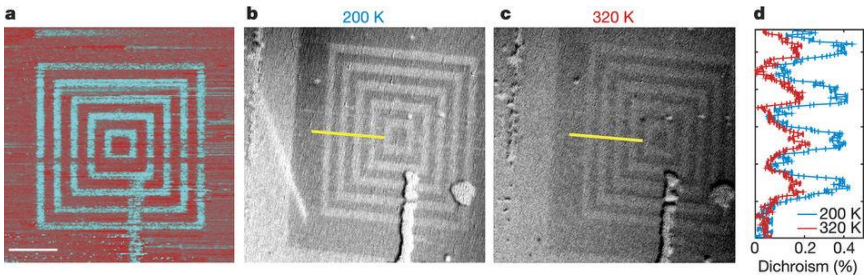

Figure 7.4. Magnetoelectric coupling in the $(LuFeO_3)_9/(LuFe_2O_4)_1$ superlattice. **a**, Out-of-plane PFM image at 300 K of the domain structure following electrical poling using a DC bias applied to the proximal tip. The 'up' and 'down' c-oriented domains appear in turquoise and red, respectively. Scale bar, 3 μm. **b**, **c**, XMCD PEEM ratio images from the Fe L3 edge acquired at 200 K (**b**) and 320 K (**c**). The correlation between the electrical poling and magnetic imaging demonstrates electric-field control of ferrimagnetism at 200 K. **d**, Comparison of the dichroic signals along the yellow lines in **b** and **c**. PFM and PEEM done by J. Clarkson, A. Farhan, and R. Ramesh

[14] PEEM by Alan Farhan, Zhiqi Li, James Clarkson, Ramamoorthy Ramesh and Andreas Scholl

7.3 STEM characterization of domains

We analyzed the displacements of the lutetium columns in the HAADF-STEM data with *m* ranging from 1 to 15. For each image, we extract the polarization, *P*, by measuring the lutetium displacement and comparing to DFT. The order parameter can also be extracted to obtain the trimerization phase, Φ, and amplitude, *Q*. Figure 7.5 shows data from one HAADF-STEM image of $(LuFeO_3)_9/(LuFe_2O_4)_1$ superlattice.

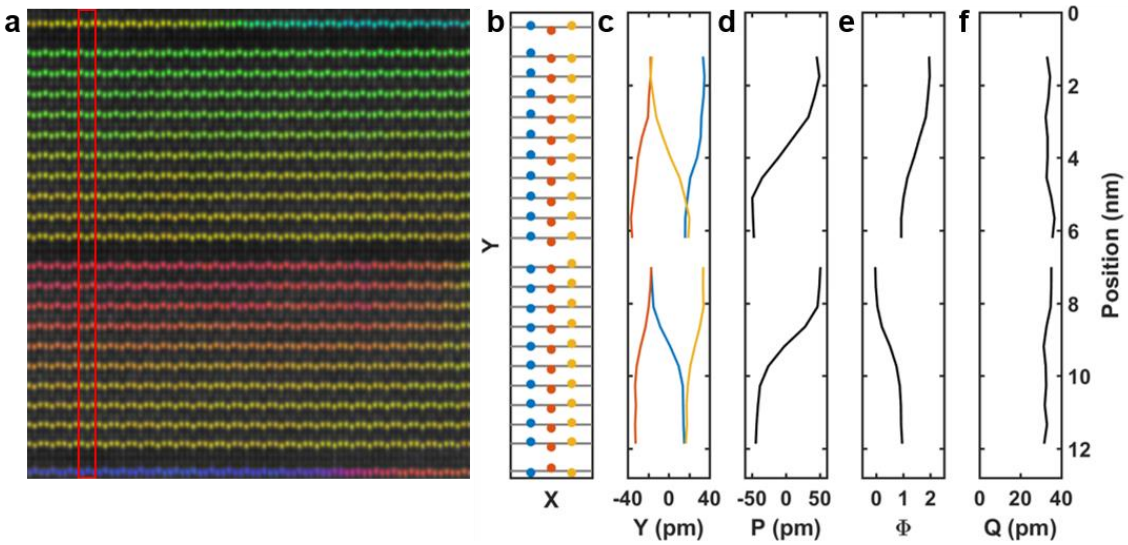

Figure 7.5. Atomic displacements and ferroelectric order parameter from a HAADF-STEM image of a $(LuFeO_3)_9/(LuFe_2O_4)_1$ superlattice. **a**, the image with Φ overlay on top. The red box indicates the region of data taken for **b**-**f**. **b**, cartoon of the positions of the atoms in the box, with the grey line noting the mean. **c**, deviation of the first (blue), second (red), and third (yellow) atoms from the mean in the $LuFeO_3$ layers. **d**, measured polarization displacement, **e**, Φ line profiles, where each integer of the phase corresponds to $n\pi/3$, and **f**, *Q* amplitude of displacement.

Figure 7.5a shows the Φ overlay, illustrating the different domains, highlighting a red box where data is extracted for Figure 7.5b-f. Figure 7.5b shows the atomic displacements in the *y*-

direction for the first, second and third atoms in the red box (blue, red and yellow). The displacement from the mean, *u*, is plotted for these atoms in Figure 7.5c. The extracted polarization displacement, phase Φ and amplitude *Q* are shown in Figure 7.5d-f. We see the amplitude of the displacements *Q* is roughly constant throughout the film, and the change in phase Φ drives the change in polarization.

Representative Φ overlays for different *m* in $(LuFeO_3)_m/(LuFe_2O_4)$ superlattices are shown in Figure 7.6. Figure 7.6a shows the $m = 2$ structure, showing regions of small domains with no regular domain structure. For larger layering types, such as the $m = 7$ layer shown in Figure 7.6b, the domain structure appears more regular with polarization down (-*P*) domains on the top of the $LuFeO_3$ block, and polarization up (+*P*) domains on the bottom of the block. We observe that the neighboring domains within the $LuFeO_3$ block have a $\Delta\Phi = \pm \pi/3$. At the end of one of the domains in the in-plane direction, the neighboring domain of opposite polarization will wrap around the domain up to the $LuFe_2O_4$ layer. Then, to maintain the tail-to-tail walls at the $LuFe_2O_4$ layer, there is another domain wall within 1-2 unit cells, leading to the next domain in the progression – causing three domains come together at the $LuFe_2O_4$ layer. The domains tend to progress in the same direction of Φ in the $LuFeO_3$ layer – either all clockwise (all $-\pi/3$) or counterclockwise (all $+\pi/3$). We show two examples of this regular winding and instances where there are multiple domains in a vortex pattern in Figure 7.6 b for long domains in-plane, and Figure 7.6 c for short domains in-plane. Rarely, five domains come together at a point (Figure 7.6d). In the bulk material, six domains would join forming vortices and antivortices. In these thin layers, we never see a full vortex.

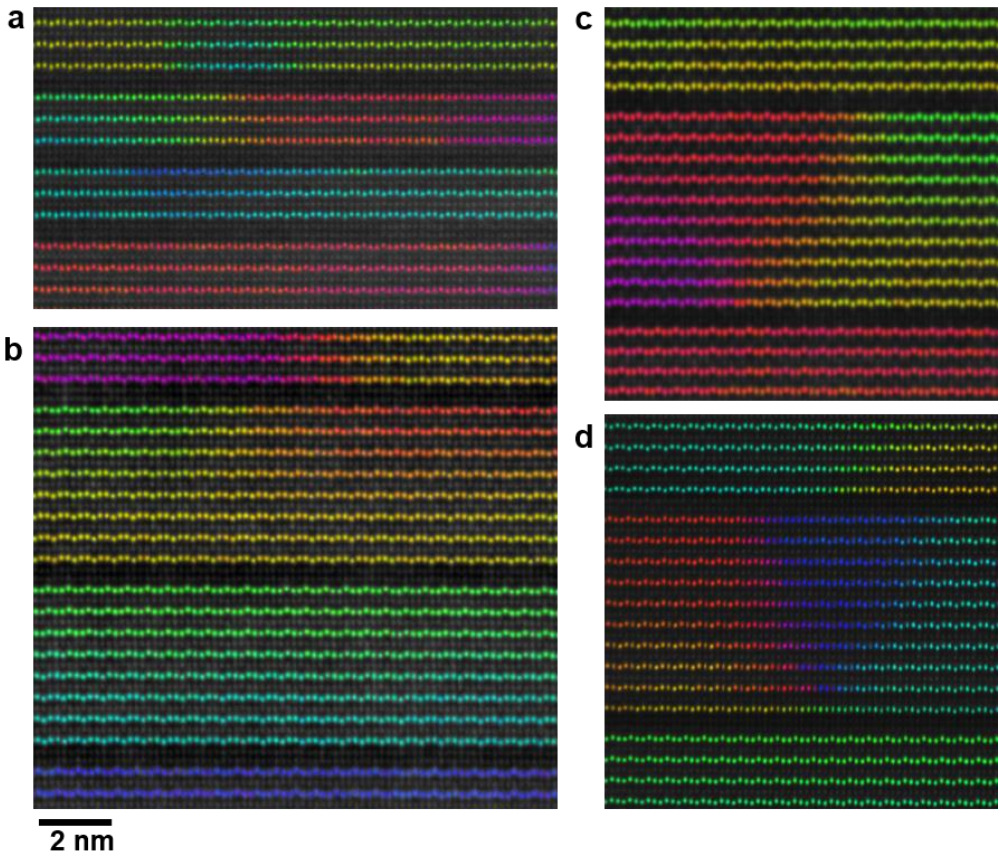

Figure 7.6. Φ overlay of STEM images showing the domain structure in $(LuFeO_3)_m/(LuFe_2O_4)$ superlattices. (a) m = 2 and 3 layers have irregular domain shape, although tends to maintain $\Delta\Phi = \pm\pi/3$ progression. (b) by m = 7, the most domains have +P domains on the bottom of the $LuFeO_3$ block and -P domains on the top of the $LuFeO_3$ block, and the domain structure is very regular. Typically, the domains are long in-plane and roughly half the size of the $LuFeO_3$ block out of plane. When the domain terminates in the in-plane direction, it touches the $LuFe_2O_4$ layer before progressing to the next (opposite polarization) domain briefly, then to the next domain in the progression (ie, the top block in (a) goes from $\Phi = 2\pi/3$ through $\pi/3$ to 0). Usually the domains are long, but sometimes they are short, as seen in panel (c). Rarely, the domain terminates in a partial-vortex pattern going through 5 domains (d).

Because there is significant deviation in the images, we performed statistics of the data from over 14,000 nm^2 (data from 142,640 atomic columns). We find that tail to tail domain walls form on the double iron layers, most of the time for layers of $m \geq 5$ (Figure 7.7a). The symmetrical structure of the superlattice determines that the tail-to-tail walls at the $LuFe_2O_4$ layers enforce the presence of head-to-head walls in the $LuFeO_3$ block, effectively confining the topological defect in a plane with a thickness determined by *m*. From the statistics, we see that head to head walls are found in the $LuFeO_3$ block, while no tail-to-tail walls are (Figure 7.7b). This is confirmed visually in the STEM images in Figure 7.6, where the regularity increases with *m* as shown in the statistics. The size of the domain in the direction of the c-axis is a fraction of the height of the $LuFeO_3$ block, and below $m \leq$ 3-4, the domain size becomes small enough that the domains become increasingly irregular.

We can also use statistics about the change in order parameter going across the $LuFe_2O_4$ block to determine if the $LuFeO_3$ blocks are isolated from each other. Looking at the change in order parameter across $LuFe_2O_4$ in Figure 7.7c, we observe that there is more likely to be a domain wall with higher *m*, and there are equal numbers of domain walls with $\Delta\Phi = \pm \pi/3$ and $\pm \pi$, with relatively little $\Delta\Phi = \pm 2\pi/3$. This indicates that there is no correlation between the $LuFeO_3$ blocks, with the exception that there is a tail-to-tail domain wall present (with increasing regularity for higher *m*). Within the $LuFeO_3$ blocks, the phase between adjacent domains changes by $\pm \pi/3$, as it would within bulk hexagonal manganites (Figure 7.7d).

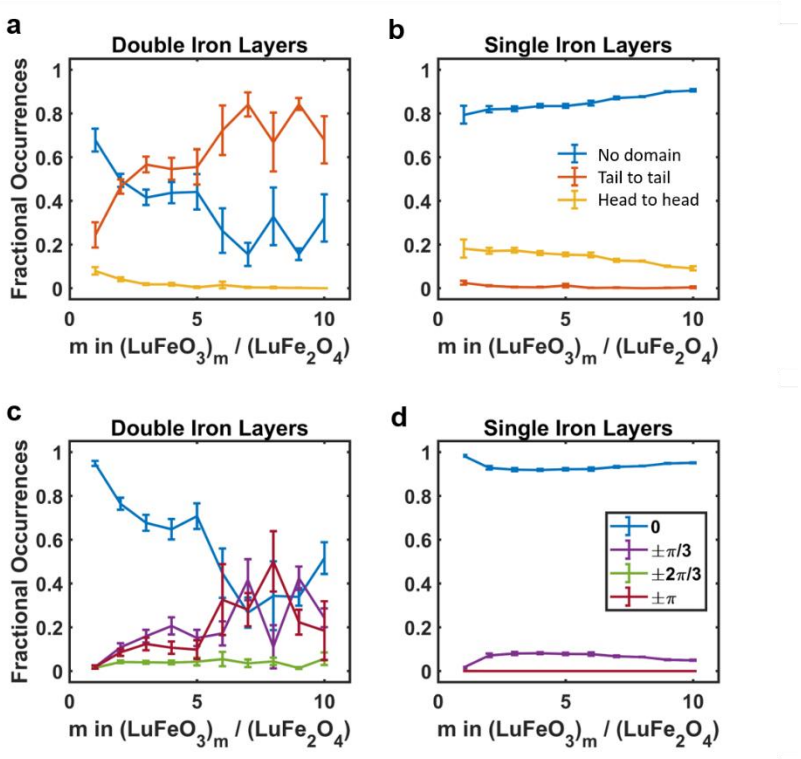

Figure 7.7. Occurrences of different types of domain walls going across $LuFe_2O_4$ (double iron layers) and within the $LuFeO_3$ blocks (single iron layers). **a** and **b** are distributions of head-to-head type walls, which rarely occur across $LuFe_2O_4$ layers, occurring largely in the $LuFeO_3$ blocks. Tail-to-tail walls are dominant across $LuFe_2O_4$ layers, especially with higher *m*. **c** and **d** are distributions of the phase change from one domain to the next. Across $LuFe_2O_4$ layers, domains of opposite polarization are equally probable ($\pm \pi/3$ and $\pm \pi$) while polarization to that of the same direction of polarization ($\pm 2\pi/3$) is unlikely. In $LuFeO_3$ layers, a large majority of domain changes are $\pm \pi/3$.

We would expect there to be charge compensation on these charged domain walls: at the tail to tail domain walls there should be hole doping and at the head to head wall there should be electron doping. In the superlattice structure, the $LuFeO_3$ nominally are Fe^{3+} and the $LuFe_2O_4$ layers are nominally half Fe^{2+} and half Fe^{3+}. To see how the iron valence is affected by the charged domain walls, we perform EELS measurements shown in Figure 7.8. We observe a slight change in valence

in the spectra between the $LuFeO_3$ and the $LuFe_2O_4$ layers, but not a significant enough one to account for an iron valence change of 0.5 between the layers. This indicates that there may be hole doping in the $LuFe_2O_4$ layer. This regular domain wall structure was predicted by DFT for higher *m*, and showed hole doping on the double iron layers. The increase in Fe^{3+} boosts the magnetic moment, which may explain the increase seen in Figure 7.2d. This reflects that the ordered domain walls are enhancing the magnetic signal.

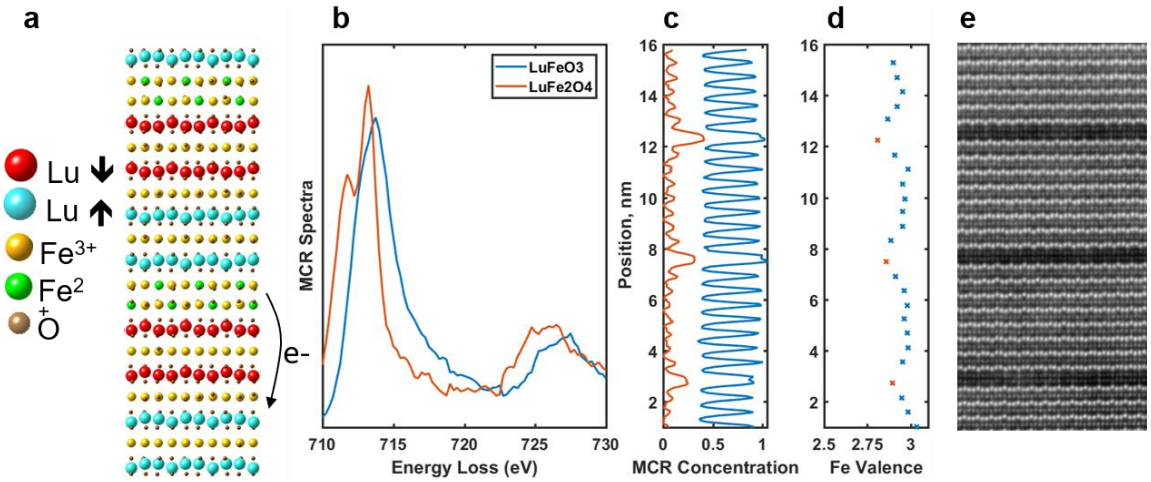

Figure 7.8. Charge compensation of domain walls in the $(LuFeO_3)_m/(LuFe_2O_4)$ superlattice. **a**.DFT showing the regular domain structure predicting more Fe^{3+} on the double iron layer for a $m = 3$ superlattice. Theory done by Hena Das and Alejandro Rebola in Craig Fennie's group. **b** MCR extracted spectra and **c** concentrations, showing a slight reduction in iron valence **d** on the "$LuFe_2O_4$"-like spectra in the $m = 7$ superlattice. However, the iron valence, found by correlating the Fe-L_3 energy [33], does not appear to change from a full 3+ state to a full 2.5+ state from the single to the double iron layers, suggesting the double iron layers are hole doped. ADF shown in **e**.

We now turn to how the ferroelectricity is affected in the domain walls that are confined in increasingly smaller thicknesses. To this end, we will plot a histogram of the logarithm of the

occurrences of the order parameter (Figure 7.9), which we have seen in the previous Chapter maps the free energy landscape of the material. For large m ($m \geq 4$), the domains have a well-defined energy landscape with six minima, with symmetry broken as we expect for a ferroelectric. There are intermediate states between the six wells, which connect neighboring domains, reflecting the fact domain walls have intermediate states going between $\pm \pi/3$. For $m = 1$, we observe the paraelectric state – showing just a parabolic well. Interestingly, for the $m = 2$ state, we observe a fairly uniform distribution of order parameters, which we might expect for Φ values if we had a state with U(1) symmetry [34]. For $m = 3$, we observe slightly more defined domains, with some paraelectric state present. This suggests that confining these domain walls is effectively reducing the ferroelectric transition temperature, which has been observed for lower m layers by XMCD and *in situ* heating TEM [35].

In the previous chapter on $ErMnO_3$, we observed that as domain walls began to overlap as they approached the vortex core, U(1) symmetry emerged. Here, as we confine the domain walls into thinner layers, the domain walls may become irregular and overlap – even annihilate – causing the U(1) state as observed before. Indeed, as the layers shrink, a higher fraction of the atoms in the layers exist in the domain wall (which is paraelectric) as opposed to being a part of the bulk of the domain, reducing the overall polarization in the material.

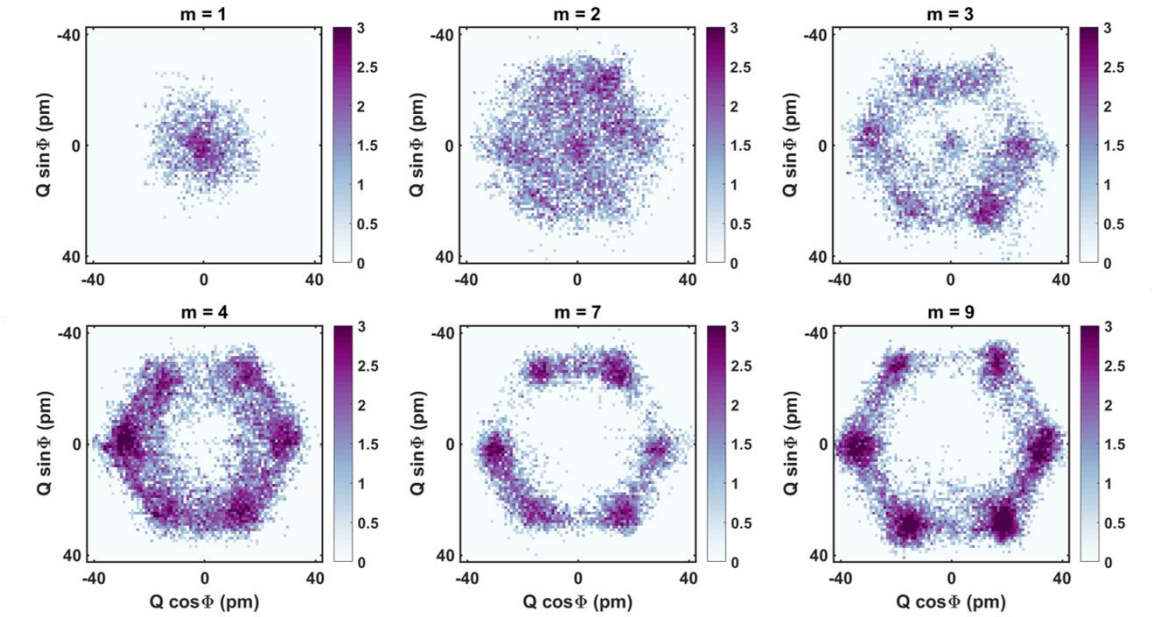

Figure 7.9. Histograms of the order parameters for different *m* layerings in $(LuFeO_3)_m/(LuFe_2O_4)$, with the logarithm of the occurrences plotted. For *m* = 1, we see a paraelectric order parameter distribution, showing a pattern consistent with a parabolic well. For *m*=2 and 3, *Q* is smaller and the values of *Φ* are more randomly spread, indicating a high domain wall density and combination of FE domains and U(1) symmetry. For *m*=4, the six ferroelectric domains are clearly visible while there is a large fraction of intermediate states in the ± π/3 direction. For *m*=7 and 9, the six ferroelectric domains make up the majority of the observed states, and the *Q* value is slightly higher.

As the $LuFeO_3$ layers become small enough in the c-axis direction to noticeably limit the domain size in the in-plane direction, we turn to investigate how the domain wall width is affected by the confinement of the thin layer. Data of *Φ* going across charged domain walls is plotted in Figure 7.10, with the length scale describing the change in phase described from Landau theory as ξ_6. Here, we are only considering walls in the confinement direction, or c-axis direction, which are contained in the $LuFeO_3$ blocks and are charged domain walls. We observe the phase *Φ* evolves from one domain to the next over a shorter distance for highly confined walls, with the ξ_6 value

increasing with increasing *m* in $(LuFeO_3)_m/(LuFe_2O_4)$ superlattices. This suggest that the domain wall width can be affected by the electrostatic confinement that is imposed by the $LuFe_2O_4$ layer.

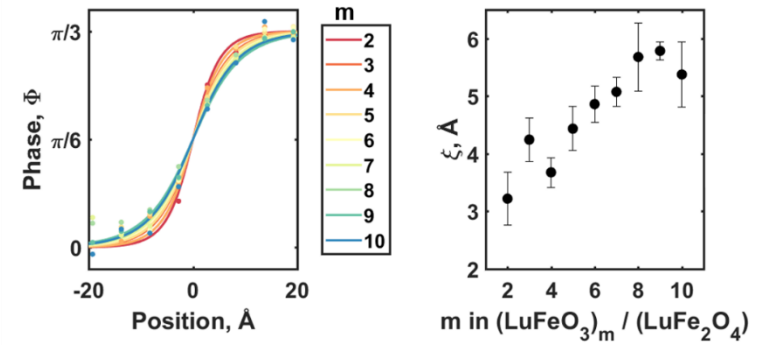

Figure 7.10. The order parameter Φ in the $LuFeO_3$ blocks as a function of thickness, *m*. (left) how the phase evolves as a function of distance from the center of the domain for the charged domain walls in the blocks. (right) the width of the domain walls is thinner in the smaller layers.

7.4 Imaging After Biasing in the PFM

To better understand how these domain walls move when biased, an *ex situ* TEM experiment was performed. In this work, the material was biased in a grid configuration like shown in Figure 7.11 by applying a voltage with a PFM tip, and a TEM specimen prepared by focused ion beam on the region specified.

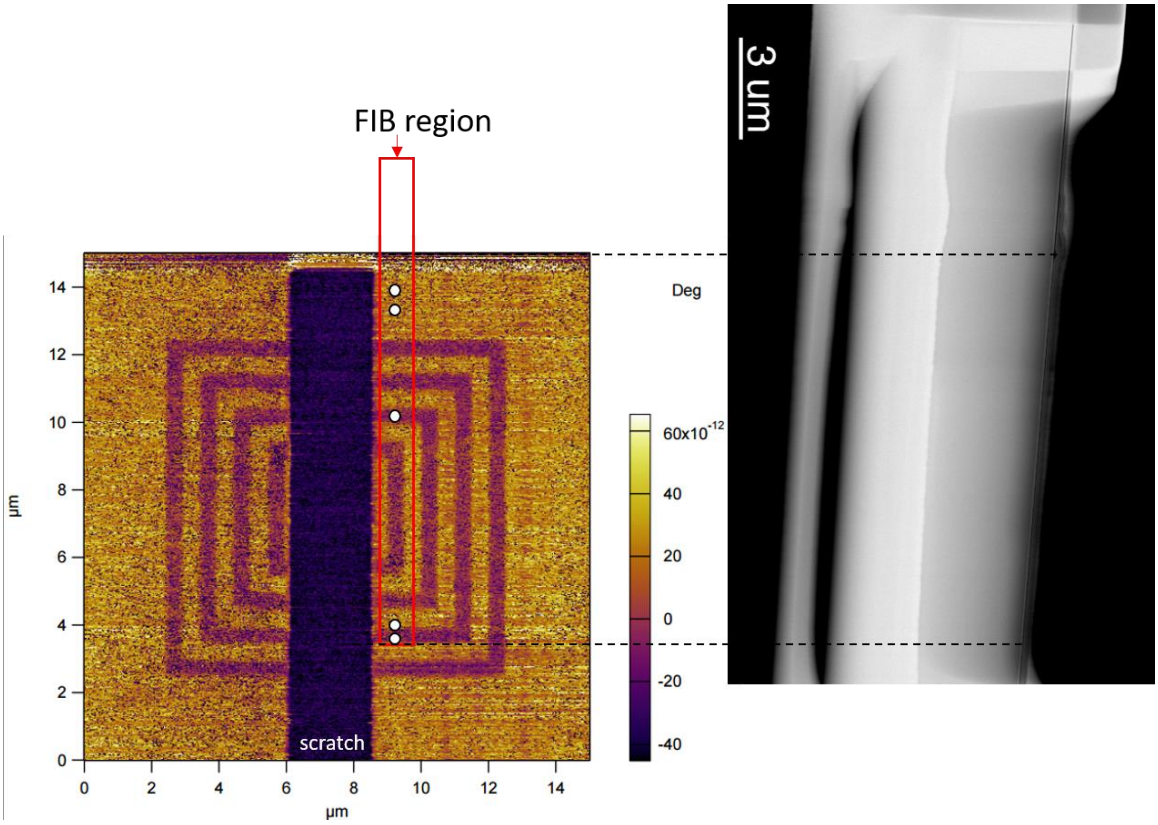

Figure 7.11. PFM image with a scratch showing the biased regions. Yellow is biased up and purple was biased down. The region prepared by FIB is marked in red, with white dots corresponding to locations imaged in the STEM. STEM image of the FIB specimen is shown on the right. Because the PFM tip pushed some debris to the edge of the biased region, we could use the resulting debris in the image to calibrate the location in the sample. PFM done by James Clarkson, R. Ramesh.

Images from the biased regions along with histograms representing the statistics are shown in Figure 7.12. In regions which were biased in the positive direction, we observed an increase of upward polarization domains in the two $LuFeO_3$ blocks which were closest to the surface of the film. Two layers below the top surface, the unbiased domain structure was observed. In the negatively poled directions of the film, we observed no change in structure. This is shown in the plots of average displacement vs the number of superlattice repeats from the surface of the film in

Figure 7.12d: at the surface, the film appears to be biased up for the poled-up film, while for the repeat layers closest to the substrate, no clear effects are observed.

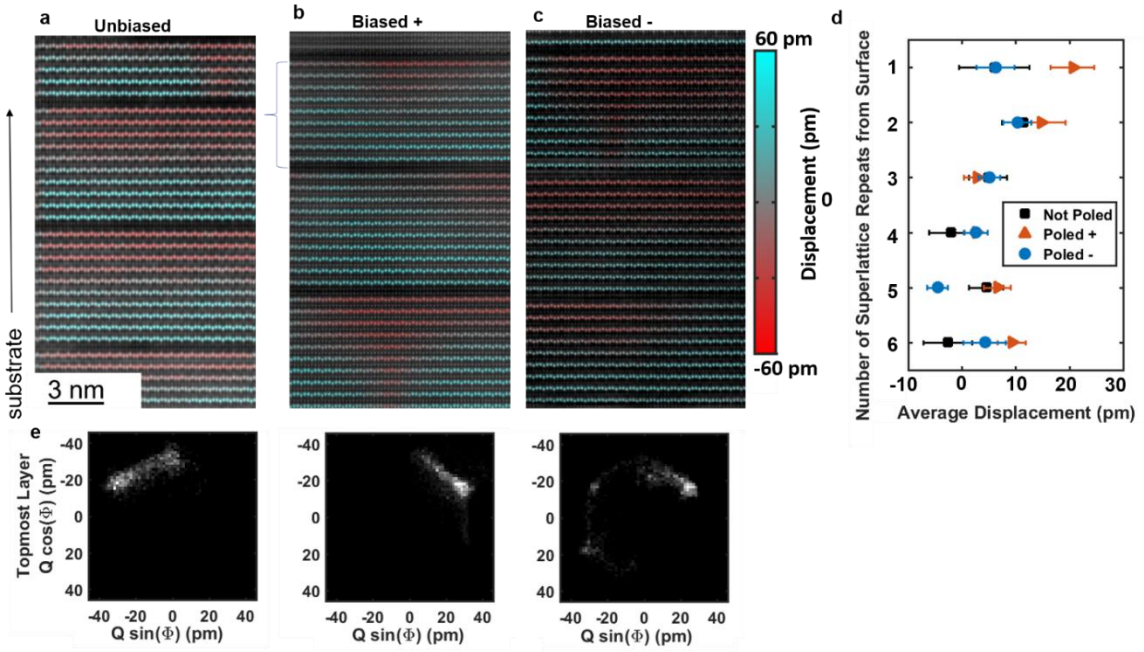

Figure 7.12. STEM data from the PFM biasing experiment, showing polarization displacement overlays for the unbiased **a**, positively biased **b** and negatively biased **c** samples. **d** Statistics over several images show that the top superlattice layer of $LuFeO_3$ in the positively biased sample (highlighted by a bracket) show a majority of polarization up atomic columns. No effect is observed for sub-surface $LuFeO_3$ blocks in the positively biased regions or any $LuFeO_3$ block in the negatively biased regions. **e** *Q*-*Φ* histograms are shown for the topmost layer of each region.

To explore the effect of the order parameter on the biased surface, we look at the histogram of *Q* and *Φ* for the uppermost layer of the film in Figure 7.12e. For the unbiased sample, we observe equal populations of a polarized up and down domain. For the positively biased sample, the surface has a large amount of a positively biased domain, but contains remnants which are not completely switched. The biased down sample shows no clear pattern.

While we cannot rule out effects of the FIB on the biased domain structure during lift out – because 30 kV Ga ions are impinging the surface and generating secondary electrons, all which may apply a field that could counteract the domain structure written by PFM – we do see evidence for domain structure change after biasing in the PFM. The head-to-head wall in the top two layers of the biased region appeared to move toward the surface of the film, leaving the structure polarized more in the positive direction than in the negative direction. The switching appears to be happening by moving the head-to-head domain walls up and down in the film – not by switching all at once. We additionally see that the polarization is suppressed near the $LuFe_2O_4$ layer where the head to head domain wall and tail to tail domain wall are not completely annihilated.

7.5 Conclusions

Atomic scale images of hexagonal improper ferroelectrics and the measurement of local polarization and order parameter has helped push the development of novel multiferroic superlattices based on the $(LuFeO_3)_m$ / $LuFe_2O_4$ system. We found the superlattices of the ferrimagnetic $LuFe_2O_4$, and ferroelectric $LuFeO_3$ showed enhanced magnetic and ferroelectric properties surpassing either end-member, which displayed magnetoelectric coupling at room temperature. STEM and DFT together teased apart the interplay between ferroelectricity and magnetism. From a fundamental physics perspective, these superlattices are also interesting due to their confinement of ferroelectric layers into thin blocks. We found that as the block size is decreases, the ferroelectric transition temperature is decreased and the disorder in the domain structure is increased. As domains shrink and domain walls comprise more of the sample, the material becomes more paraelectric and exhibits U(1) symmetry, and we find evidence that the confinement of the domain shrinks the domain wall width slightly.

References

[1] W. Eerenstein, N. D. Mathur, and J. F. Scott, Nature **442**, 759 (2006).

[2] O. Auciello, J. F. Scott, and R. Ramesh, Phys. Today **51**, 22 (1998).

[3] D. A. Allwood, G. Xiong, C. C. Faulkner, D. Atkinson, D. Petit, and R. P. Cowburn, Science **309**, 1688 (2005).

[4] S. S. P. Parkin, M. Hayashi, and L. Thomas, Science **320**, 190 (2008).

[5] J. Seidel, L. W. Martin, Q. He, Q. Zhan, Y. H. Chu, A. Rother, M. E. Hawkridge, P. Maksymovych, P. Yu, M. Gajek, N. Balke, S. V Kalinin, S. Gemming, F. Wang, G. Catalan, J. F. Scott, N. A. Spaldin, J. Orenstein, and R. Ramesh, Nat. Mater. **8**, 229 (2009).

[6] R. Xu, J. Karthik, A. R. Damodaran, and L. W. Martin, Nat. Commun. **5**, 3120 (2014).

[7] G. Catalan, J. Seidel, R. Ramesh, and J. F. Scott, Rev. Mod. Phys. **84**, 119 (2012).

[8] S. Farokhipoor, C. Magén, S. Venkatesan, J. Íñiguez, C. J. M. Daumont, D. Rubí, E. Snoeck, M. Mostovoy, C. De Graaf, and A. Müller, Nature **515**, 379 (2014).

[9] Y. L. Tang, Y. L. Zhu, X. L. Ma, A. Y. Borisevich, A. N. Morozovska, E. A. Eliseev, W. Y. Wang, Y. J. Wang, Y. B. Xu, and Z. D. Zhang, Science **348**, 547 (2015).

[10] H. Das, A. L. Wysocki, Y. Geng, W. Wu, and C. J. Fennie, Nat. Commun. **5**, 2998 (2014).

[11] N. Ikeda, H. Ohsumi, K. Ohwada, K. Ishii, T. Inami, K. Kakurai, Y. Murakami, K. Yoshii, S. Mori, Y. Horibe, and H. Kito, Nature **436**, 1136 (2005).

[12] A. D. Christianson, M. D. Lumsden, M. Angst, Z. Yamani, W. Tian, R. Jin, E. A. Payzant, S. E. Nagler, B. C. Sales, and D. Mandrus, Phys. Rev. Lett. **100**, 107601 (2008).

[13] T. Choi, Y. Horibe, H. T. Yi, Y. J. Choi, W. Wu, and S.-W. Cheong, Nat. Mater. **9**, 253 (2010).

[14] C.-L. Jia, S.-B. Mi, K. Urban, I. Vrejoiu, M. Alexe, and D. Hesse, Nat. Mater. **7**, 57 (2008).

[15] J. A. Mundy, J. Schaab, Y. Kumagai, A. Cano, M. Stengel, I. P. Krug, D. M. Gottlob, H. Doğanay, M. E. Holtz, R. Held, Z. Yan, E. Bourret, C. M. Schneider, D. G. Schlom, D. A. Muller, R. Ramesh, N. A. Spaldin, and D. Meier, Nat. Mater. (2017).

[16] S. S. P. Parkin, M. Hayashi, and L. Thomas, Science **320**, 190 (2008).

[17] M. Gajek, M. Bibes, S. Fusil, K. Bouzehouane, J. Fontcuberta, A. Barthélémy, and A. Fert, Nat. Mater. **6**, 296 (2007).

[18] E. Ascher, H. Rieder, H. Schmid, and H. Stössel, J. Appl. Phys. **37**, 1404 (1966).

[19] T. Kimura, T. Goto, H. Shintani, K. Ishizaka, T. Arima, and Y. Tokura, Nature **426**, 55

(2003).

[20] J. Wang, J. B. Neaton, H. Zheng, V. Nagarajan, S. B. Ogale, B. Liu, D. Viehland, V. Vaithyanathan, D. G. Schlom, U. V Waghmare, N. A. Spaldin, K. M. Rabe, M. Wuttig, and R. Ramesh, Science **299**, 1719 (2003).

[21] J. H. Lee, L. Fang, E. Vlahos, X. Ke, Y. W. Jung, L. F. Kourkoutis, J.-W. Kim, P. J. Ryan, T. Heeg, M. Roeckerath, V. Goian, M. Bernhagen, R. Uecker, P. C. Hammel, K. M. Rabe, S. Kamba, J. Schubert, J. W. Freeland, D. A. Muller, C. J. Fennie, P. Schiffer, V. Gopalan, E. Johnston-Halperin, and D. G. Schlom, Nature **466**, 954 (2010).

[22] D. Niermann, F. Waschkowski, J. De Groot, M. Angst, and J. Hemberger, Phys. Rev. Lett. **109**, 24 (2012).

[23] S. Lafuerza, J. García, G. Subías, J. Blasco, K. Conder, and E. Pomjakushina, Phys. Rev. B - Condens. Matter Mater. Phys. **88**, 1 (2013).

[24] A. A. Bossak, I. E. Graboy, O. Y. Gorbenko, A. R. Kaul, M. S. Kartavtseva, V. L. Svetchnikov, and H. W. Zandbergen, Chem. Mater. **16**, 1751 (2004).

[25] E. Magome, C. Moriyoshi, Y. Kuroiwa, A. Masuno, and H. Inoue, Jpn. J. Appl. Phys. **49**, 09ME06 (2010).

[26] W. Wang, J. Zhao, W. Wang, Z. Gai, N. Balke, M. Chi, H. N. Lee, W. Tian, L. Zhu, X. Cheng, D. J. Keavney, J. Yi, T. Z. Ward, P. C. Snijders, H. M. Christen, W. Wu, J. Shen, and X. Xu, Phys. Rev. Lett. **110**, 1 (2013).

[27] S. M. Disseler, J. A. Borchers, C. M. Brooks, J. A. Mundy, J. A. Moyer, D. A. Hillsberry, E. L. Thies, D. A. Tenne, J. Heron, M. E. Holtz, J. D. Clarkson, G. M. Stiehl, P. Schiffer, D. A. Muller, D. G. Schlom, and W. D. Ratcliff, Phys. Rev. Lett. **114**, (2015).

[28] V. V Roddatis, A. R. Akbashev, S. Lopatin, and A. R. Kaul, Appl. Phys. Lett. **103**, 112907 (2013).

[29] Q. Zhang, G. Tan, L. Gu, Y. Yao, C. Jin, Y. Wang, X. Duan, and R. Yu, Sci. Rep. **3**, 2741 (2013).

[30] J. A. Mundy, Q. Mao, C. M. Brooks, D. G. Schlom, and D. A. Muller, Appl. Phys. Lett. **101**, 42907 (2012).

[31] C. M. Brooks, R. Misra, J. A. Mundy, L. A. Zhang, B. S. Holinsworth, K. R. O'Neal, T. Heeg, W. Zander, J. Schubert, and J. L. Musfeldt, Appl. Phys. Lett. **101**, 132907 (2012).

[32] J. Iida, M. Tanaka, and S. Funahashi, J. Magn. Magn. Mater. **104**, 827 (1992).

[33] M. Sankararaman and D. Perry, J. Mater. Sci. **27**, 2731 (1992).

[34] S.-Z. Lin, X. Wang, Y. Kamiya, G.-W. Chern, F. Fan, D. Fan, B. Casas, Y. Liu, V. Kiryukhin, W. H. Zurek, C. D. Batista, and S.-W. Cheong, Nat. Phys. **10**, 970 (2014).

[35] J. A. Mundy, C. M. Brooks, M. E. Holtz, J. A. Moyer, H. Das, A. F. Rébola, J. T. Heron, J. D. Clarkson, S. M. Disseler, Z. Liu, A. Farhan, R. Held, R. Hovden, E. Padgett, Q. Mao, H.

Paik, R. Misra, L. F. Kourkoutis, E. Arenholz, A. Scholl, J. A. Borchers, W. D. Ratcliff, R. Ramesh, C. J. Fennie, P. Schiffer, D. A. Muller, and D. G. Schlom, Nature **537**, 523 (2016).

CHAPTER 8

INTERFACE SPECTRA OF PHONONS BY EELS

8.1 Introduction

The plasmon, which is a long-range collective excitation of electrons in response to an external stimulus, has long been studied by fast electrons, which have enough energy to excite these collective modes (10-30 eV) and high enough energy resolution to study them (0.3 eV) [1–3]. Phonons, which are also collective excitations of the material in the form of vibrational modes of the atoms in a periodic structure, are typically in the 10-100 meV and have previously been inaccessible from fast electron beams with typical energy resolutions due to the overwhelming width of the unscattered beam (or zero-loss peak). The advent of new monochromators that offer 10 meV energy resolution with Ångstrom spatial resolution opens new doors for opportunities in studying phonons with nanometer precision [4–6]. However, due to the long-range collective behavior of phonons, like plasmons, may display interface or surface effects that can significantly alter the bulk-like signal. Here we investigate the semi-classical expectations of these phonons for thin-film specimens through the dielectric formalism, similar to the work done previously for plasmons [7–10], and perform full relativistic simulations to investigate the spatial dependence of the interface modes, using code developed by M. Couillard [11,12] based on the theory by Bolton and Chen [13,14]. We find that the interface modes play a significant role in phonon scattering, as they do for plasmon scattering. They fall off exponentially with distance from the interface and are dependent on a combination of the dielectric functions in the specimen.

An overview of phonon scattering is shown in Figure 8.1. There are a few classifications of phonons: there are longitudinal and transverse phonons, and acoustic and optical phonons [15,16].

Longitudinal phonons have their phonon displacements in the direction of phonon propagation, and are similar to a compressional wave. Transverse phonons have their atomic displacements perpendicular to phonon propagation (as shown in Figure 8.1). In unit cells with more than one atom, higher modes of phonon oscillation are possible. For acoustic phonons, the atomic displacements all propagate in phase, and for optic phonons the atomic displacements are out-of-phase. In a diatomic molecule with positively and negatively charged ions, the vibration of an optical phonon is a radiating dipole, and can couple easily with electromagnetic radiation. We thus expect the scattering cross section of optical phonons to be much larger than acoustic phonons for light and electron scattering.

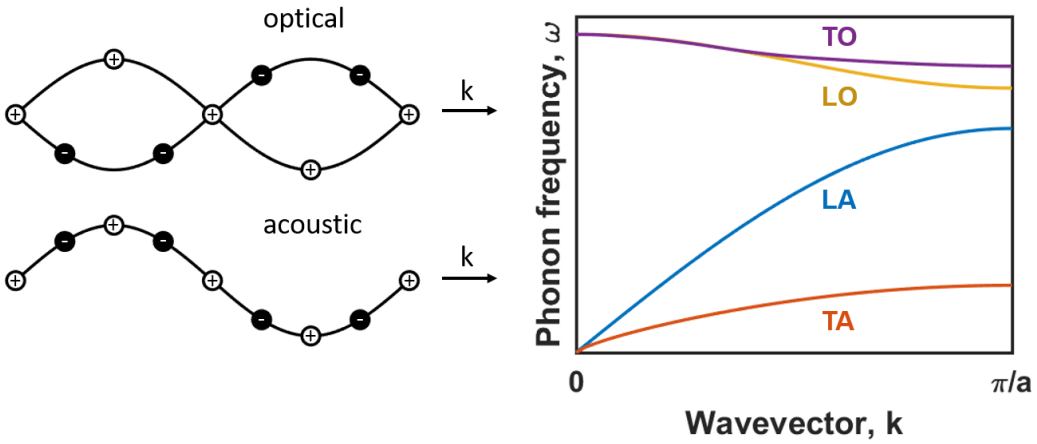

Figure 8.1. Overview of phonons. Left: cartoons of transverse optical and acoustic phonons in a diatomic lattice. When the atoms are oppositely charged, the optical phonon creates oscillating dipoles, which are easily excited by electromagnetic radiation. Right: cartoon of dispersion in the [111] direction of Ge. The longitudinal and transverse acoustic phonons (LA and TA) are at lower frequency and have $\omega \sim k$ at long wavelengths. The longitudinal and transvers optical branches (LO and TO) are at higher frequencies and have finite frequency as $k \rightarrow 0$. Due to the high symmetry of Ge, the TO and LO branches overlap as $k \rightarrow 0$. Cartoons inspired by Kittel [16].

As we can see from Figure 8.1, the energy of the acoustic branches of phonons is lower than that of the optical phonons, and as $k \rightarrow 0$ ($\lambda \rightarrow \infty$) the energy goes to 0 as the vibrations completely disappear. For optical phonons, there is still a non-zero vibrational frequency even as $k \rightarrow 0$ ($\lambda \rightarrow \infty$). This implies that for scattering from optical phonons, the signal may be fairly delocalized.

A cartoon of the scattering geometry for EELS is shown in Figure 8.2. For an incident beam with wavevector k_i and a scattered beam with a wavevector k_f, we have a scattered vector $\vec{k} = \overrightarrow{k_f} - \overrightarrow{k_i}$. For convenience, we will break the scattering vector into two components, one parallel to the incident beam (in the *z*-direction, k_z) and one perpendicular to the beam (k_y). The z component, k_z, goes as ω/v or $k\Delta E/E$, where ω is the frequency of phonon oscillation, and $\Delta E = \hbar\omega$, and v and E are the velocity and energy of the incident beam. Because the energy of the electron beam is so large compared to the energy of phonon excitation (10^5 eV vs 10^{-1}eV), k_z is quite small and the bulk of the scattering vector lies in the specimen plane. Because the atomic displacements u will be excited as a $\vec{k} \cdot \vec{u}$ term, this geometry favors longitudinal phonon scattering in the plane of the specimen [17].

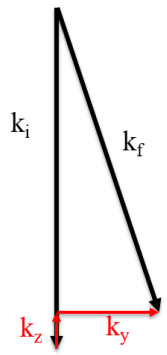

Figure 8.2. Scattering geometry for EELS. The incident beam has wavevector k_i and propagates in the *z*-direction. After scattering with the specimen, the final wavevector is k_f, with a scattering vector k. The z component, k_z, is quite small for phonon scattering of high energy electrons.

While EELS excites the longitudinal dielectric function, and can be measured with wavevector dependence, optical scattering excites the transverse dielectric function and is reported as $\varepsilon(\omega)$. While the longitudinal and transverse dielectric functions are not generally equal, they are the same within the random phase approximation for an isotropic solid, which is also true in the $k \rightarrow 0$ limit (dipole region) [3,18].

What is the angular dependence of scattering by phonons? Peter Rez has shown that they are strongly peaked about the Bragg beams, with long, non-zero, tails in between [19]. Thus, if the detector is on axis (or on a Bragg beam), the small k or dipole approximation may be a good one since the scattering is dominated by $k = 0$. The root-mean-square, mean, and median scattering angles, given in Section 3.3.1.5 of Egerton [18], can also provide a sanity check. The equations are general for a Lorentzian angular distribution (which we will see in the next section holds true) with a cutoff angle θ_C. For electronic excitations, the cutoff angle is the Bethe ridge angle ($\theta_R \approx \sqrt{E/E_0}$), where E_0 is the incident beam energy and E is the energy-loss. For plasmons, the cutoff angle is estimated by the angle at which the plasmon decays into single particle transitions, $\theta_C \approx \frac{1}{k_i} \cdot \frac{\omega_p}{v_F}$ where ω_p is the plasmon energy and v_F is the Fermi velocity. In the case of phonons, there is no obvious intrinsic cutoff vector, and the hard cutoff angle is the spectrometer entrance aperture [20]. The median scattering angle is:

$$\tilde{\theta} = \theta_E \sqrt{\frac{\theta_c}{\theta_E} - 1} \approx \sqrt{\theta_E \theta_C} \quad \text{where} \quad \theta_E = E/(\gamma m_0 c^2) \approx E/(2E_0) \qquad \text{Eq. 1}$$

At 60 keV and 100 meV energy loss, for collection angles of β = 10, 30 and 60 mrad, the median angle is 3, 5, and 7 mrad, respectively. The root-mean-squared values are quite similar. The scattering is indeed strongly peaked at small k. Unlike plasmon scattering, which dominates at large scattering vectors compared to the collection angle, the angles for phonon scattering are less than the collection angle. The integration over the collection angle does not satisfy $\beta < \theta_c$ (as it does for

plasmons) and the scattering is not uniform over *k* inside the collection aperture. However, because the signal attenuates rapidly from the center beam, the central component will dominate and integration over smaller angles (than the collection angle) may not be too bad of an approximation. For off axis detectors, which have shown localized phonon signal [5], *k* dependence must be taken into account.

The long-range nature of electrostatic forces imposes a basic limit on spatial resolution of signals measured by inelastic scattering, especially at low energies. Estimations of delocalization often refer to Bohr's adiabatic criterion, which gives an upper limit on the impact parameter for efficient energy transfer. This can be used to calculate the impact parameter for localized scattering as $b_{\max} = v/\omega$. This marks the crossover between near field and far field couplings of the probe with the sample. One way to think of this scattering parameter is in terms of a screening length [21]. The time that the electron spends in the "proximity" of the sample can be written as b/v. If this is short compared to the oscillation period $1/(2\pi\omega)$ of the specimen, the electron "sees" a stationary electron and "feels" the Rutherford scattering cross section of the specimen and is scattered. However, if the time the electron goes by the sample, b/v, is longer than the oscillation period $1/(2\pi\omega)$ of the specimen, the charge will be screened and there will be very little energy exchanged. Therefore, to have localized scattering, $b<v/\omega$. This unfortunately predicts very large delocalization for phonon energy loss, see Figure 8.3.

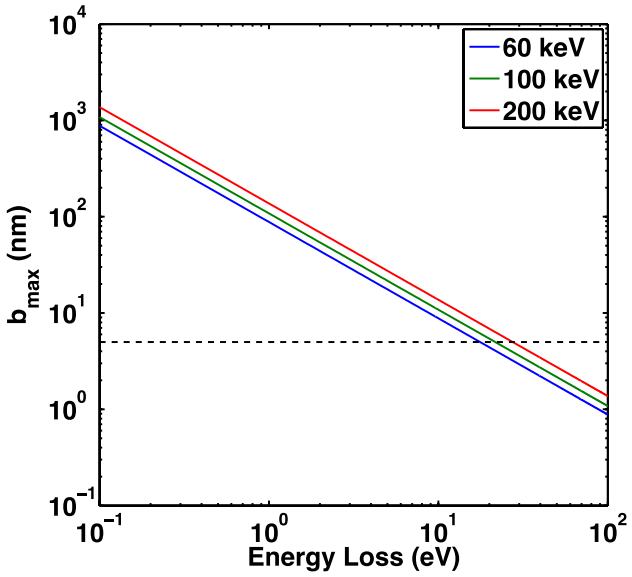

Figure 8.3. Delocalization length estimated by Bohr's adiabatic criterion of a fast electron beam for different energy loss. Dashed line is a 5 nm delocalization length.

8.2 Interface Modes in Thin Film Specimens

For a scattering geometry of an electron beam hitting a thin film specimen of thickness a, we have a geometry taken to be like that in Figure 8.4. Region A has dielectric constant ε_A which is shorthand for $\varepsilon_A(\omega)$, and the equivalent is true for Regions B and C. While the fully correct solution considers that the specimen is thin in the direction of electron beam propagation (z-direction), because surface modes may be present, to keep things manageable we only consider scattering from the interfaces which are present in the x-direction.

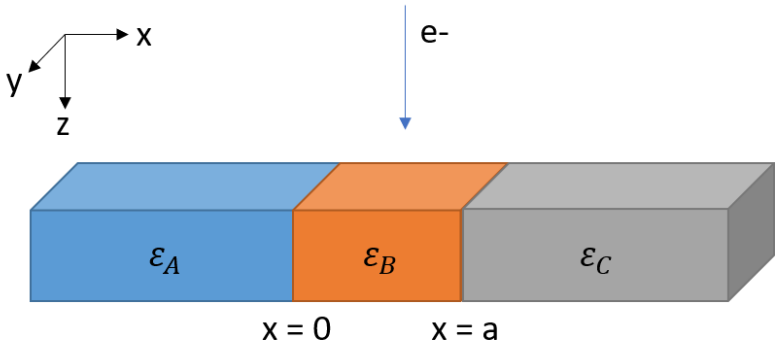

Figure 8.4. Geometry of the setup for the calculation, where there are three regions of specimen, A, B, and C. This geometry reflects a simplification of a thin film specimen, where region A is the substrate, B is a thin film of thickness *a*, and region C is the vacuum or amorphous carbon deposited on top of the sample. Both regions A and C are assumed to go out to infinity on either side in the *x* direction, and the sample is assumed to be uniform (extending to infinity) in the *y* direction.

8.2.1 Solutions to Poisson's Equation

We can calculate the response of the system to an electron beam by solving Poisson's equation:

$$-\varepsilon(\omega, \vec{q})\nabla^2\phi = 4\pi\rho(\vec{r}) \qquad \text{Eq. 2}$$

Where ε is the dielectric function dependent on the frequency ω and scattering vector q, ϕ is the electric potential, and ρ is the spatial dependence of the external charge with position $\vec{r} = x\hat{x} + y\hat{y} + z\hat{z}$. Assuming a semiclassical model of the fast electron travelling in the z direction with velocity v, we can write

$$\rho(\vec{r}) = -e\delta(x - x_0)\delta(y - y_0)\delta(z - vt) \qquad \text{Eq. 3}$$

for a given time t with a beam position of x_0 and y_0.

First, it is helpful to Fourier Transform (FT) Poisson's Equation in the *y* and *z* directions and in time, but leaving our function spatially dependent in the *x* direction. Taking the FT of Eq. 3:

$$\rho(x, k_x, k_y, \omega) = \int dy \int dz \int dt \exp(-i(k_y y + k_z z + \omega t))\rho(\vec{r})$$

$$\rho(x, k_x, k_y, \omega) = -\mathrm{e}\,\delta(\mathrm{x} - \mathrm{x}_0)\,\delta(\omega - \mathrm{k_z v}) \qquad \text{Eq. 4}$$

Combining this with Eq. 2, we have

$$-\varepsilon(\omega)\left(\frac{\partial^2}{\partial x^2} - k^2\right)\phi = -4\pi e\,\delta(x - x_0)\,\delta(\omega - k_z v) \qquad \text{Eq. 5}$$

Where now we have written $k^2 = k_y^2 + k_z^2$.

Outside the region of the beam, we are reduced to the homogeneous equation:

$$\frac{\partial^2}{\partial x^2}\phi = k^2\phi \qquad \text{Eq. 6}$$

Which results in solutions of the form

$$\phi \sim \exp(\pm kx) \qquad \text{Eq. 7}$$

Now we turn our attention to the inhomogeneous equation. To solve this problem, we finally perform the FT in the *x* direction. To simplify, we define $\alpha = 4\pi e\,\delta(\omega - k_z v)/\varepsilon_i$ and we have denoted $\varepsilon = \varepsilon_i$ since we are now only considering the region where the beam is, i.e. region *i*, where $x = x_0$. The FT in *x* yields:

$$\phi = \frac{-\alpha \exp(-ik_x x_0)}{k_x^2 + k^2} \qquad \text{Eq. 8}$$

We need to inverse FT this to retrieve ϕ (*x*). As factoring the denominator reveals, there are two poles.

$$\phi(x) = \int \frac{-\alpha \exp(ik_x(x-x_0))}{(k_x+ik)(k_x-ik)} dk_x \quad \text{Eq. 9}$$

For $x < x_0$, we consider the pole at $k_x = -ik$, and for $x > x_0$, we consider the pole at $k_x = ik$. This yields the solutions:

$$\phi(x) = \frac{4\pi^2 e}{k\varepsilon_i} \delta(\omega - k_z v) \begin{cases} \exp(-k(x-x_0)) & \text{for } x > x_0 \\ \exp(k(x-x_0)) & \text{for } x < x_0 \end{cases} \quad \text{Eq. 10}$$

Combining the homogeneous and inhomogeneous equations, we can write this as

$$\phi_N = \frac{\lambda}{\varepsilon_N} \exp(-k|x-x_0|) + N_1 \exp(kx) + N_2 \exp(-kx) \quad \text{Eq. 11}$$

Where

$$\lambda = \frac{4\pi e}{k} \delta(\omega - k_z v) \quad \text{Eq. 12}$$

And N_1 and N_2 are constants to be found from boundary conditions which are dependent on the specimen dielectric functions, beam position $\exp(\pm kx_0)$, and specimen geometry (ie, a).

In the setup described above, with three slabs, this boils down to:

$$\phi_A = \frac{\lambda}{\varepsilon_A} \exp(-k|x-x_0|) + A \exp(kx) \quad \text{Eq. 13}$$

$$\phi_B = \frac{\lambda}{\varepsilon_B} \exp(-k|x-x_0|) + B_1 \exp(kx) + B_2 \exp(-kx) \quad \text{Eq. 14}$$

$$\phi_C = \frac{\lambda}{\varepsilon_C} \exp(-k|x-x_0|) + C \exp(-kx) \quad \text{Eq. 15}$$

Where we have already thrown away two of the terms to account for the boundary condition that ϕ must be finite as $|x| \to \infty$. We will save solving the boundary conditions for specific beam positions until Section 8.8.3.

8.2.2 Energy Loss Function

The energy lost per unit path in a medium can be written as

$$-\frac{dW}{dz} = e\, E_z|_{z=vt} \qquad \text{Eq. 16}$$

And

$$E_z = -\frac{\partial}{\partial z}\phi(\vec{r},t) \qquad \text{Eq. 17}$$

Taking the inverse FT, we can write

$$\phi(\vec{r},t) = \frac{1}{(2\pi)^3}\int dk_y \int dk_z \int d\omega\, exp(i(k_y y + k_z z - \omega t))\, \phi(x,k,\omega) \qquad \text{Eq. 18}$$

Now we can plug back in to the Eq. 16 and 17. First taking the *z* derivative, we get

$$\frac{dW}{dz} = \frac{-e}{(2\pi)^3}\int dk_y \int dk_z \int d\omega\, ik_z exp(i(k_y y + k_z z - \omega t))\, \phi(x,k,\omega) \qquad \text{Eq. 19}$$

This must be evaluated at the position and speed of the electron beam, so rewriting ϕ:

$$\phi_N = \frac{1}{\varepsilon_N}\frac{4\pi e}{k} + N_1 \exp(kx_0) + N_2 \exp(-kx_0) \qquad \text{Eq. 20}$$

then using $k_z = \omega/v$ and $z = vt$ because we must evaluate this at the beam position, arbitrarily picking y=0, we can write

$$\frac{dW}{dz} = \frac{-e}{(2\pi)^3 v}\int dk_y \int d\omega\, ik_z \left[\frac{1}{\varepsilon_N}\frac{4\pi e}{k} + N_1 \exp(kx_0) + N_2 \exp(-kx_0)\right] \qquad \text{Eq. 21}$$

Rewriting to look more like Ritchie's result, and because the energy loss is a real quantity,

$$\frac{dW}{dz} = \frac{-\hbar^2}{(2\pi)^3 a_0 m_e v^2} \int dk_y \int d\omega$$

$$\times \omega k_z \frac{1}{k_y^2+\omega^2/v^2} \mathrm{Im}\left[\frac{1}{\varepsilon_N} + \frac{N_1 k}{4\pi e}\exp(kx_0) + \frac{N_2 k}{4\pi e}\exp(-kx_0)\right] \quad \text{Eq. 22}$$

We can write the energy loss probability per unit path length as $P = \frac{1}{\hbar\omega}\frac{dW}{dz}$. Also taking this to be a differential in terms of momentum and energy,

$$\frac{\partial^2 P}{\partial k_y \partial \hbar\omega} = \frac{e}{(2\pi)^3 \hbar^2 v^2 k} Im\left[\frac{1}{\varepsilon_N}\frac{4\pi e}{k} + N_1 \exp(kx_0) + N_2 \exp(-kx_0)\right] \quad \text{Eq. 23}$$

8.2.3 Solutions with Boundary Conditions

Now it is time to pick a beam position and solve the boundary conditions. The above equation (Eq. 23) is the general case: if the beam is in the slab with ε_A, then $N_1 = A$ and $N_2 = 0$. If the beam is in the slab with ε_B, then $N_1 = B_1$ and $N_2 = B_2$. Finally, if the beam is in the slab with ε_C, then $N_1 = 0$ and $N_2 = C$.

At the interface between regions A and B (which will also hold for regions B and C)

$$\phi_A(x_{interface}) = \phi_B(x_{interface}) \quad \text{Eq. 24}$$

And

$$\hat{n} \cdot (\varepsilon_A \nabla\phi_A - \varepsilon_B \nabla\phi_B) = \sigma \quad \text{Eq. 25}$$

Where $\hat{n}$ is the unit normal vector to the interface and σ is the bound charge at the interface. In this case, we have no bound charge and the relevant direction is the x direction:

$$\varepsilon_A \frac{\partial}{\partial \mathrm{x}}\phi_A = \varepsilon_B \frac{\partial}{\partial \mathrm{x}}\phi_B \quad \text{Eq. 26}$$

Evaluated at $x = x_{\text{interface}}$.

First, we will consider the case of the beam in Region A, with $\varepsilon = \varepsilon_A$, or the beam in the substrate (ie, $x_0<0$). For the solution of the boundary equations, Mathematica was used. In Region A, we find:

$$\frac{\partial^2 P}{\partial k_y \partial \hbar\omega} = \frac{e^2}{2\pi^2\hbar^2 v^2 k^2} Im\left[\frac{1}{\varepsilon_A}\left(1 + \frac{(\varepsilon_A+\varepsilon_B)(\varepsilon_B-\varepsilon_C)e^{-ka}+(\varepsilon_A-\varepsilon_B)(\varepsilon_B+\varepsilon_C)e^{ka}}{(\varepsilon_A+\varepsilon_B)(\varepsilon_B+\varepsilon_C)e^{ka}+(\varepsilon_A-\varepsilon_B)(\varepsilon_B-\varepsilon_C)e^{-ka}}\exp(2kx_0)\right)\right]$$

Eq. 27

In addition to our bulk like transition, Im($1/\varepsilon_A$), we observe an interface term which decay exponentially with position away from the interface.

Now we will consider the case where the beam is in the thin film, Region B with ε_B (ie, $x_0>0$ and $x_0<a$). Now we have two homogeneous terms:

$$\frac{\partial^2 P}{\partial k_y \partial \hbar\omega} = \frac{e^2}{2\pi^2\hbar^2 v^2 k^2} Im\left[\frac{1}{\varepsilon_B}\left(1 + e^{k(x_0-a)}(\varepsilon_B - \varepsilon_C)\frac{[(\varepsilon_B-\varepsilon_C)e^{-kx_0}+(\varepsilon_A+\varepsilon_B)e^{kx_0}]}{(\varepsilon_A+\varepsilon_B)(\varepsilon_B+\varepsilon_C)e^{ka}+(\varepsilon_A-\varepsilon_B)(\varepsilon_B-\varepsilon_C)e^{-ka}} - \frac{e^{-kx_0}(\varepsilon_B-\varepsilon_A)[(\varepsilon_B+\varepsilon_C)e^{k(a-x_0)}+(\varepsilon_B-\varepsilon_C)e^{-k(a-x_0)}]}{(\varepsilon_A+\varepsilon_B)(\varepsilon_B+\varepsilon_C)e^{ka}+(\varepsilon_A-\varepsilon_B)(\varepsilon_B-\varepsilon_C)e^{-ka}}\right)\right]$$

Eq. 28

Finally, we will consider the case of the beam in ε_C, which could be thought of the aloof beam condition (ie, $x_0>a$).

$$\frac{\partial^2 P}{\partial k_y \partial \hbar\omega} = \frac{e^2}{2\pi^2\hbar^2 v^2 k^2} Im\left[\frac{1}{\varepsilon_C}\left(1 + \frac{(\varepsilon_A+\varepsilon_B)(\varepsilon_B-\varepsilon_C)e^{ka}+(\varepsilon_A-\varepsilon_B)(\varepsilon_B+\varepsilon_C)e^{-ka}}{(\varepsilon_A+\varepsilon_B)(\varepsilon_B+\varepsilon_C)e^{ka}+(\varepsilon_A-\varepsilon_B)(\varepsilon_B-\varepsilon_C)e^{-ka}}\exp(2k(a-x_0))\right)\right]$$

Eq. 29

The solutions for each region shows the bulk like transition, Im($1/\varepsilon$), with an added interfacial term that decays exponentially with position away from the interface. The interfacial components depend on the dielectric function of all three regions and the film thickness. This means that in the

aloof-beam configuration, the dielectric function both the substrate and the film will influence the spectra observed in vacuum. The exponential decay of the interface modes also depends on *k*. As *k* is increased, the interface component is decreased, which is what we expect for either increasing energy loss or by using large or off-axial collection angles. This also holds true in the simulations which are discussed in Section 8.3: opening the collection angle may suppress the interfacial modes – although further exploration of this would require us to re-examine our assumption of small scattering angles.

The values found for the constants for the solution of the boundary equations are:

Region A:

$$A = -\frac{1}{\varepsilon_A}\frac{4\pi e}{k}\exp(k(2a-x_0))\left[\frac{(\varepsilon_A+\varepsilon_B)(\varepsilon_B-\varepsilon_C)e^{-ka}+(\varepsilon_A-\varepsilon_B)(\varepsilon_B+\varepsilon_C)e^{ka}}{(\varepsilon_A+\varepsilon_B)(\varepsilon_B+\varepsilon_C)e^{ka}+(\varepsilon_A-\varepsilon_B)(\varepsilon_B-\varepsilon_C)e^{-ka}}\right] \quad \text{Eq. 30}$$

Region B:

$$B_1 = \frac{1}{\varepsilon_B}\frac{4\pi e}{k}\exp(-ka)\left[(\varepsilon_B-\varepsilon_C)\frac{(\varepsilon_B-\varepsilon_A)e^{-kx_0}+(\varepsilon_A+\varepsilon_B)e^{kx_0}}{(\varepsilon_A+\varepsilon_B)(\varepsilon_B+\varepsilon_C)e^{ka}+(\varepsilon_A-\varepsilon_B)(\varepsilon_B-\varepsilon_C)e^{-ka}}\right] \quad \text{Eq. 31}$$

$$B_2 = \frac{1}{\varepsilon_B}\frac{4\pi e}{k}\left[(\varepsilon_B-\varepsilon_A)\frac{(\varepsilon_B+\varepsilon_C)e^{k(a-x_0)}+(\varepsilon_B-\varepsilon_C)e^{-k(a-x_0)}}{(\varepsilon_A+\varepsilon_B)(\varepsilon_B+\varepsilon_C)e^{ka}+(\varepsilon_A-\varepsilon_B)(\varepsilon_B-\varepsilon_C)e^{-ka}}\right] \quad \text{Eq. 32}$$

Region C:

$$C = -\frac{1}{\varepsilon_C}\frac{4\pi e}{k}\exp(k(2a-x_0))\left[\frac{(\varepsilon_A+\varepsilon_B)(\varepsilon_B-\varepsilon_C)e^{ka}+(\varepsilon_A-\varepsilon_B)(\varepsilon_B+\varepsilon_C)e^{-ka}}{(\varepsilon_A+\varepsilon_B)(\varepsilon_B+\varepsilon_C)e^{ka}+(\varepsilon_A-\varepsilon_B)(\varepsilon_B-\varepsilon_C)e^{-ka}}\right] \quad \text{Eq. 33}$$

8.2.4 Small Angle Approximation

To simplify this equation further, we may look at the *ka* terms. For small values of *ka*, we can expand $e^{\pm ka} \approx 1 \pm ka$, where $k^2 = k_y^2 + k_z^2 = k_y^2 + \omega^2/v^2$. To determine if $ka \ll 1$ we will consider

the *z* and *y* components separately. For the *z* component, $k_z = K\frac{\Delta E}{E}$, is quite small for phonon losses that are typically around ΔE ~ 40-200 meV and beam energies $E \geq 60$ keV, where K is the wavevector of the initial beam. The condition that $k_z a \ll 1$ is typically met for phonon scattering in films less than 50 nm thick (e.g., for a 100 meV energy loss and 60 keV beam, $\omega a/v = 0.057$ for a 50 nm thick film). Thus we see that the majority of the scattered wavevector lies in the specimen plane, and the atomic displacements making up the phonon vibrations must also be in the plane – corresponding to longitudinal phonon modes. For a 10 mrad aperture with a median scattering angle of 3 mrad, with a 100 meV energy loss and 60 keV beam, $k_y = 4$ nm^{-1}. In that case, the criterion that $k_y a \ll 1$ is not typically true for even for quite thin films. Because typical phonon dispersions do not go to zero between Bragg beams, we must keep the full k_y term (although k_z may be dropped). However, in the dipole approximation, the optical phonons under the dipole approximation are strongly peaked at the Bragg beams and near $q = 0$, and so under this circumstance of an on-axis detector, or a detector centered at a Bragg beam, the low-angle scattering will be dominant and so we will take the $ka \ll 1$ approximation.

Region A:

$$\frac{\partial^2 P}{\partial k_y \partial \hbar\omega} = \frac{e^2}{2\pi^2\hbar^2 v^2 k^2} Im\left[\frac{1}{\varepsilon_A}\left(1 + \frac{\varepsilon_B(\varepsilon_A-\varepsilon_C)+ka(-\varepsilon_B^2+\varepsilon_A\varepsilon_C)}{\varepsilon_B(\varepsilon_A+\varepsilon_C)+ka(\varepsilon_B^2+\varepsilon_A\varepsilon_C)}\exp(2kx_0)\right)\right] \quad \text{Eq. 34}$$

In Region B, we can assume that kx_0 and $k(x_0\text{-}a)$ is small since the beam satisfies o $0 < x_0 < a$.

$$\frac{\partial^2 P}{\partial k_y \partial \hbar\omega} = \frac{e^2}{2\pi^2\hbar^2 v^2 k^2} Im\left[\frac{1}{\varepsilon_B}\left(1 + \frac{(\varepsilon_A-\varepsilon_C)(3\varepsilon_B-\varepsilon_C)}{2(\varepsilon_B(\varepsilon_A+\varepsilon_C)+ka(\varepsilon_B^2+\varepsilon_A\varepsilon_C))} + \right.\right.$$

$$\left.\left.\frac{ka[-\varepsilon_B(\varepsilon_A+2\varepsilon_B)+\varepsilon_C(3\varepsilon_A+\varepsilon_B-\varepsilon_C)]}{2(\varepsilon_B(\varepsilon_A+\varepsilon_C)+ka(\varepsilon_B^2+\varepsilon_A\varepsilon_C))} + \frac{2kx_0(\varepsilon_B^2-\varepsilon_A\varepsilon_C)}{(\varepsilon_B(\varepsilon_A+\varepsilon_C)+ka(\varepsilon_B^2+\varepsilon_A\varepsilon_C))}\right)\right] \quad \text{Eq. 35}$$

Region C:

$$\frac{\partial^2 P}{\partial k_y \partial \hbar\omega} = \frac{e^2}{2\pi^2\hbar^2 v^2 k^2} Im\left[\frac{1}{\varepsilon_C}\left(1 + \frac{\varepsilon_B(\varepsilon_A-\varepsilon_C)+ka(\varepsilon_B^2-\varepsilon_A\varepsilon_C+2\varepsilon_B(\varepsilon_A-\varepsilon_C))}{\varepsilon_B(\varepsilon_A+\varepsilon_C)+ka(\varepsilon_B^2+\varepsilon_A\varepsilon_C)}\exp(-2kx_0)\right)\right]$$

Eq. 36

8.3 Simulations of Interface Modes

In order to visualize the interfacial phonon modes which are predicted by the semiclassical model, we now use a relativistic model developed by Bolton and Chen in the dielectric formalism for a slab geometry (with an arbitrary number of slabs) for normal incidence [13] and parallel incidence [14], where the latter is the case for the geometry described in this Chapter (Figure 8.4). Numerical integration of the energy loss function to obtain the observed energy loss as a function $I(x_0, E)$ has been implemented in a MATLAB package by M. Couillard [11,12]. This approach is only valid at low momentum transfer (small k) and would require modification for off-axis or large collection angle detectors. The dielectric functions used in this calculation are of the form $\varepsilon(\omega)$ and are taken from optical data for Si and $SrTiO_3$ [22].

Figure 8.5 presents simulations done on a $SrTiO_3$ (STO) thin film with thickness a = 15 nm, with a silicon substrate ($x<0$) and vacuum extending to infinity ($x>a$) on either side. A beam energy of 60 keV and a collection angle of 10 mrad was used. Figure 8.5a shows the plot of the energy loss intensity as a function of position (x_0) and energy loss. There two strong phonon modes observed at 59 and 99 meV, which are the bulk STO spectra. There are additional interface modes present at both the Si/STO (e.g., 45 and 71 meV) and STO/vacuum (e.g., 83 meV) interfaces. Profiles of the interface and STO modes are shown in Figure 8.5b for different energies as a function of position across the film. All interface modes exponentially decay away from the interfaces, with decay lengths that are quite large in the vacuum. In Figure 8.5c, we show the EELS spectra for different positions in the STO film, as well as the bulk STO spectra. We observe strong interfacial peaks at both interfaces, with the bulk modes suppressed. The STO phonons are lower in intensity in the film than calculated for bulk, and have slight deviations in energy within the film

near the interface where the mode shifts a few meV. Because the interface modes are hybridization between the three different dielectric functions, the peaks in the film and in aloof mode may experience an energy shift. This highlights how the modes arising from the substrate, film, vacuum and their interfaces may be dominant contributors to EELS phonon spectra, particularly in the aloof beam condition where no bulk signal is present.

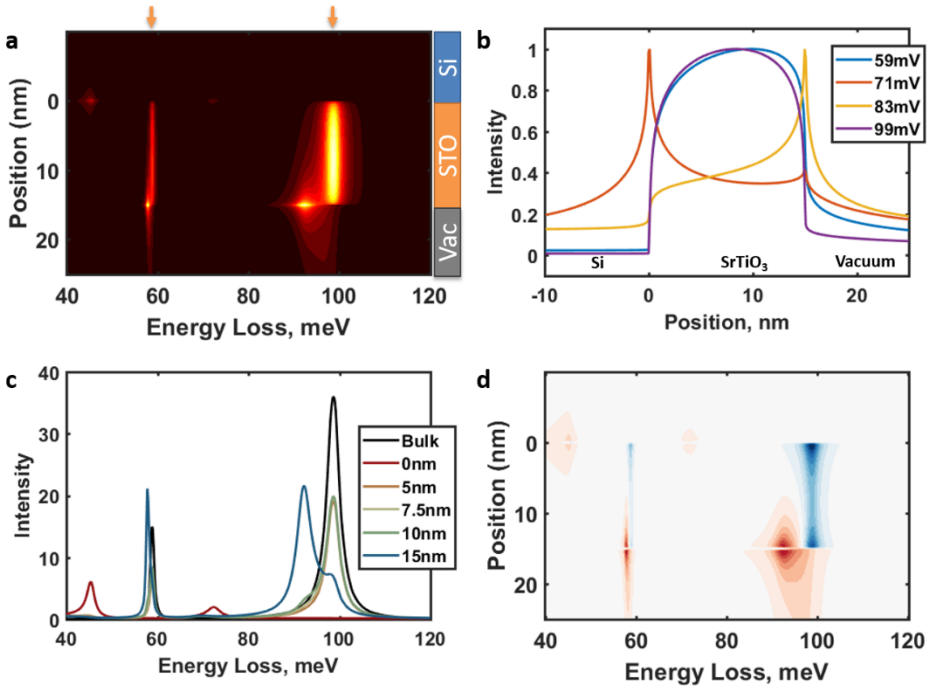

Figure 8.5. EELS spectra of phonon and interface modes in a Si/$SrTiO_3$/vacuum thin film specimen. In the $x<0$ region, there is Si, in the $0<x<15$ nm region, there is STO, and in the $x>15$ nm region there is vacuum. a) phonon modes for STO are present at 59 and 99 meV, and interface modes are shown at both interfaces which exponentially decay on either side. Orange arrows mark bulk STO modes. b) shows profile plots of the STO modes and interface modes at 71 and 83 meV. c) the EELS spectra as a function of position in the STO layer. d) the difference of scattering for a 10 mrad aperture and a 1 mrad collection aperture, with blue meaning relatively larger scattering for 10 mrad and red meaning relatively larger scattering for 1 mrad. The interface modes are less significant at larger collection angles.

Figure 8.5d shows the difference map of the energy loss intensity as a function of position and energy loss for two collection angles, i.e., $I(\beta = 10$ mrad) - $I(\beta = 1$ mrad). Blue represents a larger signal (more intensity for larger collection angle), and red represents a smaller signal (more intensity for smaller collection angle), while white is no change. We can see that at larger collection angles the interface modes are suppressed.

In the above example, there were only strong phonon peaks present in the STO layer. The situation is more complicated if there are phonon modes contributing from both the substrate and the film. Here we design a substrate with a dielectric function identical to STO but with the energy shifted 15 meV. This produces the dielectric functions with Im $\left[\frac{1}{\varepsilon}\right]$, both plotted in Figure 8.6a (the vacuum has Re[ε_C]=1 and Im[ε_C]=0). Now, we expect bulk phonon peaks in the substrate at 74 and 114 meV, and the bulk phonon peaks in the STO film at 59 and 99 meV. The full simulation of energy loss versus position are in Figure 8.6b. We see the addition of interface modes present at 107 meV at the substrate/film interface and 92.4 meV at the film/vacuum interface. The substrate peak at 74 meV is nearly completely overwhelmed by an interface mode at 73 meV, which has a long decay length from the interface.

The interfacial modes which are present at the film/substrate interface at 73 and 107 meV occurs where Re[ε_A] = -Re[ε_C] and Im[ε_C]=0 and Im[ε_A]<1. Inspecting Eq. 34, we can see that for small *ka*, we have an interface mode that has a term coming from Im[(ε_A- ε_C)/ (ε_A + ε_C)] – so when ε_A = - ε_C the denominator disappears and a strong interface mode is expected. Even though the interface mode arises from the intersection of region A and B, we see that in this case the mode is strongly determined by an interplay of the dielectric constants in regions A and C. If we change region A to activated carbon, which has a Re[ε_A] > 1 and a small imaginary component, or vacuum (as we will show for Figure 8.6d), these interface peaks are not observed because they do not cancel with the dielectric constant in the vacuum.

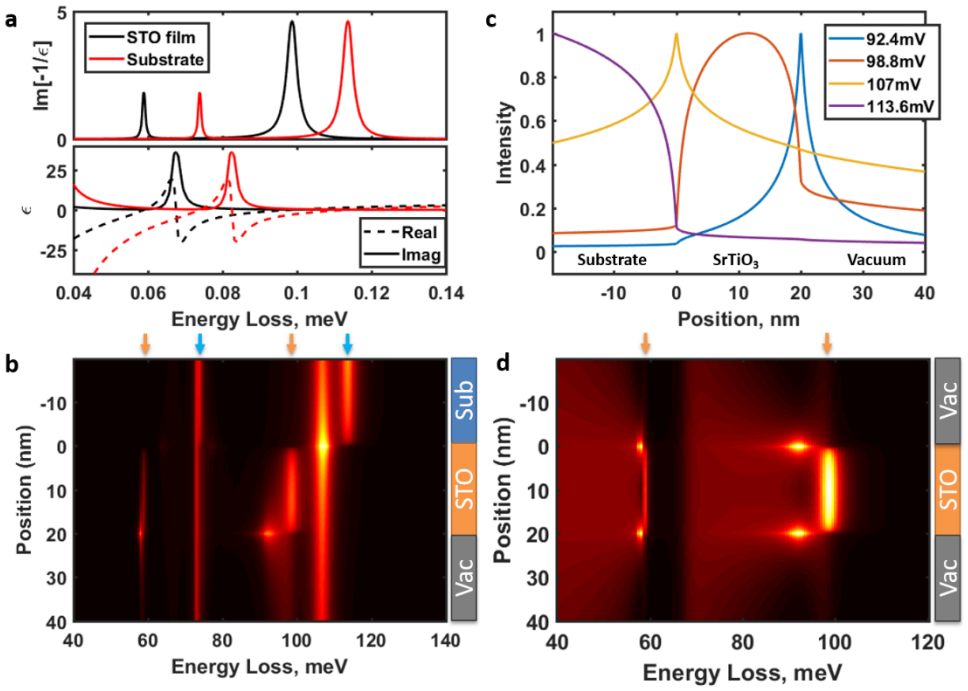

Figure 8.6. EELS spectra of phonon and interface modes in a thin film specimen with phonon modes in both the substrate and the film. In the $x<0$ region, there is the substrate, which is the same dielectric function as STO but with the energy shifted. In the $0<x<20$ nm region, there is STO, and in the $x>20$ nm region there is vacuum. a) dielectric functions of the substrate and STO and the corresponding energy loss function. b) energy loss versus position, showing phonon modes for STO are present at 59 and 99 meV, and in the substrate at 92 and 107 meV. Interface modes are observed at both interfaces which exponentially decay on either side. Orange and blue arrows mark bulk STO modes and substrate modes, respectively. c) shows profile plots of the substrate (114 meV), film (99 meV) and interface modes at 71 and 83 meV. d) the EELS spectra as a function of position in a vacuum/STO/vacuum sandwich.

We see the energy of the peaks observed for bulk STO and bulk substrate deviate by an meV at the interfaces for the 59 and 74 meV peaks. We can additionally compare the spectra observed in aloof mode to the spectra obtained in the substrate, film, and at both interfaces in Figure 8.6b.

The spatial profiles are shown in Figure 8.6c, showing interface modes exponentially decay away from the interface. We again find from Figure 8.6b-c that the scattering observed in aloof mode is determined not just by the thin film and the film/vacuum interface, but also by the substrate and the substrate/film interfacial modes.

The EELS spectra versus position is shown for a vacuum/STO/vacuum interface is shown in Figure 8.6d, showing that the interface modes in the substrate/STO/vacuum configuration that were identified as a combination of substrate and vacuum disappear. There are still interface modes which remain at 58 and 92 meV which that appear to be present in all STO/vacuum interfaces, which shift by an meV when the substrate material is changed. The spectra in the aloof mode in this case reflects a combination of the STO and the STO/vacuum interface, and is shifted ~3 meV from either the interface or the bulk STO mode.

8.4 Conclusions

In conclusion, EELS of phonon scattering in thin films will be susceptible to interface modes in a similar way as plasmon modes, but with lower energies and larger delocalization. The interface modes can extend beyond the interface for length scales that can be even larger than the film. Aloof beam geometry for scattering may be particularly suspect to interfacial effects, which depend on the hybridization of all three dielectric functions present in the system. The signal may become more localized and less suspect to interface modes with larger EELS collection apertures or off-axis detectors, but in that case, the *k* dependence must be included in the dielectric function as the dipole approximation may no longer hold.

References

[1] R. A. Ferrell, Phys. Rev. **101**, 554 (1956).

[2] R. A. Ferrell, Phys. Rev. **107**, 450 (1957).

[3] P. Nozières and D. Pines, Phys. Rev. **113**, 1254 (1959).

[4] O. L. Krivanek, T. C. Lovejoy, N. Dellby, T. Aoki, R. W. Carpenter, P. Rez, E. Soignard, J. Zhu, P. E. Batson, M. J. Lagos, R. F. Egerton, and P. a Crozier, Nature **514**, 209 (2014).

[5] C. Dwyer, T. Aoki, P. Rez, S. L. Y. Chang, T. C. Lovejoy, and O. L. Krivanek, Phys. Rev. Lett. **256101**, 1 (2016).

[6] M. J. Lagos, A. Trügler, U. Hohenester, and P. E. Batson, Nature **543**, 529 (2017).

[7] P. E. Batson, Ultramicroscopy **11**, 299 (1983).

[8] C. H. Chen and J. Silcox, Phys. Rev. B **20**, 3605 (1979).

[9] R. H. Ritchie, Phys. Rev. **106**, 874 (1957).

[10] A. Howie and R. H. Milne, Ultramicroscopy **18**, 427 (1985).

[11] M. Couillard, M. Kociak, O. Stéphan, G. A. Botton, and C. Colliex, Phys. Rev. B **76**, 165131 (2007).

[12] M. Couillard, A. Yurtsever, and D. A. Muller, Phys. Rev. B - Condens. Matter Mater. Phys. **77**, 1 (2008).

[13] J. P. R. Bolton and M. Chen, J. Phys. Condens. Matter **7**, 3373 (1995).

[14] J. P. R. Bolton and M. Chen, J. Phys. Condens. Matter **7**, 3389 (1995).

[15] N. W. Ashcroft and N. D. Mermin, *Solid State Physics* (Brooks Cole, 1976).

[16] C. Kittel, *Introduction to Solid State Physics, 8th Edition* (2004).

[17] P. Rez, Microsc. Microanal. **20**, 671 (2014).

[18] R. F. Egerton, *Electron Energy-Loss Spectroscopy in the Electron Microscope*, 3rd ed. (Plenum Press, New York, 2011).

[19] P. Rez, C. J. Humphreys, and M. J. Whelan, Philos. Mag. **35**, 81 (1977).

[20] R. F. Egerton, Microsc. Microanal. 1 (2014).

[21] D. A. Muller and J. Silcox, Ultramicroscopy **59**, 195 (1995).

[22] E. D. Palik, *Handbook of Optical Constants of Solids* (1998).

CHAPTER 9

CONCLUSIONS

9.1 Summary

Electrochemical liquid cell microscopy is a promising technique to explore the degradation and operation dynamics of energy related materials such as fuel cells and batteries. Here, we have shown that while low-loss EELS though liquids is feasible in relatively thin liquid layers (<6 inelastic mean free paths), core loss EELS is challenging in all but the thinnest liquid cells due to multiple scattering. Low-loss EELS provides a wealth of information on the electronic structure of the specimen, but prior knowledge of the specimen and its low loss spectra are required to use this method for chemical identification. As demonstrated for $LiFePO_4$, there are spectroscopic fingerprints for many battery electrode materials to indicate the state of charge, but most of the resulting changes in electronic structure may be at energies below 2 eV, requiring monochromation. In general, X-ray energy dispersive spectroscopy (XEDS) with a specially designed liquid cell holder that does not shadow the XEDS detector is a better fit for chemical identification in thick liquids.

Electrochemistry in the TEM is viable, and we have demonstrated it for fuel cell materials, observing the bending of carbon catalyst supports, carbonate formation in alkaline media, and shape degradation of octahedral Pt-Ni catalysts. We have also observed charging and discharging of the battery cathode $LiFePO_4$, and have used spectroscopic fingerprints in the low-loss to track the movement of Li-ions on the nanoscale. The combination of electrochemistry and liquid cell TEM requires a keen eye, careful thought, and control experiments to tease apart chemical, electrochemical, and beam-induced effects.

On the other front, atomic resolution STEM can provide a detailed view of the polarization, order parameter and domain structure in ferroelectric materials. In order to obtain accurate data from picometer scale atomic displacements, the crystal must be on-axis and thin enough that two domains do not overlap in projection. Collecting enough data to form a statistical picture of the sample provides information that may be missed or misrepresented by inspecting just a few images. Here, we inspect the picometer scale ferroelectric distortions in hexagonal $ErMnO_3$ and lutetium ferrite superlattices. Atomic resolution STEM uniquely allows us to experimentally probe how the order parameter changes at domain walls, vortices, and heterointerfaces. We find that there is a single length scale that describes the width of the domain walls, which is dominated by trimerization stiffness in the crystal but can be influenced by strong electrostatic effects. We additionally find that the trimerization displacements and the domain wall structure in lutetium ferrite superlattices enhances magnetism, forming a room-temperature multiferroic. *Ex situ* biasing experiments allow us to observe domain wall motion.

Finally, we find that interface modes for phonon scattering by EELS in thin films may play a large component in the ultra-low-loss spectra, as they do for plasmons at higher energies. However, due to the long-wavevector nature and extremely low energies for phonon scattering, delocalization is more severe. Off-axis geometries may help improve delocalization, but will make simulation of spectral features more challenging.

9.2 Future Work

9.2.1 Liquid Cell

JDFT from the Arias group (Deniz Gunceler) has proved very effective in identifying the solvated ion responsible for absorption in optical spectra measured by UV-VIS. For example, we observed a peak in optical absorption in a lithium sulfate aqueous solution, which was attributed

by JDFT to be $LiSO_4^-$. Work combining UV-VIS spectra and JDFT could provide identification of solvated ions in species. Extending that to EELS measurements in liquids may help characterize the excited states of different ions in liquid, especially those with large energy gaps.

The interaction between Pt-based fuel cell catalysts and carbon supports is one promising area for further investigations using *in situ* electrochemical STEM experiments. The onset of catalyst nanoparticle motion on the carbon support during extreme potential excursions may be a useful indicator of the stability of the carbon support against corrosion and the anchoring of particles on the support. For instance, we have observed Pt-Co particles at high potentials stay relatively stable on the support, while the shaped Pt-Ni nanoparticles are highly mobile. Because both catalysts were supported on Vulcan XC72 carbon black, it is possible that the synthesis technique impacts the anchoring of Pt particles on the carbon. Catalysts synthesized by impregnation methods, such as the Pt-Co specimen, are likely to be more stable than the particles dispersed on the support after solvothermal synthesis. Furthermore, the type of carbon support is also likely to impact the mobility of particles at high potential. Highly graphitic supports may have weaker adhesion to Pt particles than their more disordered counterparts, although their stability against carbon corrosion may also reduce Pt migration. *In situ* experiments to observe the onset of Pt migration may prove very informative, and perhaps less arduous than *ex situ* electrochemical cell to TEM experiments to observe the same events. The addition of ionomer or assembly of fuel cell electrodes may add additional effects to the catalysts degradation dynamics – although those effects may be more challenging to discern by liquid cell TEM.

Carbon-supported Pt particles may also be useful as a test case for further studies on electron beam interaction. High doses may corrode the carbon, similar to driving the sample to high potential, causing Pt particle motion, which is relatively easily discerned in *in situ* STEM. Trying to add scavenger species to the liquid cell to see if the damage rate slows is one interesting avenue. Preliminary results by our group found that acidic environments may be more beam friendly than

basic ones, and by doing better-controlled tests at different pH we may elucidate if this is a true effect. Additional insight on what conditions would best minimize deleterious beam effects while allowing the highest amount of dose (and therefore resolution) would be good practical knowledge for the *in situ* microscopist.

9.2.2 Oxide Materials

How the order parameter changes as a function of sample bias or approaching the critical temperature for ferroelectricity in hexagonal ferroelectrics has been studied by theory, but atomic scale details have not been elucidated. Approaching the ferroelectric transition temperature is challenging experimentally in bulk specimens because the critical temperature can be quite high – usually well above 1000 K. However, the superlattice lutetium ferrite superlattices had lower effective T_C, as evidenced by both XMCD and *in situ* STEM in an uncorrected machine, as well as by the order parameter measurements in STEM. Attempting the *in situ* STEM experiment in an aberration corrected machine to achieve Angstrom resolution could provide this information, if stable enough images could be acquired. Scanning diffraction can measure polarization on the nanoscale, but care would have to be taken to pick a sample with high crystallinity (with a small rocking curve), since the crystal mistilts dominate the diffraction pattern.

In situ and/or *ex situ* biasing of ferroelectric superlattices or bulk materials that have top and bottom electrodes is another promising route to explore ferroelectricity. While the *in situ* biasing experiments I have attempted at Lawrence Berkeley National Laboratory have unanimously failed to switch the material, bottom electrodes on the film would allow mechanically polished samples to be attempted, rather than FIB lift-outs. The polished sample would allow all regions of the film to be in electrical contact, eliminate transport through the highly resistive substrate, and allow study of a large array of thicknesses. Further improvement of the biasing holder to be a double-tilt biasing holder would make experimental success for a polished specimen more likely. The addition of

bottom and top electrodes may also make the *ex situ* biasing (by PFM or bulk methods) sample preparation more straight-forward, and in sample preparation there would be no concern of charging up the substrate and potentially affecting the polarization in the film.

There is an interesting interplay of ferroelectric and paraelectric domains and domain walls in the hexagonal manganite system. As we saw with $ErMnO_3$ and $LuFeO_3$, the ferroelectric domains intersected at a paraelectric domain wall with Φ values intermediate to the ferroelectric domains. They are also paraelectric materials, (such as $InMnO_3$, controversially) which have ferroelectric domain walls. Inspecting ferroelectricity at domain walls in paraelectric $InMnO_3$ may be another interesting avenue to explore by STEM. Combining the paraelectric material into superlattices with the ferroelectric material may make new combinations and free energy landscapes that could potentially access twelve distinct domains in the film – which would also be an avenue STEM could explore.

We have seen the promise of charged head-to-head walls in $ErMnO_3$, which have displayed electrical switching behavior which could one day be implemented in an all-domain-wall device. However, in $ErMnO_3$, these domain walls are few and far between (~micron scale). Within the lutetium ferrite superlattices, we were effectively able to confine these head-to-head walls to be in sheets within a defined window of a few nanometers in the sample. It would be interesting to attempt to measure the electrical properties of the domain walls in $LuFeO_3$ – first on the bulk scale with PFM and cAFM, if a specimen with the vortex domain structure can be formed. Then it may be interesting to try to grow a specimen that contain one charged, ferroelectric domain wall in the middle of the specimen. For example, if the domain walls in $LuFeO_3$ have interesting properties, growing a buffer layer of $LuFe_2O_4$ and a cap of $LuFe_2O_4$ should confine a head to head domain wall in the $LuFeO_3$ film. This geometry should be suitable for making switchable devices.

APPENDIX

A: METHODS FOR USING THE PROTOCHIPS ELECTROCHEMICAL CELL HOLDER

Presented in this Appendix is a guide to performing electrochemical cell experiments.

1. Clean the liquid cell chips, carefully (they are fragile).
    a. Only use carbon fiber tweezers to handle chips. Metal tweezers can crack the silicon.
    b. Check for damage of the chips in an optical microscope.
    c. Soak in ~30 mL acetone for ~5 minutes (do NOT sonicate)
    d. Soak in ~30 mL methanol for ~5 minutes (do NOT sonicate)
    e. Rinse in ultra pure water. Let rest to dry (blow dry at your own risk, only parallel to surface).
    f. Plasma clean (maximum of 30 seconds for chips with carbon electrodes, 3 minutes for chips without carbon electrodes). This makes the surface hydrophilic.
    g. Check for damage of the chips in an optical microscope. Any dark features in the SiN window is a BAD SIGN that the window is broken. Do not use chip.
2. Deposit nanoparticles onto chip.
    a. Sonicate dispersed nanoparticles for 5-10 minutes.
    b. Immediately dispense a small amount (3 μL) onto center of big chip using micropipette. You may have to touch liquid drop onto the surface of the chip to get it to leave micropipette tip, but do not touch chip with micropipette tip!
    c. Let dry. Check in optical microscope. Huge clumps of particles are a bad sign. It will make your cell too thick or puncture your window. Particles should be barely visible (or even invisible) in optical microscope.
        i. If there are clumps visible in optical microscope, rinse the chip with water or methanol to try to remove clumps and dispense another drop.
        ii. If you see nothing stuck to chip, you can dispense another drop if you wish, but because you are probably looking at nanoparticles, it is okay not to see anything by eye.
3. Prepare the holder.

a. Unscrew two screws near tip completely, and loosen but do not remove screw closer to base.
b. With carbon fiber tweezers, remove the tip by gently lifting it up and then pulling it out (along the axis of the holder rod).
c. Clean the tip in acetone and methanol, and verify there is no debris stuck to tip.
d. Under a stereoscope, inspect the holder tip (typically needed once per session).
    i. Remove the o-rings and make sure they are debris-free and properly greased (spread the *tiniest* amount of proper o-ring grease on finger of clean glove, then rub o-ring gently in between gloved fingers.) Replace o-ring if it looks swollen or damaged.
    ii. Verify that the o-ring groove has no debris
    iii. Verify that the chip grooves have no debris
    iv. If debris is found, dip tip of holder in solvents (ask John Grazul to show you if you have not done this before)
    v. For stubborn debris, you may gently use a toothpick to dislodge
    vi. Rinse tip in methanol and dry
    vii. Replace o-rings
e. Assemble the holder
    i. Insert small chip into groove on top of o-ring, membrane face up.
    ii. Optional: dispense 0.5 μL of water (or solution) onto small chip using pumping station and microfluidic tube (Pro: skip time flowing in liquid later. Con: can make thicker liquid layers if you dispense too much).
    iii. Place the large chip face down on the small chip, lining up the electrical contacts on the chip to the pads in the holder.
    iv. Use carbon fiber tweezers to fine-tune the position within the pocket (if necessary).
    v. Replace tip of holder, tightening screws with torque screwdriver.
    vi. With ohm-meter, verify that the electrical contacts between chip and holder are not shorted out (between the permutations of working electrode (WE), reference electrode (RE) and counter electrode (CE)). Typical values for an air-filled cell are >40 MΩ (or open), and for water-filled cell are >10 MΩ. Anything less than 5 MΩ is suspect. You can try to gently loosen screwdrivers and jiggle chips into place and retighten. Otherwise you must re-assemble.

vii. Verify that the holder holds vacuum in the pumping station. Pressure must go down below at least 1e-4 T while pumping on holder, or there is a leak.

f. Check PEEK microfluidic tubing for clogs
    i. Attach the syringe to one of the tubes and manually depress the syringe until you see liquid exciting the tubing.
    ii. Repeat for other tubing.
    iii. Connect tubing to holder, and put syringe in pumping station (do not try to manually depress liquid through the SiN chips!)
g. Set the flow rate to 100 – 300 μL/hr and flow liquid through the cell.
    i. Quick Start → Method Select → Infuse Only, enter the rate and push start
h. Flow liquid for 15-30 minutes
i. Meanwhile, get potentiostat set up
    i. Connect computer to Gamry potentiostat, and start Gamry Framework.
    ii. Connect Gamry to liquid cell (WE, RE, and CE only)
    iii. Check for liquid presence using electrochemical impedance spectroscopy (EIS) at 5 kHz. If there is no liquid, reading will be unstable, and the impedance will be purely capacitive (phase ~ -90 deg). When there is liquid, the impedance will be a mixture of resistive and capacitive so the phase will be around -45 degrees and the resistance with be lower (< MΩ).
j. Check for good electrochemical behavior.
    i. Ensure there is no unexpected current in your cell.
    ii. Huge current may be a sign that the window broke.
k. Load holder into *already aligned* microscope
    i. Monitor vacuum for leaks. If pressure does not go down (hovers at pressures >18 log or creeps up), remove the holder, there is a leak
    ii. Once pressure is sufficiently low, open column valves. In low mag mode, try to find the viewing window.
    iii. Focus on edge of viewing window using z-height
    iv. Get a feel for liquid thickness by how diffuse beam is.
l. You are ready to do the experiment. For troubleshooting, see Appendix B.
m. After use: flush entire system with water overnight, using fresh chips if you want to save the current chips for future analysis.

APPENDIX

B: EXPERIMENTAL TIPS TO ACQUIRING *IN SITU* DATA

The procedure and mind-set for taking *in situ* TEM data is different than for acquiring *ex situ* data. This is primarily because with *in situ* data, you are trying to best observe a process occur over a period of time. If the process is fast, you must obtain the appropriate data before the process you are trying to observe is over. If the process is slow, you must not accumulate too much beam damage before the *in situ* event is completed. With *ex situ* studies, you can probe the material for as long as your microscope time allows. Because larger sample sizes are typically involved in *ex situ* studies, you can investigate fresh part of the sample for each measurement, circumventing beam damage. With *in situ* studies, you often get one area (ie, one electrode), and if you do not take the data correctly the first time, you may be required to start over. Therefore, *in situ* experiments benefit from advanced planning and thought into what types of data should be acquired. However, *in situ* experiments usually don't go as planned, and good backup plans and the ability to think on your feet are important to success.

The other recommendation I have for *in situ* experiments is to check every step along the way to make sure everything is still fine. For example, after cleaning the chips, inspect them to make sure the silicon nitride window is intact, there is no debris on the chips, and that any electrical contacts look good. After depositing particles on the chips, check the chips again to see if there are particles where you want them, that the window is still fine, and that there aren't large clumps of particles elsewhere. After every step, make sure nothing has gone wrong. This method takes longer to perform straight through, but if something does go wrong and you do not catch it immediately, you will potentially waste hours of effort, reducing your probability of success on any given day.

Here I outline my tips for doing *in situ* experiments. The bulk of this applies directly to liquid cell and especially electrochemical cell experiments, but some tips are generalizable to my experiences during *in situ* biasing and heating experiments.

Before the day of your experiment:

1. Think about what process do you want to observe
    a. Time scale of the experiment
        i. The frame time for imaging must be able to capture steps in the reaction with enough signal to noise, but without damaging the material.
        ii. If the time scale is very large, plan to limit the dose across the experiment.
        iii. For example, for 10 minute cyclic voltammogram experiment (25 cycles at 100 mV/s over 1.2 V), a typical setup for STEM is a dwell time of 8 microseconds with 512 x 512 pixels (10 images per cycle). A typical dose is 30-60 e-/nm^{2}s for carbon supported Pt nanoparticles.
    b. Imaging mode(s) for the experiment
        i. What will give you the most useful kind of data?
    c. Plan what data you hope to collect
        i. What electrochemical / chemical / biasing / heating steps do you want to do?
            1. Do conservative initial experiments, only applying extreme conditions in the final stages of the experiment
        ii. How and when will you acquire images during the biasing?
2. Prepare: get everything ready for the experiment (takes ½ to 1 day of work)
    a. If you are doing this with a collaborator (recommended), discuss with them
    b. Prepare chips
        i. Ensure they are clean
        ii. If depositing particles, ensure they are well dispersed and not clumped.
    c. Verify that the equipment is available and ready (Potentiostat, holder, syringe pump)
    d. Prepare chemicals
    e. Recommended: test electrochemical response of system before microscope time begins
    f. Prepare yourself

Doing the experiment

3. Before loading:
    a. Check for electrical contact and presence of liquid with EIS.
    b. Check that the liquid cell holds vacuum
    c. Prepare imaging conditions on microscope
4. Once loaded, check quality of imaging. Are the conditions good enough to observe the process you want to observe? If not, troubleshoot. If so, proceed.
5. Do beam dose control experiment – especially critical for environmental work
    a. Image for roughly the time scale of each imaging experiment and lower the dose until you see no effects from the electron beam.
6. Take "before" images of promising regions of interest, and save their locations in the stage
7. Pick a good region (thin liquid, representative material) and begin *in situ* experiment.
8. Between biasing experiments, and at the end of the experiment, do beam dose checks.
    a. Image on and off the electrode (is the electrode causing the observed effect?)
    b. Image regions that haven't previously been imaged, but that have undergone the reaction (is the electron beam responsible for all or some of the observed effect?)
    c. Move to new areas which haven't been irradiated
9. If things go well, estimate thickness of liquid cell or specimen with EELS for your records
10. If at any point, the conditions degrade, troubleshoot

Troubleshooting liquid cell experiments

11. The liquid cell is loaded in the pumping station but not reaching base pressure (~8e-5)
    a. There is a leak, do not load into microscope
    b. Ensure the liquid cell tip is flush with holder. If so, that's the problem.
    c. Unload chips, check to see if the windows are broken. If so, that's the problem.
    d. Remove and inspect o-rings. Clean debris and apply a *tiny* amount of o-ring grease. If o-rings look damaged, replace them.
    e. Clean o-ring grooves in holder using solvents (methanol, IPA) and particle-free Q-tips.
    f. Clean tip of holder

g. Reload holder with unbroken chips and good o-rings.
h. If problem persists, despite everything else looking fine, an internal component may be broken in the holder.

12. The liquid is too thick
    a. Borderline too thick
        i. Stop infusing liquid into cell
        ii. Try withdrawing liquid from cell
        iii. Wobble holder and hope for good luck
        iv. If no improvement in 20 minutes, consider changing chips or proceeding anyway
    b. Way too thick
        i. Unload and start over with a new, clean chip
        ii. Use a small chip with no spacer or 50 nm spacer. Ensure it is completely clean.
        iii. Ensure that there are no clumps of nanoparticles visible on chip by optical microscopy on the SU8 protective layer
        iv. Reload cell, flow in liquid at <= 300 μL/hr.
        v. As soon as you notice liquid is present, slow to <=100 μL/hr.
13. There is no liquid there
    a. Ensure chips were plasma cleaned within last 24 hours
    b. Ensure holder lines are not clogged (is liquid coming out the other side of the holder?)
    c. Try slightly larger spacer chip (50 nm or 100 nm)
    d. Flow the liquid at different flow rates to break up equilibrium flow around chip
    e. Wobble the holder
    f. If no liquid after 1 hour, try reloading. If continued bad luck, try dropping the tiniest drop of water (<1 μL) using the syringe pump onto the chip before loading.
14. Liquid is not coming out the outlet even after flowing liquid a long time
    a. Check for leaks on inlet port, outlet port, and at chip window (or column pressure)
    b. If a leak is observed, reset microfluidic tubes or replace chip and try again
    c. If it doesn't get better, unload the chip. There may be a clog in the lines
    d. By pushing on the syringe with your hands, try to verify that liquid can flow through both the inlet tube and the outlet tube
    e. Using the syringe pump, flow liquid through both tubes

f. If you can't flow liquid, there is a clog in the tubes
g. If you can flow liquid, reload the chips and try again

15. Electrochemical signal is noisy
    a. Random noise: verify all connections are secure
    b. AC noise: verify all connections are secure. If it persists, use I channel filter.
16. Electrochemical signal is wildly large or unexpected
    a. There may be liquid outside of the o-ring or the SiN window is broken. Do not load into microscope (try pumping in the pumping station, then check again).
    b. If it is holding vacuum, proceed to troubleshoot, otherwise, unload and reload.
    c. There may be a bubble in the holder. Flow liquid (150-200 μL/hr) for 5-10 minutes and check again.
    d. If it is still wild, perform a "window opening" cyclic voltammogram. Perhaps the reference electrode is not calibrated as you expect. Find the potential range slowly. If you encounter a large current, flow liquid and wait again.
    e. If it gets worse or never gets better, chip may be damaged. Replace chip.

APPENDIX

C: ATOM TRACKING

In this section I will roughly outline the steps followed to obtain the polarization mapping images. There are three steps: 1) acquire acceptable data, 2) find the atomic positions, and 3) extract meaningful information and statistics from the atomic positions.

The first ingredient of atomic-tracking STEM measurements is well-resolved, high-signal-to-noise, and distortion-free images. To that end, images must have minimal probe tails and be well sampled. For example, in the $LuFeO_3$ system, the [110] projection which displays the trimerization rumpling has an atomic spacing of 1.7 Å per Lu ion, and I sampled at roughly 5-10 px/Å, resulting in 8-17 pixel periodicity between atomic columns. 8 pixels between atoms is probably cutting it too close – the fitting behaved better at higher values. Many fast STEM acquisitions were acquired and cross-correlated to form a high-signal-to-noise, distortion-free image. The individual scans must be quick enough to remove most effects of specimen drift, or the rigid registration will blur the image noticeably. Registration removes random scan distortions and scan noise, but cannot remove scan distortions which are present due to scan system miscalibration and are thus present in every image. In the NION system, for example, the "fly back" time of the beam from the end of one scan row to the next must be calibrated to minimize distortions at the edges of the images. Even for large fly back times, the distortion is still present – and one cheap way to solve the problem was to crop off the edge which experienced severe distortions. Another method of providing high-signal-to-noise, distortion-free images which can solve the inherent scan distortion problem is by nonlinear drift correction from two high-signal scans which are taken at 90 degrees from one another [1]. Colin Ophus's code implements this nicely to form high quality distortion free images, but fails on images which may have too much drift (a work-around is to put in several fast scans at 0 deg and 90 deg, although this slows the code considerably). There are several groups who have

been working on forming ideal images to achieve sub-picometer precision – notably using non-rigid registration [2], so-called rev-STEM where the scan direction is rotated many times [3], and spiral scanning geometries [4] – although the methods presented here achieve 2 pm precision which is suitable.

Once the image has been made, the next task is to find the atomic positions. For this, I wrote a code in MATLAB with the following steps, which are outlined in Figure A.1[15]:

1. Filter or smooth the image. I performed a Wiener Filter.
2. Background subtract the image so there is no gradual intensity gradient (ie from thickness deviations). To do this, I used a morphological opening operator (imopen.m) with a structuring element the shape of a disk with a radius of 1 nm to form the background.
3. Threshold the image. I used a threshold value of roughly 1.7 times the value estimated by Otsu's method, tailored by hand to the specific atomic numbers of the system.
4. Use regionprops.m to identify all the individual thresholded regions.
5. Use a watershed algorithm to split any atoms which were not fully separated by thresholding.
6. Manually fixed any incorrect or missing atomic positions using ginput.m – the initial threshold was adjusted such that this was only adjusting a few percent of the atoms.
7. Go atom by atom and performed 2D gaussian fitting of the form:

$$I = a \exp\left(\frac{(x-x_0)^2}{2\sigma_x^2} + \frac{(y-y_0)^2}{2\sigma_y^2}\right) + b$$

Where I is the intensity, x and y are the coordinates of the image, x_0 and y_0 are the fitted centers of the gaussian, σ_x and σ_y are the fitted widths of the gaussian, and a and b are fit parameters that scale the intensity.

[15] With assistance from Robert Hovden. Code available at reasonable request.

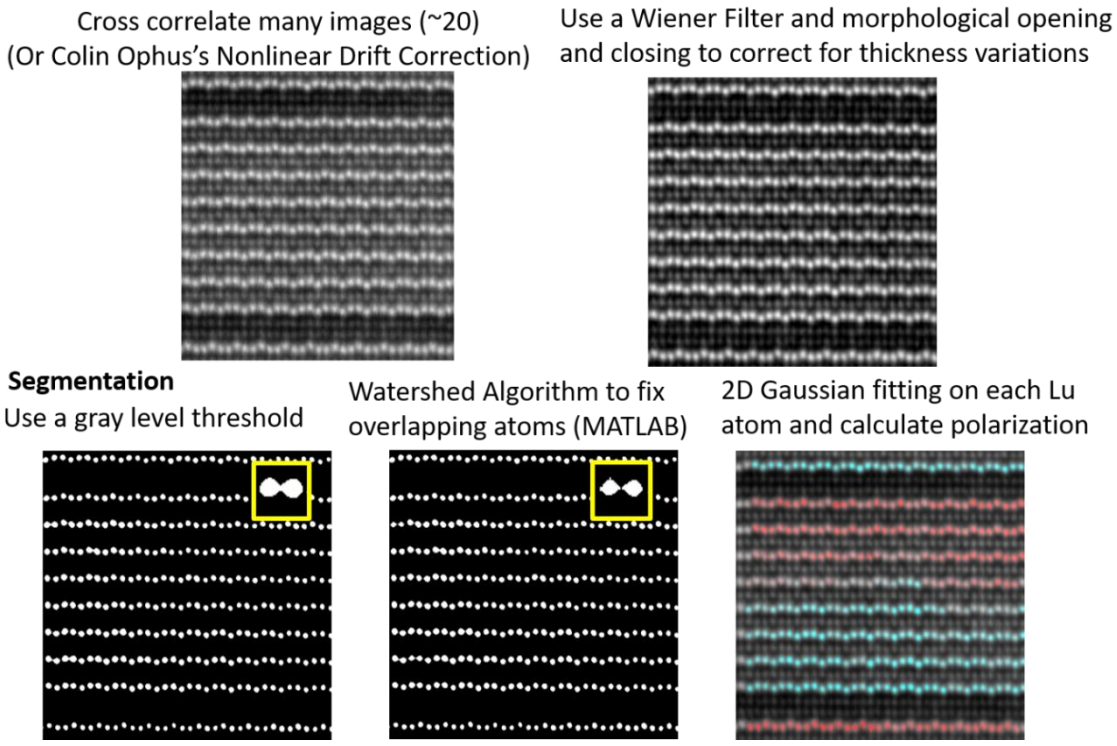

Figure A.1. Outline of the steps for finding the atomic columns. After cross-correlating many fast-scan acquisitions, the image was wiener filtered and background subtracted. Then, segmentation was performed first by using a gray level threshold, followed by the watershed algorithm to fix atomic locations that blurred together. Finally, 2D gaussian fitting was used to find the center of each atomic column.

Finally, once the atom positions are found, parameters must be extracted to identify the polarization and order parameter. The challenge in this case is organizing the data within MATLAB in a way which is flexible and easily accessible, especially when the number of images and atoms are quite large.

References

[1] C. Ophus, J. Ciston, and C. T. Nelson, Ultramicroscopy **162**, 1 (2016).

[2] A. B. Yankovich, B. Berkels, W. Dahmen, P. Binev, S. I. Sanchez, S. A. Bradley, A. Li, I. Szlufarska, and P. M. Voyles, Nat. Commun. **5**, 4155 (2014).

[3] X. Sang and J. M. LeBeau, Ultramicroscopy **138**, 28 (2014).

[4] X. Sang, A. R. Lupini, R. R. Unocic, M. Chi, A. Y. Borisevich, S. V Kalinin, E. Endeve, R. K. Archibald, and S. Jesse, Adv. Struct. Chem. Imaging **2**, 6 (2016).